Advanced Measurement Techniques and Circuits for Array-Based Transit-Time Ultrasonic Flow Meters

van Willigen, D.M.

DOI
10.4233/uuid:e2f4b411-3d8e-4b93-b037-096009c59f61

Publication date
2022

Document Version
Final published version

Citation (APA)
van Willigen, D. M. (2022). *Advanced Measurement Techniques and Circuits for Array-Based Transit-Time Ultrasonic Flow Meters*. [Dissertation (TU Delft), Delft University of Technology]. https://doi.org/10.4233/uuid:e2f4b411-3d8e-4b93-b037-096009c59f61

Advanced Measurement Techniques and Circuits for Array-Based Transit-Time Ultrasonic Flow Meters

Advanced Measurement Techniques and Circuits for Array-Based Transit-Time Ultrasonic Flow Meters

Dissertation

for the purpose of obtaining the degree of doctor
at Delft University of Technology
by the authority of Rector Magnificus prof. dr. ir. T. H. J. J. van der Hagen
chair of the Board for Doctorates
to be defended publicly on
Thursday 15 September at 12:30 o'clock

by

Douwe Manuel VAN WILLIGEN

Master of Science in Electrical Engineering,
Delft University of Technology, the Netherlands

born in de Bilt, the Netherlands

This dissertation has been approved by the promotors.

Composition of the doctoral committee:

Rector Magnificus,	Chairperson
Dr. ir. M. A. P. Pertijs	Delft University of Technology, promotor
Prof. dr. ir. N. de Jong	Delft University of Technology, promotor
Independent members:	
Prof. dr. -ing. R. Brederlow	Technische Universität München, Germany
Prof. dr. -ing. M. Vogt	Ruhr Universität Bochum, Germany
Dr. ir. R. J. Wiegerink	University of Twente
Prof. dr. K. A. A. Makinwa	Delft University of Technology
Prof. dr. P. J. French	Delft University of Technology, reserve member
Other members:	
Dr. ir. P. L. M. J. van Neer	Delft University of Technology

This work was supported by the research programme FLOW+, which is financed by the Dutch Technology Foundation STW and industrial partners Bronkhorst and KROHNE under project 15031.

Printed by: Ridderprint | www.ridderprint.nl

Cover by: Douwe van Willigen, based on FEM simulations performed in PZFlex.

This dissertation was printed on 100 % recycled paper in an effort to minimize the environmental footprint.

An electronic version of this dissertation is available at http://repository.tudelft.nl.

Contents

Acronyms

ADC	Analog-to-Digital Converter.
ASIC	Application-Specific Integrated Circuit.
AWG	Arbitrary Waveform Generator.
BCD	Bipolar-CMOS-DMOS (*IC technology*).
DAC	Digital-to-Analog Converter.
FEM	Finite-Element Method/Model.
FFT	Fast Fourier Transform.
FPGA	Field-Programmable Gate Array.
GBP	Gain-Bandwidth Product.
IC	Integrated Circuit.
ID	Inner Diameter.
IFFT	Inverse Fast Fourier Transform.
LNA	Low-Noise Amplifier.
MAD	Mean Absolute Deviation.
MUX	Multiplexer.
NDE	Non-Destructive Evaluation.
OD	Outer Diameter.
OTA	Operational Transconductance Amplifier.
PCB	Printed Circuit Board.
PD	Percentile Difference.
PRF	Pulse Repetition Frequency.
PWM	Pulse-Width Modulation.
PZT	Lead Zirconate Titanate (*piezo material*).
RMS	Root-Mean-Square.
RX	Receive.
SNR	Signal-to-Noise Ratio.
STD	Standard Deviation.
TIA	Trans-Impedance Amplifier.
TTD	Transit-Time Difference.
TX	Transmit.

1

Introduction

Flow measurement is used in a wide variety of applications to measure the velocity of fluids flowing through pipes. In industry, flow measurement is essential to guarantee process quality. Several types of flow meters exist, ranging from devices that measure flow with mechanically moving parts (positive displacement flowmeters), to flowmeters that measure changes in an electromagnetic field to calculate the flow speed of conductive liquids [1]. This thesis focuses on transit-time ultrasonic flow meters: a type of flow meter that uses acoustic waves to measure the flow velocity. Ultrasonic flow meters are attractive because they are relatively cheap, do not disturb the flow, and can be used with many different liquids and gasses.

This chapter introduces the concept of ultrasonic flow measurement and some of the difficulties in performing accurate measurements. Moreover, a flow meter based on array transducers will be introduced. Finally the organization of this thesis will be discussed.

1.1. Measurement Principle

In transit-time ultrasonic flow measurement two transducers penetrate the pipe wall and are in contact with the fluid that flows through the pipe. An acoustic signal is transmitted through the fluid, as shown in Figure 1.1. The acoustic path from transducer A to transducer B has a vector component parallel to the flow. As a result, the acoustic wave traveling with the flow (downstream) is faster than the acoustic wave traveling against the flow (upstream). The difference in speed results in a transit-time difference between an upstream and downstream measurement [1]. This time difference (Δt) is

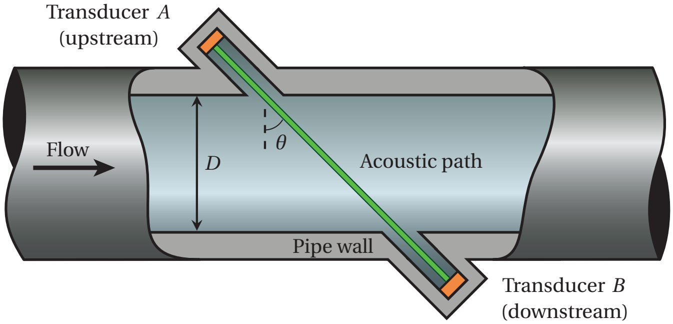

Figure 1.1: Diagram of an in-line transit-time ultrasonic flow meter.

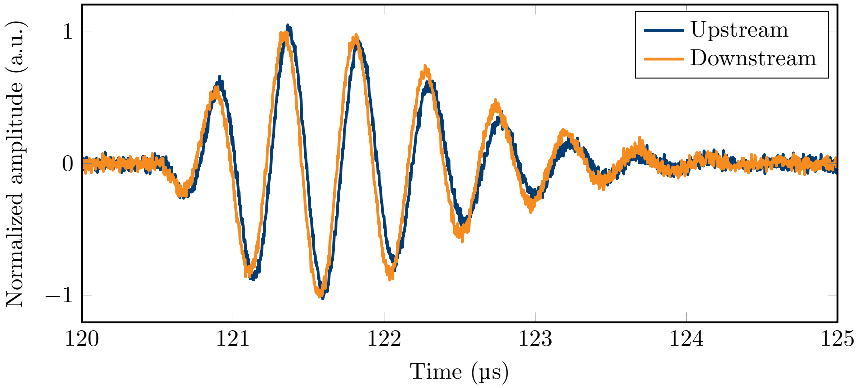

Figure 1.2: Received signals of a typical flow measurement with 2 MHz transducers, in a 40 mm diameter pipe, at a 0.5 m/s flow.

proportional to the flow velocity of the fluid:

$$v_m = \frac{D}{\sin(\theta)} \frac{\Delta t}{T_u T_d}, \tag{1.1}$$

where v_m is the measured mean flow velocity, D the inner-diameter of the cylindrical pipe, T_u and T_d the upstream and downstream transit times, respectively. The angle θ is the angle of the acoustic beam relative to the plane perpendicular to the pipe axis.

A flow measurement is performed by transmitting an acoustic pulse alternately with the upstream (A) and downstream transducer (B). The transducer that is not being used in transmission is used to receive the acoustic signal. Figure 1.2 shows the electrical signals of a typical flow measurement. These signals represent the acoustic pulse received by

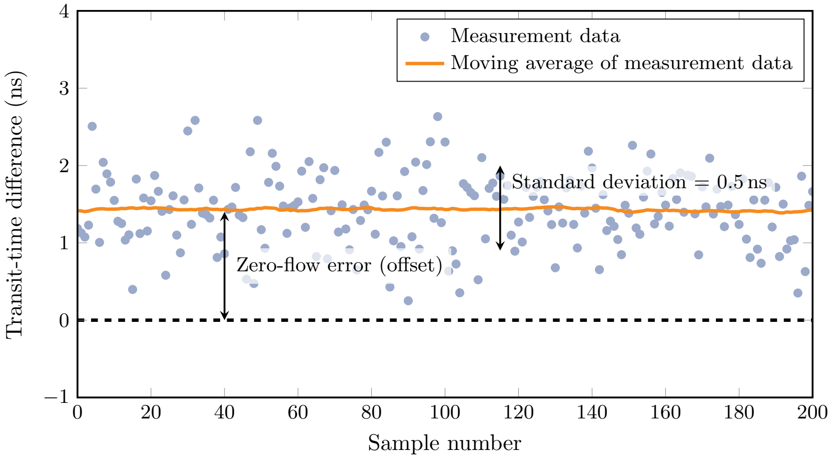

Figure 1.3: A typical flow measurement at zero-flow condition.

the upstream and downstream transducers at a mean flow velocity of 0.5 m/s. A time-difference between the upstream and downstream signal can be clearly distinguished. With lower flow velocities this time-difference becomes smaller, making it increasingly harder to accurately calculate the flow velocity.

1.2. Measurement Accuracy

Several factors influence the accuracy of a flow meter. Like any other measurement principle, a high signal-to-noise ratio (SNR) is important to achieve a good measurement precision. In transit-time flow measurement, this also means that the time-jitter of the readout equipment has to be low. Jitter requirements with a standard deviation (STD) below 1 ns are very common. An example flow measurement is shown in Figure 1.3. In the measurement several things can be noted. The measurement is not a constant value, but jumps around the actual flow value. These variations are caused by several factors, such as jitter of the measurement equipment or a low SNR of the receive signal but it can also relate to variations in the flow velocity. A common way to increase the precision is by implementing some type of averaging. However, averaging always comes at the cost of increased measurement time and therefore a lower measurement rate.

Another effect often seen in flow measurements is offset, commonly referred to as the zero-flow error [2]. In Figure 1.3 the zero-flow error is about 1.5 ns. The source of the zero-flow error will be discussed in more detail in Chapter 2. Clearly it is not desirable as an offset results in measured flow, even in the absence of any flow.

Commonly a measurement is simply represented by a transit-time difference (as is also

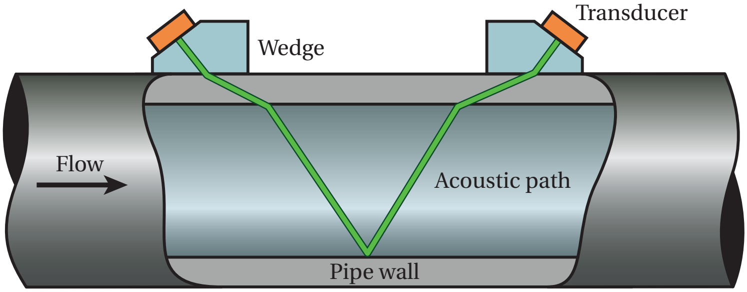

Figure 1.4: Diagram of a clamp-on ultrasonic flow meter.

done in Figure 1.3). This, however, means that a lot of data in flow measurements is discarded. By looking closer at the transient waveforms, more information can be obtained to improve measurement accuracy. In Chapter 3 an algorithm is presented that uses the extra information contained in the waveform to significantly reduce the zero-flow error, while using the same measurement setup.

1.3. Non-Intrusive Metering

Ultrasonic flow meters are especially attractive in applications where the pipe wall cannot be pierced. Since ultrasonic waves can also travel through the pipe wall, transducers can be placed on the outside of the pipe and still be used to measure flow velocity of the liquid or gas inside it. This method is called clamp-on flow measurement [3, 4]. It is so attractive, because the process does not have to be interrupted for installation, which in some industries can be very costly. Moreover, clamp-on flow measurement also guarantees intrinsic safety: In applications where, for example, dangerous gasses are used it is important to leave the wall of the pipe completely intact.

A diagram of a clamp-on flow meter is shown in Figure 1.4. It is common to have the transducers on the same side of the pipe to aid transducer alignment upon installation. The angle of the acoustic beam is defined by the angle of the wedge and can therefore not be adjusted. As a consequence, the transducers have to be positioned in such a way that the acoustic beam hits the receive array. Optimal positioning is dependent on the thickness, material and diameter of the pipe, and on the fluid properties. This alignment process is performed manually and can be time consuming.

Clamp-on flow measurement comes however with more challenges. The transducers not only generate waves that travel through the pipe wall into the fluid, but also cause waves that travel inside the pipe wall, called guided waves. These spurious waves can interfere with the measurement, causing significant errors [5]. Moreover, when mounted close to

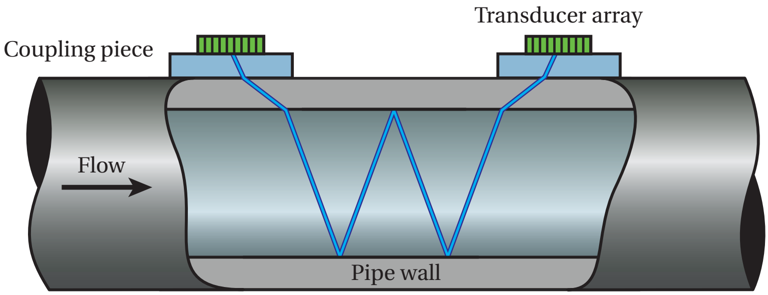

Figure 1.5: Diagram of the array-based clamp-on ultrasonic flow meter.

a flange, these spurious waves could also reflect causing even more disturbance of the acoustic signal that contains the flow information.

1.4. Array-Based Flow Metering

A potential solution to many of the drawbacks seen in clamp-on ultrasonic flow measurement can be found by employing transducer arrays. Such arrays consist of tiny transducer elements that together form a transducer that has the ability to steer an acoustic beam [6]. Transducer arrays have been used in the context of flow measurement to compensate for beam sweeping in high speed gas flow meters [7]. A multi-path flow meter that uses an array in combination with several single-element receivers was also presented [8].

An array of transducer elements placed on the pipe wall would allow the acoustic beam to be steered towards the receiving array, making manual alignment superfluous [9]. Moreover, various signal-processing techniques can be used to increase the measurement accuracy and reduce the influence of spurious waves in the pipe wall.

A conceptual diagram of a flow meter based on transducer arrays is shown in Figure 1.5. The two arrays are placed on a flat wedge (or coupling piece) and steer the acoustic beam towards the other array.

For the work throughout this thesis, transducers have been fabricated from pieces of PZT (Lead Zirconate Titanate) piezo material diced into small elements using a diamond saw. This process is described in detail in appendix A.

Steering can also be done in other directions, by employing a matrix array. A matrix array is a 2-dimensional array of transducer elements, and as such can steer in two directions. This creates additional opportunities, as the acoustic beam can be steered towards the circumference of the pipe, enabling additional measurements.

Chapter 4 describes the design process of a matrix transducer specifically made for

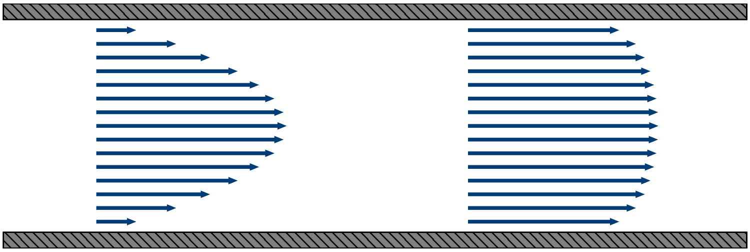

Figure 1.6: Average velocity profile of a laminar and turbulent flow. The arrows indicate the flow direction and their length the flow speed.

clamp-on flow measurement. All individual elements of the matrix transducer have to be actuated and read-out electrically, requiring a large and complex circuit. To keep the circuit compact, an application specific integrated circuit (ASIC) is designed. This circuit and its characterization are discussed in detail in Chapter 6.

The ability to steer the acoustic beam opens new opportunities in flow measurement, one of which is automatic calibration of the flow meter. Chapter 8 investigates additional measurements that can be performed with clamp-on matrix arrays, to determine the speed of sound in the liquid as well as the diameter and thickness of the pipe. When these properties can be measured automatically upon installation, it is no longer necessary to manually enter them.

1.5. Flow Velocity Profiles

Ultrasonic flow measurement with two transducer elements is limited to average flow velocity [10]. In reality the flow velocity is not constant over the pipe's cross-section, but higher in the center and lower towards the pipe-wall. In order to measure volumetric flow it is important to know the shape of this velocity profile. Figure 1.6 shows velocity profiles of a laminar and turbulent flow, with the same maximum velocity (based on the power law model [11]). It is evident that these two flow regimes have a very different velocity distribution that cannot be simply estimated based on an average value.

Matrix transducers enable the possibility to measure the flow speed via multiple acoustic paths. With sufficiently different acoustic paths it should it theory be possible to calculate the shape of the velocity profile. In Chapter 9 we will investigate whether it is feasible to measure velocity profiles with clamp-on matrix transducers. Moreover, we look at the requirements and physical limitations of such techniques.

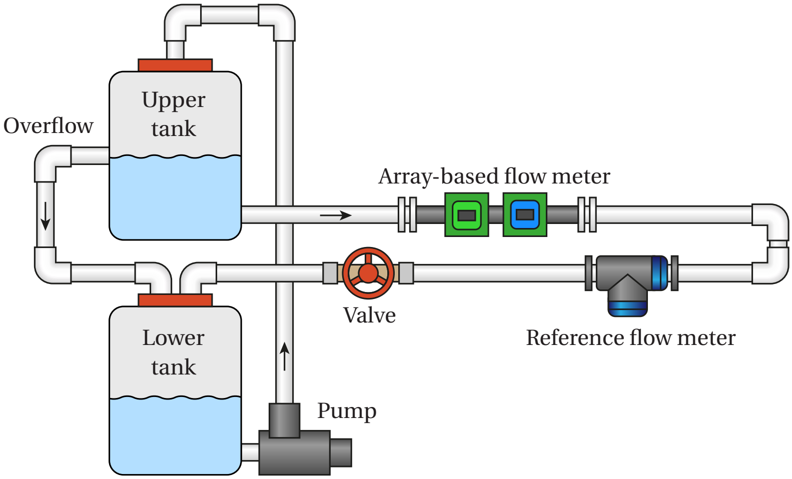

Figure 1.7: Functional diagram of the flow loop.

1.6. Measurement Setup

In order to perform flow measurements, a constant fluid flow has to be available. The setup regularly used for measurements in this thesis is a system of pipes with a 40 mm inner diameter. The setup can generate flow speeds between 0.00 and 0.60 m/s and will be referred to as the flow loop throughout this thesis. A flow loop is a closed system of pipes with a pump that recirculates a fluid at a given flow speed, as shown in Figure 1.7. Small variations in pump speed should not affect the flow speed, therefore the actual speed in our setup is determined by the water-level in an upper holding tank. An overflow-pipe makes sure the water level is constant, as long as the pump supplies more water than is flowing through the measurement pipe. A valve at the end of the measurement pipe regulates the flow speed while excess water directly returns to the lower holding tank via the overflow. Naturally, one has to wait a little while for the flow speed to settle before performing a measurement, since the overflow is not a high-speed feedback loop. It is however a simple and reliable method of creating a constant flow speed, that proved valuable in many measurements throughout this work. A picture of the flow-loop is shown in Figure 1.8. The steel section with the array-based flow meter is replaceable and will be used in the first few chapters in conjunction with an in-line flow meter.

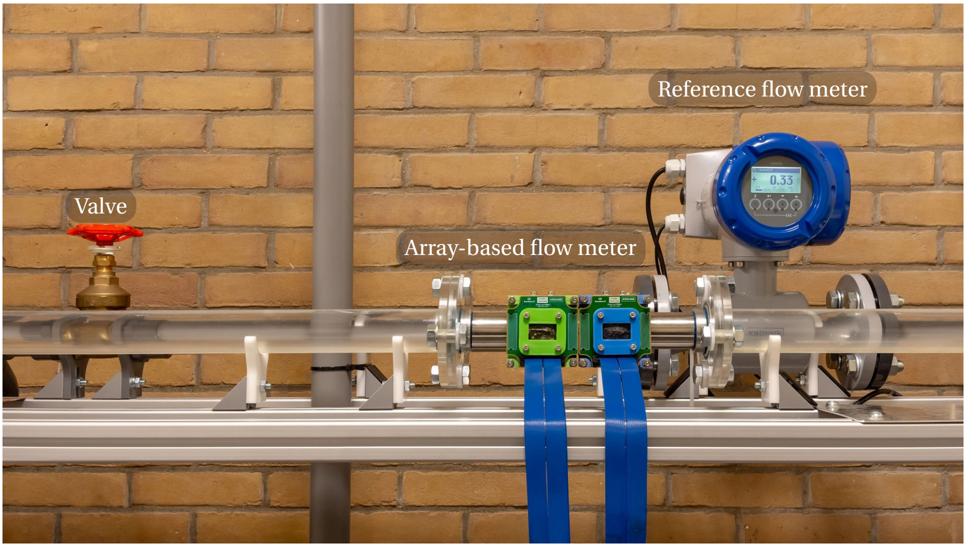

Figure 1.8: Flow loop filled with water, constructed with 40 mm inner-diameter pipes.

1.7. Thesis Outline

This thesis is written in three parts.

Part 1 discusses the origin of zero-flow errors and how the circuit that is used to drive the transducers can be optimized to minimize such errors. Next, an algorithm is presented to reduce the zero-flow error by combining the techniques of cross-correlation and zero-crossing detection.

Part 2 introduces the matrix-based flow meter. Starting with a chapter detailing the design process, followed by flow measurements with an array-based flow meter. A transceiver ASIC is then presented, that integrates the electronics into a more compact form and implements the required features for matrix-based flow measurement.

Part 3 investigates the new features and measurement techniques enabled by using clamp-on transducer arrays. A method to suppress unwanted waves in the pipe wall is discussed. The properties of the pipe and liquid are determined with the transducer array, enabling automatic calibration. Finally, simulations are performed combining multiple acoustic paths to estimate the velocity profile of the liquid.

In a concluding chapter, the findings are summarized and recommendations for future improvements are discussed.

References

[1] R. C. Baker, *Flow measurement handbook: Industrial designs, operating principles, performance, and applications.* Cambridge University Press, 2011.

[2] P. Lunde, M. Vestrheim, R. Bo, S. Smorgrav, and A. K. Abrahamsen, “Reciprocal operation of ultrasonic flow meters: Criteria and applications,” in *2007 IEEE Ultrasonics Symposium Proceedings.* IEEE, 2007, pp. 381–386.

[3] M. Sanderson and H. Yeung, “Guidelines for the use of ultrasonic non-invasive metering techniques,” *Flow measurement and Instrumentation*, vol. 13, no. 4, pp. 125–142, 2002.

[4] D. V. Mahadeva, R. C. Baker, and J. Woodhouse, “Further studies of the accuracy of clamp-on transit-time ultrasonic flowmeters for liquids,” *IEEE Transactions on Instrumentation and Measurement*, vol. 58, no. 5, pp. 1602–1609, 2009.

[5] J. Massaad, P. L. van Neer, D. M. van Willigen, M. A. Pertijs, N. de Jong, and M. D. Verweij, “Suppression of Lamb wave excitation via aperture control of a transducer array for ultrasonic clamp-on flow metering,” *The Journal of the Acoustical Society of America*, vol. 147, no. 4, pp. 2670–2681, 2020.

[6] D. H. Turnbull and F. S. Foster, “Beam steering with pulsed two-dimensional transducer arrays,” *IEEE transactions on ultrasonics, ferroelectrics, and frequency control*, vol. 38, no. 4, pp. 320–333, 1991.

[7] C. Haugwitz, A. Jäger, G. Allevato, J. Hinrichs, A. Unger, S. Saul, J. Brötz, B. Matyschok, P. Pelz, and M. Kupnik, “Flow metering of gases using ultrasonic phased-arrays at high velocities,” in *2019 IEEE International Ultrasonics Symposium (IUS).* IEEE, 2019, pp. 1129–1132.

[8] C. Haugwitz, C. Hartmann, G. Allevato, M. Rutsch, J. Hinrichs, J. Brötz, D. Bothe, P. Pelz, and M. Kupnik, “Multipath flow metering of high-velocity gas using ultrasonic phased-arrays,” *IEEE Open Journal of Ultrasonics, Ferroelectrics, and Frequency Control*, 2022.

[9] T. H. L. Nguyen and S. Park, “Multi-angle liquid flow measurement using ultrasonic linear array transducer,” *Sensors*, vol. 20, no. 2, p. 388, 2020.

[10] G. Jackson, J. Gibson, and R. Holmes, “A three-path ultrasonic flow meter with fluid velocity profile identification,” *Measurement Science and Technology*, vol. 2, no. 7, p. 635, 1991.

[11] L. Salami, “Application of a computer to asymmetric flow measurement in circular pipes,” *Transactions of the Institute of Measurement and Control*, vol. 6, no. 4, pp. 197–206, 1984.

Part I

Reciprocity in Ultrasonic Flow Measurement

The accuracy of ultrasonic flow measurements is largely dependent on the reciprocity of the flow measurement system.

This Part discusses how reciprocity influences the flow measurement and how flow meter circuits can be optimized for reciprocal operation. These principles can be used in the design process of circuits for matrix-based flow meters, which consist of significantly smaller transducer elements than standard ultrasonic flow meters.

Further, an algorithm will be presented which can significantly reduce the zero-flow error caused by a non-reciprocal circuit. The algorithm combines the benefits of cross-correlation and zero-crossing detection to measure flow with a low offset and high precision.

Contents

2

Reciprocity and the Zero-Flow Error

Transit-time ultrasonic flow meters are based on the fundamental idea that the flow is the only non-reciprocal effect between an upstream and downstream measurement. Non-identical transducers can be used in a reciprocal manner if the circuit is made reciprocal. In this paper we analyze the effect of driver- and readout electronics on the zero-flow error in transit-time ultrasonic flow meters by simulation and measurement. Using the frequency characteristic of two non-identical transducers, the cause of the zero-flow error in non-reciprocal circuits is evaluated.

Simulations and measurement results show that the lowest zero-flow error can be obtained by using circuits that have an impedance significantly higher or lower than the impedance of the transducers.

The contents of this chapter have been published in the proceedings of the IEEE International Ultrasonics Symposium [1].

2.1. Introduction

Transit-time ultrasonic flow meters are used to measure liquid flow in a large range of industrial applications where the temperature and type of liquid often vary considerably. The arrival time difference between the upstream and downstream signals is a measure of the flow velocity. The fundamental idea behind ultrasonic flow meters is that the only non-reciprocal effect in the system is the flow itself [2]. However in practical flow meters an offset in zero-flow conditions is often found, causing a measured flow velocity even in the absence of a flow. Due to process changes (e.g. temperature, liquid type) the zero-flow offset can change in operation, hence it is necessary to minimize the magnitude of the error. Operating the system in a reciprocal manner is key in minimizing the zero-flow error [2–5]. If transducers are operated in a non-reciprocal manner, the zero-flow error increases.

Prior work [3] shows that for two limit-cases, where the circuit impedances are infinite or zero, no zero-flow error is apparent. As it is impossible to make an infinite or zero circuit impedance in practice, some non-reciprocity will always remain in the electronics, resulting in the need to design the circuit such that the absolute zero-flow error is smaller than the random error in the measurement. The choice for the correct circuit topology and impedance are therefore important in designing a flow meter with a small enough zero-flow error. As the requirements differ per flow meter and application, this work discusses the cause of the zero-flow error and the trend of the error, to aid the choice for the optimal circuit.

2.2. Simulating the Zero-Flow Error

The zero-flow error is commonly described as a difference in arrival time or a phase difference between the upstream and downstream measurement in the absence of a flow. When looking at an upstream and downstream transient waveform, one can find that the phase difference between the signals increases over time, which can also be described as a frequency difference.

The Butterworth-van-Dyke model [6] is used to model the electronic behavior of the piezo material close to its resonance frequency. The model parameters were fit based on an impedance measurement of a 20 mm diameter Pz27 piezo transducer, as shown in Table 2.1.

Table 2.1: Model parameters of the Pz27 disc

C_e	R_m	L_m	C_m
2.5 nF	1.6 Ω	10.3 µH	0.6 nF

In combination with a voltage source and its finite output impedance, the resonance

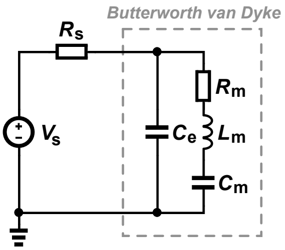

Figure 2.1: Voltage source with series impedance and piezo transducer modeled by Butterworth-van-Dyke model.

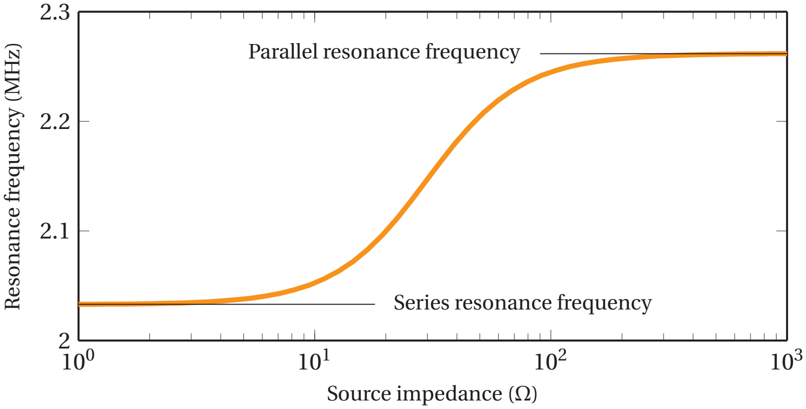

Figure 2.2: Resonance frequency variation with circuit impedance.

behaviour of the piezo and driving circuit is modeled, as shown in Figure 2.1.

Both the transmit and receive circuit load the piezo resonator with their impedance (R_S), making the model also suitable for the receive circuit. By varying the circuit impedance, the resonance behavior of the piezo material can be modeled for different circuit topologies. When increasing the circuit impedance, the resonance frequency of the transducer transitions from series resonance to parallel resonance, as depicted in Figure 2.2. The figure also shows that the resonance frequency is less sensitive to a change in circuit impedance when a very low or a very high circuit impedance is used.

In a flow measurement, the transmit impedance can be made almost equal for the upstream and downstream transducer by using the same transmit and receive circuit upstream and downstream. This can be implemented by using low impedance switches to alternate the transducer connections. Similarly, the receive impedance between the upstream and downstream measurement can be made almost equal. However it is a lot

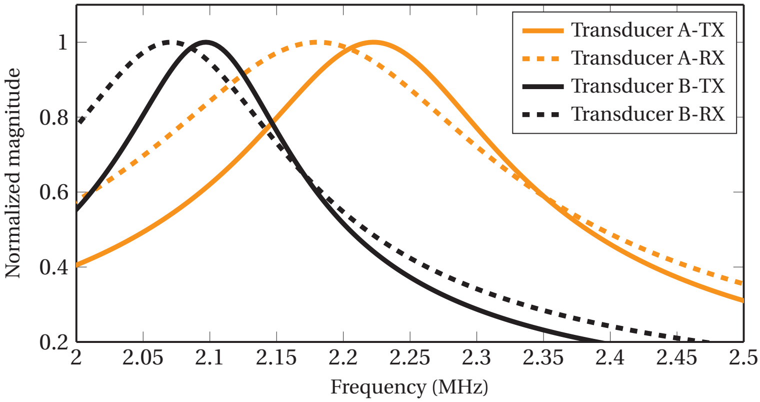

Figure 2.3: Transfer functions for TX and RX circuit with an impedance difference of 40 % and non-equal transducers (20 % mismatch in L_m).

harder to make transmit and receive circuits that have an equal impedance and at the same time load the circuit with the preferred very low or very high impedance. To show the effect of this change in resonance frequency between transmitting and receiving with the same transducer, a simulation is performed for combinations of transmit and receive impedances. Figure 2.3 shows the example transfer functions of two unequal transducers driven with a transmit impedance that is different from the receive circuit impedance. The plot shows that the resonance frequency of the transducer shifts between transmit and receive. Because the transducers are not equal, their transfer function is different in shape, causing a small frequency difference between the upstream (A-TX, B-RX) and downstream (B-TX, A-RX) waveform.

Figure 2.4 shows the simulated transit-time difference between upstream and downstream measurements for a set of transducers with a mismatch of 10 % in $\mathrm{C_m}$.

The plot shows us several insights that can be used to minimize the zero-flow error. It is clear that in the limits indeed two optimal cases can be described; the case where $Z_\mathrm{tx}, Z_\mathrm{rx} \ll Z_\mathrm{series}$ and the case where $Z_\mathrm{tx}, Z_\mathrm{rx} \gg Z_\mathrm{parallel}$, where Z_series and Z_parallel are the series resonance and parallel resonance of the transducer respectively.
Moreover, it is apparent that it is always beneficial to make the difference between the transmit impedance and receive impedance minimal, as is apparent from the diagonal shape of the plot (highlighted by a white line). In the ideal case where $Z_\mathrm{tx} = Z_\mathrm{rx}$ the impedance value of the circuit itself is not of influence. In practice there will always be a small difference in transmit and receive impedance, close to the transducer impedance the zero-flow error is very sensitive to this difference in circuit impedance, hence it is beneficial to use transmit and receive circuit impedances that are both significantly higher or both significantly lower than the impedance of the transducer at resonance.

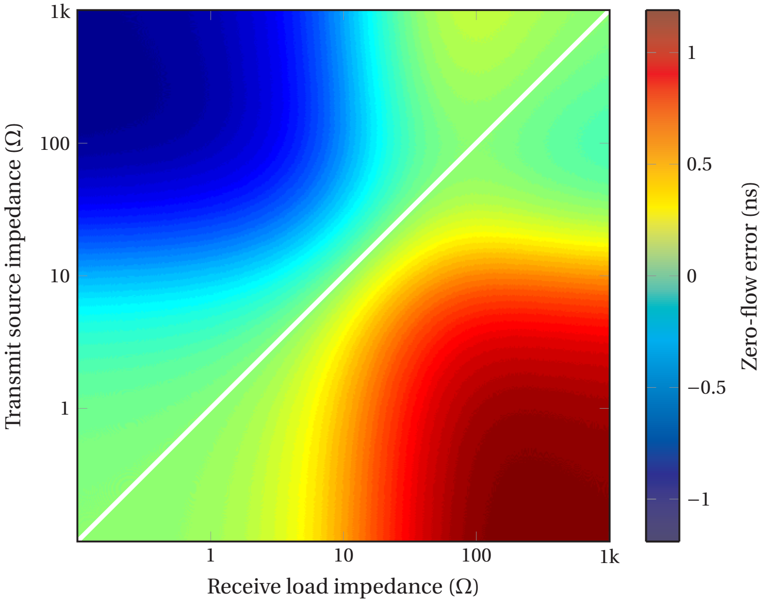

Figure 2.4: Simulation of the zero-flow error based on an upstream and downstream measurement with 10 % mismatch in C_m of the transducer model. The diagonal white line highlights equal transmit and receive impedances.

2.3. Measurement Setup

To minimize the zero-flow error it is important to use the correct circuit topology, but the algorithm used to determine the transit time difference also influences the quality of the measurements. This section discusses the circuit design and algorithm used to obtain a minimal flow error.

2.3.1. Circuit

To verify the simulation results, a circuit has been designed in which the impedance of the piezo driver can be set separately from the impedance of the receive circuit. A schematic diagram of this circuit is shown in Figure 2.5.

The transmit amplifier has an output impedance of $Z_{\mathrm{out}} = Z_{\mathrm{ol}}/(1 + A_{\mathrm{ol}}\beta)$, where Z_{ol} is the open-loop output impedance, A_{ol} the open-loop gain of the operational amplifier, and β the feedback factor. With a high open-loop gain, the output impedance is negligibly small ($< 1\Omega$) compared to the variable resistance in series with the amplifier, so that the latter defines the effective transmit source impedance. In this work the OPA847 (Texas Instruments, Texas, USA) was used, resulting in an output impedance of about $30\,\mathrm{m}\Omega$. Similarly, the trans-impedance amplifier (TIA) that amplifies the received signals, has an input impedance $Z_{\mathrm{in}} = f R_{\mathrm{f}}/_{\mathrm{GBP}}$, where R_{f} is the feedback resistor and GBP the gain-bandwidth product of the used amplifier. In this work we use a THS3001 (Texas Instruments, Texas, USA) amplifier and a feedback resistor of $100\,\Omega$. This circuit has an input impedance of about $0.5\,\Omega$, which is small compared to the variable input resistor, so that the latter defines the effective receive circuit impedance.

The formula of both impedances also shows why it is hard to make them equal. They both depend on the implementation of the chosen opamp and are frequency dependent.

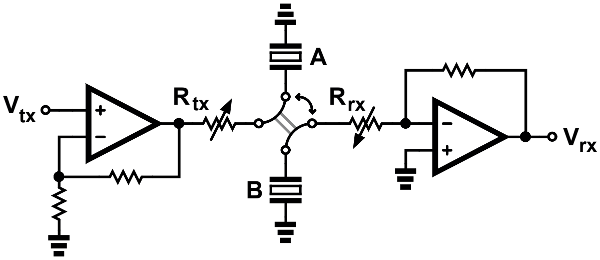

Figure 2.5: Schematic diagram of the circuit used in the measurements.

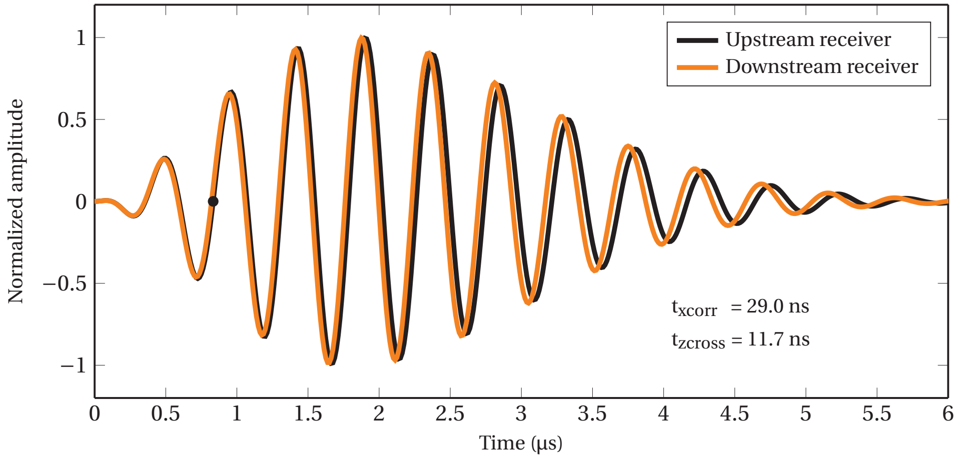

Figure 2.6: Transit-time difference determination using zero-crossings and cross-correlation.

2.3.2. Algorithm

Often cross-correlation is used to determine the transit-time difference, because it uses the information contained in the complete waveform and not just one point [7], as is the case when using zero-crossing detection. To effectively calculate the flow velocity using cross-correlation, the assumption of the flow being the only non-reciprocity in the system must hold. However the circuit will introduce a non-reciprocity, causing the cross-correlation to be less effective. Cross-correlation in essence delays one of the waveforms until both waveforms resemble each-other best. With a frequency difference between the two signals, the delay that results in the best resemblance will be around the part of the received waveform with the highest amplitude. Because of the frequency difference a significant phase shift has already developed between the waveforms.

As the time difference increases over time, the earlier the time difference is determined the smaller the error will be. If the noise level allows, it is therefore beneficial to use an early zero crossing. A simulated waveform is shown in Figure 2.6, with the calculated cross-correlation and zero-crossing based time difference.

Gaussian noise was added to measurement data of an upstream and downstream measurement, to compare the algorithms on waveforms with 20 dB SNR and 30 dB SNR. The histograms of the calculated transit time differences are shown in Figure 2.7a and Figure 2.7b respectively. The transit-time difference is calculated by using both cross correlation and the first zero crossing after the signal reaches an amplitude of $V_{\mathrm{pkpk}}/4$. From the histogram it is apparent that the standard deviation of the cross-correlated signals is much smaller than that of the zero-crossing based analysis. The zero-crossing method however becomes interesting when the SNR improves, as visible in Figure 2.7b.

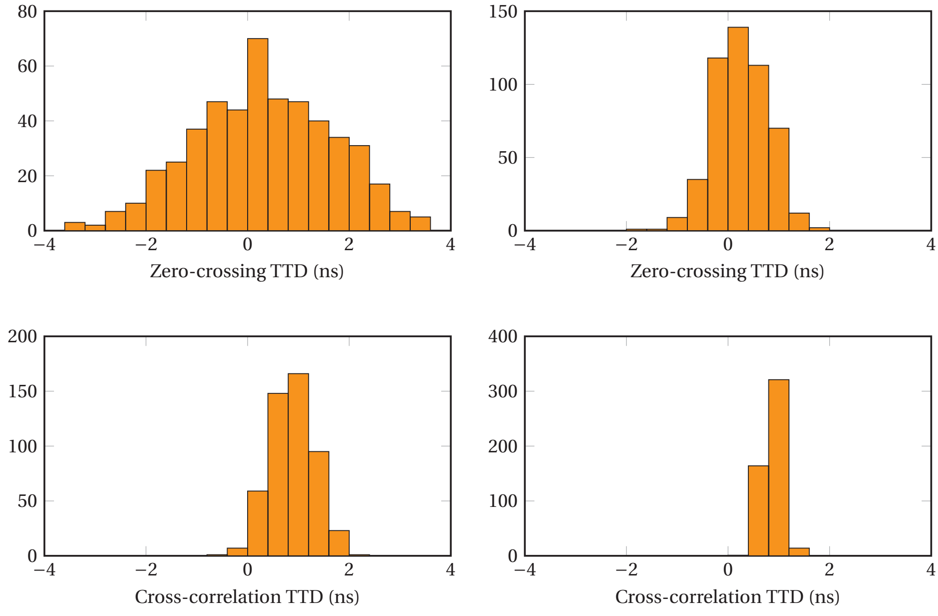

(a) 20 dB SNR **(b)** 30 dB SNR

Figure 2.7: Histogram of transit time difference (TTD) determined using cross-correlation and zero-crossings.

The zero-flow error is smaller for the zero-crossing method, despite the larger standard deviation.

In essence the choice of algorithm should be based on whether the application allows the zero-flow error to be calibrated out (for flow meters in constant process conditions), or whether the zero flow error should be made small enough to not influence the measurement. In the case where dry-calibration is performed, it is best to use the cross-correlation method, as the standard deviation is small, making the calibrated measurement repeatable. In the case where no calibration is performed and the SNR is high enough, it is beneficial to use the zero crossings as it reduces the zero-flow error.

2.4. Experimental Results

For measurement, air backed Pz27 piezoceramic discs (Ferroperm, Denmark) with a diameter of 20 mm and a resonance frequency of 2 MHz were used. The transducers were placed par-axially in a water tank, spaced 20 cm apart, as shown in Figure 2.8. The measurements were obtained by exciting the transmit transducer with a square pulse of

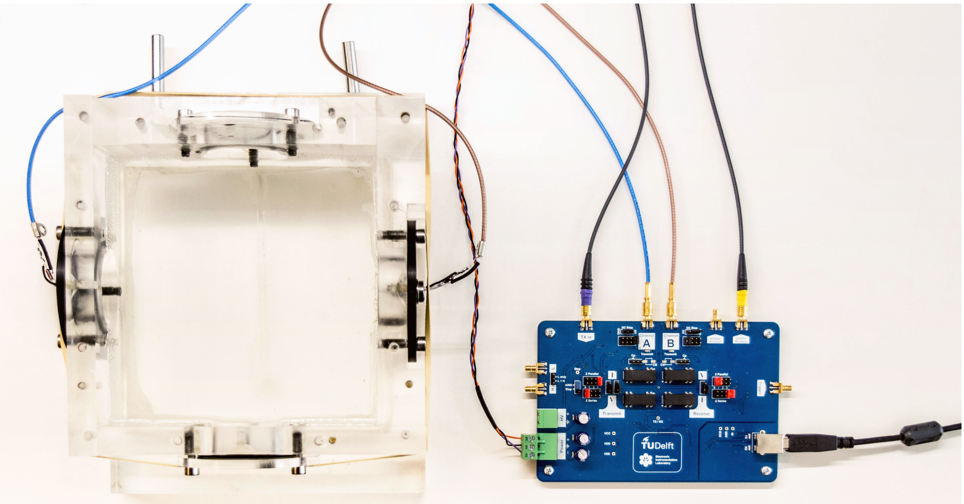

Figure 2.8: Test setup consisting of a water tank with two paraxially aligned transducers and a custom circuit board.

100 µs, using the circuit described previously. The received waveform corresponding to the rising edge of the pulse was recorded and digitized with a DP310 (Acqiris, Plan-les-Ouates, Switzerland) acquisition card.

In the measurement three different transmit impedances were used in combination with a range of receive impedances, as shown in Figure 2.9. The markers show measured arrival time differences between 100 upstream and downstream measurements, calculated using zero-crossing detection. The lines in Figure 2.9 correspond to the zero-flow error simulated using the approach discussed in Section 2.2, using the measured transducer impedance in which a mismatch was introduced to fit the curve to the measured data.

The S-shaped curvature that is found is related to the series and parallel resonance of the transducers. The closer to one of those frequencies the transducer is operated, the less sensitive the resonance frequency of the system becomes to a change in circuit impedance.

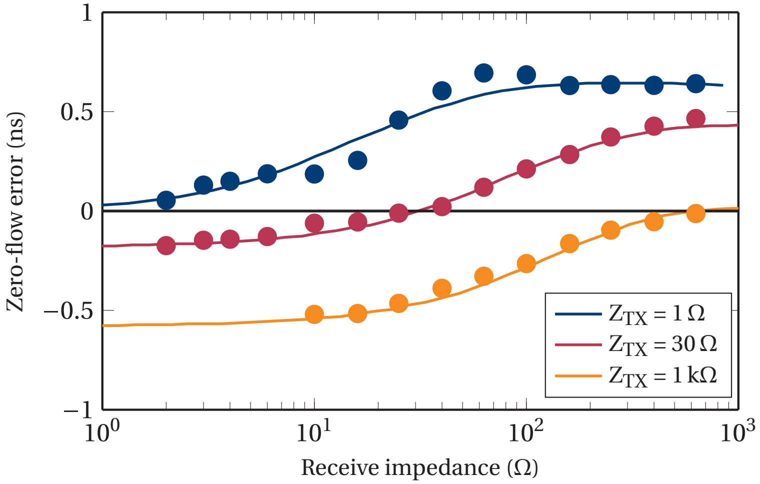

Figure 2.9: Measured zero-flow error and simulation results for several impedance combinations.

2.5. Conclusions

In this chapter we have discussed the origin of the zero-flow error in transit-time ultrasonic flow meters. We have shown how the choice of transmit and receive impedance influences the zero-flow error by simulation and measurements. The measurements show the expected influence of the circuit impedance on the zero-flow error. The algorithm used to calculate the transit-time difference has also been discussed, noting the preference for cross-correlation in a noisy environment while zero-crossing based meters are preferred if the signal level allows.

For low-impedance transducers, a high-impedance driver and readout circuit can often result in a much lower zero flow error, compared to using low-impedance circuitry, as making well matched circuits with an even lower impedance is not trivial.

References

[1] D. van Willigen, P. van Neer, J. Massaad *et al.*, “Minimizing the zero-flow error in transit-time ultrasonic flow meters,” in *2018 IEEE International Ultrasonics Symposium (IUS)*. IEEE, 2018, pp. 1–4.

[2] J. Hemp, “Flowmeters and reciprocity,” *The Quarterly Journal of Mechanics and Applied Mathematics*, vol. 41, no. 4, pp. 503–520, 1988.

[3] P. Lunde, M. Vestrheim, R. Bø *et al.*, “Reciprocity and its utilization in ultrasonic flow meters,” in *23rd International North Sea Flow Measurement Workshop Tønsberg, Norway*, 2005, pp. 18–21.

[4] Y. Bo and C. Li, “Electronic circuit design for reciprocal operation of transit-time ultrasonic flow meters,” *Flow measurement and instrumentation*, vol. 32, pp. 5–13, 2013.

[5] J. Borg, J. Johansson, J. Van Deventer *et al.*, “Reciprocal Operation of Ultrasonic Transducers: Experimental Results,” in *Ultrasonics Symposium, 2006. IEEE*. IEEE, 2006, pp. 1013–1016.

[6] K. S. van Dyke, “The piezo-electric resonator and its equivalent network,” *Proceedings of the Institute of Radio Engineers*, vol. 16, no. 6, pp. 742–764, 1928.

[7] L. Svilainis, “Review of high resolution time of flight estimation techniques for ultrasonic signals,” in *2013 International Conference NDT, Telford, UK,(Sep. 8-12, 2013)*, 2013, pp. 1–12.

3

Algorithm to Reduce the Zero-Flow Error

Transit-time ultrasonic flow meters are widely used in industry to measure fluid flow. In practice ultrasonic flow meters either show a zero-flow error or suffer from a significant random error due to a limited signal-to-noise ratio, requiring a significant amount of averaging to achieve good precision.

This chapter presents a method that minimizes the zero-flow error whilst keeping the random error low, independent of the hardware used. The proposed algorithm can adjust to changing zero-flow errors while a flow is present. The technique combines the benefits of two common methods of determining the transit-time difference between the upstream and downstream ultrasonic waves: cross-correlation and zero-crossing detection. The algorithm is verified experimentally using a flow-loop. It is shown that the zero-flow error can be greatly reduced without compromising the random error or increasing circuit complexity.

The contents of this chapter have been published in the IEEE Transactions on Instrumentation and Measurement [1].

3.1. Introduction

Transit-time ultrasonic flow meters are used to measure fluid flow in a large range of industrial applications where the temperature and type of liquid often vary considerably. The transit time difference (TTD) between the upstream and downstream signals is a measure of the flow velocity. The fundamental idea behind ultrasonic flow meters is that the only non-reciprocal effect in the system is the flow itself [2–4]. However, in practical flow meters, an offset in zero-flow conditions is often found, causing a flow velocity to be measured, even in the absence of flow. This offset error is often referred to as the zero-flow error. The offset error can originate from a slight non-reciprocity in the circuit, caused by an impedance mismatch between the transmit and receive circuit. Other sources of offset error are temperature changes [5] (and the associated changes in material properties of the components), temperature differentials across the flow meter and variations in material properties or the liquid over the flow meter geometry. Due to process changes (e.g. variations in temperature or the liquid properties) the offset error can change in operation. Hence, it is important to minimize the magnitude of the error.

Minimizing the offset error is commonly done by matching the impedance of the receive circuit to the impedance of the transmit circuit, in order to maximize the reciprocity of the measurement system [4, 6, 7]. This method is good at reducing the offset error, but a residual offset usually remains.

Industrial flow meters are usually specified for a range of flow velocities, where the accuracy of the lowest flow speed determines the minimum time-difference that has to be detected. For example, in a flow meter that spans a range from 0.1 m/s to 100 m/s with a 5% accuracy, an error below 5% of 0.1 m/s is required, corresponding to a time difference of 0.18 ns in water for a 40 mm inner diameter pipe (with the transducer at a 45° angle). For a transmit signal with a center frequency of 2 MHz this results in a very small phase difference of 360 ppm of the wavelength. Detecting phase differences that are that small imposes stringent requirements on the electronics and algorithm that are used to calculate the flow. Small errors in the measurements can therefore quickly have a significant influence on the calculated flow velocity.

Two methods that are often used to calculate the phase difference or transit-time difference are zero-crossing detection and cross-correlation. As mentioned in [6], zero-crossing based detection often results in a lower offset error, whereas cross-correlation based methods produce results with lower random error. The latter is caused by the fact that cross-correlation uses information contained in the complete waveform of the received signal rather than just one point. An alternative approach was presented in [8], where the transducers were excited with a fixed frequency until a steady state was reached. The excitation frequency was tuned to calibrate the offset error. Although an interesting approach, its practical applicability is limited as calibration must be performed in zero-flow conditions and the transducers have to be separated by a significant distance to prevent interference of reflected waves. Similar to cross-correlation, an algorithm that uses time and phase domain signals was proposed in [9], with the main objective to be less sensitive to changes in the waveform shape.

Cross-correlating the upstream and downstream signal with their averages has been proposed to increase the measurement precision, because the average has a better resemblance to the waveform than the upstream and downstream signals mutually, because they might differ in amplitude and frequency [10]. Unfortunately, also this method requires recalibration in zero-flow conditions. Other work proposes to compare the measurement to the analytical solution of an oscillator model [11] or reconstructing the signal based on a signal model [12], mitigating the drawbacks of averaging. This method, however, still faces the drawback of the higher offset error commonly seen in cross-correlation measurements.

Thus, an algorithm that minimizes the offset error without compromising on the random error, that does not require calibration measurements, is desirable. This chapter proposes a method that combines the benefits of zero-crossing and cross-correlation methods to obtain flow measurements with a minimized absolute error in combination with a small random error, while being able to adjust for changes in the offset error over longer term as caused by environmental changes such as changes in temperature and pressure.

3.2. Simulation Model

In order to simulate the upstream and downstream signals, the transducers are modeled using the KLM-model [13] in combination with a voltage source V_{in} and a source impedance R_{tx} representing the transmit circuit. The receive circuit impedance is modeled by the load impedance R_{rx}, as shown in Figure 3.1a. The cable capacitance and piezo capacitance are modeled by C_{p} and the two resonant branches represent the upstream (A) and downstream (B) transducer, coupled by an acoustic transmission line. Because we are only interested in the waveform shape and phase difference between the upstream and downstream signal, the KLM-model can be simplified by removing the acoustic transmission line and replacing it by its characteristic impedance Z_{tl} (Figure 3.1b). The current in the transmit branch, I_{pulse}, is proportional to particle velocity in the acoustic domain. The acoustic pressure at the receive side of the transmission line is modeled as a voltage source, V_{pulse}, with a source impedance equal to the transmission line impedance Z_{tl}. The transformers and transmission line impedances can be replaced by an inductor when I_{PZT} and V_{pulse} are moved to the other side of the transformer and the values of the RLC-branch are adjusted accordingly. The adjusted component values are denoted $R_{\text{A}'}$, $L_{\text{A}'}$ and $C_{\text{A}'}$. Similarly the receive side can be simplified as well. The resulting circuit model consists of two Butterworth-van-Dyke models [14], where the voltage source at the receive side is proportional to the current through the transmit transducer. The resulting simulation model is shown in Figure 3.1c.

The component values of the Butterworth-van-Dyke model were determined by analyzing

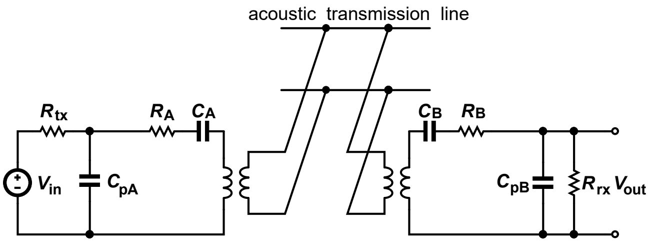

(a) KLM-model with signal source and load impedance

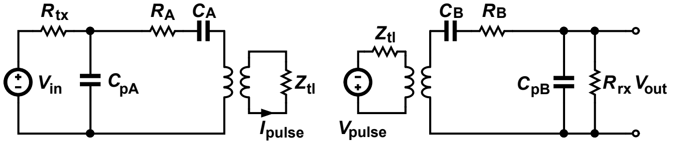

(b) KLM-model without acoustic transmission line

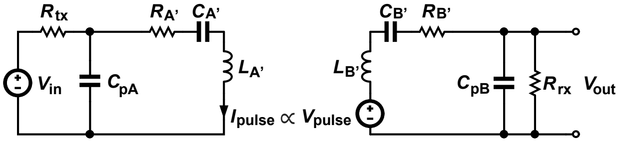

(c) Simplified KLM-model

Figure 3.1: Simulation model based on simplified KLM-model.

the impedance of a 10 mm PZT disc, and curve fitting the model parameters. The resulting parameters are shown in Table 3.1. Transducer B is assumed to be equal to transducer A except for a 5 % mismatch in C_B. To simulate the upstream and downstream waveforms the parameters of the two transducers A and B are interchanged.

3.3. Error Sources

In transit-time ultrasonic flow meters two main error sources that are affecting the flow measurements can be distinguished: The offset error, which appears as an offset to the measured flow, and the random error which influences the precision of the measurement

Table 3.1: Fitted model parameters for Butterworth-van-Dyke model

R	L	C	C_p
20 Ω	46 µH	139 pF	0.55 nF

and shows as a randomly distributed deviation from the actual flow velocity.

3.3.1. Offset Error

It is well known that the offset error is minimized by making the system as reciprocal as possible [15]. When the transducers or the circuit impedances are equal, the system is fully reciprocal and no offset error is present [4]. In a practical system a mismatch between the transducers will always be present. To minimize the offset error, one thus has to make the impedance of the transmit circuit and the impedance of the receive circuit equal and preferably both significantly lower or both significantly higher than that of the transducer [4, 6]. In practice it is not always trivial to make the circuit impedances equal, especially in mass-produced devices where batch variations have a significant impact on the performance. In those cases, often an offset error still exists. The offset error is simulated by introducing a mismatch between the transmit circuit impedance (R_{tx}) and receive circuit impedance (R_{rx}), as well as introducing a mismatch between the two transducers.

The offset error can be considered as a systematic error on the measurement: even with averaging, this error can not be reduced. Using the simplified KLM-model, an example upstream and downstream waveform are simulated, as shown in Figure 3.2a. For illustration purposes a large mismatch between R_{tx} and R_{rx} was used. As evident from the figure, the upstream and downstream transient waveforms differ slightly in amplitude and shape. Although the difference looks small in the figure, it introduces a significant error in the flow-measurement. This error becomes evident when looking at the instantaneous phase difference, or more practical, at the zero-crossings of the two waveforms. Figure 3.2b shows the transit-time difference calculated using zero-crossings detection. Note how the transit-time difference increases over time, eventually converging to a linear increase with time associated with the resonance-frequency difference between the transducers. The best estimate of zero flow can therefore be found early in the waveform, where the signal's amplitude is low. This is contradicting with the requirement of a high signal-to-noise ratio (SNR), as the best SNR can be obtained when a high signal amplitude is available. Therefore in practical systems that use zero-crossing detection, a trade-off is made between taking an early zero-crossing and having a good SNR.

The commonly used alternative to detect the phase difference between the upstream and downstream signal is by cross-correlating the signals. Cross correlation between two discrete signals f and g is defined as:

$$(f \star g)(\tau) = \int_{-\infty}^{\infty} \overline{f(t)} g(t+\tau)\, dt \tag{3.1}$$

where $\overline{f(t)}$ denotes the complex conjugate of $f(t)$. In essence cross correlation delays one of the waveforms (waveform g in equation (3.1)) and results in the highest magnitude

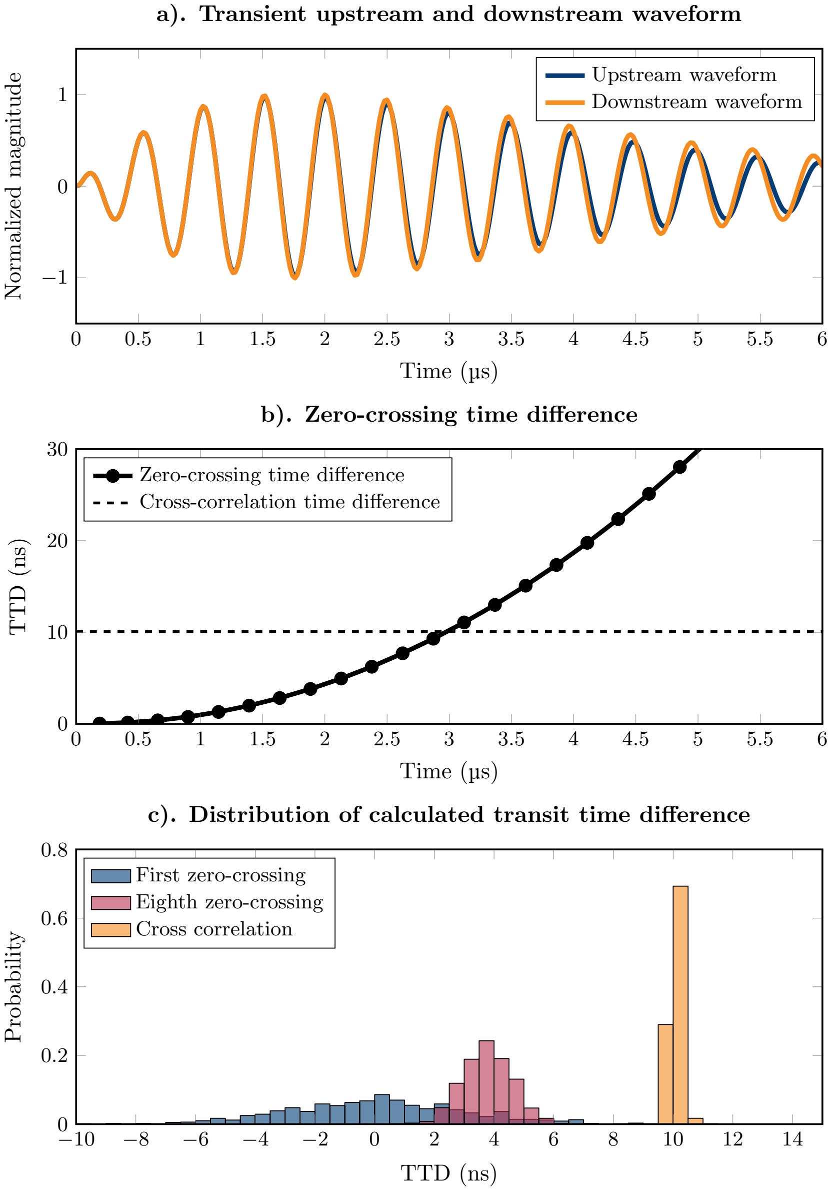

Figure 3.2: Simulated upstream and downstream signals for $R_{\mathrm{tx}} = 50\,\Omega$ and $R_{\mathrm{rx}} = 20\,\Omega$, excited with a single square pulse: a). Transient waveforms, b). Upstream-downstream time-difference (markers represent zero-crossings) and c). Probability distribution of the transit-time difference obtained using the zero-crossing and cross-correlation based algorithms for 2000 simulated waveforms with 30 dB SNR.

when both waveforms resemble each-other best. The delay τ that results in the maximum value is assumed to be the phase difference of the two waveforms. With a phase shift that increases over time, as we saw in Figure 3.2b, the delay τ that results in the best resemblance between the waveforms f and g will be at a point in time where significant phase shift is present between the waveforms (as indicated in Figure 3.2b by a dashed line). This effect will generally cause the cross-correlation to result in a higher offset error than the zero-crossing detection result

3.3.2. Random Error

In Figure 3.2c the probability distribution of 2000 simulated transit-time differences is shown for the first zero-crossing, for the eighth zero-crossing and for cross-correlation, based on a signal with 30 dB SNR. Clearly visible is the reduction of the random error when using a zero-crossing in the higher-amplitude part of the waveforms (here the eighth zero-crossing) and an even smaller deviation when cross-correlation is used.

Depending on the algorithm used to detect the transit-time difference, the random error varies. Especially in time-domain methods like zero-crossing detection, a low SNR can significantly degrade the precision of the measurement. The SNR can be improved by applying averaging, however the improvement when taking the average of N measurements is only $\sqrt{N}$ [16], so a starting point with a better SNR is beneficial.

Minimizing the random error is important to get a good measurement precision. The random error can be dominated by many sources ranging from thermal noise and clock jitter to turbulence in the flow. To guarantee a good SNR one would like to use a high amplitude transmit signal, however industrial meters are often limited in voltage to guarantee intrinsic safety. Moreover, short well-defined transmit waveforms are commonly chosen. Common transmit waveforms are a single square pulse [17] or a single-cycle sine. Although it is possible to obtain reasonable results with these methods, they suffer from low SNR because the transmit signal contains limited energy [18]. As an alternative, significantly longer transmit waveforms have been proposed, to be able to measure in a steady state [19], but with the drawback that the transducers must be far apart to not be affected by interference of reflected waves. Ideally one would like to use a transmit waveform that contains a significant amount of energy and is easy to cross-correlate to achieve a low random error on the transit-time measurements. From imaging physics, it is well known that the waveform can be optimized to improve the SNR when using cross-correlation [20].

To further improve the cross-correlation result, the receive waveform can be compared with a high SNR version of the signal [10, 11], such as an averaged waveform.

3.4. Algorithm

Processing the measurement data in such a way that the offset error is calculated using zero-crossings, while the flow measurement is based on cross-correlation, combines the benefits of both techniques. An algorithm can thus be designed that removes the offset error caused by the cross-correlation operation. Because changes in the offset error are generally slow (e.g. due to temperature change), the zero-crossing calculation can be performed on an averaged signal, reducing the noise on the offset correction signal.

A diagram showing the steps of the proposed algorithm is shown in Figure 3.3. By means of a moving average, high SNR versions of the upstream and downstream waveforms are collected: A_{avg} and B_{avg}. Since the flow velocity can change over time, waveforms A and B have to be time shifted before they can be included in the moving averages. The required time shift can be determined by means of a cross-correlation between those waveforms and their respective moving averages:

$$\tau_A = \text{xcorr}(A, A_{\text{avg}}) \tag{3.2}$$

$$\tau_B = \text{xcorr}(B, B_{\text{avg}}) \tag{3.3}$$

where the xcorr() operation represents the time delay τ corresponding to the peak of the cross-correlation. The resulting average waveforms will have an unknown time difference τ_{avg} due to the flow. This time-difference is calculated using zero-crossing detection, to obtain the lowest offset-error possible:

$$\tau_{\text{avg}} = \text{zcross}(A_{\text{avg}}, B_{\text{avg}}) \tag{3.4}$$

where the zcross() operation represents the time difference between the first zero-crossing of each waveform, after the amplitude of the signal reaches a threshold value (in this work the threshold was set to 10% of the peak amplitude). With this time-difference the flow speed associated with the moving average can be determined. The difference between this average flow speed and the instantaneous flow speed can be determined by the earlier calculated time shifts τ_A and τ_B, assuming that only the flow speed has changed. Thus a low-offset version of the time difference representing the instantaneous flow is obtained:

$$\Delta T = \tau_{\text{avg}} + \tau_A - \tau_B \tag{3.5}$$

The random error on the resulting flow value is comparable to the random error on the cross-correlation, assuming the noise level on the averaged signals is sufficiently small to be negligible.

In addition to reducing the offset error, the algorithm also reduces the random error compared to cross-correlation between the upstream and downstream signal. By calculating

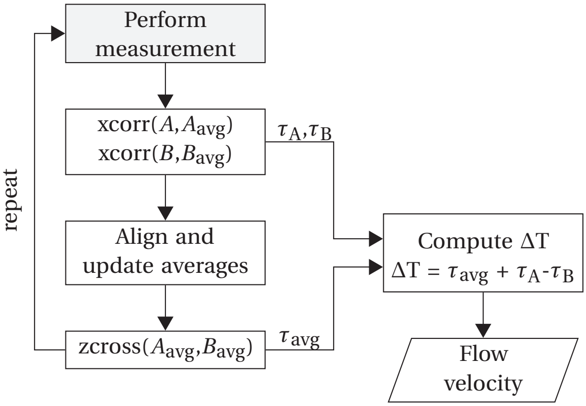

Figure 3.3: Diagram showing the steps of the algorithm.

Figure 3.4: Pair of transducers made of an air-backed piezo-ceramic disc mounted onto a PVC cylinder.

the cross-correlation between the two signals and their averages separately, the random error is reduced. The same cross-correlation results can also be used to align the signal and update the average without the flow influencing the averaged waveform.

3.5. Measurement Setup

A pair of transducers was built with 10 mm diameter Pz27 piezo-ceramic discs (Meggit A/S, Kvistgård, Denmark), with a thickness of 1 mm and a resonance frequency of 2 MHz. The piezo-discs were glued onto a PVC cylinder to create air-backed transducers, as shown in Figure 3.4. The transducers were then placed at a 45° angle in a pipe section with an inner diameter of a 40 mm (Figure 3.5) mounted in a flow-loop filled with water. A reference flow meter (Optosonics 3400, KROHNE, Dordrecht, the Netherlands) with an accuracy of ±0.3 % + 2 mm/s, placed downstream, was used to validate the measured flow rate.

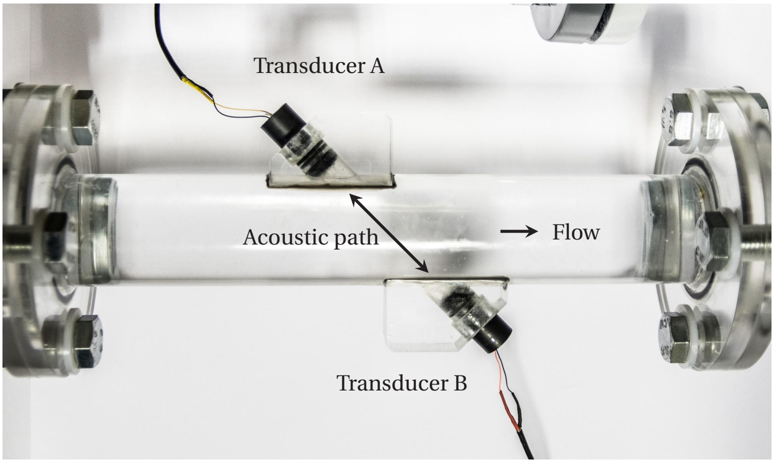

Figure 3.5: Transducers placed co-axially at a 45° angle in a 40 mm inner-diameter pipe section of the flow-loop.

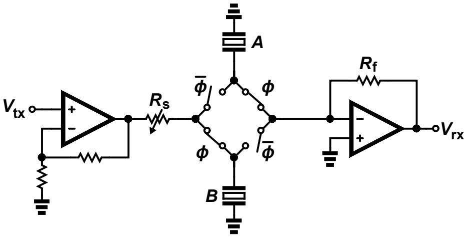

Figure 3.6: Circuit used in the measurements.

A measurement setup was built to first test several transmit waveform shapes in zero-flow condition and then measure a varying flow using the proposed algorithm. An Agilent 33522A (Agilent, Santa Clara, USA) arbitrary waveform generator was used to create a single square pulse, gaussian apodized sine and chirp signal. A printed circuit board (PCB), schematically shown in Figure 3.6, was produced. An amplifier (OPA847, Texas Instruments, Dallas, USA) mounted on the PCB was used to buffer the transmit waveform and create a low impedance output to drive the transducers. A trans-impedance amplifier (TIA) constructed using a THS3001 (Texas Instruments, Dallas, USA) amplifier was used to amplify the received acoustic signals with a low input impedance. The upstream (A) and downstream (B) transducer were alternately switched between the transmit and receive circuit using reed relays. Received signals were digitized using a Spectrum M3i.4121 (Spectrum, Grosshansdorf, Germany) acquisition card, with a sampling rate of 250 MS/s.

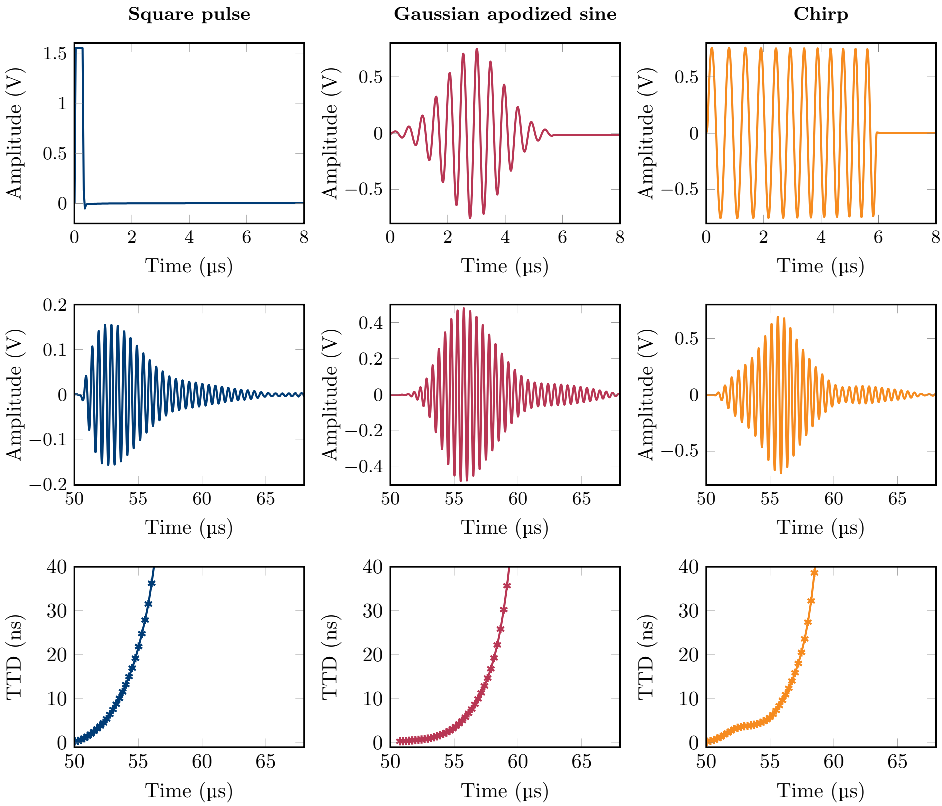

Figure 3.7: Measured transmit waveform (top), receive waveform (middle) and zero-crossing transit time-difference (bottom), for 3 different transmit waveforms with similar peak-to-peak amplitude: square pulse (left), gaussian apodized sine (middle) and chirp (right).

3.6. Experimental Results

In zero-flow conditions, measurements were performed with several transmit waveforms with equal peak-to-peak transmit voltage. In Figure 3.7 the measurements with three common transmit waveforms are compared; a square pulse, a gaussian apodized sine wave (2 MHz) and a chirp (1.5-2.5 MHz). As can be seen in the second row, the signal amplitude of the received waveform is highly dependent on the energy contained in the transmitted signal. When we plot the zero-crossing time difference (Figure 3.7, bottom row) we notice that for each type of waveform the first detected zero-crossing has the lowest transit-time difference, confirming that the first zero-crossing is the best estimate of the zero-flow value. The cross-correlation results always show a relatively large offset

Table 3.2: Measured offset error and random error (std.) calculated using zero-crossing detection and cross-correlation for three types of transmit waveforms.

	zero-crossing		**cross-correlation**	
Waveform	offset	std.	offset	std.
Square pulse	0.35 ns	2.8 ns	8.7 ns	1.49 ns
Gaussian apodized sine	0.36 ns	1.7 ns	8.6 ns	0.29 ns
Chirp	0.17 ns	1.8 ns	7.2 ns	0.20 ns

error as shown in Table 3.2.

Moreover, these examples show the benefit that can be obtained by choosing the right transmit waveform, because they result in very different random errors with the same transmit amplitude. The table also shows that the random error is larger for the zero-crossing method than for cross-correlation, as expected.

Another measurement was performed at zero-flow conditions, this time to compare the proposed algorithm with the cross-correlation and zero-crossing method to see its effect on the offset error. The inset in Figure 3.8 shows the transit-time differences for the first 400 consecutive measurements, calculated using cross-correlation, zero-crossing detection and the algorithm presented in this chapter, with a moving average of 400 samples. In this measurement averaging the signal starts at sample 1, causing the offset error to be poorly estimated for the first few samples, where the average still has a low SNR, converging towards a steadier offset estimate when the SNR of the average signal improves. It is evident from the measurement that the random error significantly improves compared to the zero-crossing detection algorithm. The offset is reduced compared to the cross-correlated data by the correction that the zero-crossing detection on the averaged signals provides. As the average waveform is based on 400 measurements only, it is not yet possible to detect the earliest zero-crossing, resulting in a residual offset. By averaging more this offset can be reduced further, because an earlier zero-crossing can be detected.

After 600 measurement the reciprocity of the circuit was gradually reduced by changing the impedance of the transmit circuit (R_s in Figure 3.6). This measurement emulates changing environmental conditions. Figure 3.8 shows how the offset error increases when the mismatch between the impedances of the transmit and receive circuit is larger. The algorithm is still dependent on the reciprocity of the system, but the offset error is significantly lower compared to cross-correlation. In this measurement the offset error is reduced by more than a factor of 7. Moreover, the random error of the algorithm is with a standard deviation of 17 ps a factor of 10 lower than with zero-crossing detection, which has a standard deviation of 182 ps in the measurement. The figure also shows that abrupt changes temporarily cause an increased offset error compared to zero-crossing detection, this is caused by the low-pass behavior of averaging.

A large benefit of the algorithm is that the average signals can be updated in the presence of flow. To show the performance with varying flow velocities, measurements were performed in a flow loop. The flow velocity was varied from 0 m/s to 0.6 m/s. The measurement results shown in Figure 3.9 confirm that the algorithm is able to calculate the flow velocity with a significantly lower offset error than obtained using cross-correlation. The random error is also significantly lower than it is for the samples based on the zero-crossings (blue markers). At low flow velocities (v<0.2 m/s) the random error of the cross-correlation result is noticeably lower. This difference is likely due to the transition from turbulent to laminar flow condition.

To test the effect of temperature changes on the algorithm, a measurement over a few hours was performed, starting with hot water of 75°C in the setup and allowing it to cool down towards ambient temperature. Figure 3.10 shows the measurements for the different algorithms. Also here the proposed algorithm is able to reduce the offset significantly. The figure includes, for comparison, a curve representing the cross-correlation results corrected based on a calibration for the offset error at the start of the measurements. This results in a significant offset error at the end of the measurement, in contrast with our algorithm, that effectively nulls the offset.

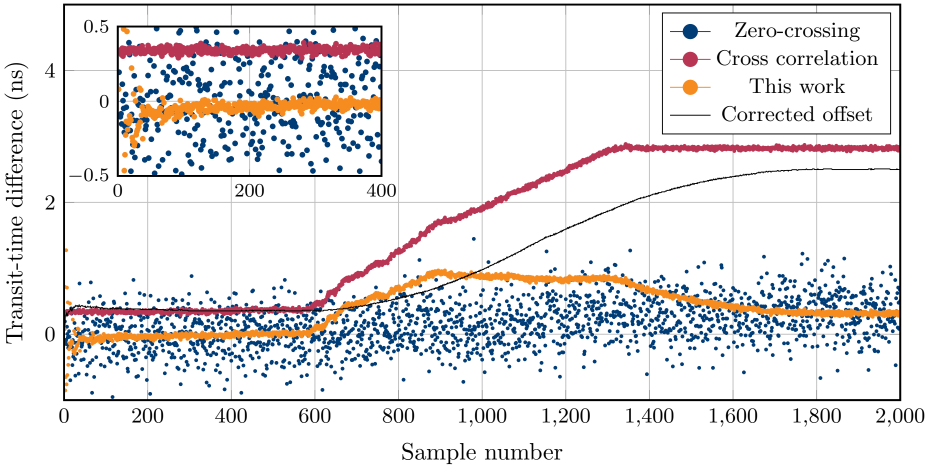

Figure 3.8: Zero flow measurement with varying reciprocity, by introducing a mismatch between the transmit and receive circuit impedance. The corrected offset shows the absolute difference between the cross-correlation algorithm and this work.

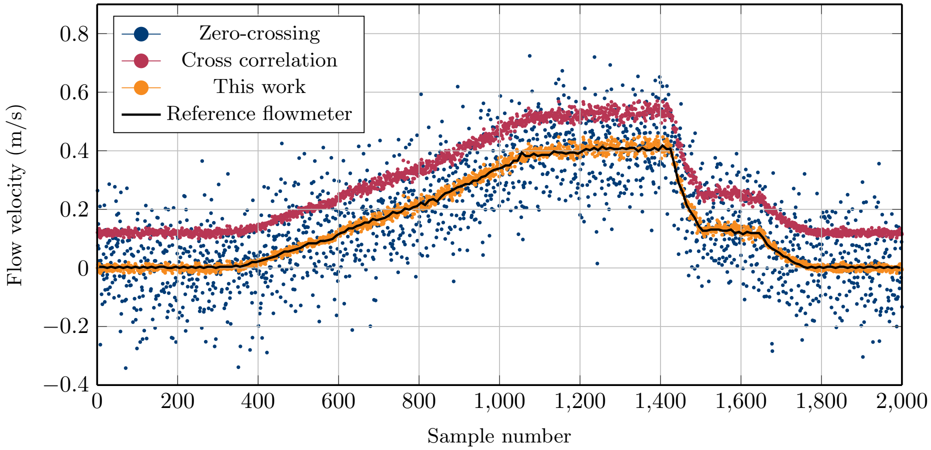

Figure 3.9: Measured flow velocity in the flow-loop with varying flow, showing the effectiveness of zero-crossing detection, cross-correlation and the method described in this work.

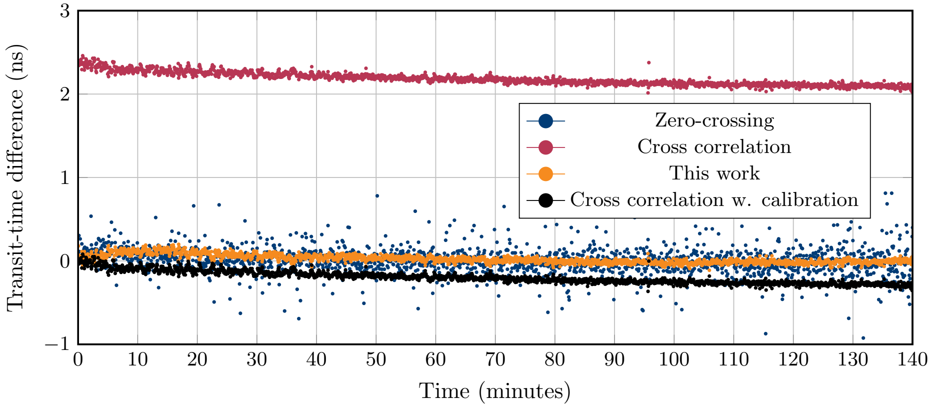

Figure 3.10: Measured transit time difference in zero-flow condition with water temperature decreasing from 75°C to 30°C.

3.7. Discussion

The algorithm presented in this work is most effective in transit-time flow meters in which the electronics suffer from non-reciprocity. In applications with quickly changing environments, such as fluctuating temperatures, it might not always be optimal because a smaller number of averages must be used, reducing the measurement accuracy. In the more common environments that have slowly changing environmental parameters, for example changing over the course of minutes, a large number of averages in the order of tens of thousands of samples can be used to make the zero-crossing detection used in the algorithm as insensitive as possible to noise on the receive signal and thus making the algorithm very robust. The flow measurements shown in this work (Figure 3.9) only use an average of 2000 waveforms, which can be recorded in a few seconds.

Naturally, averaging is only effective at reducing noise. Periodic interference, such as reflections of the acoustic wave, can still interfere with the measurement and alter the phase of the waveform. Moreover, zero-crossing detection inherently results in a residual offset, because physically the received signal cannot start with a zero-crossing, and thus the phase difference developed at a half-period will remain. Improvements can likely be made by predicting the actual start of the signal, or extrapolating the zero-crossing points.

It is important to note the distinct difference in the way averaging is implemented compared to prior work. By time-shifting the samples to align them before averaging, the average is not affected by a change in flow velocity, in fact, even instantaneous flow changes can be tolerated. The algorithm discussed here is, unlike prior work, not limited to specific waveforms with the benefit that the waveform can be optimized for maximum SNR.

In a practical implementation the sample rate can be significantly lower than that of the acquisition card used in this work. Moreover, cross-correlation can take place during the transit-time, which is in the order of 50 µs, relaxing the hardware requirements.

Several implementation variants on the algorithm are conceivable, with differing hardware complexity. For example, cross-correlation with an averaged waveform can be left out when a slight adjustment is made to the algorithm, at the cost of an increase in random error.

3.8. Conclusions

An algorithm for transit-time ultrasonic flow measurements that calculates the flow velocity with a low offset error and with high precision has been designed. It was shown that zero-crossing detection yields the lowest offset error while cross-correlation results in the lowest random error. The algorithm combines those benefits by detecting the zero-crossings of a long-term average. Cross-correlation with the same average was used to achieve the best precision. The described algorithm improved the flow measurements significantly with a 7 times reduction of the offset error compared to cross-correlation. The random error was comparable to cross-correlation and in the measurements 10 times lower compared to zero-crossing detection.

The algorithm was able to adjust to simulated environmental changes, proving it does not require calibration in zero-flow conditions. Moreover, it can be implemented on existing transit-time ultrasonic flow meters that already employ cross-correlation, by updating the software only, potentially improving the specifications with just a firmware update.

References

[1] D. M. van Willigen, P. L. van Neer, J. Massaad, N. de Jong, M. D. Verweij, and M. A. Pertijs, “An algorithm to minimize the zero-flow error in transit-time ultrasonic flowmeters,” *IEEE Transactions on Instrumentation and Measurement*, vol. 70, pp. 1–9, 2020.

[2] J. Hemp, “Theory of transit time ultrasonic flowmeters,” *Journal of sound and vibration*, vol. 84, no. 1, pp. 133–147, 1982.

[3] P. Lunde, M. Vestrheim, R. Bo, S. Smorgrav, and A. K. Abrahamsen, “Reciprocal operation of ultrasonic flow meters: Criteria and applications,” in *2007 IEEE Ultrasonics Symposium Proceedings*. IEEE, 2007, pp. 381–386.

[4] P. Lunde, M. Vestrheim, R. Bø, S. Smørgrav, and A. K. Abrahamsen, “Reciprocity and its utilization in ultrasonic flow meters,” in *23rd International North Sea Flow Measurement Workshop Tønsberg, Norway*, 2005, pp. 18–21.

[5] M. Takamoto, H. Ishikawa, K. Shimizu, H. Monji, and G. Matsui, “New measurement method for very low liquid flow rates using ultrasound,” *Flow measurement and instrumentation*, vol. 12, no. 4, pp. 267–273, 2001.

[6] D. van Willigen, P. van Neer, J. Massaad, M. Verweij, N. De Jong, and M. Pertijs, “Minimizing the zero-flow error in transit-time ultrasonic flow meters,” in *2018 IEEE International Ultrasonics Symposium (IUS)*. IEEE, 2018, pp. 1–4.

[7] J. Borg, J. Johansson, J. Van Deventer, and J. Delsing, “Reciprocal Operation of Ultrasonic Transducers: Experimental Results,” in *2006 IEEE Ultrasonics Symposium*. IEEE, 2006, pp. 1013–1016.

[8] A. Hamouda, O. Manck, M. Hafiane, and N.-E. Bouguechal, “An enhanced technique for ultrasonic flow metering featuring very low jitter and offset,” *Sensors*, vol. 16, no. 7, p. 1008, 2016.

[9] M. Kupnik, E. Krasser, and M. Groschl, “Absolute transit time detection for ultrasonic gas flowmeters based on time and phase domain characteristics,” in *2007 IEEE Ultrasonics Symposium Proceedings*. IEEE, 2007, pp. 142–145.

[10] H. Zhou, T. Ji, R. Wang, X. Ge, X. Tang, and S. Tang, “Multipath ultrasonic gas flowmeter based on multiple reference waves,” *Ultrasonics*, vol. 82, pp. 145–152, 2018.

[11] F. Suñol, D. A. Ochoa, and J. E. Garcia, “High-precision time-of-flight determination algorithm for ultrasonic flow measurement,” *IEEE Transactions on Instrumentation and Measurement*, 2018.

[12] Z. Fang, L. Hu, L. Qin, K. Mao, W. Chen, and X. Fu, “Estimation of ultrasonic signal onset for flow measurement,” *Flow Measurement and Instrumentation*, vol. 55, pp. 1–12, 2017.

[13] R. Krimholtz, D. A. Leedom, and G. L. Matthaei, “New equivalent circuits for elementary piezoelectric transducers,” *Electronics Letters*, vol. 6, no. 13, pp. 398–399, 1970.

[14] K. S. Van Dyke, “The piezo-electric resonator and its equivalent network,” *Proceedings of the Institute of Radio Engineers*, vol. 16, no. 6, pp. 742–764, 1928.

[15] J. Hemp, “Flowmeters and reciprocity,” *The Quarterly Journal of Mechanics and Applied Mathematics*, vol. 41, no. 4, pp. 503–520, 1988.

[16] S. Grzelak, J. Czoków, M. Kowalski, and M. Zieliński, “Ultrasonic flow measurement with high resolution,” *Metrology and Measurement Systems*, vol. 21, no. 2, 2014.

[17] Y. Bo and C. Li, “Electronic circuit design for reciprocal operation of transit-time ultrasonic flow meters,” *Flow Measurement and Instrumentation*, vol. 32, pp. 5–13, 2013.

[18] L. Svilainis, P. Kabisius, A. Aleksandrovas, and A. Chaziachmetovas, “Excitation signal’s influence on ultrasonic transit time flow meter’s performance,” in *IOP Conference Series: Materials Science and Engineering*, vol. 42, no. 1. IOP Publishing, 2012, p. 012047.

[19] Y. Bo, C. Li, and L. Yupin, “Forced oscillation to reduce zero flow error and thermal drift for non-reciprocal operating liquid ultrasonic flow meters,” *Flow Measurement and Instrumentation*, vol. 22, no. 4, pp. 257–264, 2011.

[20] T. Misaridis and J. A. Jensen, “Use of modulated excitation signals in medical ultrasound. Part I: Basic concepts and expected benefits,” *IEEE Transactions on Ultrasonics, Ferroelectrics, and Frequency Control*, vol. 52, no. 2, pp. 177–191, 2005.

Part II

A Matrix-Based Clamp-On Ultrasonic Flow Meter

Clamp-on flow meters are increasingly used to measure flow in an industrial setting. They are attractive because no interruption of the flow is required for installation and they present a safe and reliable way of measuring flow without piercing the pipe wall.

This Part introduces a matrix-based clamp-on flow meter. A transducer array design will be discussed and flow measurements performed in a flow loop will be presented. In order to further integrate the flow meter in a compact device, an transceiver ASIC will be presented to transmit and receive with the transducer elements of a matrix array.

Contents

4

Design of a Matrix Transducer for Ultrasonic Flow Measurement

Common ultrasonic clamp-on flow meters consist of two single-element transducers placed on the pipe wall. Flow speed is measured non-invasively, i.e. without interrupting the flow and without perforating the pipe wall, which also minimizes safety risks and avoids pressure drops inside the pipe. However, before metering, the transducers have to be carefully positioned along the pipe axis to correctly align the acoustic beams and obtain a well-calibrated flow meter. This process is done manually, is dependent on the properties of the pipe and the liquid, does not account for pipe imperfections, and becomes troublesome on pipelines with an intricate shape.

Matrix transducer arrays are suitable to realize self-alignment and to perform self-calibrated ultrasonic clamp-on flow measurements over a wide range of liquids and pipe sizes. The large number of matrix elements allows for advanced features such as two-dimensional beam steering, spatial filtering, and dedicated measurements of the mechanical properties of the pipe and liquid. This chapter presents the acoustic design of such a matrix array, including the required number of transducer elements in the axial and circumferential directions, and the layering of the acoustic stack and its dimensions. Furthermore, based on the proposed design, a linear array was fabricated and acoustically characterized to prove its suitability for ultrasonic clamp-on flow metering.

Parts of this chapter have been published in the IEEE Transactions on Ultrasonics, Ferroelectrics and Frequency Control [1], and the Proceedings of the IEEE International Ultrasonics Symposium (IUS) [2].

4.1. Introduction

Ultrasonic flow meters are used in a wide range of industrial applications [3–5], and can be divided in two categories: in-line and clamp-on flow meters. The latter consist of two single-element transducers fixed along the outside of a pipe wall. Alternatingly, one transducer emits an ultrasound wave which is transmitted through the pipe wall and refracted into the liquid, where it can bounce one or more times before refracting back into the pipe wall and being received by the other transducer. The transit time difference between the signals recorded upstream and downstream is proportional to the flow speed [6], at least for small flow velocities.

Clamp-on flow meters have advantages compared to their in-line counterparts with transducers fixed inside the pipe wall. They can be installed without interruption of the flow and without the addition of extra pipe sections or making cuts through existing ones. Nevertheless, clamp-on flow meters also have disadvantages. For alignment of the transducers and calibration of the flow meter, a priori knowledge of the properties and geometry of the pipe, as well as the speed of sound in the liquid is needed. In practice, these values are uncertain and therefore limit the accuracy of the calibration and, consequently, the measurements. Alternatively, the transducers can be aligned using a manual calibration procedure, which is cumbersome, labour intensive and operator dependent.

Common clamp-on flow meters use a specific wave type in the pipe wall (typically a bulk shear wave, but in principle this may also be a bulk compressional wave). This wave will refract into the fluid to obtain information about the flow speed. However, it also excites Lamb waves in the pipe wall. These Lamb waves interfere with the compressional wave refracting back from the liquid and introduce an offset error in the transit time differences and hence in the measurement of the corresponding flow speed. To tackle this issue, current clamp-on flow meters may incorporate an absorbing layer placed around the pipe wall and in-between both transducers with the purpose of attenuating these interfering Lamb waves [7]. Unfortunately, this solution is not always practical, as access to the pipe is often limited, and/or the pipe is covered by material with other purposes, e.g. heat isolation.

A pair of matrix transducer arrays has the potential to tackle the current problems and limitations of clamp-on flow meters. Prior to flow measurements, the properties of the pipe and the liquid can be obtained using dedicated measurements. The measured parameters can be combined with electronic beam steering capabilities to create a self-calibrated flow sensor [8]. Furthermore, the transducer arrays can be cleverly excited to suppress, in transmission, the spurious Lamb waves in the pipe wall while maintaining a beam shape in the liquid with a clearly defined flat wavefront [9].

Here, the design of a matrix transducer array for ultrasonic clamp-on flow metering within a wide range of liquid and pipe parameters is presented.

4.2. Ultrasonic Clamp-On Flow Meters

Consider two single-element transducers with a certain axial separation x on the outer pipe wall, as shown in Figure 4.1. Between each transducer and the pipe wall there is an angled wedge, which allows the compressional wave generated by the transducers to impinge the pipe wall under a certain angle with respect to the normal of the pipe surface. At the interface between the wedge and the pipe wall, wave mode conversion occurs, i.e. a compressional and a shear wave get excited in the pipe wall. Then, at the interface between the pipe wall and the liquid, wave mode conversion takes places again. Here, both waves in the pipe wall refract into the liquid as compressional waves. Given the sound speeds of common metal pipe walls and of common liquids, Snell's law predicts that shear waves in the pipe wall refract under higher angles into the liquid compared to the compressional waves in the pipe wall. For this reason, common ultrasonic clamp-on flow meters use wedges with sufficiently-high angles to only excite shear waves in the pipe wall (the compressional waves will be evanescent), so that the longest horizontal path in the fluid is obtained and the highest possible sensitivity of the acoustic wave to the flow is achieved. However, during propagation through such long travel paths, the beam also experiences more attenuation compared to shorter travel paths. The compressional wave propagating in the liquid may reflect a few times within the pipe before finally refracting back into the pipe wall and towards the other transducer. This procedure occurs both upstream and downstream, and given that the flow velocity adds-up vectorially to the velocity of the wave in the liquid, both signals will be recorded with a transit time difference that will finally be proportional to the desired flow speed, at least for flow speeds well below the wave speed in the fluid.

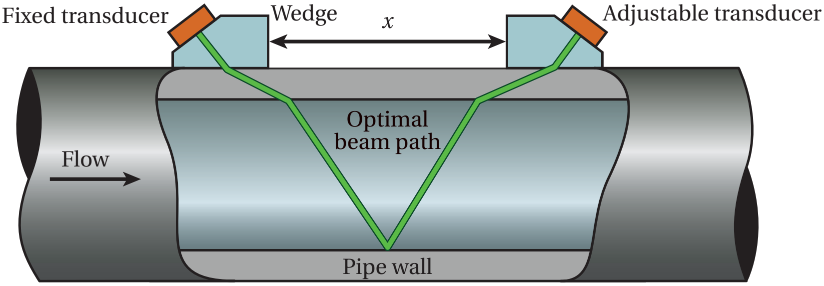

Figure 4.1: Diagram of a conventional ultrasonic clamp-on flow meter. Upon installation, one single-element transducer is manually moved along the pipe wall to find the optimal axial transducer separation x, which ultimately depends on the properties and geometry of the pipe wall, and on the sound speed of the liquid. The green line represents the acoustic beam path in the flow sensor. Here the beam bounces only once inside the pipe.

From Figure 4.1 it can be understood that, to make an accurate flow measurement, the axial transducer separation x must be adjusted correctly. This parameter depends on the bulk wave sound speeds of the pipe wall, the pipe wall thickness, the pipe diameter, the sound speed of the liquid, and also on the number of bounces inside the pipe. Upon installation, the axial transducer separation x is found by fixing one of the transducers and manually moving the other one along the pipe wall until a peak amplitude is detected. In practice, this results in a cumbersome and time-consuming process for the operator, especially in hardly accessible places. Moreover, most of the parameters required for calibration are not exactly known and the procedure doesn't account for pipe imperfections (e.g. variations of pipe wall thickness and diameter, effects of corrosion). An ultrasonic clamp-on flow meter based on two matrix arrays could be used to measure the required parameters of the pipe and the liquid [8], and its beam steering capabilities can be applied to achieve correct alignment of the transducers without the need to manually move the transducers.

4.3. Basic Requirements

4.3.1. Measurement Accuracy

Currently available ultrasonic clamp-on flow meters are able to measure flow within an inaccuracy below 2 % [10]. It is reasonable to attempt to improve this value by designing a better sensor. Therefore, it is aimed to measure flow speeds above 1 m/s with an inaccuracy below 1 %.

4.3.2. Parameter Ranges of Liquid and Pipe

Because of the wide range of liquids used in practice, the sensor should be able to measure the flow of liquids with sound speeds ranging from 1000 m/s to 2000 m/s, and attenuation coefficients $\alpha \leq 1$ dB/MHz·cm [11].

The pipelines of most industrial processes consist of metallic pipes, which was also assumed here. The sensor should operate on pipes with inner diameters ranging from 25 – 100 mm. Next to that, a wide range of pipe wall thicknesses occurs in practice, therefore the sensor should be able to deal with pipe wall thicknesses ranging from 1 – 5 mm.

4.3.3. Measurement of Elastic Parameters

Before performing flow measurements, the matrix array-based sensor should be able to estimate the elastic properties of the pipe and the liquid. These measured properties are then used as input to estimate the flow speed. As reported in [8], guided waves in the pipe wall would be very useful to measure the required parameters.

4.4. Derived Requirements

4.4.1. Operational Frequency Range

Currently, clamp-on flow meters operate at central frequencies that may range between 0.2 MHz and 2 MHz. This depends on the property range of the liquid (notably the sound speed and attenuation) and the pipe wall diameter (determining the length of the beams). Hence, the bandwidth of the flow meter design is aimed at 0.2 – 2 MHz.

4.4.2. Pitch

To enable spatial filtering, beam steering, and the required calibration measurements, the matrix array should be properly spatially sampled, i.e. have a sufficiently small pitch. To ensure this, Lamb wave modes of the thickest considered stainless steel pipe wall (5 mm) were analyzed. From this study, the pitch was set to 0.72 mm, which is half the wavelength of the slowest propagating Lamb wave mode at a frequency of 2 MHz ($c_{\mathrm{low}} = 2900\,\mathrm{m/s}$).

4.4.3. Suppression Level of the Lamb Waves

To achieve the required accuracy of the flow measurements, it is necessary to suppress the amplitude of the spurious Lamb waves in the pipe wall down to a particular level

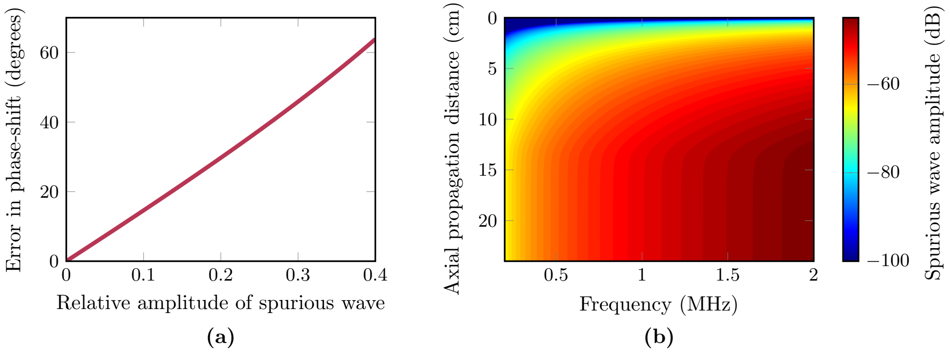

Figure 4.2: (a) Phase-shift error induced by spurious signals, versus the normalized amplitudes of these spurious signals. Normalization is performed with respect to the maximum amplitude of the 'clean' upstream and downstream signals. (b) Required amount of suppression of the spurious waves, versus frequency and axial transducer separation. The suppression is relative to the compressional wave refracting from the liquid, and indicates what is needed for measuring flow speeds above 1 m/s within an inaccuracy of 1 %.

relative to that of the wave refracting from the liquid.

A frequency independent study was performed, in which two ‘clean’ waveforms (5-cycle Gaussian-modulated sine waves with a center frequency of $f_c = 1\,\text{MHz}$), representing upstream and downstream signals in a flow measurement, were used. These were phase-shifted by a known amount that was also reconstructed by a cross-correlation algorithm. A linear relationship was obtained between the imposed phase-shift and the one computed by cross-correlation, as expected. However, when a spurious signal (a continuous sine wave with a center frequency of $f_c = 1\,\text{MHz}$) is added to the ‘clean’ waveforms, this relation is not linear anymore since the spurious signals introduce an offset error in the relative phase-shift between upstream and downstream signals. A slightly nonlinear relation between the amplitude of the spurious wave and the induced phase shift error was obtained. As Figure 4.2a shows, the induced error is directly proportional to the amplitude of the spurious wave.

Next, it was needed to obtain the required amount of suppression for achieving a measurement inaccuracy of 1 %. This made it necessary to estimate the phase-shift error that corresponds to the change in transit time difference when a flow speed of 1 m/s changes by 1 %. This was done for different frequencies and axial transducer separations. The obtained phase shift error estimations, in combination with the information in Figure 4.2a, resulted in Figure 4.2b, from which it can be seen that, at 1 MHz and for axial transducer separations ≥ 5 cm, the amplitude of the Lamb waves needs to be 55 dB below the amplitude of the compressional wave refracting from the liquid.

4.4.4. Signal-to-Noise Ratio

Current ultrasonic clamp-on flow meters perform flow measurements with a signal-to-noise ratio (SNR) as low as 20 dB. Therefore, it is desired aim to obtain a flow meter design that produces this minimum value of SNR within the desired frequency range and for all considered liquids.

4.5. Array Requirements and Positioning on the Pipe Wall

4.5.1. Center Frequency

We choose the center frequency of the array at 1 MHz, which is almost in the middle of the required frequency band of 0.2 – 2 MHz. This should be the frequency of the main thickness resonance mode. Moreover, the frequencies of all modes with lateral vibrations should have at least, three times this frequency [12].

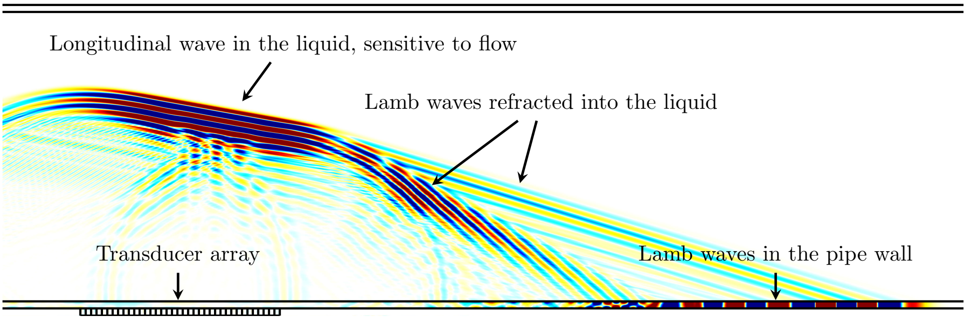

Figure 4.3: Finite element simulation of a transducer array with beam steering and focusing for clamp-on flow measurements, on the bottom side of a 1 mm-thick stainless steel pipe.

4.5.2. Transducer Array Aperture: Axial Direction

Finite Element simulations using the software package PZFlex (Onscale, Redwood City, CA, USA) were performed for a clamp-on flow measurement setting with standard beam steering and focusing, see Figure 4.3, and a liquid with the highest considered attenuation ($\alpha = 1\,\text{dB/MHz}\cdot\text{cm}$). For this case it was found that Lamb waves have amplitude levels that are 20 dB below the amplitude of the compressional wave that refracts from the liquid (Figure 4.4). According to Section 4.4.3, it was therefore necessary to further suppress the Lamb waves by 35 dB to achieve the desired flow measurement inaccuracy of 1 %.

Because the flow sensor consists of transducer arrays, several signal processing techniques based on phase-shift and amplitude manipulation of the element signals could be exploited to suppress the generated Lamb waves in transmission [13–16]. Unfortunately, the element phases required for this suppression would add to the element phases required for beam steering, which would result in a significantly deformed acoustic beam. Therefore, it was decided to manipulate the element amplitudes, i.e. apply apodization, for Lamb wave suppression and use the element phase shifts for beam steering and focusing. This method was described in [9], where it was concluded that, for an array satisfying the given requirements, 37 piezo-elements are enough to generate an acoustic wave with a sufficiently smooth beam profile to achieve 35 dB suppression of the Lamb waves along the axial direction. At the same time, upon reception a beam having the same width as the receiving array aperture is obtained, which maximizes SNR during flow measurements.

4.5.3. Transducer Array Aperture: Circumferential Direction

To calculate the pipe diameter, it is very important to accurately estimate the sound speeds in the pipe wall. In the design, an inaccuracy in sound speed of 1 m/s was aimed for. Assessing the situation in which two waves with propagation speeds of

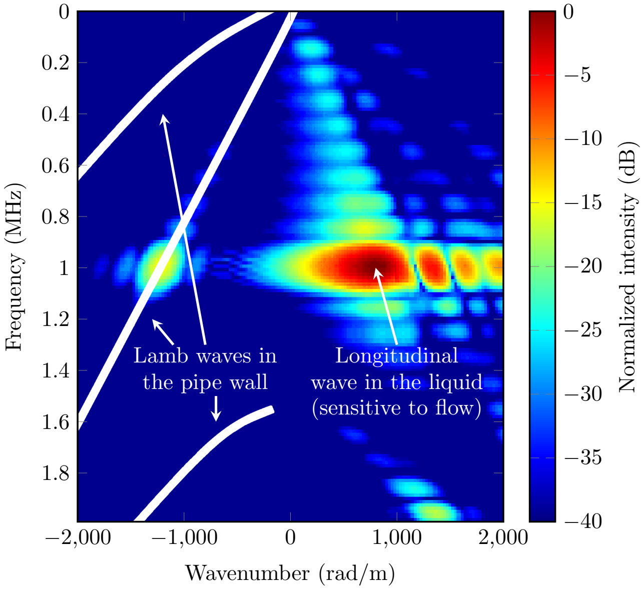

Figure 4.4: Magnitude in the wavenumber-frequency domain of the narrow-banded time signals recorded along the bottom pipe wall (i.e. along the same surface on which the array is located) of the geometry in Figure 4.3. The Lamb waves have an approximately 20 dB lower amplitude relative to the compressional wave that is refracted from the liquid. The white lines represent the theoretical Lamb wave dispersion curves.

$c_{\mathrm{low}} = 2900\,\mathrm{m/s}$ and $c = 2901\,\mathrm{m/s}$ would travel around a pipe with an inner diameter of 40 mm, an arrival time difference of 29 ns was obtained. Based on the relation in Figure 4.2a, this translated into a relative amplitude of around 0.08, i.e. a 22 dB lower amplitude of the Lamb waves. Next, the method described in [9] predicted that 17 elements are enough to achieve the desired suppression of the Lamb waves along the circumferential direction of the pipe.

4.5.4. Coupling piece

Current ultrasonic clamp-on flow meters excite shear waves in the pipe wall to achieve higher refraction angles in the liquid, and therefore improve beam sensitivity to the flow. The way to excite such waves is by impinging a compressional wave on the pipe wall beyond the critical angle for the refracted compressional wave. Without a coupling layer between the transducer and the pipe wall, such an angle would be impractically high, and therefore difficult to achieve, due to similar compressional sound speed values of the transducer's piezoelectric material (PZT) and the metal pipe wall. To obtain shear waves in the pipe wall at much lower incidence angles, plastic wedges with a much lower compressional sound speed are commonly placed between the transducer and the pipe wall.

Nevertheless, the acoustic impedance of plastic ($Z_{\text{wedge}} \approx 2.5\,\text{MRayl}$) relative to that of the metal pipe wall ($Z_{\text{pipe}} \approx 47\,\text{MRayl}$) might not guarantee the right performance for all required angles, since most of the impinging energy gets reflected back into the wedge. Therefore, it was necessary to consider a coupling material that had roughly the same compressional sound speed as plastic ($c_{\text{plastic}} = 2290\,\text{m/s}$) to achieve wave mode conversion at reasonably low incidence angles, but a much higher density than plastic ($\rho_{\text{plastic}} = 1.24\,\text{kg/m}^3$) to get sufficient energy into the pipe wall. Therefore, lead ($c_{\text{lead}} = 2200\,\text{m/s}$, $\rho_{\text{lead}} = 11200\,\text{kg/m}^3$) was chosen as the appropriate coupling material between the transducer array and the pipe wall.

4.5.5. Axial Positioning

To measure flow for liquids with $c_{\text{liquid}} = 1000 - 2000\,\text{m/s}$ and $\alpha \leq 1\,\text{dB/MHz}\cdot\text{cm}$, it was necessary to determine the appropriate axial separation between both transducer arrays. This value was found via ray tracing. Assuming compressional waves in the pipe wall and six bounces (v-shapes) of the beam in the liquid (Figure 4.5a), and assuming shear waves in the pipe wall and two bounces of the beam in the liquid (Figure 4.5b), it was found that an axial transducer separation of 80 mm makes it possible to measure flow in both scenarios for the entire range of liquids considered, avoiding at the same time the critical angles for which this value goes to infinity (see Figure 4.6). Moreover, at this axial transducer separation, the acoustic beam width at the −3 dB level (26.1 mm) is almost the same as the array aperture along the axial direction of the pipe (26.6 mm) [9].

4.6. Acoustic Stack Design of the Array

In this section, the design process of the acoustic stack of the transducer arrays for ultrasonic clamp-on flow metering is explained. This process has been partially described in [2].

4.6.1. Signal level

An important check of the suitability of the transducer array are the achievable SNR levels. With the acoustic path shown in Figure 4.5a (or in Figure 4.5b), the expected SNR levels can be determined via the sonar equation

$$V_{\text{open}} = V_{\text{in}} T_t T_r T (RW)^{2b-1} W. \tag{4.1}$$

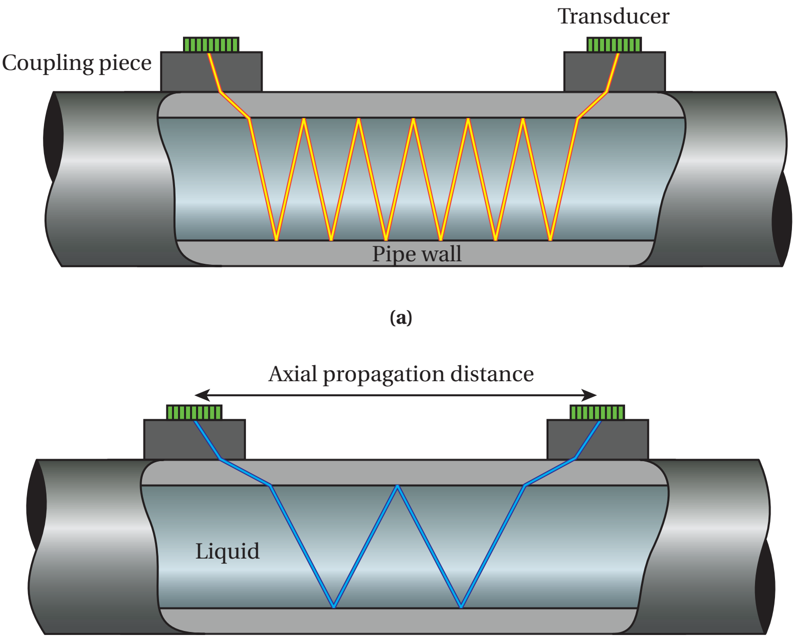

(a)

(b)

Figure 4.5: Travel path of an acoustic beam during ultrasonic clamp-on flow measurements using (a) compressional, and (b) shear waves in the pipe wall.

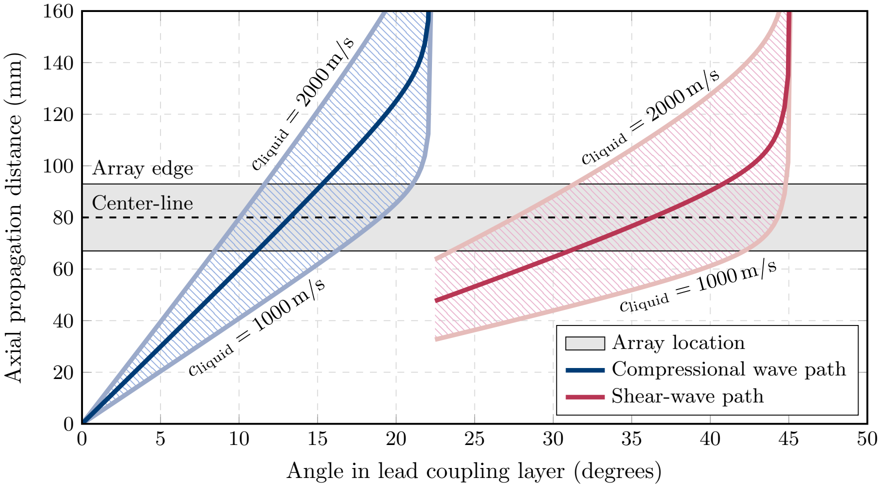

Figure 4.6: Axial propagation distance of the beam (equal to the axial transducer separation) versus the beam angle in the coupling layer, for a pipe with an inner diameter of 40 mm. The black dashed line represents the physical location of the center of the receiver transducer array (80 mm), and the black solid lines give the boundaries of its aperture in the axial direction.

Here, V_{open} is the open-clamp voltage measured at the receiving transducer, V_{in} is the input voltage on the transmitting transducer (in this case $V_{\text{in}} = 5\,\text{V}$), T_t and T_r are the transmit and receive transfer functions of the transducer array, respectively, T is the product of the transmission coefficients at all interfaces in Figure 4.5a (or in Figure 4.5b) through which the acoustic wave propagates, R is the reflection coefficient of the liquid-pipe interface, b is the number of bounces (v-shapes) of the acoustic wave within the pipe, and $W = e^{\alpha L} G D$, where α is the attenuation coefficient of the liquid and L is the total length of the acoustic travel path in the fluid, G is the focusing gain factor, and D accounts for the diffraction of the propagating wave through the liquid. Here, G is set equal to 1 because the width of the transmitted beam and the received beam are both approximately equal to the aperture of the transducers, and D is approximated using the expression given in [17].

4.6.2. Finite Element Model

The software package PZFlex was used to simulate the waves in the various materials of the configuration. In PZFlex, the linear wave equation is solved. Linear isotropic elasticity was assumed for the pipe wall and the coupling piece. The anisotropic piezo-electric constitutive equations were solved for the piezo-materials. Damping was considered to be visco-elastic and to be present in all materials, and its effects on wave propagation were mainly noticed in the backing material behind the transducer, and in the liquid. Moreover, to ensure proper spatial sampling, the lowest expected wavelength at 1 MHz was estimated, and the mesh grid consisted of square elements with side length of $1/30^{\text{th}}$ of this minimum wavelength.

4.6.3. Piezo layer

In most ultrasonic clamp-on flow metering settings, there is a large difference between the acoustic impedance of the liquid and that of the pipe wall. Therefore, most of the acoustic energy produced by the transmitting transducer reflects back into the pipe wall, resulting in signals with low amplitude from the receiver transducer. One way to increase this amplitude is to use a PZT piezo material that gives the most efficient conversion of electric energy into mechanical energy. This convergence efficiency is proportional to the dielectric constant ϵ_{33}^{S} and the coupling factor k_{33} of the material.

There is a wide spectrum of PZT materials, typically, with values of $\epsilon_{33}^{S} = 100-7000$ and $\mathrm{k}_{33} = 0.70-0.80$. In different medical and industrial applications, materials such as PZT5A ($\epsilon_{33}^{S} = 1800$, $\mathrm{k}_{33} = 0.72$) and PZT5H ($\epsilon_{33}^{S} = 3800$, $\mathrm{k}_{33} = 0.75$) are used. On the other hand, when SNR is a critical issue, single crystals are used because of their higher efficiency ($\epsilon_{33}^{S} = 4000-7500$, $\mathrm{k}_{33} = 0.89-0.95$) relative to typical PZTs. However, matrix arrays are typically made from sub-diced plates, and single crystals do not usually behave as expected after being sub-diced. Therefore, the logical choice for the application was a PZT with the highest possible dielectric constant and coupling factor. The material of choice was HK1HD ($\epsilon_{33}^{S} = 6800$, $\mathrm{k}_{33} = 0.72$, TRS Technologies, Inc., State College, PA).

An HK1HD PZT element on top of a steel half-space was simulated, and resonance modes were determined by computing the transmit transfer function at the interface between the piezo-element and the steel half space. The dimensions of the piezo-element were optimized to achieve a thickness resonance mode with a center frequency of 1 MHz and modes with lateral vibrations occurring at frequencies of at least 3 MHz.

The initial thickness and width of a transducer element were $h_{\mathrm{PZT}} = \lambda_{\mathrm{PZT}}/4 = 1.0\,\mathrm{mm}$ ($\lambda_{\mathrm{PZT}} = 4.1\,\mathrm{mm}$ at 1 MHz,), and $w = 0.72\,\mathrm{mm}$, but these values were optimized at a later stage.

4.6.4. Printed Circuit Board

On the backside of the PZT, a printed circuit board (PCB) (modeled as FR4 material with a standard thickness of 1.6 mm) was placed. The PCB is used to wire out the electric signals from all the PZT elements of the matrix transducer array ($37 \times 17 = 629$ elements in total).

4.6.5. Backing Layer

Reflections from the back side of the PCB layer are unwanted because these can be recorded by the other transducer elements and induce errors in the measurements. Therefore, it is necessary to reduce these reflections. For this purpose, an absorbing backing material was placed behind the PCB layer. To ensure maximum transmission from the PCB into the backing and to minimize reflection back into the PCB layer, the impedance of the backing material was chosen to be the same as that of the PCB layer ($Z = 6.7\,\text{MRayl}$). This is a relatively soft backing material, and its attenuation coefficient was set to 5 dB/MHz·cm based on practical experience with these kinds of materials. Other ultrasound applications, such as medical imaging, aim to attenuate the waves that return from the backing after a two-way travel path by ≈ 40 dB. Based on this, the same level of damping is aimed for. Hence, the thickness of the backing layer was set to 40 mm.

4.6.6. Coupling Layer

The upper surface of our coupling piece runs parallel to the pipe wall in the axial direction, i.e. the coupling piece is not an angled wedge, and the lower surface conforms to the pipe wall. The bandwidth of the designed acoustic stack placed on a lead half space generated a time pulse with a length of ≈ 2.5 µs (equivalent to ≈ 5.5 mm in lead). To be able to properly window-out in time this pulse, and also to avoid interference with its reflection from the lead - pipe wall interface, the thickness of the lead piece was set to 11 mm at the center (i.e. 2× the pulse length), and thicker towards the edges in the circumferential direction. The addition of both PCB, backing, and coupling layers added losses and shifted the resonance frequency of the acoustic stack. Therefore, PZT thickness had to be optimized to $h_{\text{PZT}} = 0.35\,\lambda_{\text{PZT}} = 1.4\,\text{mm}$ to shift the thickness resonance mode back to 1 MHz. To achieve the desired resonance profile, the width of the elements was optimized to $w = 0.42\,\text{mm}$, respectively.

4.6.7. Lateral Width of the Piezo-Elements

Now, all 37 PZT elements along the axial direction of the matrix array were considered in the simulations. The PCB and backing materials had a width equal to the array aperture. The width of the lead coupling piece was large enough to be able to steer the acoustic beam up to 45° without hitting the edges, which is enough to achieve all the desired angles for wave mode conversion in the pipe wall (see Figure 4.6). The performance of the 37 PZT elements showed an interference effect of a propagating Rayleigh wave on the surface of the coupling layer, which was avoided by optimizing the width of the elements to $w = 0.62\,\text{mm}$ (see Figure 4.7).

The location of the lateral mode on the blue curve of Figure 4.7 moved very close to the frequency band of interest. To shift it back to a frequency of at least 3 MHz, the PZT elements were sub-diced. The width of the sub-dicing kerf was 50 µm, which is the same as for the kerfs of the array, to preserve the required array pitch of 0.72 mm. A sub-dicing depth of 95 % of the thickness of the PZT element was sufficient to shift the peak of the lateral mode to the right position.

4.6.8. Vias in the PCB

So far, the PCB layer has been modeled as a single solid material. In practice, PCB layers are manufactured with metalized holes, called vias, to make vertical connections, e.g. to the elements. Here, these vias have a diameter of 200 µm across and their walls are covered by a 20 µm copper layer.

To study the effect of vias on the acoustic response of the transducer, the vias were included in the FEM simulations. The center of each via was aligned with the center of the electrode of each PZT element (see Figure 4.8). The transmit transfer function was computed at the interface between the piezo-elements and the lead coupling piece. It turned out that the thickness resonance mode of the acoustic stack shifted away from 1 MHz due to the presence of the vias. Therefore, the thickness of the PZT elements had to be optimized once again to $h_{\text{PZT}} = 0.30\lambda_{\text{PZT}} = 1.2\,\text{mm}$ to achieve the desired resonance profile given in Figure 4.9. Further it was computed that the designed stack will have a transmit efficiency of $T_t = 36.4\,\text{kPa/V}$ and a receive sensitivity of $T_r = 9.2\,\mu\text{V/Pa}$, both at resonance.

4.6.9. Signal-to-Noise Ratio

To compute the noise produced by one of the sub-diced PZT elements in receive, thermal noise at room temperature was assumed, and the Johnson-Nyquist equation was used:

$$v_n = \sqrt{4 k_b T R \Delta f} \tag{4.2}$$

Here, v_n represents the root-mean-square (RMS) noise voltage produced by the PZT element, k_b represents Boltzmann's constant, T is the absolute temperature, R is the real component of the electrical impedance of the PZT element, and Δf represents the frequency bandwidth over which the noise is computed.

The real part of the electrical impedance of the PZT elements was extracted from FEM simulations on the acoustic stack in Figure 4.8, and within the bandwidth of interest it was estimated that the average noise produced by the element would be in the order of $1.1\,\mu\text{V}_{\text{RMS}}$. This implies that the required 20 dB SNR translates into a minimum required value of $11\,\mu\text{V}_{\text{RMS}}$ for V_{open} in equation (4.1) to perform a useful flow measurement.

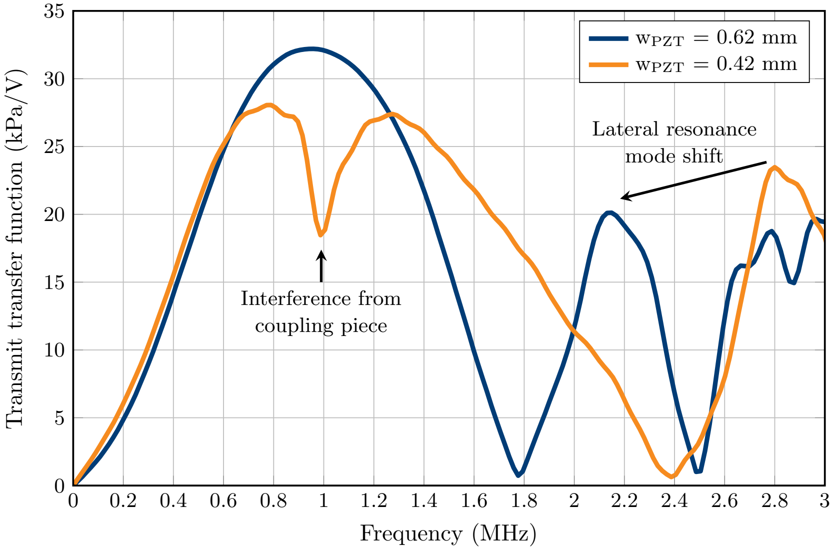

Figure 4.7: Transmit transfer functions obtained from Finite Element simulations of a 37-element HK1HD PZT transducer array with $h_{PZT} = 0.35\lambda_{PZT}$ on top of a lead coupling piece and with PCB and backing layers on the back side. The transmit transfer function was computed at the interface between the piezo-elements and the lead. The black arrow indicates the shift of the mode with lateral vibrations towards a lower frequency that is achieved by increasing the width of the piezo-elements.

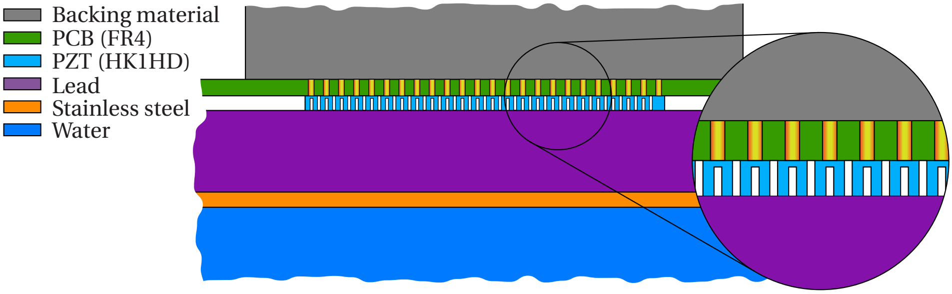

Figure 4.8: Acoustic stack of the designed transducer array. The sub-dicing kerfs of the PZT elements run up to 95 % of the element thickness. The vias in the PCB are 200 µm diameter and their walls are covered by a 20 µm thin copper layer.

SNR levels should be ≥ 20 dB for the entire range of liquids involved. Using the obtained performances from Figure 4.9, SNR estimates were computed with equation (4.1) for the acoustic travel paths shown in Figure 4.5a and Figure 4.5b. Figure 4.10 shows the expected SNR levels for the designed transducer array. From the figure it can be concluded that, at resonance (1 MHz), SNR ≥ 20 dB for all considered liquids.

4.7. Acoustic Characterization of a Linear Array Prototype

Based on the proposed transducer design, a 36-element linear array was fabricated and acoustically characterized to test its potential and suitability for self-calibrated ultrasonic clamp-on flow metering in the wide range of scenarios defined previously.

4.7.1. Fabrication

Off-the-shelf plates of PZ26 (Meggit A/S, Kvistgård, DK), with a thickness of 1.67 mm, were diced with a 0.1 mm thick diamond saw to produce linear arrays of 36 elements. In the azimuth direction, each array element had a width of 0.62 mm, and a kerf of 0.1 mm. In the elevation direction, each element has a height of 12 mm (i.e. ≈ 17 × 0.72 mm). Although the dielectric constant of PZ26 is approximately half of that of HK1HD, the

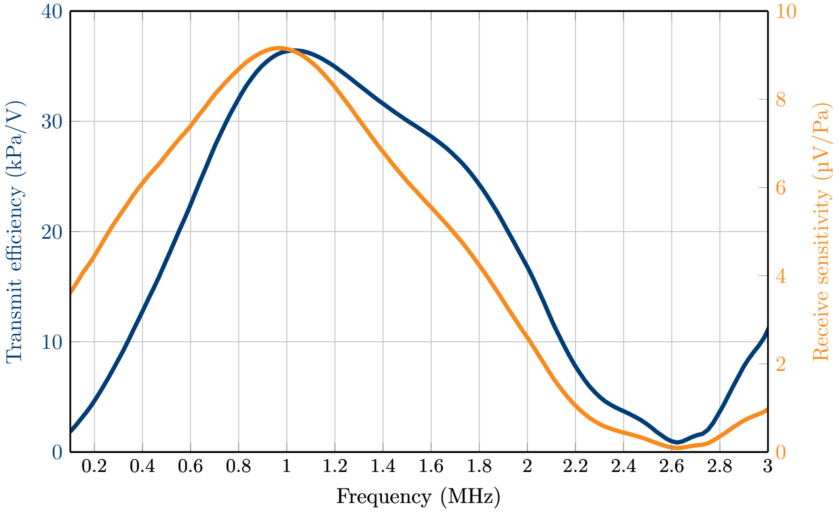

Figure 4.9: Expected performance of the designed transducer array. There are no modes with lateral vibrations within the frequency band of interest (0.2 – 2 MHz). Both the transmit efficiency and the receive sensitivity were computed at the interface between the piezo-elements and the lead.

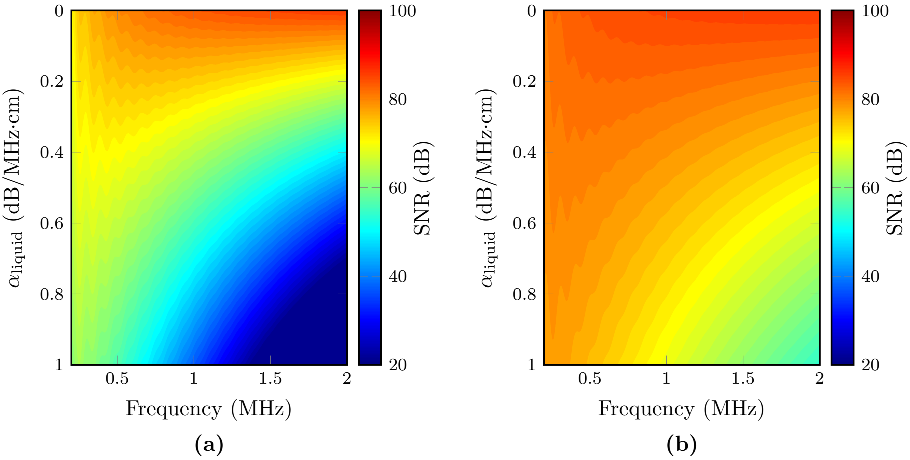

Figure 4.10: Computed SNR of the designed transducer array versus frequency and attenuation coefficient of the liquid for compressional waves in the pipe wall and six bounces within the pipe (a) and shear waves in the pipe wall and two bounces within the pipe (b).

estimated SNR levels for flow measurements of water, computed with equation (4.1), are still significantly above the 20 dB level requirement.

In addition, a backing material was also fabricated. It consisted of a mix of epoxy and tungsten particles of different sizes. The backing had an acoustic impedance of $Z \approx$ 6.7 MRayl, and an attenuation coefficient at 1 MHz of $\alpha \approx$ 15 dB/MHz·cm. Therefore, a 13 mm-thick backing was sufficient to achieve the required 40 dB attenuation of the waves reflecting at the backside of this layer.

Molten lead was poured into custom-made molds to fabricate the desired coupling pieces. To characterize the array, a flat 11 mm thick lead piece was cast (see Figure 4.11). For performing the flow measurements, pieces with a concave shape were made that would fit on top of a stainless steel pipe with an outer diameter of 42 mm. This piece had a minimum thickness of 11 mm in its center. Figure 4.12 shows the fabricated linear array prototype, including the array after the dicing process.

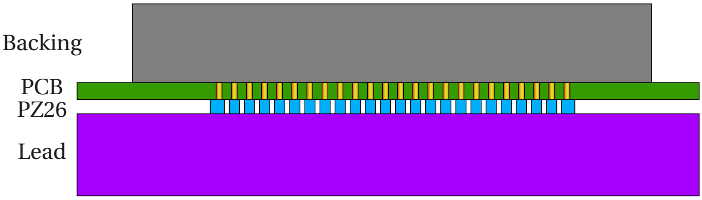

Figure 4.11: Geometry of the fabricated linear transducer array prototype. The PCB included air-filled vias with a diameter of 200 μm and a 20 μm-thick copper layer on the sides.

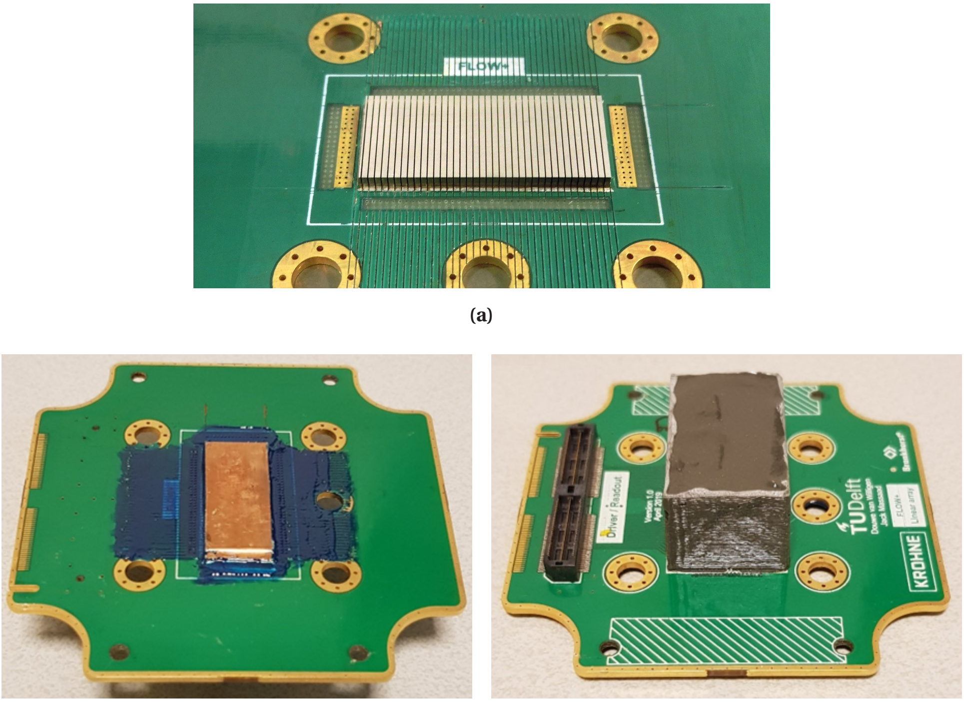

(a)

(b)

(c)

Figure 4.12: Fabricated prototype of one of the linear arrays. (a) Array obtained after dicing the PZ26 plate on top of the PCB, before applying a copper ground foil. (b) PZT array with a 20 μm thick copper ground foil and (c) backing poured on top of the custom-made PCB.

4.7.2. Beam Profile

The fabricated acoustic stack was placed on top of a 1 mm-thick stainless steel plate, and finally on a water surface (see Figure 4.13). The transducer array was excited via a Verasonics V1 system (Verasonics Inc., Kirkland, WA, USA), with a 1-cycle square wave pulse with a center frequency of 1 MHz and a peak amplitude of 5 V. Measurements of the acoustic wavefield were performed 107 mm below the water column, in a plane parallel to the surface of the transducer array using a 0.2 mm-diameter hydrophone (Precision Acoustics Ltd., Dorchester, UK), and amplified by 60 dB (AU-1519, Narda-MITEQ, Hauppauge, NY, USA) before being finally recorded.

Peak amplitudes of the envelopes of the measured signals show a relatively symmetric pattern (Figure 4.14), although the imperfect shape may be caused by the slight inter-element efficiency variation, and/or by a slight relative inclination between the plane that defines the surface of the transducer array and the measurement plane.

4.7.3. Efficiency

As shown in Figure 4.9, FEM simulations of the designed array reported an efficiency, in lead, of ≈ 36.4 kPa/V. However, in practice, transducer efficiency is usually measured in water, where an efficiency of ≈ 1.95 kPa/V was reported for the same array. In contrast, for the fabricated linear array prototype shown in Figure 4.11 and 4.12, FEM simulations reported an efficiency, in water of ≈ 0.88 kPa/V.

Considering the measured time signal, $V_{out}(t)$, associated to the coordinate of maximum

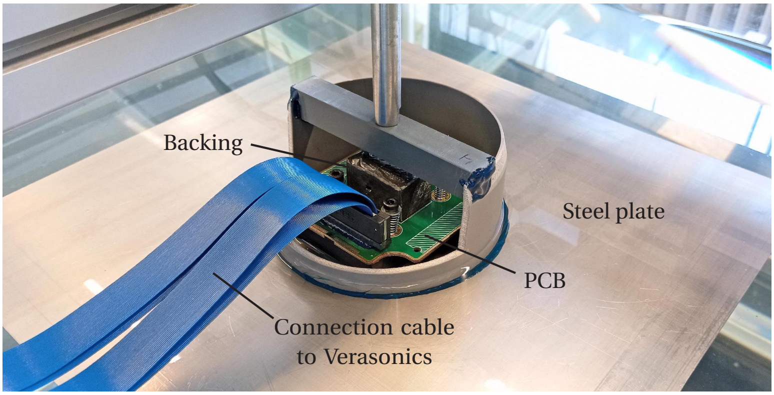

Figure 4.13: Experimental setup to characterize the fabricated linear transducer array prototype shown in Figure 4.12. The Backing and PCB layers are shown. The linear array (not shown here) is located below the PCB.

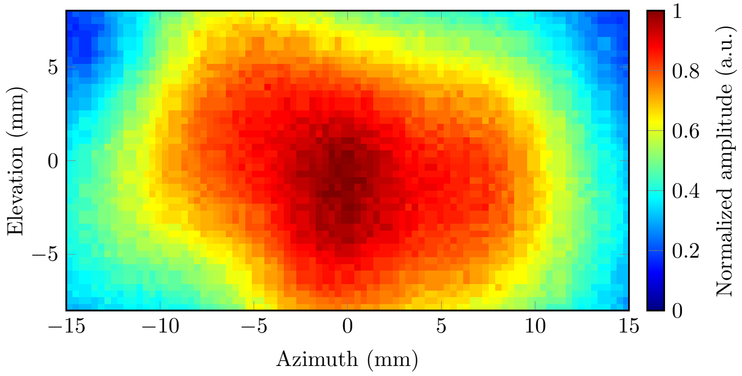

Figure 4.14: Beam profile hydrophone measurements of the fabricated linear transducer array prototype. The time signals were recorded at an axial distance of 107 mm with respect to the array.

amplitude in Figure 4.14, the transmit transfer function of the fabricated linear transducer array, $T_t(\omega)$, was estimated via the method of [18] as

$$T_t(\omega) = \frac{V_{tr}(\omega)}{V_{rc}(\omega) D(\omega) T_{amp}(\omega) T_{hyd}(\omega)}, \tag{4.3}$$

where ω represents the angular frequency, $V_{tr}(\omega)$ represents the Fourier transform of the transmitted time signal, and $V_{rc}(\omega)$ represents the Fourier transform of the signal measured by the hydrophone. $T_{amp}(\omega)$ and $T_{hyd}(\omega)$ represent the transfer functions of the amplifier and hydrophone, respectively. The symbol $D(\omega)$ represents the diffraction correction of the acoustic wavefield. Simulations of the acoustic wavefield produced by the fabricated array aperture were performed using Field II [19, 20] to obtain the diffraction correction term, which was computed as

$$D(\omega) = \frac{p_{z0}(\omega)}{p_0(\omega)}, \tag{4.4}$$

where $p_{z_0}(\omega)$ represents the FFT of the on-axis acoustic pressure signal at $z_0 = 113.5$ mm, and $p_0(\omega)$ represents the FFT of the averaged acoustic pressure signal located along the surface of the transducer array but also in the far field of the mathematical elements simulated by Field II.

Measurements were performed with and without the lead coupling piece, and compared with the simulated efficiencies. Figure 4.15 shows two distinctive resonance peaks: one at ≈ 1.5 MHz and another one at ≈ 0.6 MHz, which correspond to the PZT and the coupled PCB-PZT resonance, respectively. Moreover, the PZT and the steel layer destructively

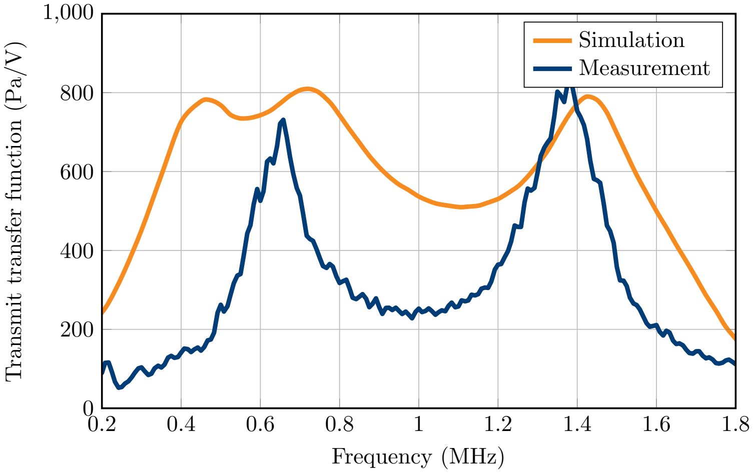

Figure 4.15: Measured and simulated transmit transfer function, in water, of the prototype linear transducer array of Figure 4.12, without the lead coupling piece.

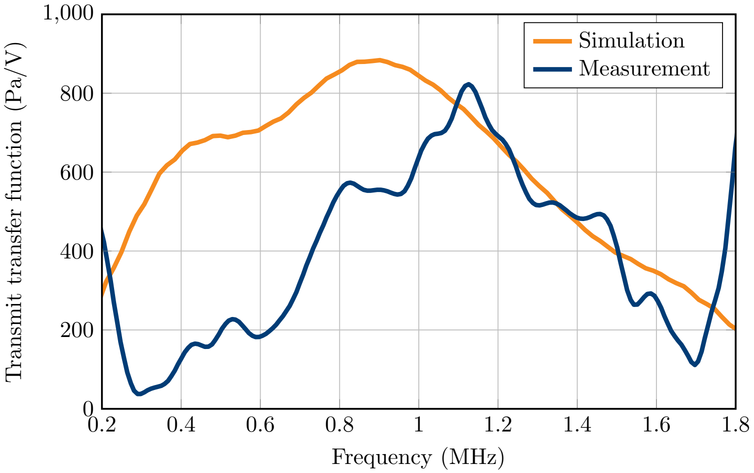

Figure 4.16: Measured and simulated transmit transfer function, in water, of the prototype linear transducer array of Figure 4.12, with the lead coupling piece.

interfered at $\approx 1\,\text{MHz}$. On the other hand, Figure 4.16 shows the matching effect of the lead, where only one resonance frequency was observed. Although the measured and simulated magnitudes of the efficiencies shown in Figures 4.15 and 4.16 correspond reasonably well, they also show some distinct differences in their shape, which are mainly due to practical limitations during the measurements. First, due to the relatively low operation frequency of the array, in combination with space constrains in the water tank, the wavefield used to compute efficiencies was not measured in the far field as it is usually done, but just near the natural focus of the azimuth aperture (focal distance $\approx 113.5\,\text{mm}$). Second, PZTs are complex materials, and it is not uncommon for some of their nominal properties, which were used in simulations, to have fabrication uncertainties of up to $10\,\%$. The combination of these two likely factors may be the cause for the measured sharper resonance peaks in Figure 4.15 and the $\approx 10\,\%$ in peak resonance shift observed in Figure 4.16. Furthermore, since the diffraction correction term was also computed near the natural focus and not in the far field as usual, the resultant correction presented a ripple-like shape along the bandwidth of interest, which directly caused the ripple-like behavior around the measured resonance frequency of Figure 4.16 and to report a lower bandwidth relative to the simulation. However, at a measured resonance frequency of $1.12\,\text{MHz}$, Figure 4.16 reports a measured efficiency of the fabricated linear array of $\approx 0.82\,\text{kPa/V}$, which is reasonably close to the $0.88\,\text{kPa/V}$ reported by FEM simulations. Furthermore, the measured efficiency reported a $-20\,\text{dB}$ bandwidth between $0.38 - 1.70\,\text{MHz}$.

4.7.4. Beam Steering and Wave Mode Conversion

It was important to also investigate the ability of the fabricated array to achieve wave mode conversion in the pipe wall and measure flow speed in the scenarios of Figure 4.5a and Figure 4.5b. In the experimental setup, time delays were applied to the array elements to steer an acoustic beam through the lead coupling piece, the metal layer, and finally into the water, where a linear scan of the wave field was performed in the water, at a depth of $z_0 = 113.5\,\text{mm}$ and along the azimuthal direction of the array.

Three steering angles were tested: $\theta_{\text{lead}} = 0°$, $\theta_{\text{lead}} = 20°$ and $\theta_{\text{lead}} = 40°$. Given the compressional bulk wave sound speed of lead ($c_L = 2200\,\text{m/s}$) and stainless steel ($c_L = 5800\,\text{m/s}$), Snell's law predicts a critical angle of $22\,°$, beyond which only shear waves will propagate in the pipe wall. Therefore, for the steering angle of $40\,°$, the shear bulk wave speed of stainless steel ($c_T = 3100\,\text{m/s}$), was used. Figure 4.17 shows the measured linear scans. As expected, the peak pressure shifts as a function of the steering angle. Furthermore, given the azimuthal location x_{max} of the main peak of a linear scan profile and the associated time signal from which the transit time t_{w} of the acoustic beam can be extracted, the measured steering angle of the acoustic beam in water ($c_{\text{w}} = 1500\,\text{m/s}$) was determined as

$$\theta_{\text{w}} = \arcsin\left(\frac{x_{\text{max}}}{c_{\text{w}}\,t_{\text{w}}}\right) \tag{4.5}$$

For the considered angles $\theta_{\text{lead}} = 20\,^{\circ}$ and $\theta_{\text{lead}} = 40\,^{\circ}$ beams steered in lead, the measured angles in water were $\theta_{\text{w}} = 15.8\,^{\circ}$, and $\theta_{\text{w}} = 30.6\,^{\circ}$, respectively. These were comparable to the theoretical values of $\theta_{\text{w}} = 13.2\,^{\circ}$, and $\theta_{\text{w}} = 25.4\,^{\circ}$. The discrepancies are most likely due to the sound speeds considered in the theoretical calculations. Other evidence was the constant offset between the theoretical and measured peak locations for each considered angle. At $\theta_{\text{lead}} = 20\,^{\circ}$, an interference effect was observed between the bulk compressional and shear waves in the steel, which refracted into the water with a similar angle and produced the dip in the amplitude measured in the azimuthal range between 20 – 30 mm. The results of Figure 4.17 confirmed that, with the fabricated array, it is possible to also excite shear waves in the pipe wall and measure flow with either scenario Figure 4.5a or scenario Figure 4.5b.

The noise floor is slightly different for each scan in Figure 4.17 because, in each case, different interfering waves were occurring. This resulted in measurements with a slightly different peak amplitude before normalization.

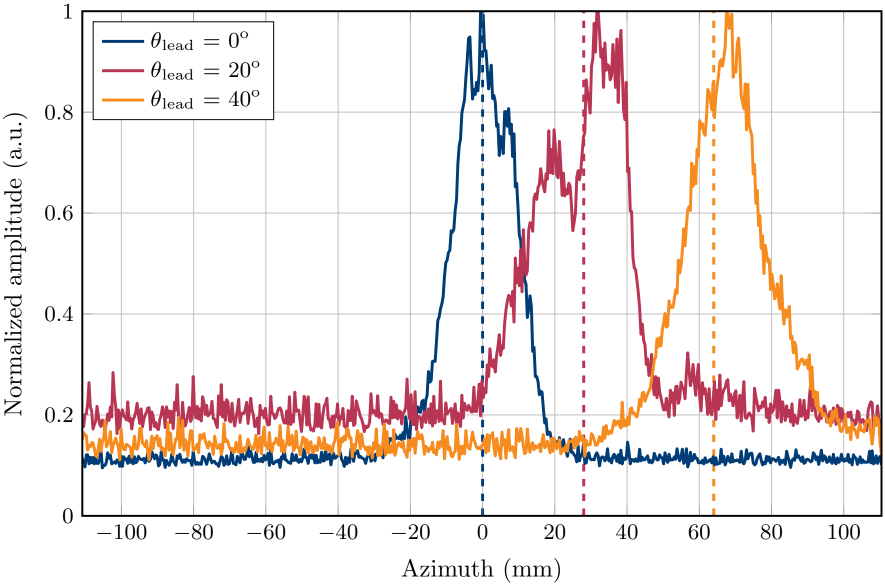

Figure 4.17: Measured linear scans of the amplitude of the acoustic wave field in water, generated by the transducer array of Figure 4.12 for three different beam steering angles. The dashed vertical lines indicate the theoretical expected position of the peak pressures for the theoretical sound speeds involved.

4.8. Discussion

The region of low SNR predicted in Figure 4.10a for relatively high-damping liquids may be narrowed-down in two simple ways: The beam steering angle could be increased and the acoustic beam could reflect fewer times within the pipe, therefore increasing SNR. or the beam steering angle could be increased enough to operate the sensor in the shear wave mode shown in Figure 4.5b. On the other hand, the input voltage may be increased to also achieve higher SNRs, however, this value is usually limited in practical applications to 5 V for intrinsic safety, especially when measuring flow speed of fluids in an industrial setting.

Good confidence was built around the simulation tool for the design of a matrix array for ultrasonic clamp-on flow measurements. Based on the fabrication of a linear array prototype, and the results of its acoustic characterization, its potential for the desired application was demonstrated. These results motivate the fabrication of a first prototype ultrasonic clamp-on flow meter consisting of two of these linear arrays. More details about this are presented in Chapter 5.

4.9. Conclusions

In this chapter, the design of an ultrasonic clamp-on flow meter based on matrix transducers has been presented. A proof-of-concept linear array prototype has been fabricated based on the proposed design. The prototype was characterized acoustically and it showed good agreement with FEM simulations. Its measured efficiency and beam steering capabilities demonstrated its ability to achieve wave mode conversion in metal pipes and its suitability for ultrasonic clamp-on flow metering of a wide range of liquids.

References

[1] J. Massaad, P. L. M. J. van Neer, D. M. van Willigen *et al.*, "Design and proof-of-concept of a matrix transducer array for clamp-on ultrasonic flow measurements," *IEEE Transactions on Ultrasonics, Ferroelectrics, and Frequency Control*, 2022.

[2] J. Massaad, D. van Willigen, P. van Neer *et al.*, "Acoustic design of a transducer array for ultrasonic clamp-on flow metering," *IEEE Int. Ultrason. Symp.*, pp. 1133–1136, 2019.

[3] R. C. Baker, *Flow measurement handbook: industrial designs, operating principles, performance, and applications.* Cambridge University Press, 2005.

[4] W.-S. Cheung, H.-S. Kwon, K.-A. Park *et al.*, "Acoustic flowmeter for the measurement of the mean flow velocity in pipes," *J. Acoust. Soc. Am.*, vol. 110, no. 5, pp. 2308–2314, 2001.

[5] J. C. Wendoloski, "On the theory of acoustic flow measurement," *J. Acoust. Soc. Am.*, vol. 110, no. 2, pp. 724–737, 2001.

[6] D. Kurniadi and A. Trisnobudi, "A multi-path ultrasonic transit time flow meter using a tomography method for gas flow velocity profile measurement," *Part. Part. Syst. Charact.*, vol. 23, no. 3-4, pp. 330–338, 2006.

[7] M. Sanderson and H. Yeung, "Guidelines for the use of ultrasonic non-invasive metering techniques," *Flow. Meas. Instrum.*, vol. 13, no. 4, pp. 125–142, 2002.

[8] J. Massaad, P. L. M. J. van Neer, D. M. van Willigen *et al.*, "Towards a calibration-free ultrasonic clamp-on flow meter: Pipe geometry measurements using matrix arrays," *Proc. Meet. Acoust.*, vol. 39, no. 1, pp. 1–7, 2019.

[9] J. Massaad, P. L. M. J. van Neer, D. M. van Willigen *et al.*, "Suppression of Lamb wave excitation via aperture control of a transducer array for ultrasonic clamp-on flow metering," *J. Acoust. Soc. Am.*, vol. 147, no. 4, pp. 2670–2681, 2020.

[10] F. Hofmann, "Fundamentals of ultrasonic-flow measurement for industrial applications," *KROHNE Messtechnik GmbH & Co. KG, Duisburg*, pp. 1–31, 2000.

[11] A. S. Dukhin and P. J. Goetz, *Characterization of liquids, dispersions, emulsions, and porous materials using ultrasound.* Elsevier, 2017.

[12] P. L. M. J. van Neer, S. Blaak, J. G. Bosch *et al.*, "Mode vibrations of a matrix transducer for three-dimensional second harmonic transesophageal echocardiography," *Ultrasound Med. Biol.*, vol. 38, no. 10, pp. 1820–1832, 2012.

[13] C. Adams, S. Harput, D. Cowell *et al.*, "An adaptive array excitation scheme for the unidirectional enhancement of guided waves," *IEEE Trans. Ultrason. Ferroelectr. Freq. Control*, vol. 64, no. 2, pp. 441–451, 2016.

[14] J. Li and J. L. Rose, “Implementing guided wave mode control by use of a phased transducer array,” *IEEE Trans. Ultrason. Ferroelectr. Freq. Control*, vol. 48, no. 3, pp. 761–768, 2001.

[15] K.-C. T. Nguyen, L. H. Le, T. N. H. T. Tran *et al.*, “Excitation of ultrasonic Lamb waves using a phased array system with two array probes: Phantom and in vitro bone studies,” *Ultrasonics*, vol. 54, no. 5, pp. 1178–1185, 2014.

[16] W. Zhu and J. L. Rose, “Lamb wave generation and reception with time-delay periodic linear arrays: A bem simulation and experimental study,” *IEEE Trans. Ultrason. Ferroelectr. Freq. Control*, vol. 46, no. 3, pp. 654–664, 1999.

[17] P. H. Rogers and A. L. Van Buren, “An exact expression for the lommel-diffraction correction integral,” *J. Acoust. Soc. Am.*, vol. 55, no. 4, pp. 724–728, 1974.

[18] P. L. M. J. van Neer, G. Matte, J. Sijl *et al.*, “Transfer functions of US transducers for harmonic imaging and bubble responses,” *Ultrasonics*, vol. 46, no. 4, pp. 336–340, 2007.

[19] J. A. Jensen and N. B. Svendsen, “Calculation of pressure fields from arbitrarily shaped, apodized, and excited ultrasound transducers,” *IEEE Trans. Ultrason. Ferroelectr. Freq. Control*, vol. 39, no. 2, pp. 262–267, 1992.

[20] J. A. Jensen, “Field: A program for simulating ultrasound systems,” 10^{th} *Nordic-Baltic Conference on Biomedical Imaging, Vol. 4, Supplement 1, Part 1*, vol. 34, no. 1, pp. 351–353, 1996b.

5

Flow Measurements with a Clamp-On Transducer Array

An ultrasonic clamp-on flow meter prototype consisting of two 36-element linear arrays was fabricated based on the matrix transducer design proposed in Chapter 4. Flow speed measurements of water were performed in a custom-made flow loop and in two scenarios: using compressional and shear waves in the pipe wall.

Mean flow measurements were achieved by electronic beam steering of the acoustic beams and using both compressional and shear waves generated in the pipe wall. Correlation coefficients of $R^2 > 0.99$ *between measured and reference flow speeds were obtained, thus showing the operational concept of an array-based clamp-on ultrasonic flow meter.*

Parts of this chapter have been published in the IEEE Transactions on Ultrasonics, Ferroelectrics and Frequency Control [1].

5.1. Introduction

In Chapter 4, the design of a matrix transducer array for ultrasonic clamp-on flow metering was described in detail for a wide range of liquids and pipe sizes. The matrix design inspired the fabrication of a 36-element linear transducer array, whose acoustic characterization reported a very good agreement with the simulations. With two of those linear arrays, an ultrasonic clamp-on flow meter prototype was fabricated.

This chapter shows how this custom-built device was used to measure flow, and how new tools and techniques were used within this context to further improve accuracy of the flow measurements.

5.2. Experimental Setup

A custom-made flow loop was built (see Figure 5.1). It mainly consisted of PVC and acrylic pipes with a constant inner diameter of 40 mm, and a reference in-line ultrasonic flow meter (Optosonics 3400, KROHNE Nederland B.V., Dordrecht, NL). The liquid used was water. The flow rate was manually controlled with a valve. With this setup it was possible to achieve flow speeds of water up to 0.6 m/s.

A 30 cm long section of the setup consisted of a 304 stainless steel pipe ($c_L = 5920$ m/s, $c_T = 3141$ m/s), with a wall thickness of $h = 1$ mm and an inner diameter of $D = 40$ mm. Both fabricated linear arrays were centrally clamped on this pipe section with custom-

(a) (b)

Figure 5.1: Custom-made flow loop to perform ultrasonic clamp-on flow measurements with the fabricated prototype arrays. Gravity was used to drive flow from left to right through the stainless steel pipe section on which the arrays were installed. A close-up picture (b) shows the custom-made 3D-printed green and blue frames of the prototype arrays. They were designed with a system of screws and springs to achieve good mechanical coupling of the array with the coupling piece (inner 4 screws), and of the coupling piece with the pipe wall (outer 4 screws).

made 3D-printed frames to ensure proper mechanical coupling with the pipe. As can also be seen in Figure 5.1, the arrays were not clamped on the top of the pipe but rather at the side of the pipe to avoid the potential non-reciprocal effects of bubbles on the measurements.

The center-to-center distance between the transducers was 80 mm, and flow speed was measured with compressional waves in the pipe wall, as well as with shear waves. For compressional waves in the pipe wall, the required steering angle was 12.85°, and the desired wave mode was expected to arrive at $\approx 340\,\mu\text{s}$. For shear waves in the pipe wall, the steering angle of the acoustic beam within the coupling piece was 32.75°, and the desired wave mode was expected to arrive at $\approx 130\,\mu\text{s}$. These transit times were also cross-checked with FEM simulations.

5.3. Data Acquisition

Two custom-made PCBs were designed to wire-out each piezo-element of both linear arrays to a Verasonics Vantage 256 system. This machine was used to excite the piezo-elements with a 1-cycle square pulse with a center frequency of $f_c = 1\,\text{MHz}$ and a peak voltage of 5 V. Time delays in transmission were also implemented with this machine to produce steered acoustic beams.

Measurements with different pairs of piezo-elements confirmed that the Verasonics machine kept the timing of the signals stable enough to perform flow measurements. The time jitter of the machine was reported to be $\approx 4\,\text{ps}$, which was an acceptable value given the few tens of nanoseconds of the expected transit-time differences to be measured with the setup.

Upstream and downstream measurements were performed in an interleaved fashion to minimize the effects of temperature change on the sound speed of the liquid, and therefore on the flow speed estimates. One thousand measurements were performed in each direction, with a pulse repetition frequency (PRF) of $\approx 87\,\text{Hz}$. This allowed to record all measurements in 23 s. The received signals of the transducer elements were recorded with a sampling frequency of 62.5 MHz and finally saved to a file for further processing.

5.4. Data Processing Sequence

For each flow speed, the signals were processed as shown in the flowchart of Figure 5.2. The bandpass filter applied to the raw signals consisted of a 5^{th}-order Butterworth filter. The measured time signals were interpolated with a sampling frequency of 250 MHz, i.e. 4 ns, which was considered enough to estimate the expected few tens of nanoseconds of transit-time differences. Lastly, the signals corresponding to each individual receiving element were delayed to align the signals for a given beam direction, and subsequently

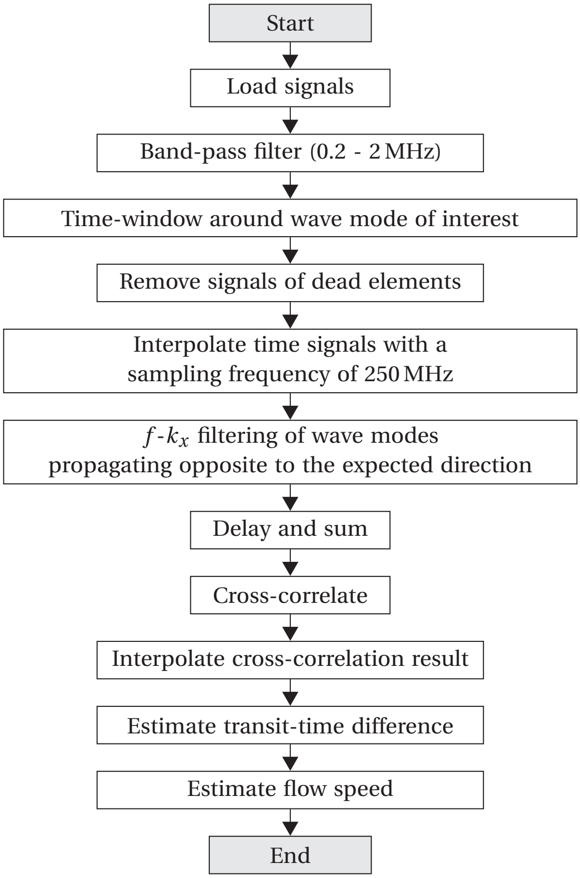

Figure 5.2: Signal processing sequence applied to the measured signals of the flow sensor.

summed together. The two final signals obtained from an upstream and a downstream measurement were then cross-correlated to obtain their transit-time difference. This was finally used as input, together with the properties of the pipe and the liquid, to estimate the flow speed.

5.5. Measurements

5.5.1. Time Signals

Raw time signals for the two considered acoustic paths were recorded. Figure 5.3 and 5.4 show the measured signals at zero flow conditions for compressional waves and shear

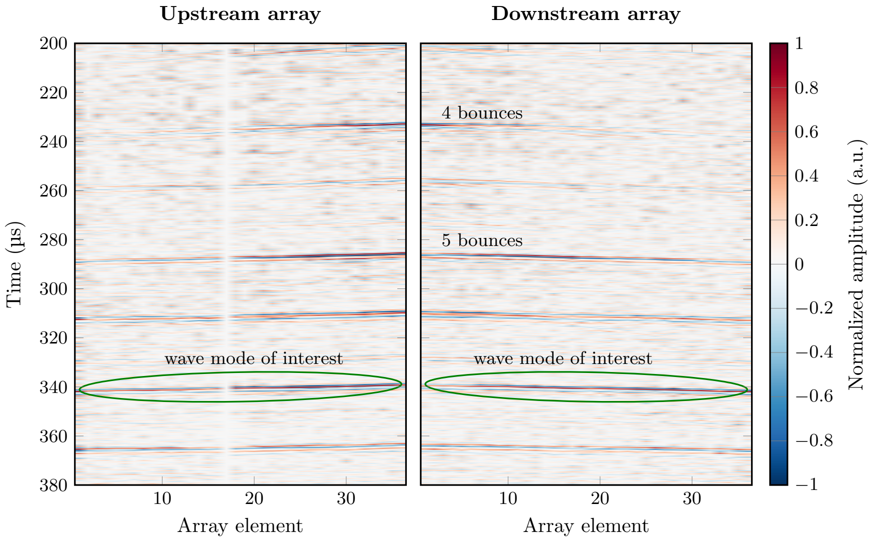

Figure 5.3: Time signals measured at zero-flow conditions with the custom-built ultrasonic clamp-on flow meter based on two linear arrays, for compressional waves in the pipe wall and 6 v-shaped bounces of the acoustic beam within the pipe.

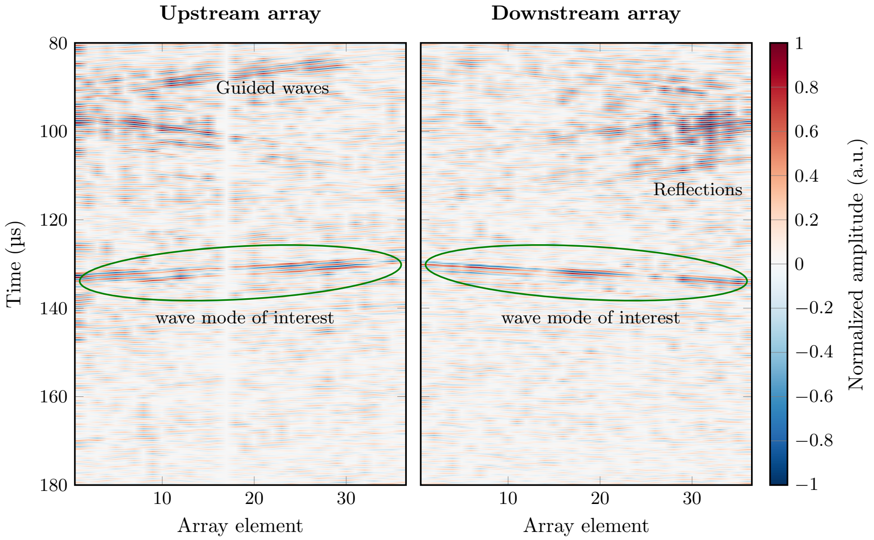

Figure 5.4: Time signals measured at zero-flow conditions with the custom-built ultrasonic clamp-on flow meter based on two linear arrays, for shear waves in the pipe wall and 2 v-shaped bounces of the acoustic beam within the pipe.

waves in the pipe wall respectively. In both scenarios, the desired wave mode of interest was recorded within the expected transit time. Furthermore, other wave modes, including guided waves and reflections from flanges were also recorded. Moreover, as expected, the amplitude of the wave mode of interest was recorded with a higher SNR relative to the amplitudes of the other acoustic paths, which also aided towards its identification within the time domain signals.

The upstream array (Array 1 in Figure 5.1b) had 1 broken element. The signals corresponding to this element was removed from the analysis, as well as the signal corresponding to its mirror counter-part from the downstream array (Array 2 in Figure 5.1b). This way, system reciprocity was kept.

5.5.2. f-k_x Filtering

A particularly powerful new tool that linear arrays bring to ultrasonic flow metering is the possibility to filter out undesired spurious wave modes. Given the recorded signals of several transducer elements, it is possible to visualize the propagating wave modes, both in the time domain (see Figure 5.5) and, after applying a 2D Fourier transformation, in the f-k_x domain (see Figure 5.6). Although the wave modes could be identified in the time domain, it may not always be possible to easily window out the desired wave mode because it may overlap with the undesired ones. The probability of this overlap increases when the transducers are installed closer to each other, and also when the sensor is installed nearby other features of the pipeline, such as flanges and/or valves. However, the direction (i.e. steering angle) of the transmitted beam is always known during ultrasonic flow metering. Therefore, the expected direction from which it should arrive is also known, and will correspond with a specific straight line in the f-k_x domain. Thus, with linear arrays it is possible to identify this wave mode in the f-k_x domain and filter-out all other undesired wave modes, including guided waves and reflections, to finally obtain cleaner time signals to estimate the flow speed (see Figure 5.5b).

In principle, to properly implement f-k_x filtering, all piezo-elements of the array should output a coherent signal, so as to achieve uniform sampling in both time and space. Otherwise, the f-k_x spectrum of non-uniformly sampled signals would be distorted, i.e. the wave modes would be located at the wrong positions, and the technique would be sub-optimal. Therefore, in the future, it would be very useful to develop an interpolation-based method that aids towards the inevitable practical malfunctioning of the piezo-elements, so that filtering techniques could still be implemented. Nevertheless, in the particular case of the measurements taken with the setup of Figure 5.1, it was possible to window out the wave mode of interest in the time domain and still estimate flow speed.

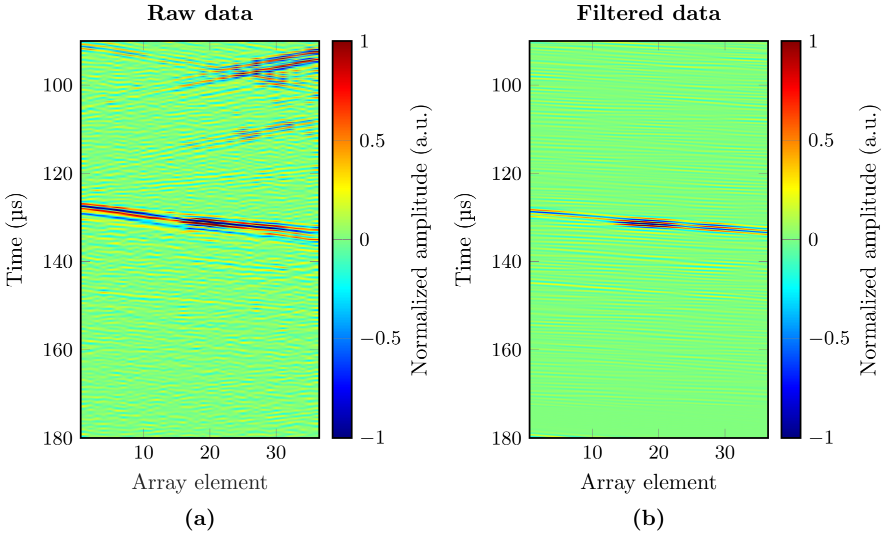

(a) (b)

Figure 5.5: Measured raw signals with the 36-element downstream array at zero-flow conditions (a) and time signals after filtering the undesired spurious wave modes in the Fourier domain (b).

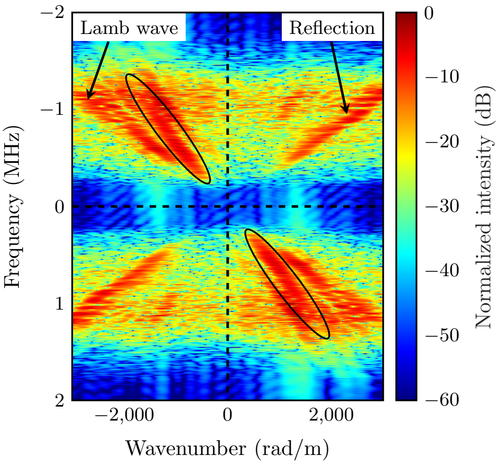

Figure 5.6: Magnitude of the 2D Fast Fourier Transform (FFT) applied on the time signals of Figure 5.5a, where different wave modes are identified. Based on the location of the desired wave mode of interest (black oval), the 1st and 3rd quadrant may be filtered out, as well as certain regions of the 2nd and 4th quadrant.

5.5.3. Flow Speed

Considering a sound speed in water of $c_{\text{liquid}} = 1500\,\text{m/s}$, it was possible to compute the theoretical transit-time difference Δt between upstream and downstream signals measured for the acoustic paths with compressional waves and with shear waves. At zero-flow conditions, a transit-time of $\Delta t = 0\,\text{ns}$ is expected for both scenarios. However, in practice, an ultrasonic flow metering system is never completely reciprocal, and a transit-time difference is still measured at zero-flow conditions.

With the fabricated pair of linear arrays, and considering the acoustic beam paths of a compressional wave and a shear wave in the pipe wall, values of $\Delta t = 0.55\,\text{ns}$ and $\Delta t = 0.19\,\text{ns}$ respectively, were measured at zero-flow conditions. These values are lower than the usual few nanoseconds of zero-flow error reported for common single-element ultrasonic clamp-on flow meters [2]. Furthermore, these values were obtained with a median absolute deviation (mad) of $\text{mad} = 2.19\,\text{ns}$ and $\text{mad} = 1.06\,\text{ns}$, respectively. The measured transient signals after processing and delay-and-sum beamforming are shown in Figure 5.7 and Figure 5.8.

For the highest possible reference flow speed, i.e. $v_{\text{ref}} = 0.6\,\text{m/s}$, theoretical transit-time differences of $\Delta\text{t} = 39.27\,\text{ns}$ and $\Delta\text{t} = 33.86\,\text{ns}$ were computed, for the compressional wave and shear wave acoustic path, respectively. The measured values for this flow speed were $\Delta\text{t} = 38.46\,\text{ns}$ and $\Delta\text{t} = 33.80\,\text{ns}$, with median absolute deviation of $\text{mad} = 4.05\,\text{ns}$ and $\text{mad} = 2.39\,\text{ns}$, respectively. Measured time signals are shown in Figure 5.7b and Figure 5.8b. The reported median absolute deviations, like those shown in Figure 5.9, apply to a single measurement. The slight discrepancies between measured and theoretical values are likely due to the chosen theoretical sound speed of the water. Also, when considering compressional waves in the pipe wall, the transit time of the acoustic waves is higher than with shear waves, which is the reason for the higher transit-time differences in the former scenario relative to the latter.

The flow speed v_{f} can be obtained from the acoustic beam path, the properties of the pipe, the sound speed of the liquid, and the measured transit-time differences between upstream and downstream measurements. This requires computing the positive root of the second-order equation:

$$\left[\Delta\text{t}\sin^2(\theta_{\text{liquid}})\right] v_{\text{f}}^2 + \left[4bD\tan(\theta_{\text{liquid}})\right] v_{\text{f}} - \Delta\text{t}c_{\text{liquid}}^2 = 0, \tag{5.1}$$

where θ_{liquid} represents the steering angle of the acoustic beam in the liquid, and b represents the number of bounces (v-shapes) of the acoustic beam within the pipe wall before arriving at the receiving transducer.

For the measurement scenario with compressional waves in the pipe wall, as well as for shear waves in the pipe wall, the flow speed was obtained and compared with the measurement of the reference flow meter. At zero-flow conditions, flow speeds of $v_{\text{f}} =$

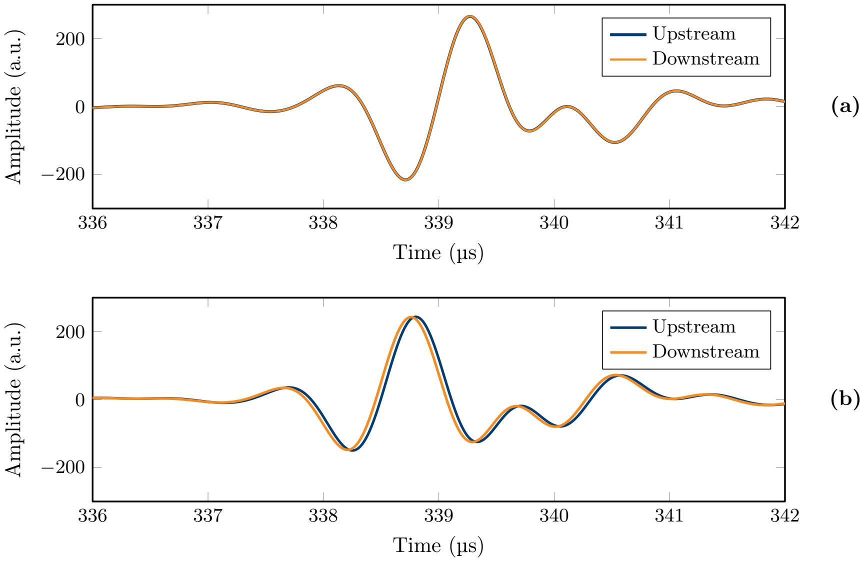

Figure 5.7: Processed upstream and downstream time signals at zero-flow conditions (a) and at a flow speed of $v_{\text{ref}} = 0.6\,\text{m/s}$ (b), considering compressional waves in the pipe wall.

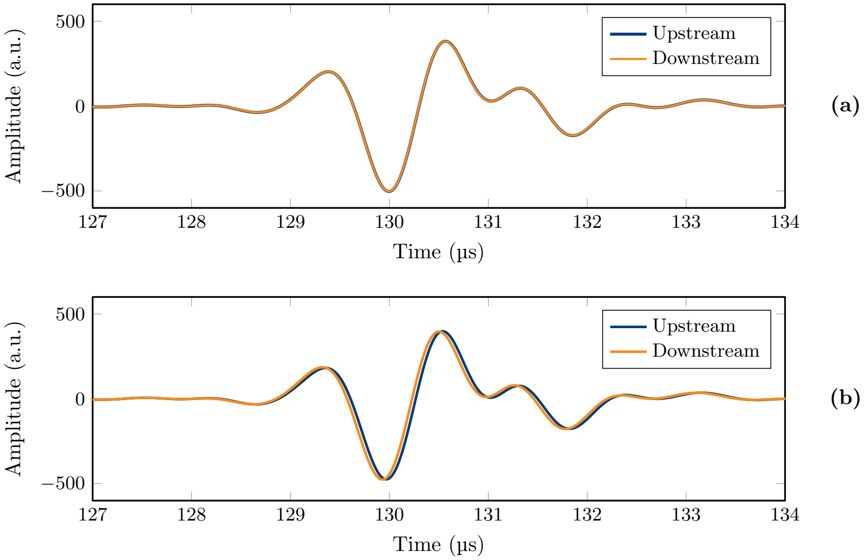

Figure 5.8: Processed upstream and downstream time signals at zero-flow conditions (a) and at a flow speed of $v_{\text{ref}} = 0.6\,\text{m/s}$ (b), considering shear waves in the pipe wall.

0.008 m/s and $v_\mathrm{f} = 0.02$ m/s, were estimated, with a median absolute deviation of mad = 0.04 m/s and mad = 0.01 m/s, respectively. Furthermore, at a reference flow speed of $v_\mathrm{ref} = 0.6$ m/s, the measured flow speeds with the prototype were $v_\mathrm{f} = 0.59$ m/s and $v_\mathrm{f} = 0.65$ m/s, with a median absolute deviation of mad = 0.06 m/s and mad = 0.03 m/s, respectively.

A linear fit between the reference flow speeds and those measured with the fabricated prototype was performed. The slopes of the linear fits shown in Figures 5.10 and 5.11 were 0.977 and 1.054, respectively, which indicates a good correspondence between reference and measurements.

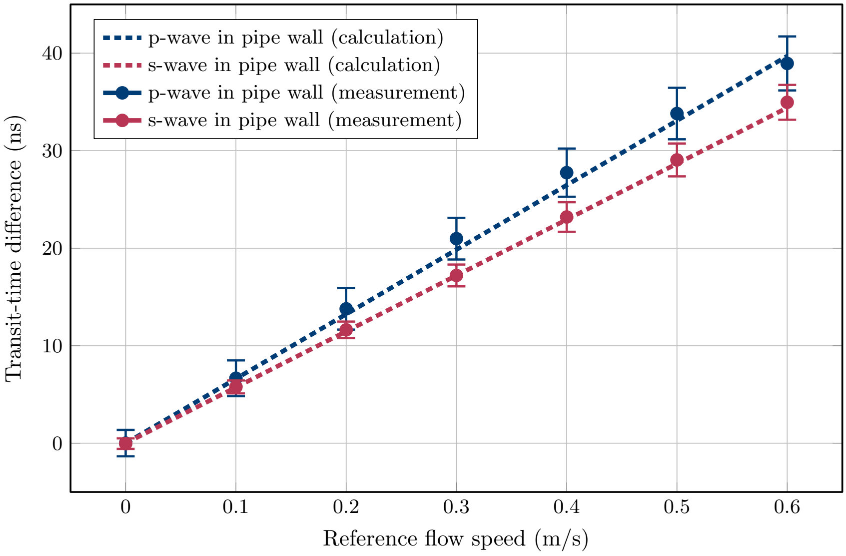

Figure 5.9: Theoretical (dashed lines) and measured (markers) transit-time difference between upstream and downstream signals, versus flow speed, for compressional waves (p-waves) and shear waves (s-waves) in the pipe wall. Vertical bars indicate median absolute deviations.

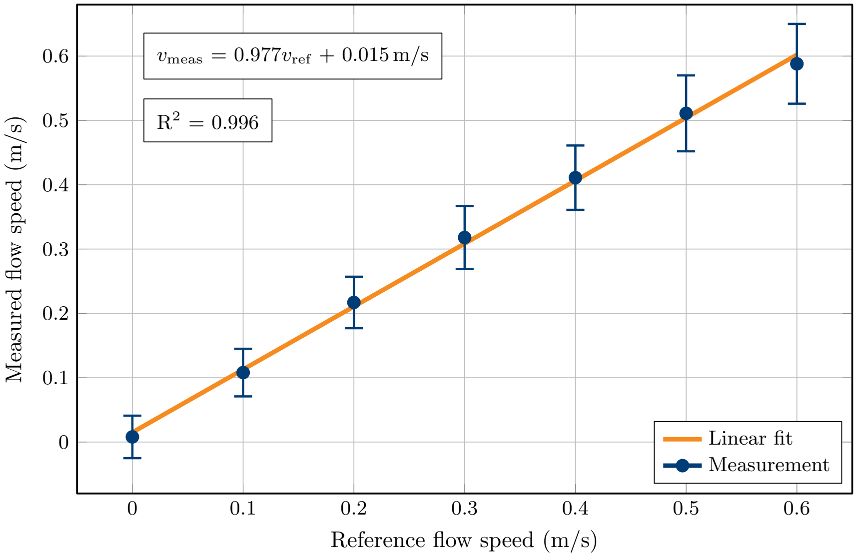

Figure 5.10: Measured and reference flow speed of water considering a compressional wave in the pipe wall. The vertical bars indicate median absolute deviations.

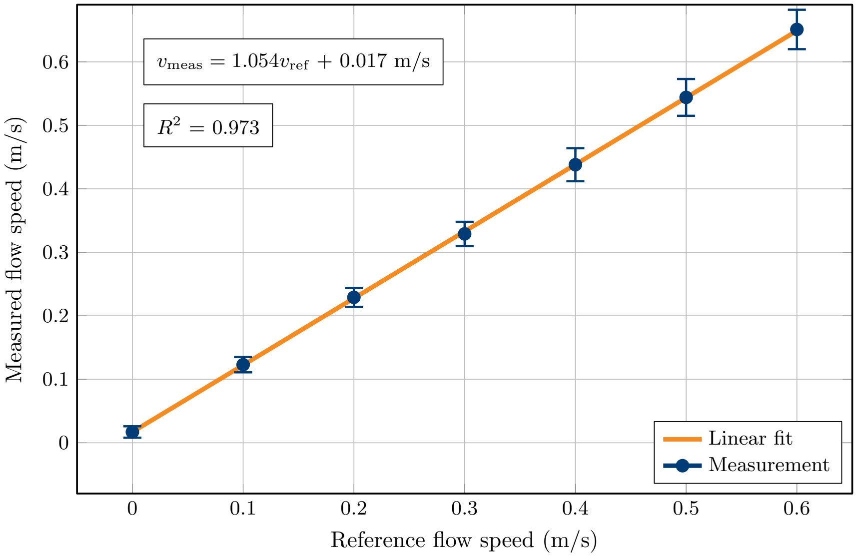

Figure 5.11: Measured and reference flow speed of water considering shear waves in the pipe wall. The vertical bars indicate median absolute deviations.

5.6. Monitoring the Zero-Flow Error

It is important to study the stability of a flow metering system over time because there are factors that may dynamically affect reciprocity, such as temperature changes of the surrounding environment and/or the nonlinear behavior of transducers and the electronic components of the sensor. Therefore, to test whether these factors have a significant effect on the flow speeds measured with the fabricated sensor, it was used to measure flow speed at zero-flow conditions for a relatively long period of time.

5.6.1. At Room Temperature

A 24h-measurement of the flow speed was performed using both measurement modes: compressional waves (see Figure 5.12) and shear waves in the pipe wall (see Figure 5.13). Each flow speed measurement, i.e. upstream-downstream signal pair, together with a reference measurement, was taken every second in intervals of 30 minutes during a 24 h period. Between each measurement interval there was a gap of ≈ 10 minutes due to buffer memory limits and re-initialization of the acquisition machine.

The spread of the measured data points considering compressional waves (Figure 5.12) was wider compared to that obtained with shear waves (Figure 5.13). This was expected from the measured uncertainties shown in Figures 5.10 and 5.11. Nevertheless, for both scenarios, a moving median of these measurements was computed taking into account 300 data points, i.e. corresponding to a 5 minute measurement interval, to visualize in a more practical way any potential drifts of the zero-flow error over time. In the figures, no significant drift of the flow measurements can be observed, and the recorded variations were within the same order as those recorded with the reference flow meter. These measurements show that the fabricated ultrasonic clamp-on flow meter system was fairly stable.

Some quantitative analysis also explained these measurements and lead to the same conclusion. Considering the scenarios of Figure 5.12 and Figure 5.13, the recorded temperature drifted by $\approx 0.4\,{}^{\circ}C/24h$ and $\approx 0.3\,{}^{\circ}C/24h$, respectively. The temperature change between an upstream and a downstream signal, sampled with a PRF of 87 Hz ($T = 11.5\,\mathrm{ms}$), was of $\approx 5.32 \times 10^{-8}\,{}^{\circ}\mathrm{C}$ and $\approx 3.99 \times 10^{-8}\,{}^{\circ}\mathrm{C}$, respectively. A typical temperature gradient of the sound speed of water [3] reports that, around the measured temperatures, the sound speed of water changes with a rate of $\approx 3\,\mathrm{m/s/{}^{\circ}C}$, which combined with the previous estimations of temperature change translates into a change of the sound speed of $\approx 15.97 \times 10^{-8}\,\mathrm{m/s}$ and $\approx 11.98 \times 10^{-8}\,\mathrm{m/s}$, respectively. These changes of the sound speed are insignificantly small to produce a visible effect in the change of the zero-flow error.

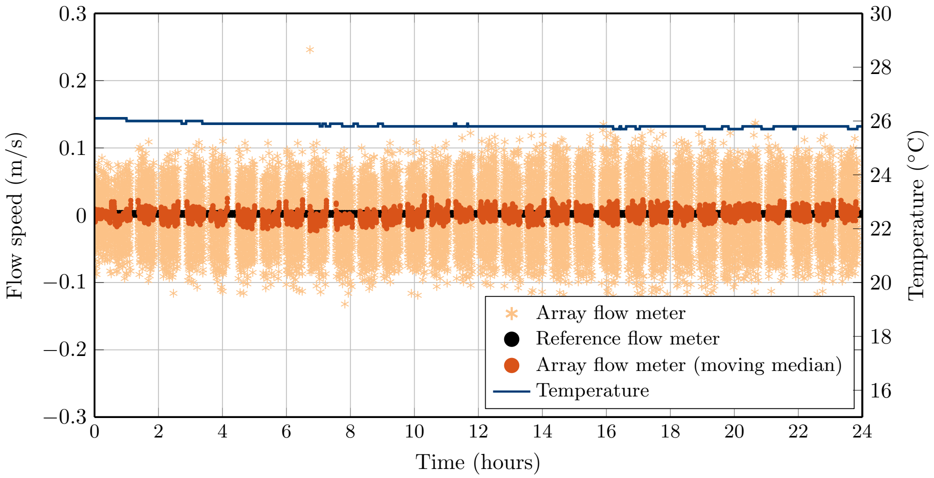

Figure 5.12: 24 h-monitoring of the flow speed at zero-flow conditions, measured with the fabricated sensor considering a compressional wave in the pipe wall. Reference flow speed measurements are shown in black, and a temperature log of the water is shown in blue. A moving median of the measured flow speeds with the fabricated sensor is shown in orange, considering a time window of 300 points (i.e. 5 min).

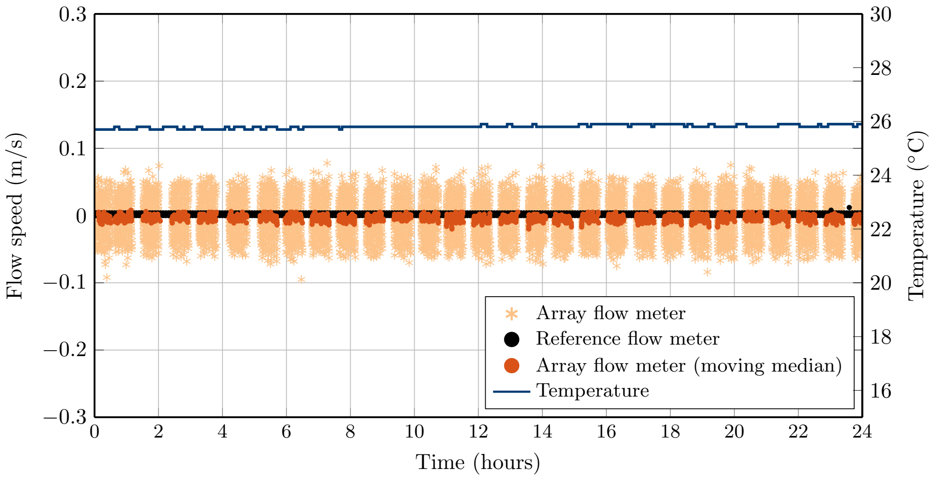

Figure 5.13: 24 h-monitoring of the flow speed at zero-flow conditions, measured with the fabricated sensor considering a shear wave in the pipe wall. Reference flow speed measurements are shown in black, and a temperature log of the water is shown in blue. A moving median of the measured flow speeds with the fabricated sensor is shown in orange, considering a time window of 300 points (i.e. 5 min).

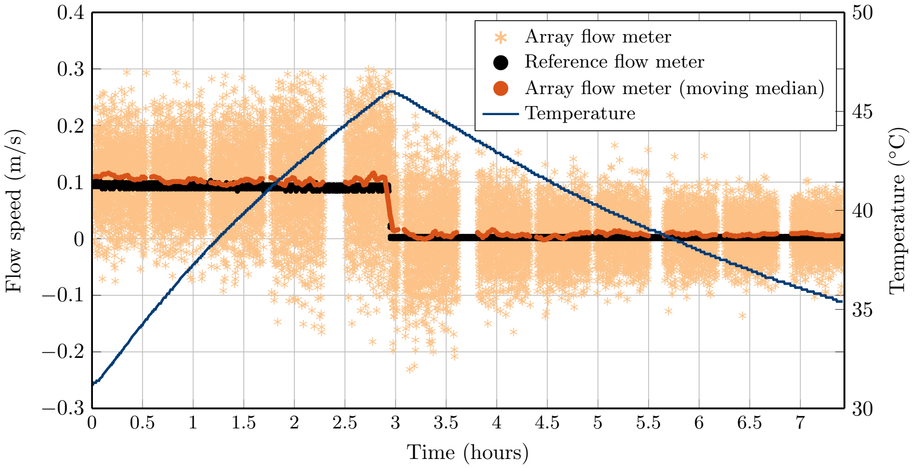

Figure 5.14: 7.5 h-monitoring of the flow speed measured with the fabricated sensor while heating the water. A shear wave in the pipe wall was considered. Reference flow speed measurements are shown in black, and a temperature log of the water is shown in blue. A moving median of the measured flow speeds is shown in orange, considering a time window of 300 points (i.e. 5 min).

5.6.2. Heating the Liquid

The stability of the built ultrasonic clamp-on flow metering system was tested even further by directly heating the water in the flow loop. In this way it could be assessed whether the flow speeds, measured at zero-flow reference conditions, report a dynamic drift due to changes in the sound speed of the liquid.

To perform this measurement, a heater was placed in the upper water tank of the flow loop, and a low flow speed of $v_\mathrm{f} = 0.1\,\mathrm{m/s}$ was used to distribute the heat through the flow loop. This process increased the temperature of the water from ≈ 32 °C to ≈ 46 °C (see Figure 5.14). Some pipe sections of the flow loop consisted of acrylic and PVC. For safety purposes, the heater was turned-off and temperature was not increased further. This heating process lasted ≈ 3 h. At this point, the valve of the flow loop was closed and and measurements were continued at zero-flow conditions for another ≈ 3.5 h, while the water cooled down. From the recorded temperature log in Figure 5.14, it can be observed that water was being heated at a rate of $\approx 4.67\,{}^{\circ}\mathrm{C/h}$. Considering the 11.5 ms of sampling time between an upstream and a downstream signal, the temperature change of the water between these measurements was $\approx 1.49 \cdot 10^{-5}\,{}^{\circ}\mathrm{C}$. Given that the sound speed gradient is $\approx 3\,\mathrm{m/s/{}^{\circ}C}$, this translates into a change in the sound speed of only $\approx 4.48 \cdot 10^{-5}\,\mathrm{m/s}$ which, as also reported in the previous section, is an extremely low value for temperature changes in the liquid to play a significant role in the stability of the flow speeds recorded with the fabricated sensor.

5.7. Discussion

Flow speeds measured considering compressional waves in the pipe wall (Figure 5.10) showed a slightly higher uncertainty than those considering shear waves in the pipe wall (Figure 5.11). This matches in terms of SNR, because the amplitudes of the time signals measured in the first scenario were $\approx 1.7\,\mathrm{dB}$ lower than the amplitudes of the time signals measured in the second scenario. This value is reasonably close to the $\approx 3.3\,\mathrm{dB}$ expected SNR difference from the theoretical calculations for water ($\alpha = 0.002\,\mathrm{dB/MHz \cdot cm}$) shown in Figure 4.10. Moreover, the proof that both measurement scenarios are possible opens the door to the possibility of deciding whether to operate the flow sensor by using either compressional or shear waves in the pipe wall. Since the acoustic paths for the former are usually much longer than for the latter, this last one would be more preferable for measuring the flow speed of highly attenuating liquids or gases. On the other hand, compressional waves in the pipe wall could be used when the length of the pipe section in which the sensor would need to be installed is very limited and only relatively small beam steering angles are possible.

Although the transducer array was designed to measure flow speed using an optimized acoustic beam that propagates through a specific acoustic path, the finite-sized aperture of the array also allows for other acoustic paths which are also sensitive to the flow. Even though the SNR of these other acoustic paths is lower compared to that of the optimized beam they can still be used in combination with the optimal acoustic path to achieve a more precise estimate of the flow speed. A correction for the path length is however required, as discussed in Appendix C.

5.8. Conclusions

In this chapter, flow measurements with the fabricated clamp-on ultrasonic flow meter consisting of two linear arrays were presented. A high degree of reciprocity of the built system was obtained: zero-flow transit time differences $< 1\,\mathrm{ns}$ were measured. Moreover, the correlation factor between measured and reference flow speed was > 0.99. Also, flow measurements were achieved using both compressional and shear waves in the pipe wall.

The potential of f-k_x filtering of undesired wave modes was shown, which is a unique operation for array-based flow meters. Furthermore, it was demonstrated that different recorded acoustic paths could be combined to improve even further the flow speed estimations and decrease measurement uncertainty.

Finally, the proven beam steering capabilities and advanced processing demonstrated with linear arrays point towards matrix array-based flow meters being highly suitable for automated calibration procedures.

References

[1] J. Massaad, P. L. M. J. van Neer, D. M. van Willigen *et al.*, “Design and proof-of-concept of a matrix transducer array for clamp-on ultrasonic flow measurements,” *IEEE Transactions on Ultrasonics, Ferroelectrics, and Frequency Control*, 2022.

[2] R. C. Baker, *Flow measurement handbook: industrial designs, operating principles, performance, and applications*. Cambridge University Press, 2005.

[3] W. D. Wilson, “Speed of sound in distilled water as a function of temperature and pressure,” *J. Acoust. Soc. Am.*, vol. 31, no. 8, pp. 1067–1072, 1959.

6

A Transceiver ASIC for a Matrix-Based Flow Meter

This chapter presents an ASIC capable of driving a two-dimensional array of 6 × 16 ultrasound transducer elements based on only three inputs: a clock signal, configuration data, and a pulse-width modulated digital representation of the transmit waveform. The circuit delays the waveform on element level to beamform the transmit signal. Apodization (amplitude weighting) can be applied per element and configured by column- and row-level settings. A prototype ASIC has been fabricated in a 180 nm BCD technology for use in a transit-time clamp-on ultrasonic flow meter based on matrix transducers. We show effective waveform generation using the PWM-based transmit amplifier and the capability of the ASIC to create delayed and apodized versions of the TX waveform. The acoustic beam can be steered with inter-element delays of up to 250 ns, in clock-period long increments of nominally 15.6 ns. Apodization can be configured with 5-bit values on column and row level. A pair of ASICs is used in a flow measurement setup, where the mean flow velocity is successfully measured in a flow loop with a 40 mm diameter stainless steel pipe, filled with water.

Parts of this chapter are in preparation for submission to the IEEE Journal of Solid State Circuits.

6.1. Introduction

Ultrasound transducer arrays are used in many fields, of which the most well-known field is probably medical imaging. Also in industry, ultrasound arrays are sometimes used, for example in non-destructive testing and for ultrasonic flow measurement [1–4]. All these applications require transmit circuits that drive the elements of the transducer array with appropriate timing such that a desired acoustic beam is formed [5]. Moreover, usually a specific waveform is required which ranges from simple pulses to amplitude-modulated sine waves or more complex coded excitation signals [6]. When a large number of elements has to be driven and in order to keep the system compact, it is desirable to integrate these functions in an application specific integrated circuit (ASIC) [7–10]. Moreover, an ASIC can be placed close to the transducer elements, which is beneficial for the signal quality. Matrix elements commonly have a very high impedance, loaded heavily by the capacitance of a cable. With an ASIC these cables can be made significantly shorter or even be omitted. We present an ASIC capable of driving the elements of a matrix transducer array (i.e., a two-dimensional array) designed for use in a clamp-on transit-time ultrasonic flow meter.

Ultrasonic flow meters are used in industry to measure the flow velocity of fluids in pipelines [1]. The commonly used in-line flow meters perforate the pipe wall. Installing such flow meters requires interrupting the process, making it a costly and cumbersome operation. Moreover, because the transducers pierce the pipe-wall, safety is compromised in cases where toxic or explosive fluids are used. Clamp-on flow meters, in contrast, are installed on the outside of the pipe and do not require interrupting the flow for installation [11], making them an attractive alternative. They are therefore increasingly used, despite their lower precision compared to in-line flow meters. Standard ultrasonic clamp-on flow meters consist of two single-element transducers placed on the pipe-wall. The acoustic path is commonly designed such that it follows a v-shaped path through the fluid, as shown in Figure 6.1. Upon installation the two transducers have to be aligned manually, so the acoustic beam reaches the other transducer with optimal signal

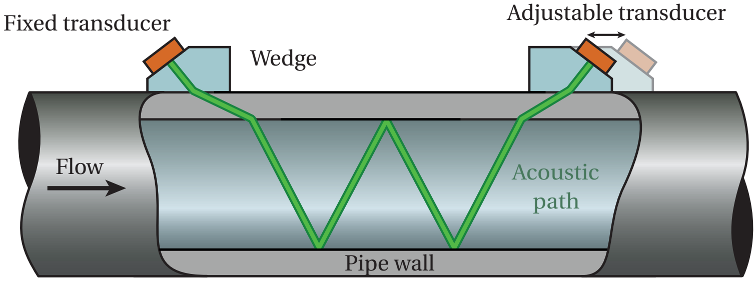

Figure 6.1: Diagram of a clamp-on ultrasonic flow meter.

amplitude. Moreover, the properties of the pipe and fluid have to be known in order to perform a flow measurement. We propose to use matrix arrays to steer the acoustic beam instead of manually aligning the transducer. In addition, methods have been developed to automatically determine the properties of the pipe and fluid prior to metering, by using the possibilities of the matrix array [4], as will be discussed in Chapter 8. A matrix can furthermore be used to improve accuracy by reducing spurious wave modes in the pipe wall [12] (discussed in Chapter 7) and to measure flow via multiple acoustic paths (discussed in Chapter 9).

Figure 6.2 shows a drawing of the proposed matrix-based clamp-on flow meter. It consists of two arrays with 6 × 16 transducer elements. The arrays, A and B, alternately transmit and receive the acoustic waves. The waves travel through the pipe wall and the liquid to the other transducer. The transit-time difference of the measurements upstream (against the flow) and downstream (with the flow) is proportional to the flow velocity [1]. An ASIC is used to transmit and receive the acoustic signals with each of the arrays.

ASICs with built-in transmit beamformers are often designed based on pulser structures, which generate unipolar [8] or bipolar [9, 10] square wave signals. In order to provide more versatile waveforms, multilevel pulsers are sometimes used [7]. However, pulser circuits lack the ability to generate arbitrary waveforms, and are unable to provide the channel-level amplitude apodization required for flow metering. Arbitrary waveform generators, on the other hand, are presented in designs with discrete components [13, 14], which would be too bulky for this application. Integrated arbitrary waveform generators often have few output channels [15–17], which would require a significant amount of ASICs to drive the full 6 × 16 element matrix array.

In this chapter, an ASIC is presented that is able to drive a matrix array of 6 × 16 channels. The circuit allows accurate steering of the acoustic beam to automatically align it with the receive transducer. At the same time the transmitted beam is apodized to minimize the generation of guided waves in the pipe wall and allow accurate flow measurement.

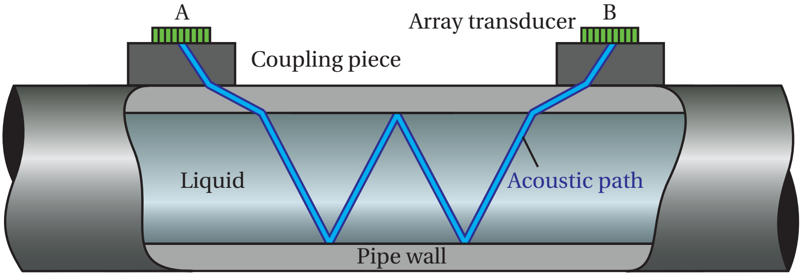

Figure 6.2: Clamp-on flow meter based on two matrix arrays.

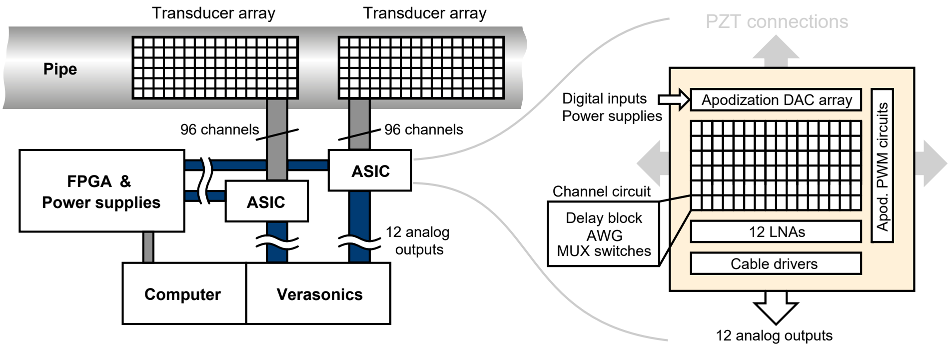

Figure 6.3: System architecture of the prototype flow meter.

Since liquids inside the pipe can significantly attenuate the signal, it is desirable to be able to generate more complex acoustic waveforms, such as chirps or coded excitation [6], in order to improve the SNR. A pulse width modulation (PWM) waveform generator is used to allow the generation of arbitrary waveforms in transmission.

This chapter is organized as follows. Section 6.2 introduces the system architecture of the ASIC. In Section 6.3 a detailed description of the circuit blocks is presented. Section 6.4 presents experimental results of electronic and acoustic measurements. Finally, Section 6.5 discusses the results and Section 6.6 presents the conclusions.

6.2. System Architecture

The flow measurement system consists of two matrix arrays, each of which is connected to an ASIC. The ASICs are supplied with power by a motherboard, that also contains a field-programmable gate array (FPGA) to configure the ASICs. Amplified receive signals are buffered and provided to a Verasonics Vantage (Verasonics Inc., Kirkland, WA, USA) imaging system for further processing. A diagram of the system architecture is shown in Figure 6.3. Flow measurement requires that the ASIC can generate arbitrary waveforms that can be delayed to steer the acoustic beam and apodized to create the required amplitude taper. Apart from an amplitude difference (which is constant over time) and a time delay, the waveforms on each channel should be equal. To implement the required features, a column- and row-level approach is taken: The settings are defined for the whole column or row and are combined inside each channel. This results in a more compact channel circuit compared to creating a circuit and configuration register in every channel, allowing more transmit channels to be designed in the same die area. Moreover, it reduces the amount of required configuration data considerably compared to configuration at the channel level.

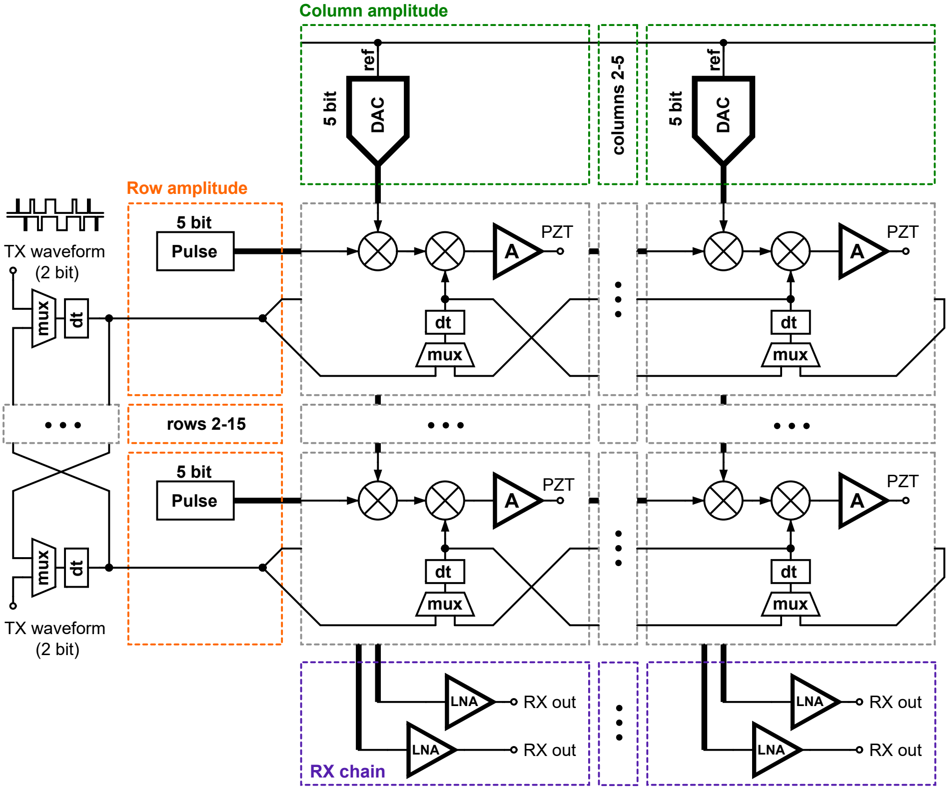

Figure 6.4: Block diagram of the prototype ASIC.

The apodization (i.e., amplitude weighting) of a channel has to be a multiplication of the column and row settings, because the amplitude taper is defined as a gain on the transmit signal. On the other hand, the delay for steering can be a summation of the settings, because the signal is delayed relative to the adjecent channel. Figure 6.4 shows a block diagram of the ASIC. In order to generate the required acoustic signals, a 3-level (2-bit) PWM signal is input to the chip. To support transmit waveforms at the transducer's center frequency of 1 MHz with sufficiently fine-grained amplitude and delay control, the PWM signal is sampled at 64 MHz. This allows the waveform to be delayed using shift registers (the 'dt' blocks in Figure 6.4) as it is distributed across the array. The length of these shift registers, and hence the delay, can be programmed via a digital shift register (not shown). Thus, the signal is passed from row to row and from element to element, with multiplexers defining the propagation direction, so as to generate a delay profile across the array that leads to the desired beam steering. In contrast to timer-based TX beamformers [7–10] this allows an arbitrary PWM waveform to be delayed.

Each channel has a constant apodization amplitude. This amplitude is defined by an internal reference voltage, which is derived from a column setting defined by a 5-bit DAC and a row setting defined by a pulse with a configurable length (5-bit). Inside each channel, the PWM transmit waveform is multiplied by the apodization amplitude and then amplified by a fixed-gain transmit amplifier that drives the piezoelectric transducer element (indicated as PZT in the diagram), which forms a mainly capacitive load of about 20 pF.

6.3. Circuit Implementation

6.3.1. Amplitude Apodization

Each channel contains a circuit that defines the amplitude of the output signal, based on a column and row-level setting. When used to gradually apodize or taper the amplitude of the array elements, the apodization settings for each column (5-bit DAC) and row (5-bit PWM) have to be multiplied by a circuit. A compact implementation of this multiplication is realized by the circuit shown in Figure 3. The circuit transforms the row-level PWM apodization signal into a voltage V_{apod}, by charging a capacitor during a time interval set by the pulse width of V_{row}. In order to obtain a well-defined gain in this time-to-voltage conversion, a calibration phase is used to bias current source M_1 such that it delivers a well known current. In the calibration phase, the row-level PWM signal is set to its maximum width and transistor M_2 resets integration capacitor C_2, nulling V_{apod}. The comparator compares the column amplitude to V_{apod} and increases or decreases the voltage on C_1 with a pulse from the current source. This repeats until transistor M_1 delivers the current that charges C_2 until V_{apod} reaches the column level amplitude V_{column}. After the calibration phase, C_2 is charged to a fraction of V_{column} by applying the configured pulse width from the row amplitude setting.

6.3.2. Beam Steering

In order to steer the acoustic beam, the PWM signal is delayed for each consecutive transducer element by a variable-length shift register. The implementation of these shift registers is shown in Figure 6.6. Special care has been taken for the zero-delay case, where the beam is not steered and all channels have to transmit at once. Since the propagation delay of a chain of multiplexers would be too long, a pass gate has been added for the zero-delay setting, which has a significantly smaller delay if the drive strength of the preceding cell is chosen properly. This beam steering implementation is similar to the circuit proposed in [18]. After calibration a constant beam-steering setting is used for flow measurement. In order the precisely hit the center of the receive array, the clock frequency of the shift register clock can be slightly adjusted to fine-tune the steering angle of the acoustic beam.

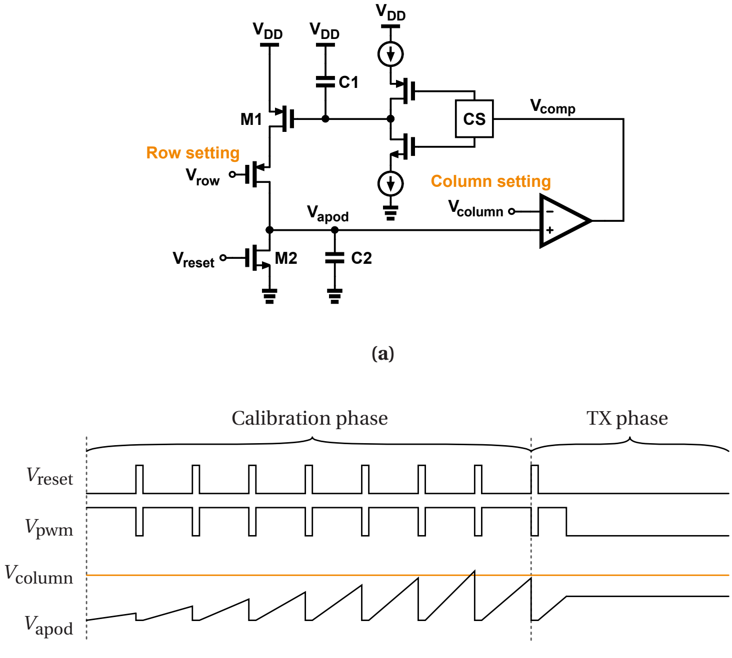

(a)

(b)

Figure 6.5: Circuit used to multiply the column and row-level apodization settings (a) and waveforms of relevant signals (b).

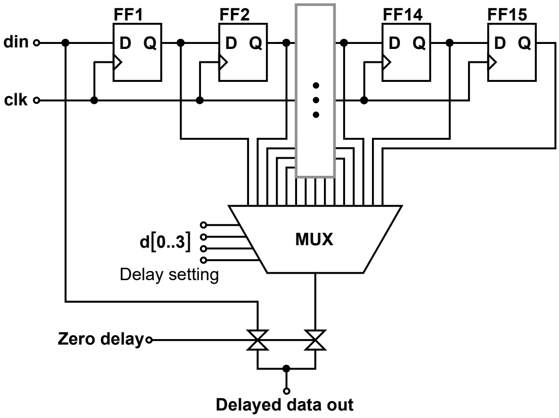

Figure 6.6: Delay circuit implemented as a variable-length shift register.

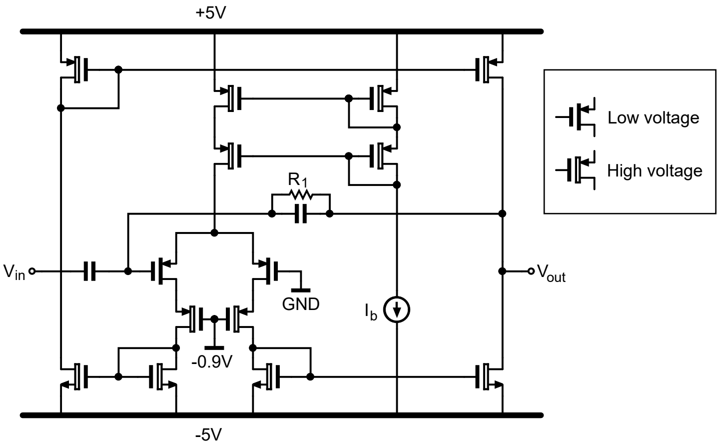

Figure 6.7: Circuit implementation of the output amplifier.

6.3.3. Output Amplifier

The output amplifier, shown in Figure 6.7, is an inverting amplifier with capacitive feedback, built around a class-A current-mirror OTA that amplifies the TX-waveform to a maximum of ±4.5 V. Higher transmit voltages cannot be used in this particular application, to guarantee intrinsic safety. Gain and noise performance are improved by using low-voltage transistors as input. R_1 is a high valued feedback resistor to maintain the DC operating point.

6.3.4. Receive Amplifier and Multiplexer

Acoustic signals are received in groups of 12 channels at a time, to reduce the number of output channels of the ASIC, by means of a multiplexer. The channels are grouped symmetrically around the center of the array, such that 2 rows of each column can be read out simultaneously. Each multiplexer selects one of eight channels to connect to the receive circuit upon reception. A block diagram of the receive circuit is shown in Figure 6.8. The transducers' signal is amplified with a trans-impedance amplifier which has a low input impedance compared to the transducer, in order to obtain sufficiently good reciprocity [19]. The gain is switchable over a 30 dB range in 6 steps to enable measurement of the spurious waves in the pipe wall, which can be used for measurement of pipe and fluid properties [4], as well as to measure the weak acoustic signals with flow information refracting from the liquid.

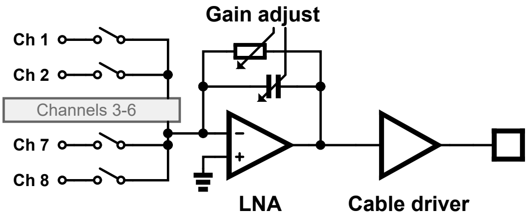

Figure 6.8: Implementation of the receive circuit consisting of a multiplexer, LNA and cable driver.

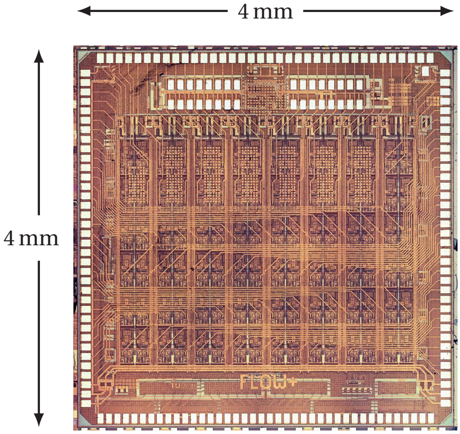

Figure 6.9: Die micrograph of the fabricated ASIC.

6.4. Experimental Results

The ASIC has been realized in a 0.18-µm BCD technology and has a total area of $4 \times 4\,\text{mm}^2$, as shown in Figure 6.9. The bond pads connecting to the piezo elements are located to the left, top, and right side of the ASIC, whereas the bottom connections are power supplies, control signals and reference voltages.

6.4.1. Electrical Characterization

The ASIC was directly bonded to a printed circuit board (PCB) to evaluate its performance. Different PWM signals were programmed as transmit signals to test the ability to generate arbitrary signals. Figure 6.10 shows a 20 cycle linear chirp between 0.5 MHz and 1.5 MHz, with different delay settings configured in the ASIC. A 5-cycle gaussian apodized sine wave was generated on 32 output channels of the ASIC, whilst the apodization setting

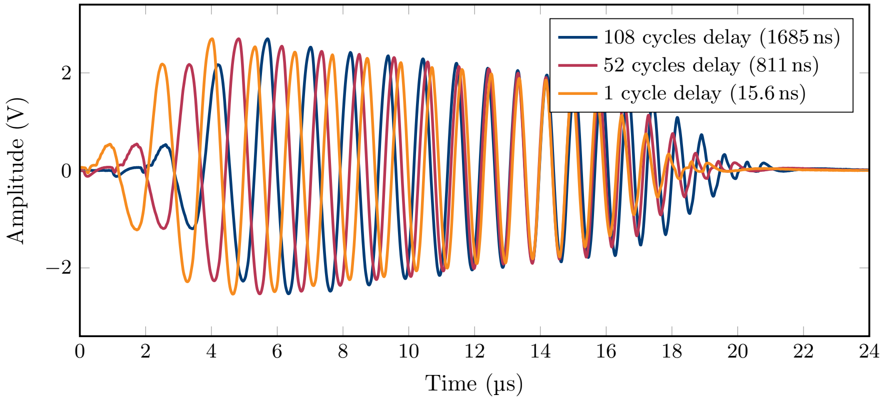

Figure 6.10: Measured electrical signal for a 20 cycle linear chirp from 0.5-1.5 MHz at 3 different delay settings.

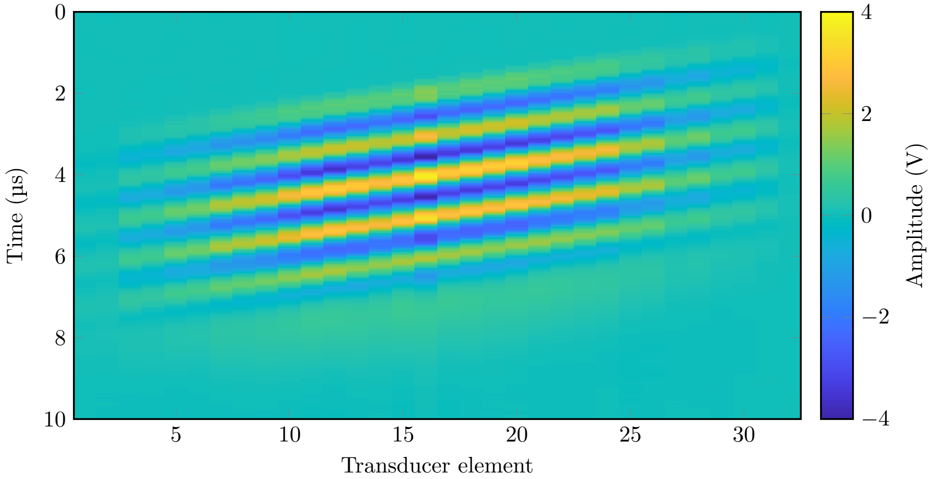

Figure 6.11: Measured electrical transmit signal for a steered 5-cycle Gaussian apodized sine wave with amplitude apodization for 32 channels.

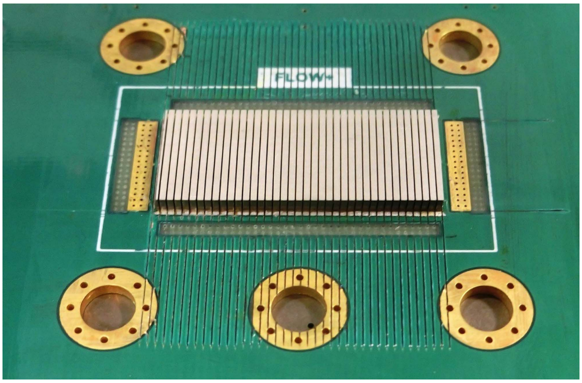

Figure 6.12: Piezo array before placing the ground foil.

was used to create a tapered amplitude along the array. Figure 6.11 shows the output signals of the 32 channels. In the same measurement, a delay setting was programmed to test the steering capability.

6.4.2. Integration

A pair of transducer arrays was fabricated [20] by gluing a piece of lead zirconate titanate (PZT) material (PZ26) onto a PCB with conductive glue. It was then diced into 36 elements using a dicing saw, as shown in Figure 6.12. A copper foil was glued on top to create a common ground connection for the transducers. Traces on the back of the PCB route the signals to a connector, which in turn connects to the ASIC. A detailed description of the fabrication steps can be found in Appendix A. Although the ASIC in this work has been designed for matrix transducers, the measurements were performed with a linear array. Development of the matrix transducer is ongoing and at the time of writing not ready for flow measurement. With a linear array, all the required steps for flow measurement can be performed. The main difference is that some of the proposed calibration steps would not be possible, because they require steering of the acoustic beam in circumferential direction.

6.4.3. Acoustic Characterization

To evaluate the acoustical performance, one of the arrays was mounted onto a 1 mm thick steel plate, immersed in water. A hydrophone was used to measure the acoustic signal at roughly 60 mm distance from the plate. The received acoustic signal is shown in Figure 6.13. The signal arrives at the receiver at 43 µs, followed by several reverberations of the signal, corresponding to multiple reflections inside the coupling piece.

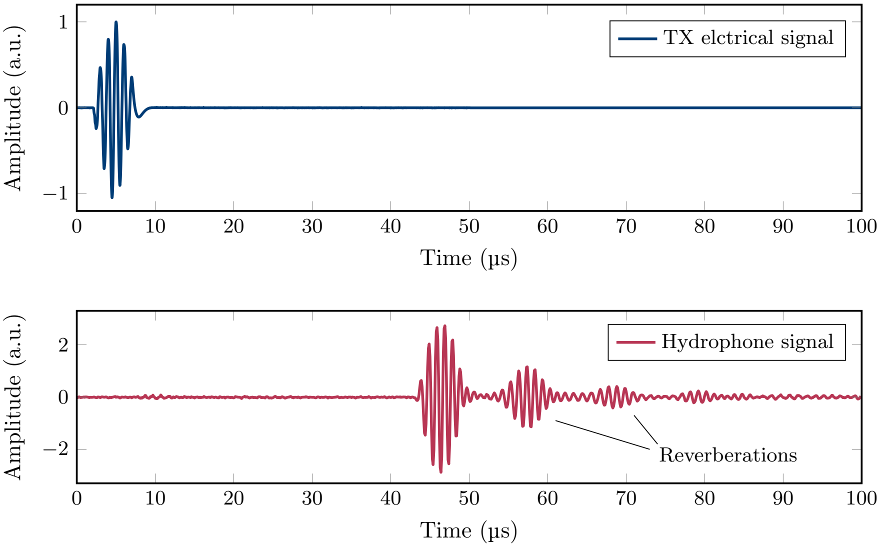

Figure 6.13: Transmit signal (electrical) generated with the ASIC, and acoustic signal in water measured with a hydrophone. The reverberations are caused by reflections inside the coupling piece.

6.4.4. Flow Measurement

The arrays were mounted with a lead coupling piece onto a 1mm thick steel pipe section with an inner diameter of 40 mm. Figure 6.14 shows the arrays mounted in a flow loop setup. A reference flow meter (Optosonics 3400, KROHNE, Dordrecht, the Netherlands) was used to validate the measurement results. With a Verasonics Vantage (Verasonics Inc., Kirkland, WA, USA) imaging system the received and amplified signals were recorded for further processing.

In order to align the acoustic beam with the receive array, the transmit angle was swept over a range from 10° to 18°, by sweeping the transmit clock frequency between 48 MHz and 80 MHz. Figure 6.15 shows the signal amplitude for 3 different acoustic paths, with a transmit beamforming delay of 5 clock periods.

A flow measurement was performed with the acoustic path with 12 path sections ($b = 12$) and its optimal beamforming angle of 13.4°. In a single acquisition, the acoustic signals arriving via several acoustic paths can be observed, as indicated in Figure 6.16. This measurement was repeated 64 times at constant flow speeds between 0.00 m/s and 0.60 m/s. The results are shown in Figure 6.17. In the flow measurements a linear chirp of 20 cycles from 0.5 MHz to 1.5 MHz was used, followed by chirp compression (see also Appendix B. The acoustic signal arriving via the desired acoustic path was time-windowed.

Figure 6.14: Array transducers mounted onto a steel pipe section in the flow loop, with the reference flow meter in the back.

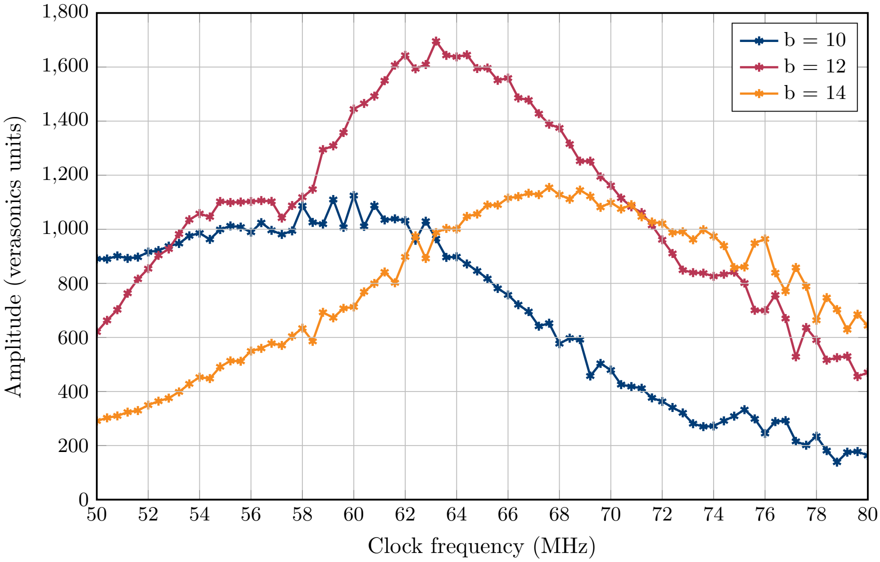

Figure 6.15: Receive signal amplitude for acoustic paths with 10, 12 and 14 path sections for various transmit clock frequencies. The maximum signal amplitude determines the optimal beam angle.

Table 6.1: Comparison with prior art

	Jung ’18 [8]	Igarashi ’19 [9]	Tan ’20 [10]	This work
Delay resolution	5 ns	25 ns	5 ns	15.6 ns
Delay dynamic range *	72 dB	66 dB	54 dB	57 dB
Target frequency	7 MHz	2 MHz	9 MHz	1 MHz
Channels	64	3072	64	96
TX circuit	pulser	pulser	pulser	PWM

* Delay dynamic range = $20 \cdot \log_{10}$(max. delay / min. delay)

Finally, cross-correlation between the upstream and downstream signals was used to determine the transit-time difference (see Chapter 5 for the full processing algorithm), which is directly related to the flow speed.

6.5. Discussion

A comparison of this work with other published transmit circuits is shown in Table 6.1. In contrast with prior transmit beamformers, the ASIC presented in this work provides a PWM transmitter, enabling the use of arbitrary transmit waveforms. The delay resolution is coarser compared to some of the prior work, because of the different requirements in flow measurement. If required by the application, the circuit can be implemented with higher clock frequencies to achieve a finer delay resolution.

Although the ASIC has been designed to connect to a matrix array, its functionality was demonstrated here in combination with linear transducer arrays. A valuable next step will be to evaluate the ASIC with a matrix consisting of 6 × 16 transducer elements.

The initial flow measurements performed with the linear arrays look promising, but improvements can definitely be made. The SNR in the measurement is poor, partly because of the significantly larger load of the linear transducer elements compared to matrix elements. Furthermore, the signals are not fully reciprocal, which requires closer inspection of the whole processing algorithm.

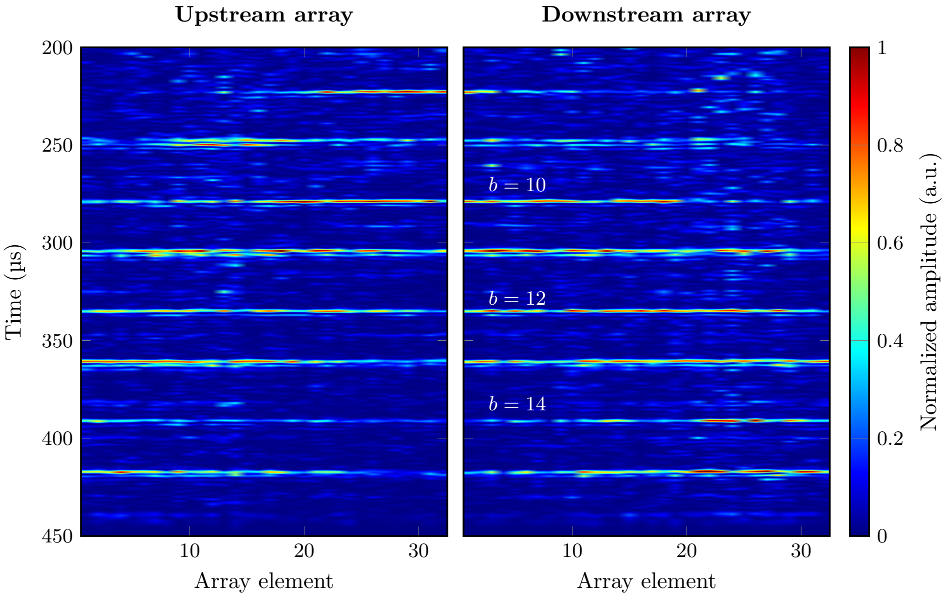

Figure 6.16: Acoustic signals of the upstream and downstream array, obtained in a single flow measurement. The wavefronts arriving via several acoustic paths can be observed.

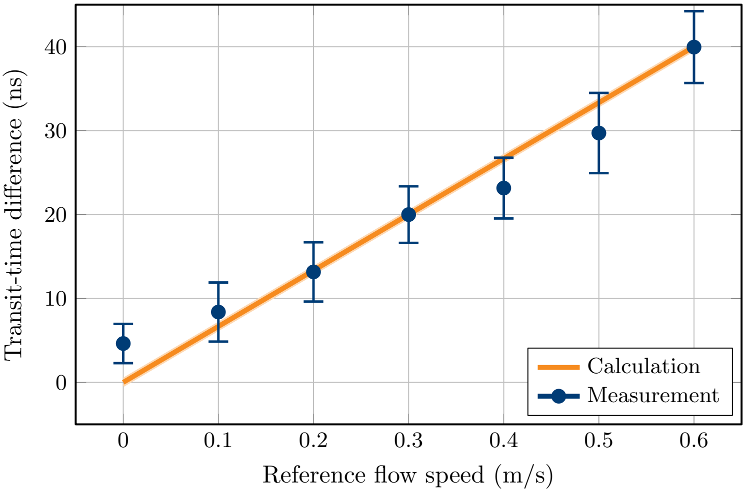

Figure 6.17: Transit-time differences obtained in a flow measurement performed with two ASICs connected to a pair of 32-element transducer arrays.

6.6. Conclusions

We have presented a 96-channel transceiver ASIC for clamp-on ultrasonic flow measurement. The ASIC contains a beamforming circuit with column- and row-level delay and amplitude settings, that are combined at the channel level in a compact PWM-based waveform generator.

The waveform generator is able to create clean signals with a well-defined delay. Row and column level delay settings with a 15.6 ns resolution allow accurate steering of the beam. Tuning the clock frequency allows for a fine delay adjustment to precisely hit the center of the array and achieve optimal SNR. Furthermore, column and row level apodization have been implemented to create the possibility of controlling the side-lobe levels, which can for example be used in cases where reduction of spurious waves is required.

A clamp-on flow measurement was performed with a pair of ASICs showing the combined features of the ASIC and the capability of measuring the flow velocity of water in a steel pipe.

The ASIC and array-based flow meter show great potential for clamp-on flow measurement and open the way towards automatic beam alignment, calibration and flow measurement with improved accuracy.

References

[1] R. C. Baker, *Flow measurement handbook: industrial designs, operating principles, performance, and applications.* Cambridge University Press, 2016.

[2] C. Haugwitz, A. Jäger, G. Allevato *et al.*, "Flow metering of gases using ultrasonic phased-arrays at high velocities," in *2019 IEEE International Ultrasonics Symposium (IUS).* IEEE, 2019, pp. 1129–1132.

[3] T. H. L. Nguyen and S. Park, "Multi-angle liquid flow measurement using ultrasonic linear array transducer," *Sensors*, vol. 20, no. 2, p. 388, 2020.

[4] J. Massaad, P. L. M. J. van Neer, D. M. van Willigen *et al.*, "Measurement of pipe and fluid properties with a matrix array-based ultrasonic clamp-on flow meter," *IEEE Transactions on Ultrasonics, Ferroelectrics, and Frequency Control*, vol. 69, no. 1, pp. 309–322, 2021.

[5] D. H. Turnbull and F. S. Foster, "Beam steering with pulsed two-dimensional transducer arrays," *IEEE transactions on ultrasonics, ferroelectrics, and frequency control*, vol. 38, no. 4, pp. 320–333, 1991.

[6] T. Misaridis and J. A. Jensen, "Use of modulated excitation signals in medical ultrasound. Part I: Basic concepts and expected benefits," *IEEE transactions on ultrasonics, ferroelectrics, and frequency control*, vol. 52, no. 2, pp. 177–191, 2005.

[7] K. Chen, H.-S. Lee, A. P. Chandrakasan *et al.*, "Ultrasonic imaging transceiver design for CMUT: A three-level 30-Vpp pulse-shaping pulser with improved efficiency and a noise-optimized receiver," *IEEE Journal of Solid-State Circuits*, vol. 48, no. 11, pp. 2734–2745, 2013.

[8] G. Jung, C. Tekes, M. W. Rashid *et al.*, "A reduced-wire ICE catheter ASIC with TX beamforming and RX time-division multiplexing," *IEEE transactions on biomedical circuits and systems*, vol. 12, no. 6, pp. 1246–1255, 2018.

[9] Y. Igarashi, S. Kajiyama, Y. Katsube *et al.*, "Single-chip 3072-element-channel transceiver/128-subarray-channel 2-D array IC with analog RX and all-digital TX beamformer for echocardiography," *IEEE Journal of Solid-State Circuits*, vol. 54, no. 9, pp. 2555–2567, 2019.

[10] M. Tan, E. Kang, J.-S. An *et al.*, "A 64-channel transmit beamformer with±30-v bipolar high-voltage pulsers for catheter-based ultrasound probes," *IEEE Journal of Solid-State Circuits*, vol. 55, no. 7, pp. 1796–1806, 2020.

[11] M. Sanderson and H. Yeung, "Guidelines for the use of ultrasonic non-invasive metering techniques," *Flow measurement and Instrumentation*, vol. 13, no. 4, pp. 125–142, 2002.

[12] J. Massaad, P. L. van Neer, D. M. van Willigen *et al.*, "Suppression of lamb wave excitation via aperture control of a transducer array for ultrasonic clamp-on flow metering," *The Journal of the Acoustical Society of America*, vol. 147, no. 4, pp. 2670–2681, 2020.

[13] A. A. Assef, J. M. Maia, F. K. Schneider *et al.*, "A reconfigurable arbitrary waveform generator using PWM modulation for ultrasound research," *Biomedical engineering online*, vol. 12, no. 1, pp. 1–13, 2013.

[14] P. R. Smith, D. M. Cowell, and S. Freear, "Width-modulated square-wave pulses for ultrasound applications," *IEEE transactions on ultrasonics, ferroelectrics, and frequency control*, vol. 60, no. 11, pp. 2244–2256, 2013.

[15] J. Borg and J. Johansson, "An ultrasonic transducer interface IC with integrated push-pull 40 Vpp, 400 mA current output, 8-bit DAC and integrated HV multiplexer," *IEEE Journal of Solid-State Circuits*, vol. 46, no. 2, pp. 475–484, 2011.

[16] Y. Guo, C. Aquino, D. Zhang *et al.*, "A Four-Channel, ±36 V, 780 kHz Piezo Driver Chip for Structural Health Monitoring," *IEEE Journal of Solid-State Circuits*, vol. 49, no. 7, pp. 1506–1513, 2014.

[17] D. Bianchi, F. Quaglia, A. Mazzanti *et al.*, "A 90V pp 720MHz GBW linear power amplifier for ultrasound imaging transmitters in BCD6-SOI," in *2012 IEEE International Solid-State Circuits Conference*. IEEE, 2012, pp. 370–372.

[18] S. D. Cogan and L. Bauer, "Delta delay approach for ultrasound beamforming on an asic," Sep. 13 2016, uS Patent 9,439,625.

[19] P. Lunde, M. Vestrheim, R. Bo *et al.*, "Reciprocal operation of ultrasonic flow meters: Criteria and applications," in *IEEE Ultrasonics Symposium Proceedings*. IEEE, 2007, pp. 381–386.

[20] J. Massaad, D. M. van Willigen, P. L. M. J. van Neer *et al.*, "Acoustic design of a transducer array for ultrasonic clamp-on flow metering," in *2019 IEEE International Ultrasonics Symposium (IUS)*. IEEE, 2019, pp. 1133–1136.

Part III

Techniques Enabled by Matrix-Based Flow Meters

The use of clamp-on matrix transducers in ultrasonic flow measurement introduces several new opportunities.

Spurious waves can be reduced upon transmission, parameters of the liquid and pipe can automatically be determined prior to measurement and even flow velocity profiles can be reconstructed.

This Part introduces new techniques enabled by clamp-on matrix transducers.

Contents

7

Suppression of Lamb-Wave Excitation

During ultrasonic clamp-on flow metering, Lamb waves propagating in the pipe wall may limit the measurement accuracy by introducing absolute errors in the flow estimates. Upon reception, these waves can interfere with the up and downstream waves refracting from the liquid, and disturb the measurement of the transit time difference that is used to obtain the flow speed. Thus suppression of the generation of Lamb waves might directly increase the accuracy of a clamp-on flow meter. Existing techniques apply to flow meters with single element transducers. This work considers the application of transducer arrays and presents a method to achieve a predefined amount of suppression of these spurious Lamb waves based on appropriate amplitude weightings of the transducer elements.

Finite element simulations of an ultrasonic clamp-on flow measurement setting will be presented to show the effect of array aperture control on the suppression of the Lamb waves in a 1 mm-thick stainless steel pipe wall. Furthermore, a proof-of-principle experiment will be shown that demonstrates a good agreement with the simulations.

The contents of this chapter have been published in the Journal of the Acoustical Society of America [1].

7.1. Introduction

Acoustic waves are widely used to measure flow [2–4]. The most basic ultrasonic flow meters consist of two single-element transducers, located a certain distance apart along a pipe wall. Both transducers can be used to excite and record acoustic waves, which enables point-to-point transmission of waves that propagate upstream or downstream relative to the direction of the flow. The transit time difference between these two waves, in combination with the acoustic length of the travel paths and the wave speeds, can be used to obtain a flow speed estimate [5]. The transducers of a flow meter can be in contact with the liquid in an in-line fashion, or be mounted on the outside of the pipe wall in a clamp-on fashion. In the latter case, the acoustic waves will make one or more bounces at the opposite pipe wall. The advantage of the clamp-on type is that they can be installed without interruption of the flow in the pipe and without affecting the mechanical strength of the pipe wall.

Unfortunately, clamp-on flow meters generate multiple wave modes, such as Lamb waves, in the pipe wall. These are mainly caused when the acoustic waves in the fluid reflect at the pipe wall. At the receiving transducer, these modes can interfere with the longitudinal acoustic waves refracting from the liquid. This will disturb the measurement of the transit time difference between up-and down-going waves in the fluid, thus cause an absolute error in the estimation of the flow speed. Current solutions to this problem are: use of a specific incidence angle of the acoustic waves when these hit the pipe wall to minimize the excitation of the Lamb waves; liquid-dependent transmitter-receiver placement along the pipe to enable proper time-windowing of the Lamb waves; and placement of absorbing layers around the pipe wall to reduce propagation of Lamb waves [6]. In view of Snell's law, a fixed angle of the acoustic beam in the pipe wall (e.g. defined by an angled wedge) results in a wave speed-dependent refraction angle of the beam in the liquid. This means that the travel path of the acoustic beam is liquid-dependent, and the distance between transmitter and receiver has to be modified (i.e. calibrated) accordingly for every fluid. Therefore, the dependence on the liquid prohibits a calibration-free flow meter.

Time-windowing of the longitudinal wave is not possible for all cases, since for pipe walls with a large thickness to wavelength ratio, a considerable amount of Lamb wave modes can be excited, and the probability of overlapping in time with the longitudinal wave refracting from the liquid increases. This problem is even more serious because Lamb waves are dispersive and the different Lamb wave modes have different group speeds. Moreover, the installation of absorbing layers around intricate pipe lines is difficult to perform in practice and sometimes not possible, especially in confined spaces. This motivates the development of an ultrasonic flow meter solution that provides Lamb suppression without compromising measurement precision, is independent of the specific liquid, and is calibration-free.

Selectivity of wave mode excitation with single-element transducers via angled wedges is described in literature [7]. However, by exploiting the wedge angle for Lamb wave suppression, this degree of freedom is lost for simultaneously steering the angle of the beam that will refract into the fluid. With transducer arrays and their capabilities for element-wise phase and amplitude control, considerably more control can be achieved.

There are a number of articles on suppression of transmitted Lamb waves [8–16]. These methods are based on phase manipulation of the time domain signals for the suppression of one specific Lamb wave mode. On the other hand, methods for boosting the generation of Lamb waves in a plate via an ultrasonic array have been previously described as well [17–21]. These are also based on phase manipulation of the time domain signals. Apart from suppression of specific Lamb wave modes in the pipe wall, during flow metering it is desired to have an acoustic beam with a very well-defined wave front and propagation direction. Although both individual goals can be achieved with manipulation of the phase, it is not possible to reach both goals simultaneously. This is because the phase appears in the exponent of the complex representation of a signal, so the addition of two phases has the effect of one overall time delay. This is appropriate for concatenated time delay effects like beam steering and beam focusing. However, phase addition does not work for effects that require two separate time delays, like simultaneously generating two beams in different directions. Because Lamb wave suppression and acoustic beam generation are effects involving two different directions, these also cannot be achieved by the addition of phases.

Separating the aperture function of a transducer array by splitting it into its amplitude and phase behavior has been used in medical imaging [22–24]. Here is described a method that uses the amplitude of the transmitting elements of an array transducer to suppress Lamb waves, while the phase of the elements is used to control the direction and shape of the acoustic beam.

7.2. Theory

In this section, the relevant equations for Lamb wave propagation are described, as well as how their excitation can be controlled by means of the apodization of a transducer array.

7.2.1. Lamb Waves

Lamb waves are plane elastic waves that propagate in a flat plate with traction free surfaces [25, 26]. In a cylindrical geometry (such as a pipe), the mathematical treatment is analogous, using the boundary value problem for a hollow elastic cylinder [19, 27, 28]. Here, it is assumed that the considered pipe has a sufficiently large diameter, therefore the approximation of a flat plate can be made [29]. Furthermore, forward models of dispersion curves of flat plates and hollow cylinders of the same thickness (comparable

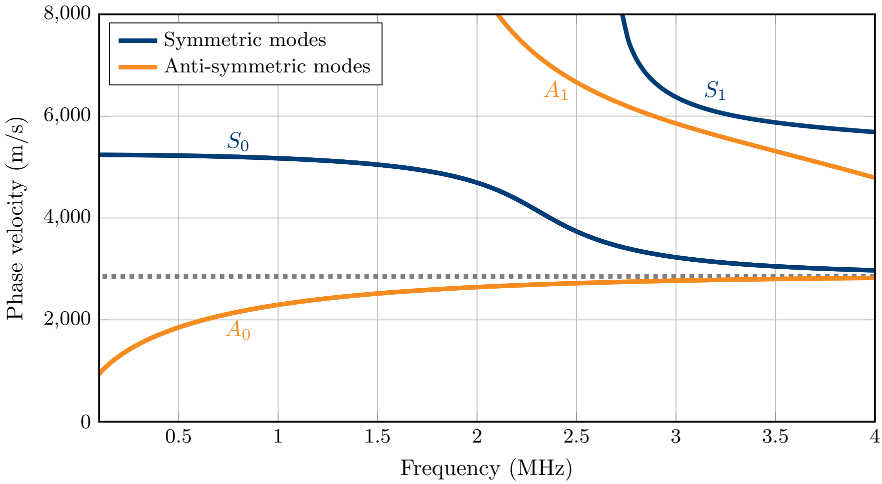

Figure 7.1: Phase velocity dispersion curves of the zero and first order Lamb wave modes that can propagate along a stainless steel plate with a thickness of 1 mm ($c_L = 5800\,\mathrm{m/s}$, $c_L = 3100\,\mathrm{m/s}$). The dashed line indicates the Rayleigh wave speed c_R at a single free surface.

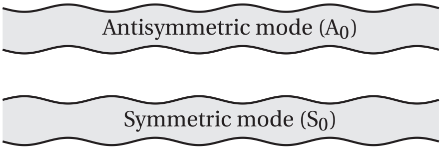

Figure 7.2: Retrograde surface motion of symmetric (S) and anti-symmetric (A) Lamb waves in a plate.

to its radius) show discrepancies at frequencies that are very low to make a practical flow measurement anyway.

Lamb waves exist in the form of symmetric and anti-symmetric vibration modes, which can be further specified by their mode number. As mentioned earlier, Lamb waves are dispersive, see Figure 7.1. Both vibration modes produce in-plane and out-of-plane particle displacement. For symmetric modes, the main motion is in-plane, while for anti-symmetric modes it is out-of-plane, as depicted in Figure 7.2.

For an infinite plate of thickness $2h$, the Lamb modes are mathematically described by the Rayleigh-Lamb dispersion relations for symmetric modes

$$\frac{\tan(qh)}{\tan(ph)} = -\frac{4k^2pq}{(q^2-k^2)^2}, \tag{7.1}$$

and for anti-symmetric modes

$$\frac{\tan(qh)}{\tan(ph)} = -\frac{(q^2-k^2)^2}{4k^2pq}. \tag{7.2}$$

In equations (7.1) and (7.2), p and q are defined as

$$\begin{aligned} p^2 &= \left(\frac{\omega^2}{c_L^2}\right)^2 - k^2, \\ q^2 &= \left(\frac{\omega^2}{c_T^2}\right)^2 - k^2. \end{aligned} \tag{7.3}$$

In equation (7.3), ω represents the angular frequency; k represents the wavenumber; c_L and c_T the longitudinal (compressional) and transversal (shear) wave speed in the material, respectively. The solutions to the dispersion equations can be found numerically [19].

The total wave field propagating in a solid slab can be expressed as the sum of symmetric and anti-symmetric mode functions for both in-plane, and out-of-plane particle motion. Considering x as the coordinate in the thickness direction, and z as the coordinate in the propagation direction, in-plane particle displacement can be mathematically expressed as

$$u(\omega,x,z) = \sum_{n=0}^{\infty} A_n(\omega)\,\Phi_{s,n}(\omega,x)e^{ikz} + B_n(\omega)\,\Phi_{a,n}(\omega,x)e^{ikz}, \tag{7.4}$$

where $\Phi_{s,n}(\omega,x)$ and $\Phi_{a,n}(\omega,x)$ represent the symmetric and anti-symmetric in-plane mode functions, respectively, and $A_n(\omega)$ and $B_n(\omega)$ represent the expansion coefficients of both modes.

Correspondingly, out-of-plane particle displacement can be expressed as

$$w(\omega,x,z) = \sum_{n=0}^{\infty} A_n(\omega)\,\Psi_{s,n}(\omega,x)e^{ikz} + B_n(\omega)\,\Psi_{a,n}(\omega,x)e^{ikz}, \tag{7.5}$$

where $\Psi_{s,n}(\omega, x)$ and $\Psi_{a,n}(\omega, x)$ represent the symmetric and anti-symmetric out-of-plane mode functions.

Mode functions $\Phi_{s,n}(\omega, x)$ and $\Phi_{a,n}(\omega, x)$ are orthogonal in x. This property allows to compute an expression for the expansion coefficients $A_n(\omega)$ and $B_n(\omega)$, at some location $z = z_0$

$$A_n(\omega) = \frac{\int_a^b u(\omega, x, z_0)\Phi^*_{s,n}(\omega, x)e^{-ikz_0}\,dx}{\int_a^b \Phi_{s,n}(\omega, x)\Phi^*_{s,n}(\omega, x)\,dx}, \tag{7.6}$$

$$B_n(\omega) = \frac{\int_a^b u(\omega, x, z_0)\Phi^*_{a,n}(\omega, x)e^{-ikz_0}\,dx}{\int_a^b \Phi_{a,n}(\omega, x)\Phi^*_{a,n}(\omega, x)\,dx}. \tag{7.7}$$

The limits of the integrals in equations (7.6) and (7.7) comprise the thickness of the solid slab being examined, and * indicates the complex conjugate. For each frequency, the expansion coefficients indicate the importance of the contribution of a particular mode to the total field distribution. The location z_0 should be outside the area where the modes are generated, i.e. outside the transducer range.

Frequency dependence of the amplitudes of the zero-order Lamb wave modes for a 5 mm-thick stainless steel plate is shown in Figure 7.3. Even though an appropriate excitation frequency can help with the suppression of Lamb waves by a factor of 2, it is often not enough to achieve the needed accuracy for clamp-on flow metering.

7.2.2. Beam Transmission with Transducer Arrays

Ultrasonic arrays have been designed and used for different purposes including medical imaging and NDE [30] (Non-Destructive Evaluation). The far field directivity pattern of the acoustic beam produced by a transducer array consisting of rectangular elements radiating into a half-space can be described by the directivity function [24]

$$D(\theta) = d\,\mathrm{sinc}\left(-\frac{d}{\lambda}\sin\theta\right)\sum_{n=-\frac{N-1}{2}}^{\frac{N-1}{2}} F_n e^{jn(\Delta\phi_n + kd\sin\theta)}, \tag{7.8}$$

in which the amplitude F_n and phase $\Delta\phi_n$ of each element are parts of the complex apodization or aperture function $F_n \exp(i\Delta\phi_n)$ in the Fourier domain. Moreover, d is the pitch of the array; θ is the observation angle relative to the normal on the transducer surface, and N is the total number of elements of the array. In a clamp-on flow measurement setting, λ is the wavelength in the liquid.

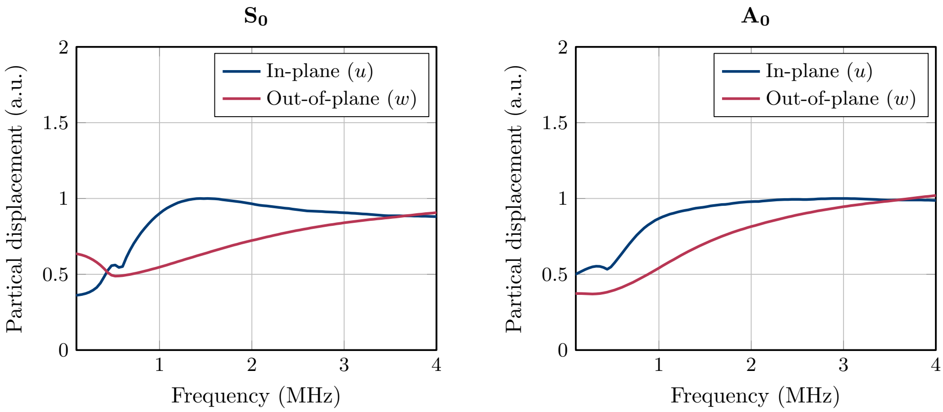

(a) **(b)**

Figure 7.3: Amplitudes of the particle displacement of the zero-order Lamb waves in a 5 mm-thick stainless steel plate, loaded by water on one side, and by vacuum on the other side. A transducer array, placed on the vacuum-loaded surface of the plate, was used to excite an acoustic beam that impinged the steel-water interface with an angle of 45°. The displacements $u(\omega, x, z_0)$ and $w(\omega, x, z_0)$ were computed across the thickness of the pipe wall $(-h \leq x \leq h)$, at a propagation distance (z_0) located at the edge of the transducer array.

Considering equation (7.8) in an ultrasonic clamp-on flow measurement setting, the transducer array is virtually placed in the pipe wall - liquid interface. Furthermore, the effect of the pipe wall on equation (7.8) is directly observed in Figure 7.4, by the amount of energy located beyond the critical angles of the Lamb wave modes. These angles depend on Snell's law through the sound speed of each mode at a particular frequency (1 MHz in case of Figure 7.4) and the sound speed of the liquid.

During flow metering, significant Lamb wave modes are excited each time the acoustic beam impinges from the liquid onto the pipe wall. Such wave modes are excited even more efficiently when the incidence angle is close to their critical angle [31] (Figure 7.4). Therefore, it may be necessary to suppress the amount of energy leaking into Lamb wave excitation at each beam reflection. Proper phase control of the transmitting array may result in steering the incidence angle as to avoid excitation of Lamb waves [21]. In contrast to previous work, in this research the phase shifts $\Delta\phi_n$ are reserved to steer and shape the beam, and the amplitude factors F_n are manipulated to suppress, the generation of undesired Lamb waves at each reflection of the acoustic beam.

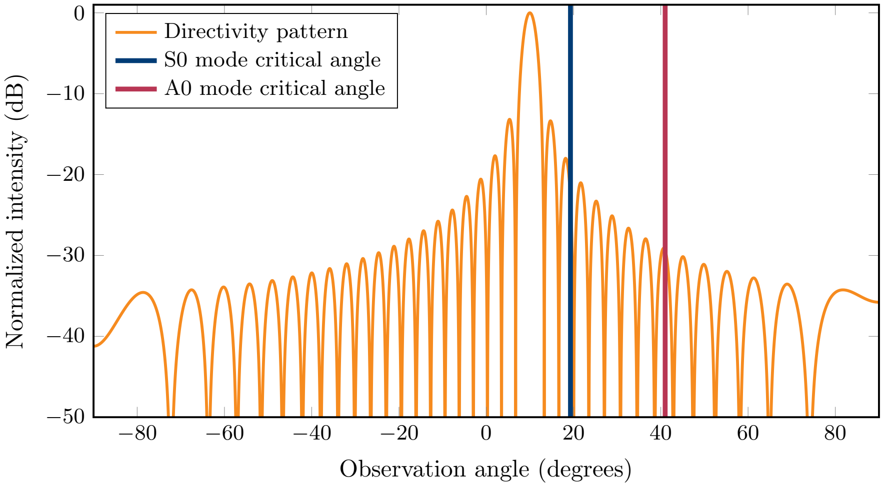

Figure 7.4: Directivity pattern of a steered acoustic beam ($\Psi = 10°$) in water ($c_m = 1500\,\mathrm{m/s}$) produced by a 37-element transducer array with a pitch of 0.72 mm excited at 1 MHz. To compute it, equation (7.8) was implemented, where $F_n = 1$, and $\Delta\phi_n = nkd\sin(\Psi)/c_m$, with k being the wavenumber of the acoustic beam in water at 1 MHz. The vertical blue and purple lines indicate the critical angles beyond which only the zero-order Lamb wave modes propagate when such a beam impinges on a 1 mm-thick stainless-steel pipe wall. Due to the presence of side lobes, some energy from the beam may leak into these Lamb modes.

7.3. Algorithm

The beam spot width W of an acoustic beam that hits the pipe wall with an incident angle θ relative to the normal of the pipe wall, can be computed as

$$W = \frac{2L\tan(\alpha/2)}{\cos(\theta)}. \tag{7.9}$$

Here, α is the opening angle of the beam at the -3 dB power level, and L is the distance traveled by the acoustic beam, i.e. the total length of the beam path from transmitter to receiver.

In clamp-on flow metering, the best accuracy is achieved when a maximum signal-to-noise ratio (SNR) is reached. This occurs when the entire aperture of the array is insonified by the entire in-coming beam. Therefore, it is desired to have an array aperture of N array elements that allows to generate a narrow acoustic beam on the transmission side and also to record this beam on all N elements on the receiving side. In receive, this will average out the noise by a factor of $\sqrt{N}$ compared to a single element.

However, such beams require small opening angles, and therefore demand a considerable number of elements. Cost and complexity of application-specific integrated circuits (ASICs) are proportional to the number of elements needed to drive a transducer array, and may become prohibitive for the number of elements that are needed to produce theoretically ideal beams. In practice, only a limited number of elements will be available, which will have an impact on the beam. Therefore, it is necessary to find a way to reduce the number of elements while retaining a good signal-to-noise ratio and a sufficient suppression of Lamb waves.

A flowchart of the algorithm to achieve this is shown in Figure 7.5, and will be described in detail below.

7.3.1. Step 1: Define Known Parameters for Beam and Transducer

First, the known parameters for the beam and the transducer are set. These are: the length L of the travel path of the beam, the level s of the first side lobe relative to the level of the main beam, and the pitch p of the array. These parameters are application dependent. Moreover, an initial number of e array elements is set. As an example, a transducer array with a center frequency of 1 MHz will be designed. Moreover, a pipe inner diameter of 40 mm and a beam propagating in water under an angle of $\theta = 10^\circ$ with the normal of the pipe wall and making six bounces (v-shapes) within the pipe will be considered. For this geometry, a travel path length $L = 488\,\mathrm{mm}$ can be determined.

Moreover, it will be assumed, as an external demand, that a suppression $s = 35\,\mathrm{dB}$ of the spurious Lamb waves is needed. As a worst case scenario, it is assumed that all side lobes of the acoustic beam are converted into spurious Lamb modes, and that side lobe and Lamb mode amplitude are equivalent.

For a frequency band up to 2 MHz, a pitch $p = 0.72\,\mathrm{mm}$ was considered to properly sample all possible propagating Lamb wave modes in stainless steel pipes with wall thicknesses between 1 mm and 5 mm.

A relatively large number of array elements e is recommended to produce a narrow beam in reception and to ensure that all of its energy gets recorded. As an example, the algorithm is explained by showing the results with $e = 152$ initial array elements.

7.3.2. Step 2: Compute Desired Beam

To achieve the desired suppression level, the element amplitudes F_n in equation (7.8) were set to form a Blackman window. Figure 7.6a shows that the first side lobe is conveniently below the required 35 dB level. Furthermore, at the −3 dB level, the beam has an opening angle $\alpha = 3^\circ$ in water, which according to equation (7.9), produces a beam spot width $W = 25.1\,\mathrm{mm}$ upon reception.

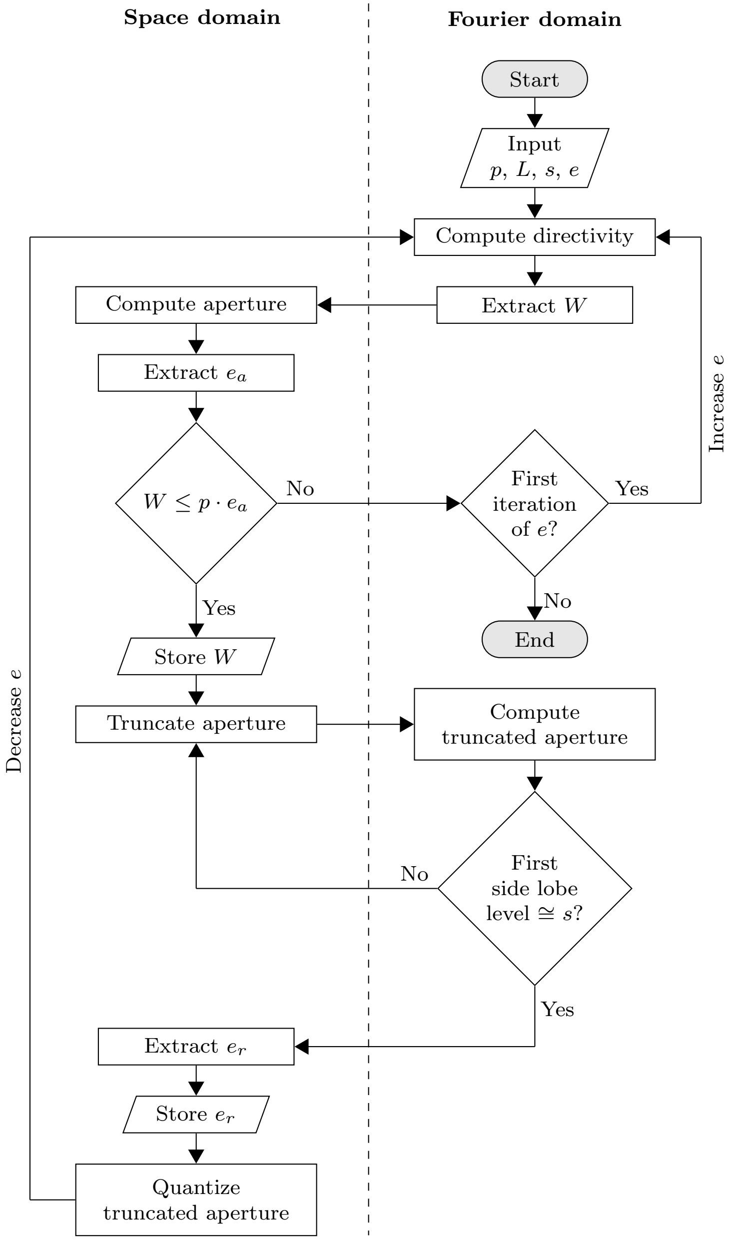

Figure 7.5: Flowchart of the proposed algorithm to obtain a transducer array aperture giving a good signal-to-noise ratio and sufficient suppression of Lamb waves. The ideal transmit beam yields a receive beam spot width that is equal to the recording array aperture.

7.3.3. Step 3: Compute Desired Aperture

The aperture to produce the beam shown in Figure 7.6a is computed via the Inverse Fast Fourier Transform (IFFT) of equation (7.8). The obtained original aperture in Figure 7.6b suggests that $e_a = 50$ active elements are sufficient to produce such a beam. The corresponding effective aperture of 36 mm ensures that the whole beam width gets recorded upon reception. Otherwise, the algorithm would ask for a higher initial number of array elements e to produce a narrower beam.

7.3.4. Step 4: Truncate Aperture and Extract Residual Active Elements

The challenge is to reduce the number of elements e below the obtained number of active elements e_a. Aperture truncation in the space domain is performed by multiplying the function in Figure 7.6b with a rectangular window. This has the physical meaning of reducing the total number of elements of the array (purple curve in Figure 7.6b), at the cost of increasing the side lobe levels compared to the initial beam. In this case, truncation is performed until the amplitude of the first side lobe reaches 35 dB (blue curve in Figure 7.6c). This resulted in $e_r = 37$ residual active elements, which cover an aperture of 26.6 mm.

7.3.5. Step 5: Quantize the Truncated Aperture

In practical electronic transmit circuits, the amplitudes F_n of the elements will be quantized, and the aperture will have a step-like shape. In the current case, a 4 bit-quantization of the aperture has been applied (orange curve in Figure 7.6b). This further modifies the shape of the resultant beam.

7.3.6. Step 6: Compute Practical Beam

By again invoking equation (7.8), the beam resulting from the truncated and quantized aperture can be obtained. At this stage it is possible to see whether the quantization still leads to an acceptable performance. For the described 4-bit case, the beam has a very similar width as the non-quantized one and keeps the side lobe levels below 35 dB (dashed line in Figure 7.6c). Higher quantization levels would produce a smoother aperture, but the complexity of the electronics would increase proportionally. Lastly, the -3 dB opening angle α can be extracted and the spot width W of the quantized beam can be computed. In this case, the beam has an opening angle $\alpha = 3.1°$ and produces a beam spot width $W = 26.1$ mm upon reception, which is close to the 26.6 mm size of the array aperture.

The algorithm will loop steps 2-6 with a smaller initial number of array elements e. This happens until the beam spot width becomes larger than the residual active array aperture.

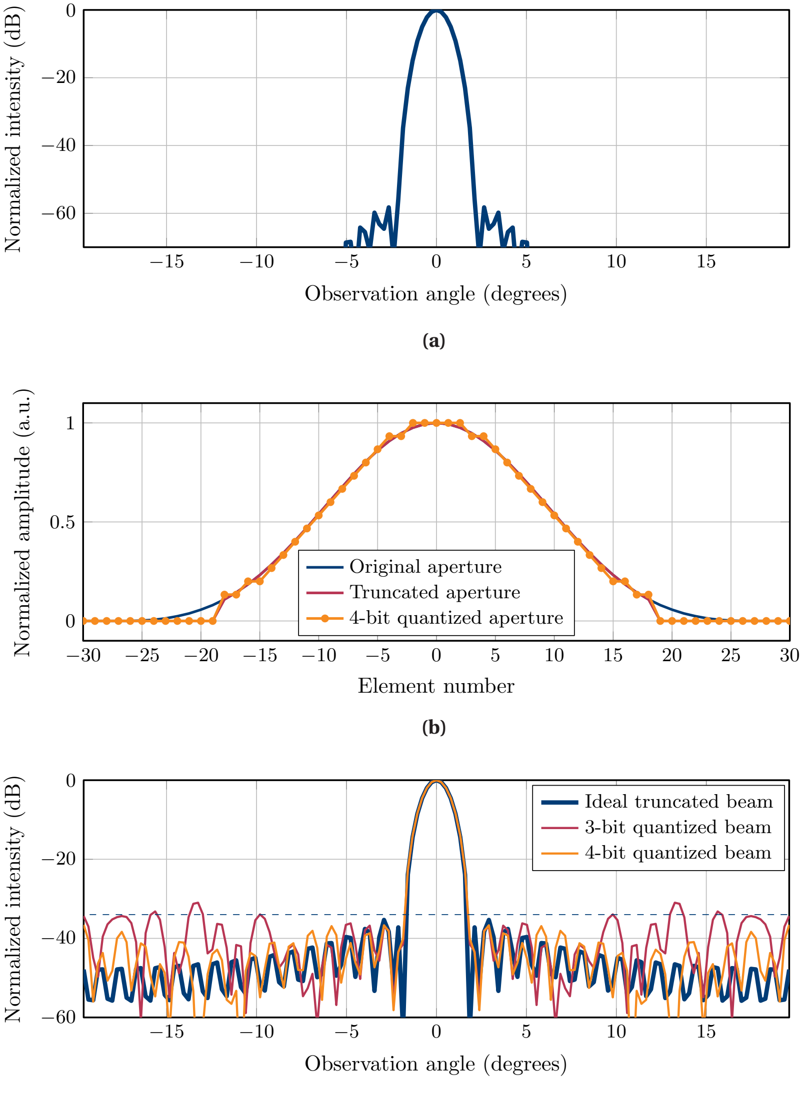

(a)

(b)

(c)

Figure 7.6: Beams and apertures involved in the design of a 1 MHz-transducer array with a 0.72 mm pitch for ultrasonic clamp-on flow measurements, capable of suppressing Lamb waves of a 1 mm-thick stainless steel wall by 35 dB during transmission. (a) Ideally desired beam: small opening angle and low side lobe levels. (b) Ideal and truncated aperture function. After truncation, the aperture region with non-zero amplitudes is quantized. (c) Effect of truncation: rise of the side lobes relative to the ideal beam, and of quantization: small variation in side lobe levels.

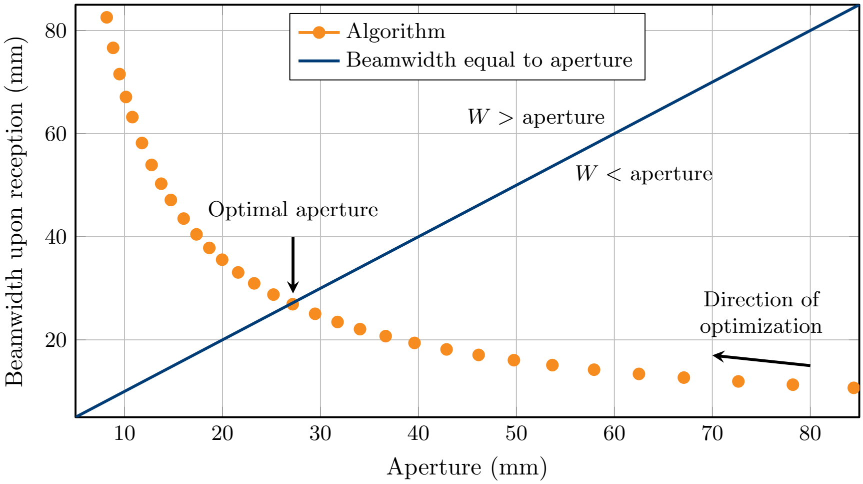

Figure 7.7: Beam spot width upon reception as a function of aperture size, as computed by the algorithm, for a 1 MHz transducer array with a 0.72 mm pitch and 35 dB suppression of Lamb waves. The optimal aperture size of 26.6 mm corresponds to 37 array elements.

Figure 7.7 shows the beam spot size upon reception, as a function of the aperture size. From this figure it is possible to graphically find the optimal number of array elements for the ultrasonic clamp-on flow metering application: the one whose aperture has the same (or very similar) length as the produced beam spot width upon reception.

7.4. Simulation Study

In this Section, 2D simulations are presented for a water-filled stainless steel pipe with 40 mm inner diameter and 1 mm wall thickness, in combination with a transducer array with a pitch of 0.72 mm clamped outside the pipe wall. Furthermore, two different center frequencies will be considered in two separate scenarios: 1 MHz and 1.5 MHz. The first one will be the center frequency of a sensor under development, and the second one is the center frequency used in experimental studies presented in the next section.

7.4.1. Simulation Settings

At 1 MHz, the fastest Lamb wave mode that can propagate in a 1 mm-thick stainless steel pipe wall is the zero-order symmetric (S_0) mode ($c_{S_0} = 5173\,\mathrm{m/s}$, see Figure 7.1). It was found in the previous section that 37 elements are enough to produce a 35 dB suppression of this mode. In this case, a beam steered at 45° through the pipe wall would refract into water at 10° with an opening angle of 3.1°, which is below the critical angle for the S_0

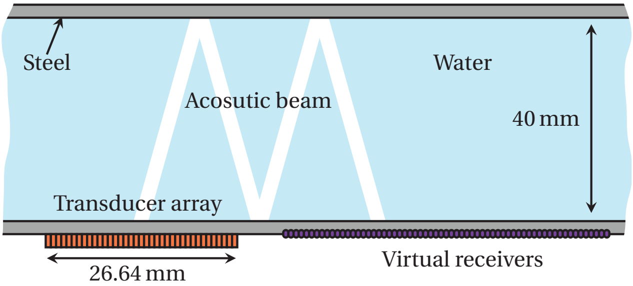

Figure 7.8: Cross-section of the pipe used in 2D FEM simulations of a 37-element transducer array with a center frequency of 1 MHz. The acoustic beam was steered 45° through the 1 mm-thick pipe wall, traveling to the right. Stress perpendicular to the steel surface was recorded by the virtual receivers to identify propagating waves in post-processing.

mode, being 16.9°.

On the other hand, to suppress the S_0 wave mode at 1.5 MHz, the implementation of the algorithm proposed in the previous section would report an optimal $e_r = 25$ residual active elements (aperture of 18 mm) with a beam spot width of $W = 18.64$ mm upon reception. Considering the dispersion curves of Figure 7.1, and the same 10° angle of refraction of the acoustic beam into the water, it is expected to suppress the S_0 wave mode, and also to have some leakage towards the excitation of the A_1 wave mode since this last one has a faster sound speed, relative to the S_0 wave mode, that is not accounted by the beam direction.

Two-dimensional Finite Element Modeling (FEM) was used to simulate the effect of controlling the amplitudes of the elements of a transducer array for the suppression of Lamb waves. The simulations were performed in the software package PZFlex (Onscale, Redwood City, CA, USA). A 2D longitudinal cross section of a water-filled pipe was defined (Figure 7.8), including an array consisting of lead-zirconate-titanate (PZT) elements made of HK1HD (TRS Technologies, Inc., State College, PA, USA).

For each scenario (i.e. center frequency), two simulations were carried out. In both, the driving function on the PZT elements consisted of a 2-cycle sine wave, and the acoustic beam was steered 45° by means of phase shifting. For the first simulation, a uniform amplitude function was applied to the driving signals of the elements. For the second simulation, a tapered amplitude function obtained by the previously described algorithm was applied (Figure 7.9). Virtual receivers were placed along the steel-air interface to record the total perpendicular stress component from all waves in the pipe wall, including the longitudinal wave refracting from the liquid. These waves were subsequently identified in the Fourier domain. The simulations were run until the beams had bounced six times (v-shapes) within the pipe.

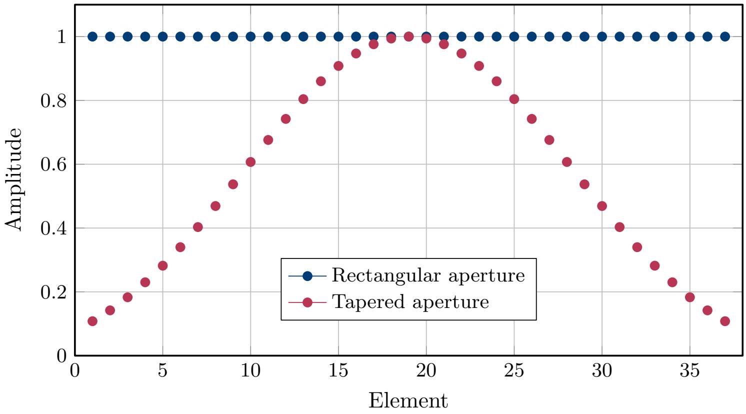

Figure 7.9: Amplitude functions (F_n) applied to the driving signals of the elements.

7.4.2. Results for 1.0 MHz

For the applied uniform and tapered amplitudes, the stress component perpendicular to the steel surface is shown in Figure 7.10a and Figure 7.10b. In Figure 7.10a the excitation of Lamb waves at each bounce of the beam is visible, and in Figure 7.10b it is shown that these waves are highly suppressed. To demonstrate the working of the algorithm, the geometry in Figure 7.8 was chosen such that the longitudinal wave and the Lamb waves are independently visible in the time domain.

The magnitude of the 2D Fast Fourier Transform (FFT) of the time signals in Figure 7.10 was computed to quantitatively get the amount of Lamb wave suppression achieved in each case. Figure 7.11a and Figure 7.11b show the independently normalized magnitudes with a dynamic range of 35 dB. It can be noticed that, after the implementation of a tapered amplitude function (Figure 7.11b), the S_0 Lamb wave mode was suppressed below 35 dB, as desired.

The striped nature of the information in Figure 7.11a and Figure 7.11b is a result of applying an FFT to the entire time-space domain of Figure 7.10a and Figure 7.10b, respectively, rather than to individual echoes. Furthermore, the side lobes located around 0.25 MHz and 1.7 MHz are the result of space-time windowing effects of the signal.

7.4.3. Results for 1.5 MHz

The time signals in Figure 7.12a and Figure 7.12b show the effect of a suppression of the Lamb wave modes when a tapered aperture of the transducer array is implemented. Moreover, the 2D FFTs shown in Figure 7.13a and Figure 7.13b quantitatively indicate a suppression of the amplitude of the problematic S_0 Lamb wave mode by 35 dB relative

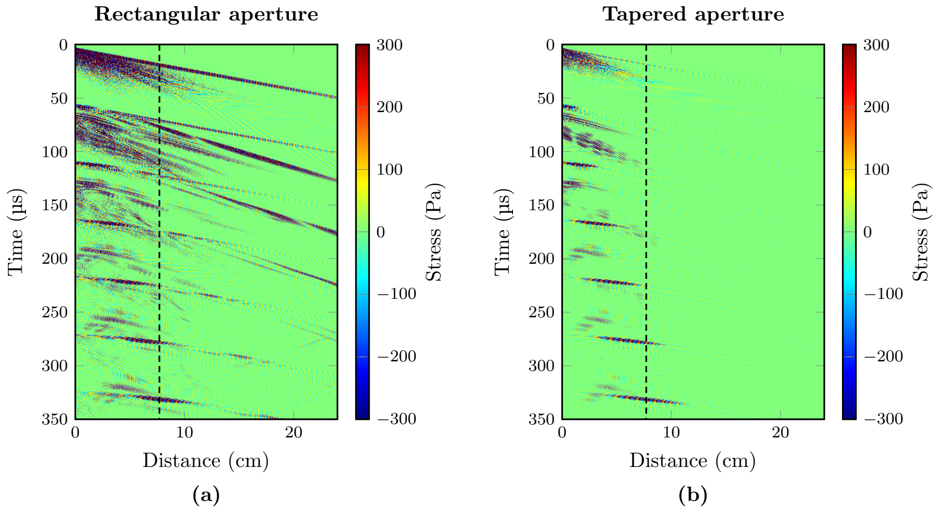

(a) (b)

Figure 7.10: Stress (perpendicular component) recorded along the steel-air interface for simulations with a 37-element transducer array with a center frequency of 1 MHz and a rectangular aperture function (a) and tapered aperture function (b). The longitudinal wave refracting from water bounced six times within the pipe wall. The black dashed lines mark the time signal located 77 mm away from the source.

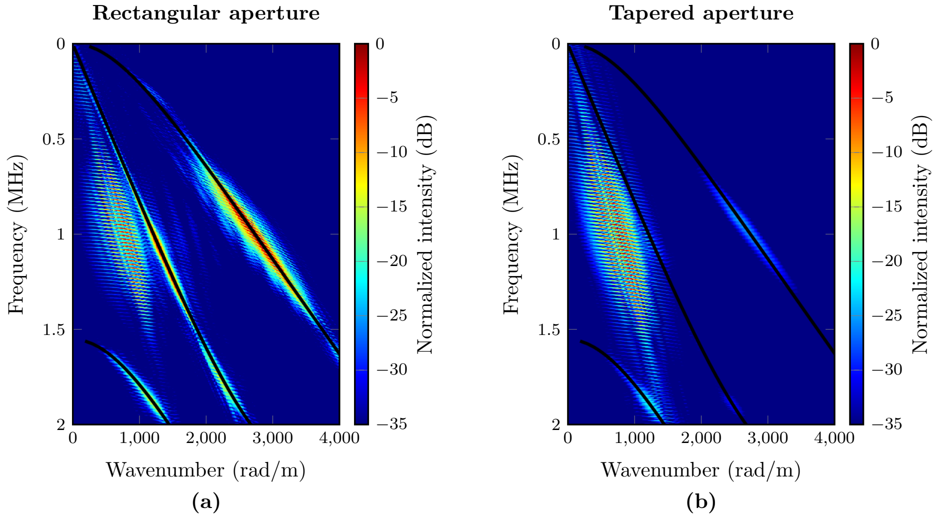

(a) (b)

Figure 7.11: Normalized 2D FFT of the recorded space-time signals in Figure 7.10. The black lines represent the theoretical dispersion curves of the Lamb waves that propagate within the steel.

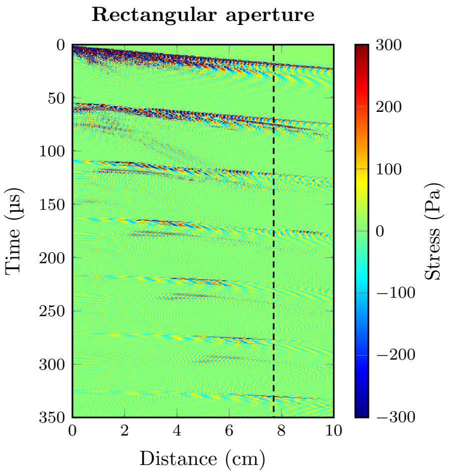

(a) (b)

Figure 7.12: Stress (perpendicular component) recorded along the steel-air interface for the two considered simulations with a 25-element transducer array with a center frequency of 1.5 MHz. (a) Rectangular aperture function (b) Tapered aperture function. The longitudinal wave refracting from water bounced six times within the pipe wall. The black dashed lines mark the time signal located 77 mm away from the source.

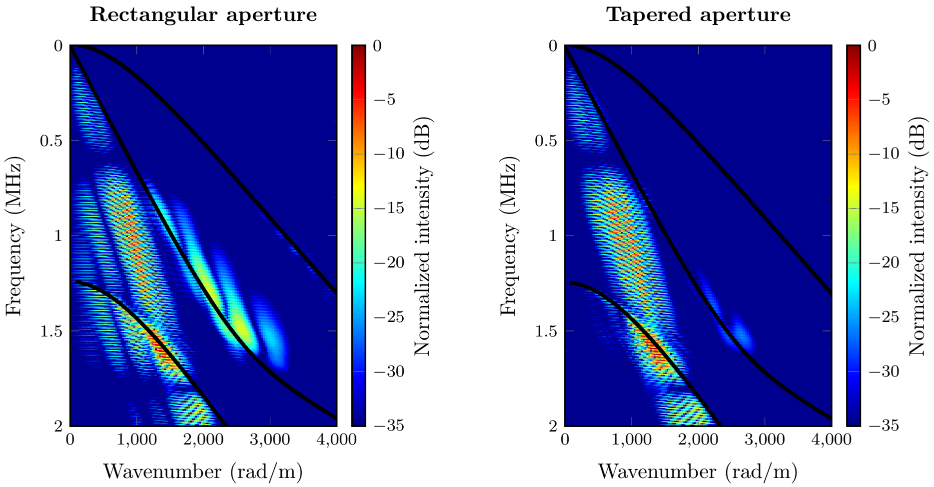

(a) (b)

Figure 7.13: Normalized 2D FFT of the recorded space-time signals in Figure 7.12. The black lines represent the theoretical dispersion curves of the Lamb waves that propagate within the steel.

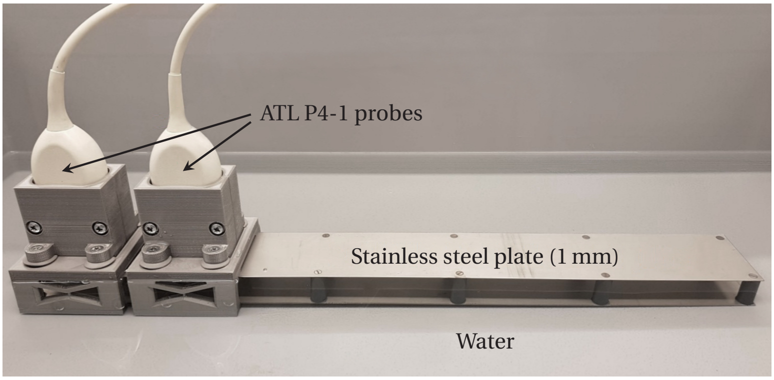

Figure 7.14: Experimental setup with two ATL P4-1 phased array probes on top of one of the two 1 mm-thick stainless steel plates. The centers of the probes were separated by 77 mm. The distance between both plates was 40 mm and filled with water. The upper side of the top plate was still loaded by air. Probe holders are made of a material with a similar acoustic impedance as that of water to avoid reflection effects on the recorded data.

to the longitudinal wave refracting from the liquid, as designed and expected from the algorithm described here.

In view of the previously described points, the transducer array apertures leading to the signals of Figure 7.10b and Figure 7.12b will make a more accurate estimate of flow relative to those of Figure 7.10a and Figure 7.12a, since the disturbing Lamb wave mode (in particular the one closest to the longitudinal wave carrying information from the water) has been suppressed below the required level. If necessary, other types of methods (e.g. filtering, time windowing) can be applied afterwards to suppress less problematic spurious Lamb waves.

7.5. Experimental Validation

7.5.1. Measurement Description

For a proof of principle, the experimental setup of Figure 7.14 was built. It consisted of two 1 mm-thick parallel stainless-steel plates separated by a 40 mm column of water. Two ATL P4-1 phased array probes (Philips, Bothell, WA, USA) were horizontally aligned and placed on top of one of the plates. These probes consist of 96 single elements with a pitch of 295 µm and a −20 dB frequency bandwidth from 1 MHz to 4 MHz. A Verasonics Vantage 256 system (Verasonics Inc., Kirkland, WA, USA) was used to drive the probes and record the data.

In transmission, a 16-cycle sine wave with a center frequency of 1.5 MHz was used as a driving signal of one of the probes. Moreover, time delays were applied to its individual elements to excite a longitudinal wave in the steel plate that impinges the steel-water interface under a 45° angle. In reception, the second probe was horizontally placed 77 mm away from the first one (center to center distance), where according to the simulation results in Figure 7.10 and Figure 7.12, it is expected to receive the 5th bounce of the longitudinal wave.

Two experiments were performed. First, a rectangular amplitude weighting function was applied along the elements of the array. Second, a tapered aperture was applied. This aperture was computed using the algorithm previously described.

7.5.2. Results and Discussion

Figure 7.15a and Figure 7.15b show the recorded time signals for each case with all elements of the receiving probe. Five bounces of the beam can be noticed. Due to the bounded spatial region where these signals were recorded (63 – 91 mm away from the center of the transmitting probe), it is not as straightforward to identify different propagating wave modes in this domain as it is in Figure 7.10a, Figure 7.10b, Figure 7.12a and Figure 7.12b.

Several transformations, like the Radon transform, can be used to identify the recorded wave modes [32]. In this case, the magnitude of a 2D FFT of the measured signals was computed for identifying the propagating wave modes. Figure 7.16a and Figure 7.16b show the independently-normalized magnitudes for each aperture with a dynamic range of 35 dB, where the longitudinal wave as well as the S_0 Lamb wave mode can be observed. With a controlled aperture, a suppression of 20 dB for the S_0 wave mode was achieved. The stripe patterns are due to the implementation of the FFT for the full space-time domain.

The space-limited information of the 28.3 mm probe aperture gives a less clear suppression effect in Figure 7.16b relative to Figure 7.13b. Therefore, a fairer one-to-one comparison was made. The 2D FFTs of the simulated data were computed using the same spatial range as in the experiments. The difference between both aperture schemes was computed and compared to that of the experimental data (see Figure 7.17). It is observed that the level of suppression of the problematic S_0 Lamb wave mode, within the spatial range of the receiving transducer, is the same for the simulated and measured data, i.e. around 20 dB. Moreover, during suppression, no reduction of the energy of the longitudinal wave took place, as can also be seen in Figure 7.16b.

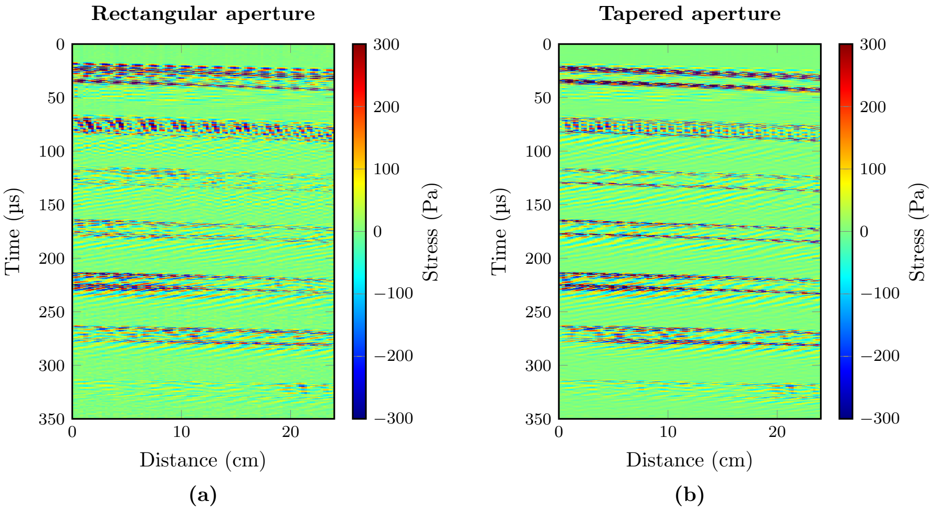

Figure 7.15: Signals recorded with all 96 elements of the receiving probe in the experimental setup for a rectangular aperture function (a) and tapered aperture function (b). It becomes challenging to identify the fifth bounce of the longitudinal wave in this domain.

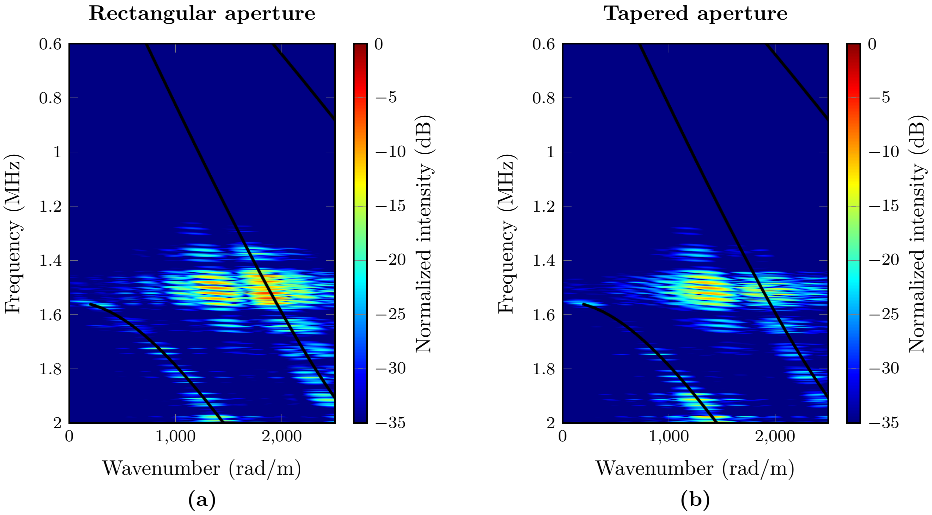

Figure 7.16: Normalized 2D FFT of the measured space-time signals in Figure 7.15. The black lines represent the theoretical dispersion curves of the Lamb waves that propagate in the steel plate.

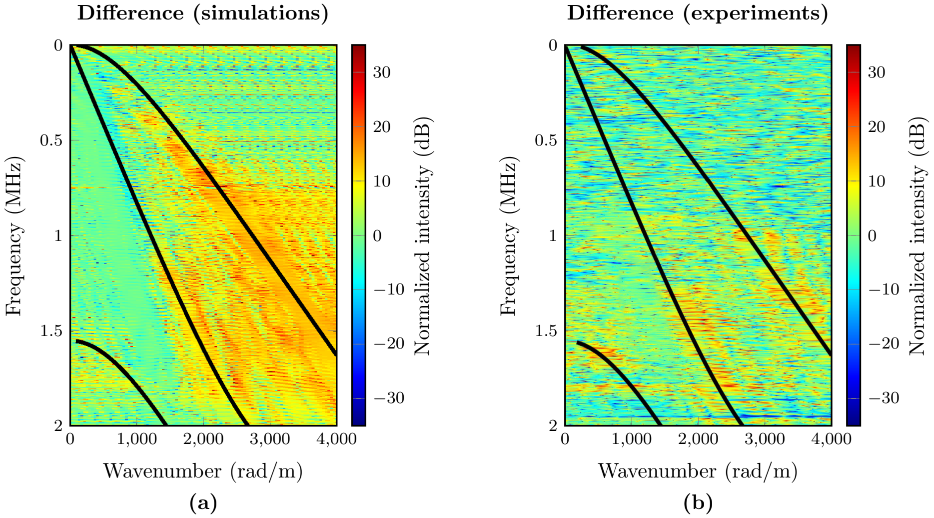

Figure 7.17: Difference between 2D FFTs of space-time signals for a rectangular and a tapered aperture. The spatial domain is located at 63 – 91 mm away from the center of the source. (a) Simulations. (b) Experiments. The black lines represent the theoretical dispersion curves.

7.6. Conclusions

In this chapter, a method has been described to steer an acoustic beam through a pipe wall while suppressing, in transmission, the excitation of spurious Lamb waves. In this way, absolute errors caused by these waves during clamp-on flow metering can be reduced. An algorithm to estimate the transducer array aperture (i.e. the number of elements and their amplitudes) required to achieve a desired performance has been described.

Due to its particular application for clamp-on flow metering, the method is based on amplitude manipulations of the aperture function of a transducer array, while phase shifts are used to control the shape of the propagating acoustic beam. Simulations and experimental results of an ultrasonic clamp-on flow measurement setting using 1 mm-thick stainless steel plates have been performed as validation and show a good agreement.

References

[1] J. Massaad, P. L. M. J. van Neer, D. M. van Willigen *et al.*, "Suppression of Lamb wave excitation via aperture control of a transducer array for ultrasonic clamp-on flow metering," *J. Acoust. Soc. Am.*, vol. 147, no. 4, pp. 2670–2681, 2020.

[2] J. C. Wendoloski, "On the theory of acoustic flow measurement," *J. Acoust. Soc. Am.*, vol. 110, no. 2, pp. 724–737, 2001.

[3] W.-S. Cheung, H.-S. Kwon, K.-A. Park *et al.*, "Acoustic flowmeter for the measurement of the mean flow velocity in pipes," *J. Acoust. Soc. Am.*, vol. 110, no. 5, pp. 2308–2314, 2001.

[4] R. C. Baker, *Flow measurement handbook: industrial designs, operating principles, performance, and applications.* Cambridge University Press, 2005.

[5] D. Kurniadi and A. Trisnobudi, "A multi-path ultrasonic transit time flow meter using a tomography method for gas flow velocity profile measurement," *Part. Part. Syst. Charact.*, vol. 23, no. 3-4, pp. 330–338, 2006.

[6] M. Sanderson and H. Yeung, "Guidelines for the use of ultrasonic non-invasive metering techniques," *Flow. Meas. Instrum.*, vol. 13, no. 4, pp. 125–142, 2002.

[7] K. Xu, D. Ta, B. Hu *et al.*, "Wideband dispersion reversal of Lamb waves," *IEEE Trans. Ultrason. Ferroelectr. Freq. Control*, vol. 61, no. 6, pp. 997–1005, 2014.

[8] C. Prada and M. Fink, "Separation of interfering acoustic scattered signals using the invariants of the time-reversal operator. Application to Lamb waves characterization," *J. Acoust. Soc. Am.*, vol. 104, no. 2, pp. 801–807, 1998.

[9] K. G. Sabra, A. Srivastava, F. Lanza di Scalea *et al.*, "Structural health monitoring by extraction of coherent guided waves from diffuse fields," *J. Acoust. Soc. Am.*, vol. 123, no. 1, pp. EL8–EL13, 2008.

[10] K. Xu, D. Ta, P. Moilanen *et al.*, "Mode separation of Lamb waves based on dispersion compensation method," *J. Acoust. Soc. Am.*, vol. 131, no. 4, pp. 2714–2722, 2012.

[11] G. Dib, O. Karpenko, M. Haq *et al.*, "Advanced signal processing algorithms in structural integrity monitoring," *Procedia Eng.*, vol. 86, pp. 427–439, 2014.

[12] J.-L. Le Calvez and T. M. Brill, "A method to separate flexural and extensional signals from mixed-mode ultrasonic signals," *IEEE Int. Ultrason. Symp.*, pp. 1–4, 2016.

[13] L. Bai, K. Xu, N. Bochud *et al.*, "Multichannel wideband mode-selective excitation of ultrasonic guided waves in long cortical bone," *IEEE Int. Ultrason. Symp.*, pp. 1–4, 2016.

[14] H. Li, X. Liu, and L. Bo, "A novel method to analysis strong dispersive overlapping Lamb-wave signatures," *J. Vibroeng*, vol. 19, no. 1, pp. 641–656, 2017.

[15] F. Gao, L. Zeng, J. Lin *et al.*, “Mode separation in frequency–wavenumber domain through compressed sensing of far-field Lamb waves,” *Meas. Sci. Technol.*, vol. 28, no. 7, p. 075004, 2017.

[16] V. Serey, N. Quaegebeur, P. Micheau *et al.*, “Selective generation of ultrasonic guided waves in a bi-dimensional waveguide,” *Struct. Health Monit.*, vol. 18, no. 4, pp. 1324–1336, 2019.

[17] W. Zhu and J. L. Rose, “Lamb wave generation and reception with time-delay periodic linear arrays: A BEM simulation and experimental study,” *IEEE Trans. Ultrason. Ferroelectr. Freq. Control*, vol. 46, no. 3, pp. 654–664, 1999.

[18] J. Li and J. L. Rose, “Implementing guided wave mode control by use of a phased transducer array,” *IEEE Trans. Ultrason. Ferroelectr. Freq. Control*, vol. 48, no. 3, pp. 761–768, 2001.

[19] J. L. Rose, *Ultrasonic guided waves in solid media.* Cambridge University Press, 2014.

[20] K.-C. T. Nguyen, L. H. Le, T. N. H. T. Tran *et al.*, “Excitation of ultrasonic Lamb waves using a phased array system with two array probes: Phantom and in vitro bone studies,” *Ultrasonics*, vol. 54, no. 5, pp. 1178–1185, 2014.

[21] C. Adams, S. Harput, D. Cowell *et al.*, “An adaptive array excitation scheme for the unidirectional enhancement of guided waves,” *IEEE Trans. Ultrason. Ferroelectr. Freq. Control*, vol. 64, no. 2, pp. 441–451, 2017.

[22] D. Guyomar and J. Powers, “A Fourier approach to diffraction of pulsed ultrasonic waves in lossless media,” *J. Acoust. Soc. Am.*, vol. 82, no. 1, pp. 354–359, 1987.

[23] R. J. Zemp, J. Tavakkoli, and R. S. Cobbold, “Modeling of nonlinear ultrasound propagation in tissue from array transducers,” *J. Acoust. Soc. Am.*, vol. 113, no. 1, pp. 139–152, 2003.

[24] R. S. Cobbold, *Foundations of Biomedical Ultrasound.* Oxford University Press, 2006.

[25] V. Pagneux, “Revisiting the edge resonance for Lamb waves in a semi-infinite plate,” *J. Acoust. Soc. Am.*, vol. 120, no. 2, pp. 649–656, 2006.

[26] J. D. N. Cheeke, *Fundamentals and Applications of Ultrasonic Waves.* CRC Press, 2016.

[27] I. A. Viktorov, *Rayleigh and Lamb Waves: Physical Theory and Applications. Transl. from Russian. With a Foreword by Warren P. Mason.* Plenum Press, 1967.

[28] R. E. Bunney, R. R. Goodman, and S. W. Marshall, “Rayleigh and Lamb Waves on Cylinders,” *J. Acoust. Soc. Am.*, vol. 46, no. 5B, pp. 1223–1233, 1969.

[29] A. Velichko and P. D. Wilcox, “Excitation and scattering of guided waves: Relationships between solutions for plates and pipes,” *J. Acoust. Soc. Am.*, vol. 125, no. 6, pp. 3623–3631, 2009.

[30] R. M. Levine and J. E. Michaels, “Model-based imaging of damage with Lamb waves via sparse reconstruction,” *J. Acoust. Soc. Am.*, vol. 133, no. 3, pp. 1525–1534, 2013.

[31] V. Dayal and V. K. Kinra, “Leaky Lamb waves in an anisotropic plate. I: An exact solution and experiments,” *J. Acoust. Soc. Am.*, vol. 85, no. 6, pp. 2268–2276, 1989.

[32] K. Xu, D. Ta, D. Cassereau *et al.*, “Multichannel processing for dispersion curves extraction of ultrasonic axial-transmission signals: Comparisons and case studies,” *J. Acoust. Soc. Am.*, vol. 140, no. 3, pp. 1758–1770, 2016.

8

Measurement of Pipe and Fluid Properties

Current ultrasonic clamp-on flow meters consist of a pair of single-element transducers which are carefully positioned before use. This positioning process consists of manually finding the distance between the transducer elements, along the pipe axis, for which maximum SNR is achieved. This distance depends on the sound speed, thickness and diameter of the pipe, and on the sound speed of the liquid. However, these parameters are often known with low accuracy, making it a manual and troublesome process. Furthermore, even when sensor positioning is done properly, uncertainty about the mentioned parameters limits the final accuracy of flow measurements. In this chapter, we address these issues using an ultrasonic clamp-on flow meter consisting of two matrix arrays, which enables the measurement of pipe and liquid parameters by the flow meter itself.

Automatic parameter extraction, combined with the beam steering capabilities of transducer arrays, yields a sensor capable of compensating for pipe imperfections. Three parameter extraction procedures are presented. First, axial Lamb waves are excited along the pipe wall and recorded with one of the arrays. A dispersion curve-fitting algorithm is used to extract bulk sound speeds and wall thickness of the pipe from the measured dispersion curves. Second, circumferential Lamb waves are excited, measured and corrected for dispersion to extract the pipe diameter. Third, pulse-echo measurements provide the sound speed of the liquid. The effectiveness of the first two procedures has been evaluated using simulated and measured data of stainless steel and aluminium pipes, and the feasibility of the third procedure has been evaluated using simulated data.

The contents of this chapter have been published in the IEEE Transactions on Ultrasonics, Ferroelectrics, and Frequency Control [1].

8.1. Introduction

Ultrasound is widely used to measure flow in industrial environments. There are two major classes of ultrasonic flow meters: in-line and clamp-on. The former typically consists of pairs of single-element transducers positioned inside the pipe and in direct contact with the fluid. The latter generally consists of a single pair of transducers placed on the pipe wall [2]. In both cases, the flow speed will be obtained by measuring the difference between upstream and downstream transit times of the propagating acoustic waves.

The design of in-line flow meters includes a pipe section with known dimensions, around which the transducers are aligned. This alignment depends on the expected range of flow speeds. For very high flow speeds, the acoustic beams might be deflected by the flow, resulting in lower signal-to-noise ratios (SNRs). Nevertheless, since the dimensions of the pipe are known, the acoustic path is completely characterized, and provided the speed of sound of the liquid contents is known, in-line flow meters do not have to be calibrated.

On the other hand, clamp-on flow meters are commonly placed onto pipes whose wall properties (bulk wave sound speeds, diameter, and thickness) and liquid contents properties (sound speed) are not known with enough accuracy or, less often, are completely unknown [3]. Therefore, this type of flow meter needs to be manually calibrated for each pipe. Apart from measuring the pipe and fluid parameters, this calibration consists of manually aligning the transducers by moving these along the pipe and finding the position for which the transmitted acoustic beams are recorded with the highest amplitude (Figure 8.1). The main advantage of these flow meters is that, contrary to their in-line counter-parts, they can be installed without interrupting the flow in the pipeline, which represents a valuable advantage in several industries.

The manual alignment procedure of ultrasonic clamp-on flow meters can be tedious when the pipe properties are not known, and also troublesome when working in confined areas. Moreover, pipe imperfections (e.g. corrosion, thickness and diameter variations) remain unnoticed and will not be accounted for when calibrating single-element transducers. Furthermore, even when the axial distance between the transducers in Figure 8.1 is found properly, there still remain uncertainties on the pipe properties and geometry, as well as on the sound speed of the liquid. This leads to uncertainties in the conversion of travel time difference into flow speed. Therefore, it would be very valuable to develop a clamp-on flow meter that is able to measure the properties of the pipe and the liquid, find the optimal beam path and proper travel time difference to flow speed translation, and thus automatically calibrate itself prior to metering.

To achieve this, we propose an ultrasonic clamp-on flow meter based on a pair of matrix transducer arrays. With such arrays, we can measure the properties of the pipe (bulk wave sound speeds, diameter, and wall thickness) and the liquid (sound speed). From these parameters, and the beam steering capabilities of matrix arrays, the optimal travel path of the acoustic waves can be automatically found without manual displacement of the sensors.

Information about the material properties and the geometry of solid objects can be extracted from their wave guide modes and/or resonant modes. The use of guided waves has been described in classical texts like [4–8], several of which describe the application to pipe walls. Works [9, 10] are a mathematical treatment of acoustic waves scattering from a cylinder or sphere submerged in water. In [10] it is explained that scattering from a submerged sphere is a combination of guided surface modes, and the resonant behavior of its interior. In [11] it is shown that the latter is absent for a fluid filled, submerged cylinder, and that the peaks of the frequency-dependent amplitude of the scattered waves correspond to different guided wave modes of the cylinder wall. In [12, 13], resonances were used to measure the Young's modulus of metallic rods and spheres submerged in water. Ultrasound-Stimulated Vibro-Acoustic Spectrography (USVAS) was used to measure the frequency-dependent amplitude response of the objects, and the resonance that registered a peak amplitude was used to compute the Young's modulus of the objects. However, all these techniques are performed completely underwater without a solid mechanical contact between the transducers and the solid medium. Thus, their implementation is sub-optimal in the setting of ultrasonic clamp-on flow meters.

In this work, we propose to excite and measure dispersion curves of guided waves in the pipe wall using transducer arrays. These curves will depend on the the pipe wall thickness and bulk wave sound speeds. By finding for which combination of parameters the corresponding theoretical curves will best fit the measured ones, these parameters

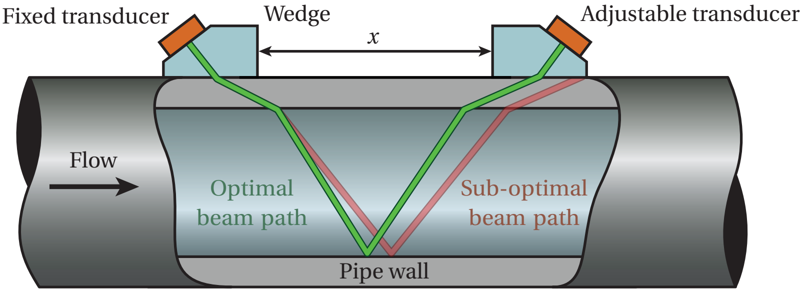

Figure 8.1: Cross-section of a conventional ultrasonic clamp-on flow meter. The beam path depends on pipe and liquid properties. Before flow metering, the optimal beam path is found by manually moving one of the transducers along the pipe axis, thus varying the separation distance x, until a peak amplitude is measured. For clarity, other beam paths, e.g. those related to helical waves that propagate around the pipe wall, standing waves, shear waves, and the ultrasonic wave reflected by the outer surface of the pipe wall, are not shown.

can be extracted. The approach of fitting dispersion curves to extract the elastic parameters of materials has been reported for medical [14–16] and industrial [17] applications. However, the fitting process in these cases is performed in a trial-and-error scheme involving the different parameters, and the assessment of the fitting procedure is done more qualitatively (i.e. visual comparison of theoretical dispersion curves with experimental ones) rather than quantitatively. Other approaches [18, 19] are more quantitative with respect to extracting and fitting dispersion curves. However, proper initial guesses of the parameters are needed as inputs for achieving convergence of the optimization algorithms. Furthermore, the approaches have not been tested with ground truth data from simulations, and thus their accuracy has not been verified. In this work, dispersion curves from the measured data are directly compared to pre-computed theoretical dispersion curves for a whole score of bulk wave sound speed and thickness values. Initial guesses of parameters may be used to narrow-down the database search, but they are ultimately unnecessary. Since there is no optimization procedure involved, there are no convergence issues.

Another important parameter to determine in ultrasonic clamp-on flow metering is the sound speed of the liquid. This has been done non-invasively in similar applications. In [20–22], transmission measurements were performed with single-element transducers placed in diametrically opposite locations on a liquid-filled pipe to determine the water cut level and the sound speed of different oil-water mixtures. The measured signals contained information from the liquid as well as the pipe wall (i.e. guided waves). The amplitudes associated to the guided waves were estimated based on a priori information about the parameters of the pipe, and subtracted from the measured signal before determining the desired parameters of the fluid. However, in this work, we propose to measure the sound speed of the liquid without needing a priori knowledge of the pipe. A large benefit of using a transducer array, as opposed to single-element transducers, is that a perpendicular pulse echo measurement may be performed to measure the time required for traversing the fluid twice. Moreover, the obtained data may be analyzed in the frequency - horizontal wavenumber (f-k_x) domain, where the perpendicular echo related may be singled out by only considering the information centered around the wavenumber $k_x = 0\,\mathrm{rad/m}$.

In this chapter, the concept of the proposed measurements, as well as simulation and experimental results are presented.

8.2. Guided Waves

The wall of a pipe acts as a waveguide, and when a pipe wall is mechanically excited, dispersive Lamb waves are generated. In a pipe, three types of Lamb wave modes exist: longitudinal, torsional and flexural. The first two modes are axisymmetric, while the last one is not. The mathematical treatment of such waves has been described in [23, 24], and the results are summarized in [8].

Generally, ultrasonic clamp-on flow meters operate in a frequency range from 0.2 MHz up to 2 MHz [2]. In many flow metering scenarios, the pipe circumference is much larger than the wavelength of the acoustic waves propagating in the pipe wall, i.e. $\lambda \ll 2\pi R$, with R being the pipe radius. Therefore, the approximation of a flat plate can be made [25], and the dispersion behavior of longitudinal Lamb wave modes in pipes may be described by the Rayleigh-Lamb equation for symmetric modes:

$$\frac{\tan(qh)}{\tan(ph)} = -\frac{4k^2pq}{\left(q^2-k^2\right)^2} \tag{8.1}$$

and for anti-symmetric modes:

$$\frac{\tan(qh)}{\tan(ph)} = -\frac{\left(q^2-k^2\right)^2}{4k^2pq} \tag{8.2}$$

In equations (8.1) and (8.2), k represents the wavenumber, h represents the thickness, and p and q are defined as:

$$p^2 = \left(\frac{\omega^2}{c_L^2}\right)^2 - k^2 \tag{8.3}$$

$$q^2 = \left(\frac{\omega^2}{c_T^2}\right)^2 - k^2 \tag{8.4}$$

In equations (8.3) and (8.4), ω represents the angular frequency; and c_L and c_T the longitudinal (compressional) and transversal (shear) bulk wave speed in the material, respectively. The solutions to the dispersion equations can be found numerically [8].

Equations (8.1) and (8.2) assume that the plate has two free surfaces. In the context of ultrasonic clamp-on flow metering, one surface is loaded by a liquid, which modifies the dispersion behavior of the wave modes. However, from Finite Element simulations, it was found that dispersion curves of plates with one water loaded surface deviate from those with two free surfaces only at frequencies below 0.1 MHz, which are outside the operational frequency range of ultrasonic clamp-on flow meters. Therefore, equations (8.1) and (8.2) were used as reasonable approximations to develop the methods proposed in this chapter.

8.3. Bulk Wave Sound Speeds and Wall Thickness of the Pipe

The procedure for measurement of the bulk wave sound speeds and the wall thickness of the pipe is based on a quantitative fitting of the measured dispersion curves to the relevant dispersion equations. For simplicity, in this section it will be assumed that the transducer array is directly placed on top of the pipe wall i.e., without a coupling piece.

8.3.1. Approach

A cross-section along the axial direction of a clamp-on flow meter with two transducer arrays is shown in Figure 8.2. To measure the relevant pipe wall parameters, Lamb waves are generated in the pipe wall by exciting one or several elements of one array, and these are recorded by all the elements of the second array. The measured time-distance (t-x) signals can be analyzed in the frequency - horizontal wavenumber (i.e. f-k_x) domain, which yields the dispersion curves of the observed symmetric and anti-symmetric modes. The parameters c_L, c_T and h can be found by identifying which combination of these generates the theoretical dispersion curves of equations (8.1) and (8.2) that best match the observed dispersion curves.

In principle, this fitting approach could be implemented for dispersion curves of any order. However, for simplicity, we have worked under the assumption that fitting the A_0 and S_0 wave modes (zero-order anti-symmetric and zero-order symmetric wave modes, respectively) is sufficient to uniquely determine c_L, c_T and h. Below, a description of the curve extraction and fitting procedure is given, followed by its application to numerical and experimental data.

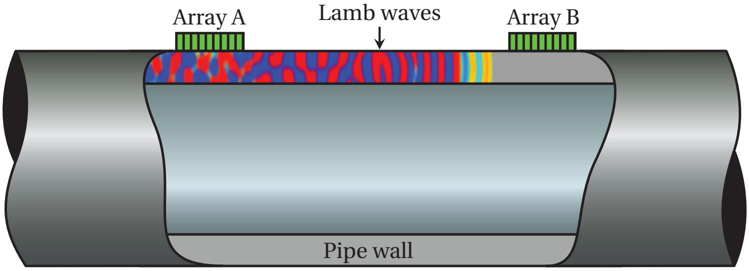

Figure 8.2: Axial cross-section of a clamp-on flow meter with transducer arrays. For measurement of the bulk wave sound speeds and wall thickness of a pipe, one or few elements of one array can be excited, and the propagating guided waves can then be recorded by the other array.

8.3.2. Curve Fitting Procedure

To quantitatively compare theoretical dispersion curves to experimental ones, it is first of all necessary to extract the curves from the measured data. In practical terms, converting t-x signals into f-k_x data yields a matrix that associates an amplitude and a phase to each f-k_x coordinate, whereas what is needed is the set of f-k_x coordinates corresponding to a wave mode, i.e. its f-k_x data points. These were identified via the amplitude maxima in the 2D Fourier domain, and their assignment to either wave mode, A_0 or S_0, was performed on the basis of order of appearance along the k_x direction (at every frequency, the horizontal wavenumber k_x belonging to A_0 has a lower value than the one belonging to S_0).

Next, it is necessary to calculate the theoretical dispersion curves corresponding to different sets of the three parameters c_L, c_T and h, i.e. make a look-up table. Each theoretical curve is then compared to the experimental one, and a measure of error (i.e. the mismatch between the two curves) is defined and computed. Finally, the theoretical curve with the smallest error is identified, thus finding which set of parameters describes the recorded dispersion the best.

An alternative way of approaching this problem would be to implement an optimization procedure to identify the theoretical curve corresponding to the smallest error. The disadvantage of such procedures, however, is that they require the computation of a potentially high number of theoretical curves every time that c_L, c_T and h are sought. With the approach adopted in the present work, the fitting procedure is reduced to comparing every new set of experimental curves to the already existing database. Compared to optimization algorithms, our approach reduces the computational cost considerably since the database can be computed off-line and once (i.e. before the measurements). A potential drawback of this approach is that the accuracy of the fit is limited by the resolution of the parameter space, which is set at the time of the generation of the database. Moreover, similarly to optimization algorithms, there is a trade-off between target precision and computation time: the higher the precision, the larger is the database and the longer the computation time, both for database generation and for the fitting procedure.

The comparison between theoretical and experimental curves was performed by computing the magnitude of an error function that quantifies, at each frequency, the deviation of one curve from the other along the k_x direction. The chosen error function represents the root mean square percentile difference (RMS-PD) between a given theoretical curve and the experimental one:

$$E = \frac{100}{N} \sum_{i=1}^{N} \sqrt{\left(\frac{k_i^{\text{theo}} - k_i^{\text{exp}}}{k_i^{\text{theo}}} \right)^2} \tag{8.5}$$

In equation (8.5), E is the RMS-PD error, N is the number of frequencies that are considered, k_i^{exp} is the horizontal wavenumber of the i^{th} frequency for the experimental curve, and k_i^{theo} is the horizontal wavenumber of the same frequency for the theoretical curve.

This error function has several advantages: first of all, normalizing the difference at each frequency by the corresponding horizontal wavenumber (either the theoretical or the experimental one) helps to assign the same weight to all points; without this correction, relatively small deviations at higher frequencies impact the error much more than comparable deviations at lower frequencies (a 10% variation from $k_i = 1000\,\text{rad/m}$ is much larger than a 10% from $k_i = 100\,\text{rad/m}$). Moreover, normalizing the error by the number of points used to compute it allows to compare curves where different values of N are used. Finally, a percentile scale is intuitively easy to interpret, even for very small errors.

One last thing that should be noted is that the dispersion curves of the A_0 and S_0 wave modes are not equally sensitive to all three parameters c_L, c_T and h at all frequencies. From theoretical dispersion curves of Lamb waves for a typical set of metallic pipe properties, it was found that the phase speed of the A_0 wave mode, for instance, is sensitive to h mainly at low frequencies (i.e. $f \leq 1\,\text{MHz}$), whereas at higher frequencies it is more sensitive to c_T. The S_0 wave mode, on the other hand, shows a stronger sensitivity to h in the range $1.5\,\text{MHz} \leq f \leq 3\,\text{MHz}$, and is especially sensitive to c_L for $f \leq 1\,\text{MHz}$. This means that any fitting procedure could yield more or less accurate for a given property, depending on which wave mode is fitted at which frequency range.

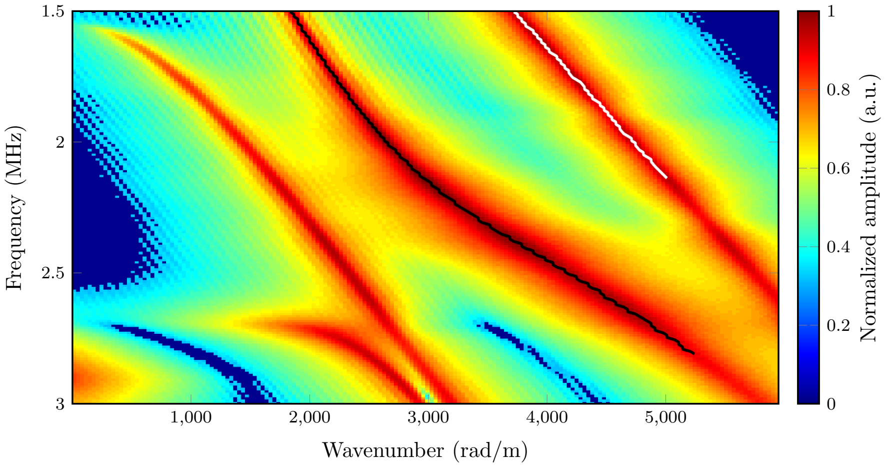

Figure 8.3: Magnitude of a 2D FFT applied on simulated space-time signals of Lamb waves recorded on the surface of a 1 mm-thick stainless steel plate. The black and white lines show the extracted data points of the S_0 and A_0 wave modes, respectively.

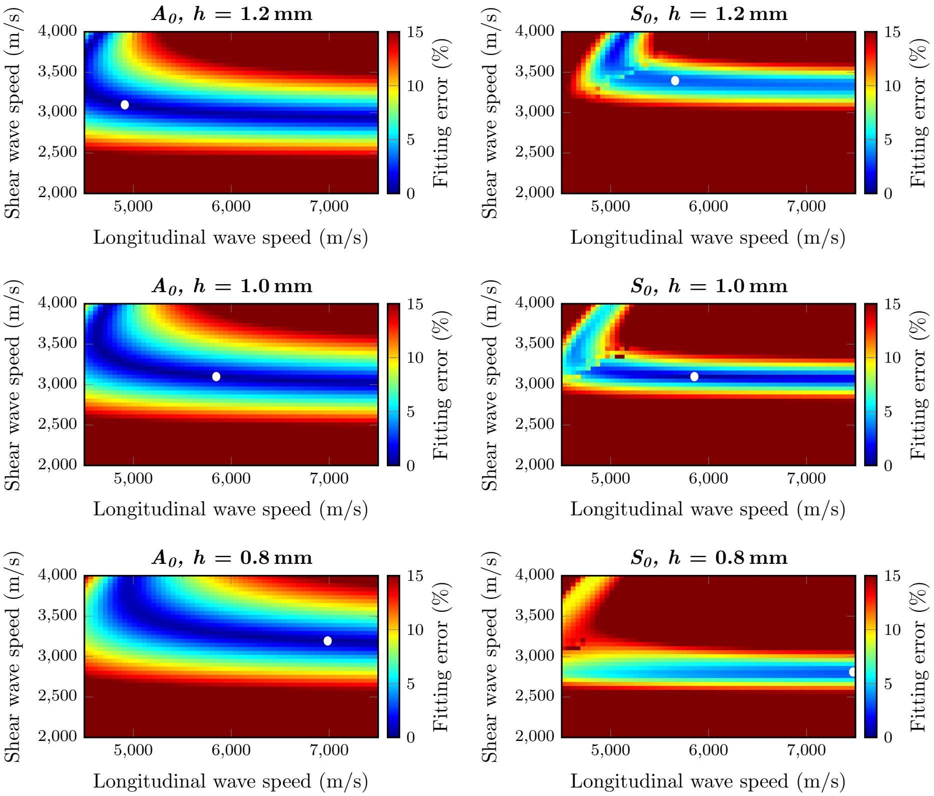

A_0, h = 1.2 mm

S_0, h = 1.2 mm

A_0, h = 1.0 mm

S_0, h = 1.0 mm

A_0, h = 0.8 mm

S_0, h = 0.8 mm

Figure 8.4: Error maps obtained by comparing the A_0 and S_0 wave mode dispersion curves extracted from simulated data to the theoretical database, for thickness values of $h = 0.8$ mm, $h = 1.0$ mm and $h = 1.2$ mm. The white dot in each error map indicates the location of minimum error.

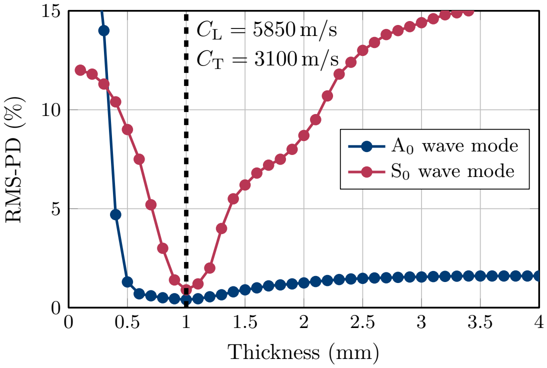

Figure 8.5: Minimum RMS-PD error of the simulated error maps of Figure 8.4, as a function of thickness h, for the A_0 mode and the S_0 mode. The values of longitudinal and shear wave speeds are shown for the thickness $h = 1\,\mathrm{mm}$, which is the one that reports the minimum error.

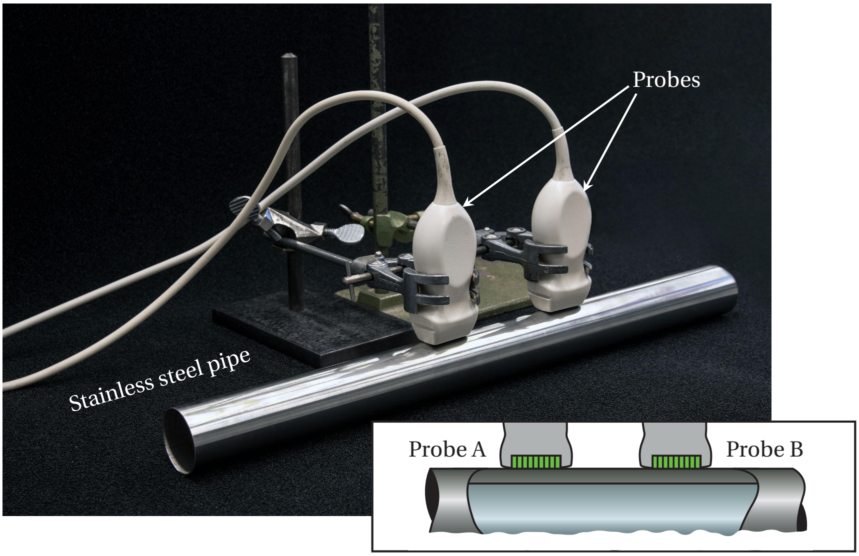

Figure 8.6: Experimental setup used to excite and measure Lamb waves with transducer arrays on a 1 mm-thick 304-stainless steel pipe (nominal values: $c_L = 5920\,\mathrm{m/s}$ and $c_T = 3141\,\mathrm{m/s}$). The array elements of each probe are oriented along the pipe axis, as indicated by the diagram.

8.3.3. Numerical validation

The procedure described above was first tested on simulated data. A vacuum-loaded stainless steel plate ($c_L = 5800\,\mathrm{m/s}$ and $c_T = 3100\,\mathrm{m/s}$) with a thickness of $h = 1\,\mathrm{mm}$ was simulated using the Finite Element Modeling (FEM) software package PZFlex (Onscale, Redwood City, CA, USA). On one of the surfaces, a small transducer element (HK1HD, TRS Technologies Inc., State College, PA, USA) with a thickness of 0.5 mm and width of 0.3 mm, was placed and excited with a 1-cycle sine wave with a center frequency of 2.25 MHz. Receivers were placed with a pitch of 0.02 mm along a distance of 90 mm next to the excited transducer and on the same side of the plate to record the propagating Lamb waves.

The recorded t-x signals were then transformed into f-k_x data by means of a 2D Fast Fourier Transform (FFT), and the A_0 and S_0 wave modes were extracted following the procedure explained above (see Figure 8.3). The A_0 wave mode was identified within the frequency range $1.5\,\mathrm{MHz} \leq f \leq 2.1\,\mathrm{MHz}$, and the S_0 wave mode was observed within the frequency range $1.5\,\mathrm{MHz} \leq f \leq 2.8\,\mathrm{MHz}$.

Considering the elastic properties of common metals, theoretical dispersion curves were computed for a wide range of fitting parameters: $4500\,\mathrm{m/s} \leq c_L \leq 7500\,\mathrm{m/s}$, $2000\,\mathrm{m/s} \leq c_T \leq 4000\,\mathrm{m/s}$ and $0.1\,\mathrm{mm} \leq h \leq 4\,\mathrm{mm}$, with a sound speed resolution of 50 m/s and a thickness resolution of 0.1 mm, forming a database of $\approx 10^5$ theoretical curves with a total size of 50 MB. The fitting procedure using this database took $\approx 70\,\mathrm{s}$ on a 64-bit Dell laptop (RAM = 8 GB, Processor: Intel(R) Core(TM) i7-6600U).

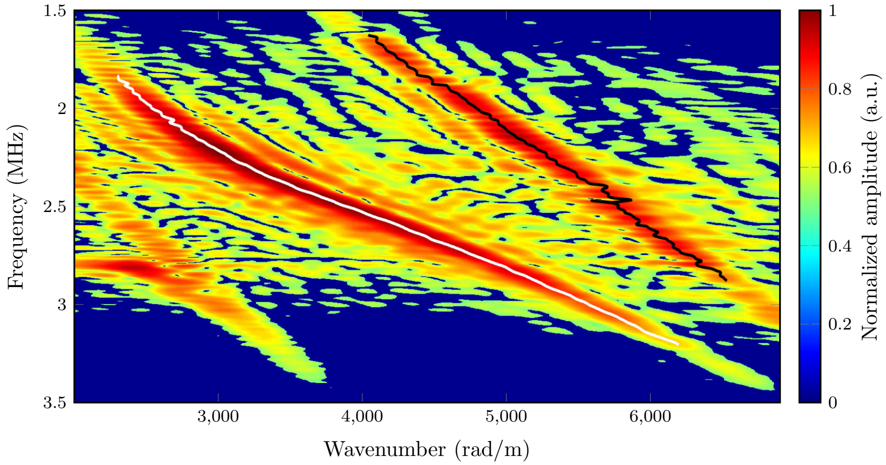

Figure 8.7: Magnitude of 2D FFT applied on the measured time signals. The black and white lines show the extracted data points of the A_0 and S_0 wave modes, respectively.

Figure 8.4 shows several 2D error maps, computed via equation (8.5) from the extracted curves and those in the database. These maps show the distribution of the error as a function of the two bulk wave speeds. Each map corresponds to a fixed thickness value h. Figure 8.4 shows the error maps for the A_0 and S_0 wave mode. From each map, the (c_L, c_T) coordinate that reports the minimum error was extracted. However, to locate this minimum, only those (c_L, c_T) coordinates that report a Poisson ratio relevant for metals, i.e. with a value between $\nu = 0.15 - 0.45$, were considered. Figure 8.5 shows, for the two wave modes, a plot of the minimum RMS-PD error as a function of the thickness h. It can be observed that the final parameters obtained via the fitting algorithm were $c_L = 5850\,\mathrm{m/s}$, $c_T = 3100\,\mathrm{m/s}$ and $h = 1\,\mathrm{mm}$. Compared to the simulation parameters ($c_L = 5800\,\mathrm{m/s}$, $c_T = 3100\,\mathrm{m/s}$ and $h = 1\,\mathrm{mm}$), this implies only a discrepancy of 0.86 % between the values of c_L. Considering that this discrepancy of 50 m/s is also the speed resolution of the database, it is possible that a database with higher resolution would yield even more accurate results.

8.3.4. Measurements

The fitting procedure was applied to measurements obtained from a 40 mm-inner diameter 304-stainless steel pipe (nominal values [26]: $c_L = 5920\,\mathrm{m/s}$ and $c_T = 3141\,\mathrm{m/s}$) with a wall thickness of $h = 1\,\mathrm{mm}$. The sound speeds of Lamb waves in typical industrial pipe walls are much faster than the sound speed of typical liquids. Therefore, these are very likely to be easily windowed-out in time, and for this reason the air-filled pipe setup of Figure 8.6 is still representative of a real practical scenario.

As shown in Figure 8.6, two ATL P4-1 probes (Philips, Bothell, WA, USA) were placed within a center-to-center distance of 10 cm, and driven with a Verasonics Vantage 256 system (Verasonics Inc., Kirkland, WA, USA). A one-cycle square bipolar pulse with a center frequency of 2.25 MHz was used to electrically excite one element of one probe. The square excitation pulse was translated by the transfer function of the transducer into a sine-like mechanical excitation pulse. All 96 elements of the other probe were used to record the propagating Lamb waves. A 2D FFT was applied on the measured time signals, and from its magnitude (Figure 8.7) the A_0 wave mode was observed within a frequency range of $1.6\,\mathrm{MHz} \leq f \leq 2.8\,\mathrm{MHz}$, whereas the S_0 wave mode was identified within $1.8\,\mathrm{MHz} \leq f \leq 3.2\,\mathrm{MHz}$.

Comparing Figure 8.3 and Figure 8.7, we notice the effect of noise in the mapping of the dispersion curves obtained from experiments, as well as a difference in spatial resolution of the dispersion curves due to a more limited spatial sampling aperture during experiments. Regardless, the error maps of Figure 8.8 and Figure 8.9 show that the thickness of the pipe wall is correctly identified when fitting either wave mode. The S_0 wave mode, as already mentioned above and observed from simulations, appears to be more sensitive to thickness variations. Conversely, the values of c_L and c_T extracted by fitting the A_0 wave mode are closer to the nominal properties of the pipe than those found by fitting the S_0

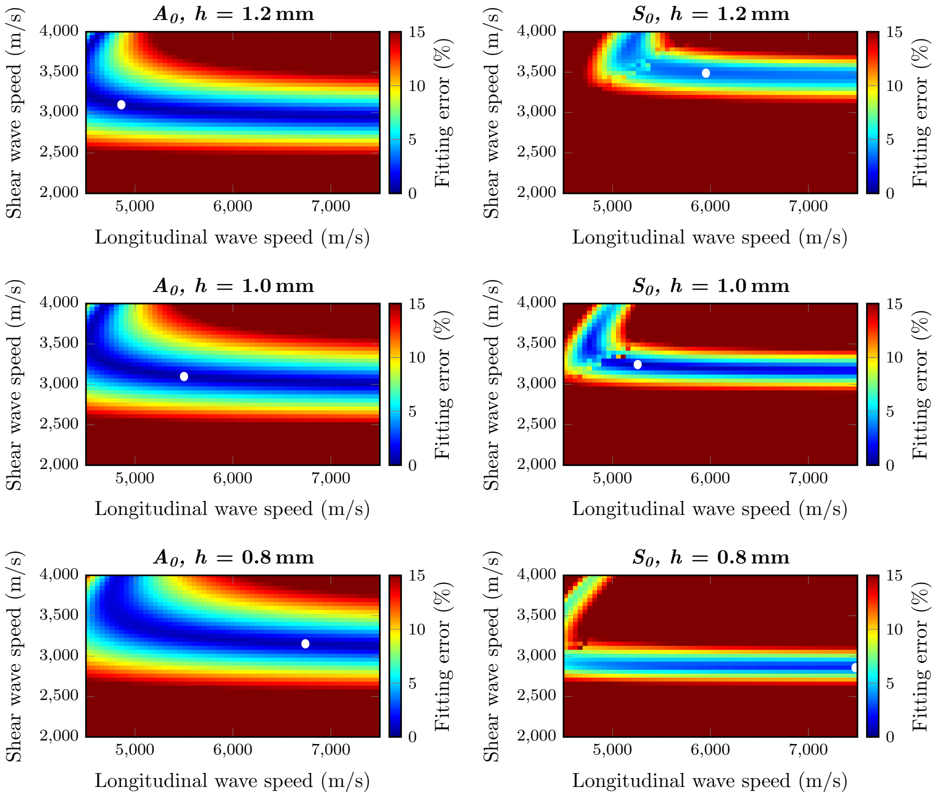

Figure 8.8: Error maps obtained by comparing the A_0 and S_0 wave mode dispersion curves extracted from measured data to the theoretical database, for thickness values of $h = 0.8\,\text{mm}$, $h = 1.0\,\text{mm}$ and $h = 1.2\,\text{mm}$. The white dot in each error map indicates the location of minimum error.

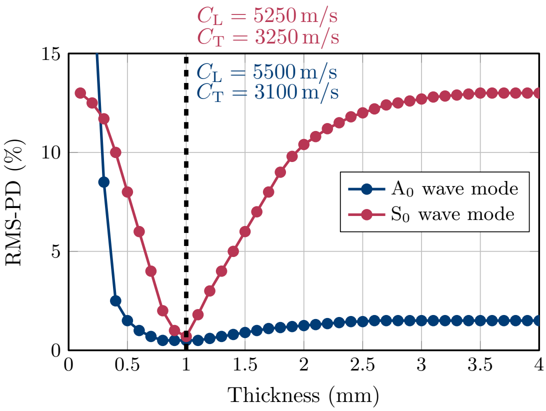

Figure 8.9: Minimum RMS-PD error of measured error maps of Figure 8.8, as a function of thickness h, for the A_0 mode (blue) and the S_0 mode (purple). The values of longitudinal and shear wave speeds are shown for the thickness $h = 1.0\,\mathrm{mm}$, which is the one that reports the minimum error.

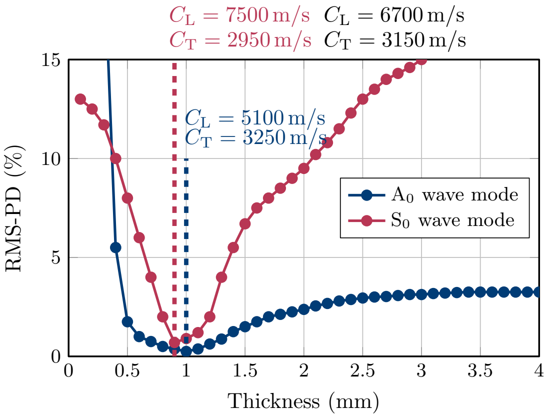

Figure 8.10: Minimum RMS-PD error of measured error maps for an aluminium pipe as a function of thickness h for the A_0 mode (blue) and the mode S_0 (purple). The values of longitudinal and shear wave speeds are expressed for thicknesses with lowest error ($h = 0.9\,\mathrm{mm}$ for the S_0 wave mode, $h = 1.0\,\mathrm{mm}$ for the A_0 wave mode). The wave speeds obtained by fitting the A_0 mode with a plate of thickness $h = 0.9\,\mathrm{mm}$ are reported in black.

wave mode. The properties reported in Figure 8.9 by fitting the A_0 wave mode suggest a discrepancy with nominal values of c_L and c_T of 7.09 % and 1.27 %, respectively.

The fitting procedure was also applied to measurements obtained from a 62 mm-inner diameter ENAW6063.T66-aluminium pipe (Nedal Aluminium BV, Utrecht, NL; nominal values: $c_L = 6306\,\mathrm{m/s}$, $c_T = 3114\,\mathrm{m/s}$), with a wall thickness of $h = 1\,\mathrm{mm}$. With these measurements it is also shown that the extracted parameters from one dispersion curve may be used as input in the fitting procedure of another curve to obtain more accurate results. For this pipe, f-k_x data points of the A_0 and S_0 wave modes were extracted within the frequency range $1\,\mathrm{MHz} \leq f \leq 2.4\,\mathrm{MHz}$. The properties extracted by fitting each wave mode individually varied considerably from the nominal values. From the A_0 wave mode, values of $c_L = 5100\,\mathrm{m/s}$, $c_T = 3250\,\mathrm{m/s}$, $h = 1.0\,\mathrm{mm}$ were obtained, and for the S_0 wave mode, values of $c_L = 7500\,\mathrm{m/s}$, $c_T = 2950\,\mathrm{m/s}$, $h = 0.9\,\mathrm{mm}$ were obtained. Because at high frequencies the S_0 wave mode is more sensitive to h than the A_0 wave mode, the value of h obtained by fitting the S_0 wave mode was used as input in the fitting procedure of the A_0 wave mode to obtain a more accurate estimate of the bulk wave sound speeds of the pipe. By implementing this approach, values of $c_L = 6700\,\mathrm{m/s}$ and $c_T = 3150\,\mathrm{m/s}$ were finally obtained (see Figure 8.10), which represent a discrepancy from nominal values of 8.96 % and 1.49 % respectively, with a thickness estimated at 0.9 mm (a deviation of 10 % from the nominal value).

8.4. Diameter of the Pipe

The average diameter of the pipe is determined by measuring the transit time of a particular Lamb wave traveling around the circumference of the pipe, by looking at the arrival of the envelope of the corresponding pulse. The wave mode is dispersive, therefore, its frequency components will have different transit times $t(\omega)$. Since the dispersive group speed $c_g(\omega)$ of the excited wave mode is known by now, the pipe outer diameter (OD) can in principle be computed as:

$$\mathrm{OD}(\omega) = \frac{c_g(\omega)\, t(\omega)}{\pi} + h \tag{8.6}$$

In practice, however, it becomes challenging to identify the transit time of the measured dispersive signal and the corresponding frequency component. A more accurate estimate of the transit time can be made by performing dispersion correction, i.e. correct for the frequency-dependent phase speed.

8.4.1. Lamb Wave Dispersion Correction

Dispersion correction has been applied in non-destructive testing applications at macroscopic [27] and nanoscopic [28] scale. Such correction effectively flattens-out the phase speed dispersion curve of the measured wave mode. After correction, group and phase speed are the same, therefore providing a more accurate estimation of the pipe diameter. Furthermore, since the phase of all frequency components is the same after dispersion correction, a maximum amplitude of the time signal will be achieved at the arrival of the wave, providing the highest possible SNR to estimate the transit time.

Considering a dispersive signal $g(t)$, a frequency component f_0 (associated with phase speed $c(f_0)$) arrives at a time $t(f_0)$. The phase difference between this frequency component and another one is:

$$\Delta\Phi = \omega\Delta t = 2\pi\left[f\,t\left(f\right) - f_0\,t(f_0)\right] \tag{8.7}$$

Given that all frequency components travel the same path length p, the following relation holds:

$$p = t(f_0)c(f_0) = t(f)c(f) \tag{8.8}$$

$c(f)$ represents the phase speed of the measured wave mode. Solving for $t(f)$ in equation (8.8), and substituting the result in equation (8.7), we get:

$$\Delta\Phi = \omega\Delta t = 2\pi\,t(f_0)\left[\frac{c(f_0)}{c(f)} - \frac{f_0}{f}\right] \tag{8.9}$$

Given the Fourier Transform of the measured signal $g(f)$, the corrected signal can be computed as:

$$g_{\text{corr}}(t) = \mathfrak{F}^{-1}\left\{g(f)\exp\left[2\pi f\,t(f_0)\left(\frac{c(f_0)}{c(f)} - \frac{f_0}{f}\right)\right]\right\} \tag{8.10}$$

where $\mathfrak{F}^{-1}$ represents the inverse Fourier transformation. In equation 8.10 it is observed that only the phase of the signal is being manipulated.

8

Given a phase speed $c(f_0)$ towards which the dispersion curve is being flattened-out, equation (8.10) is repeated for a given range of transit times $t(f_0)$. For each trial $t(f_0)$, the envelope of the compressed signal is computed and its peak value monitored. The final dispersion-corrected signal would be the one with the highest peak amplitude of its envelope, and the transit time associated to that peak, together with $c(f_0)$, would be the parameters to use in equation (8.6) to finally compute pipe diameter.

8.4.2. Simulations

Finite Element simulations of Lamb wave propagation were performed with PZFlex to obtain data that allows us to validate the dispersion correction algorithm explained above, as well as equation (8.6).

The same transducer element as considered in the previous section was simulated on top of an aluminium pipe (OD = 60 mm, $h = 1$ mm), as seen in Figure 8.11. The element was excited with a 2-cycle sine wave with a center frequency of 2.25 MHz. According

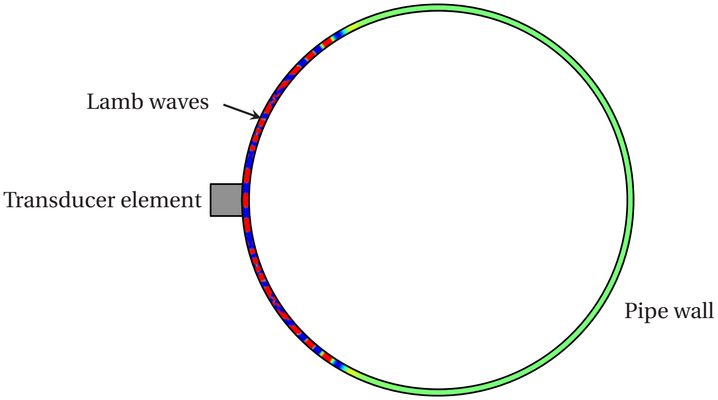

Figure 8.11: Finite Element simulation of an aluminium pipe (OD = 60 mm, h = 1 mm). The transducer element was excited with a 2-cycle sine wave with a center frequency of 2.25 MHz, and receivers were placed around the outer surface of the pipe wall. Transducer element dimensions (0.5 × 0.3 mm) are exaggerated for visualization purposes.

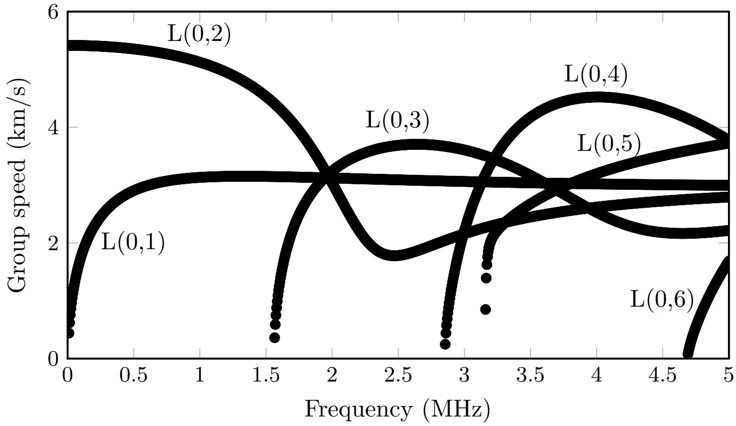

Figure 8.12: Group speed dispersion curves of Lamb waves for the pipe. Around 2.25 MHz, at least three different wave modes are expected to be excited.

to the dispersion curves for the pipe, see Figure 8.12, the L(0, 1), L(0, 2) and L(0, 3) wave modes are expected to be excited. Lamb waves were recorded by receivers placed around the outer surface of the pipe wall. From the recorded time signals, a spectrogram was computed considering a moving Hanning window with a time length of 9.5 µs. The different wave modes could be identified in Figure 8.13.

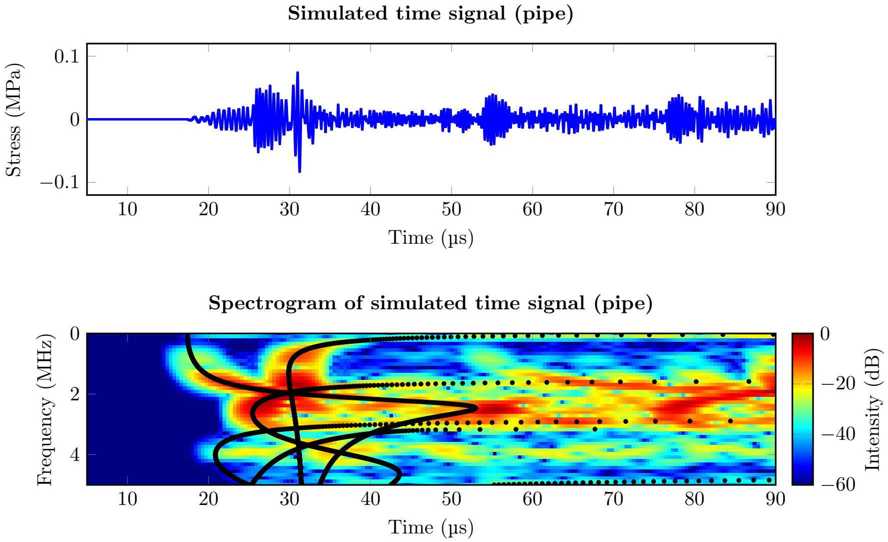

Figure 8.13: Simulated stress signal on the opposite side of the pipe and its spectrogram. The black dotted lines are computed from the theoretical group speeds.

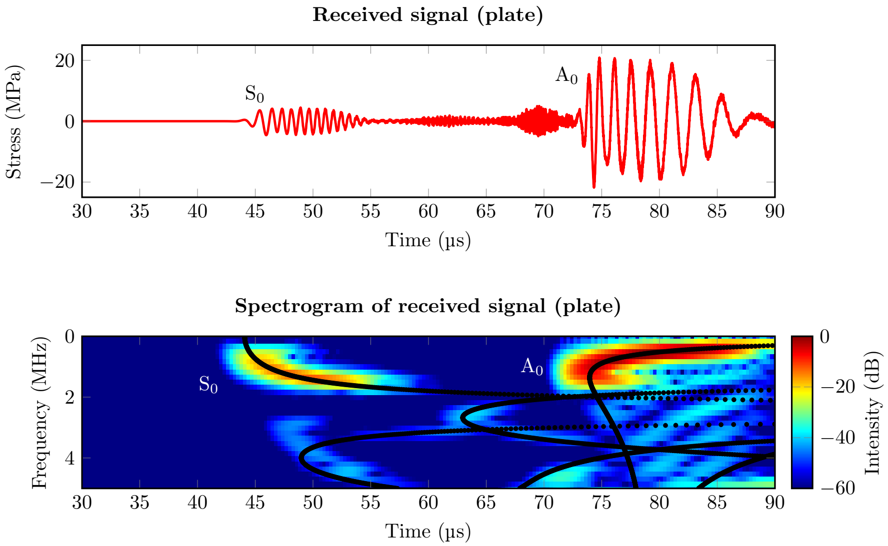

Figure 8.14: Simulated stress signal on a flat stainless steel plate, and its spectrogram. The black dotted lines are computed from the group speeds, and overlap with the theoretical curves.

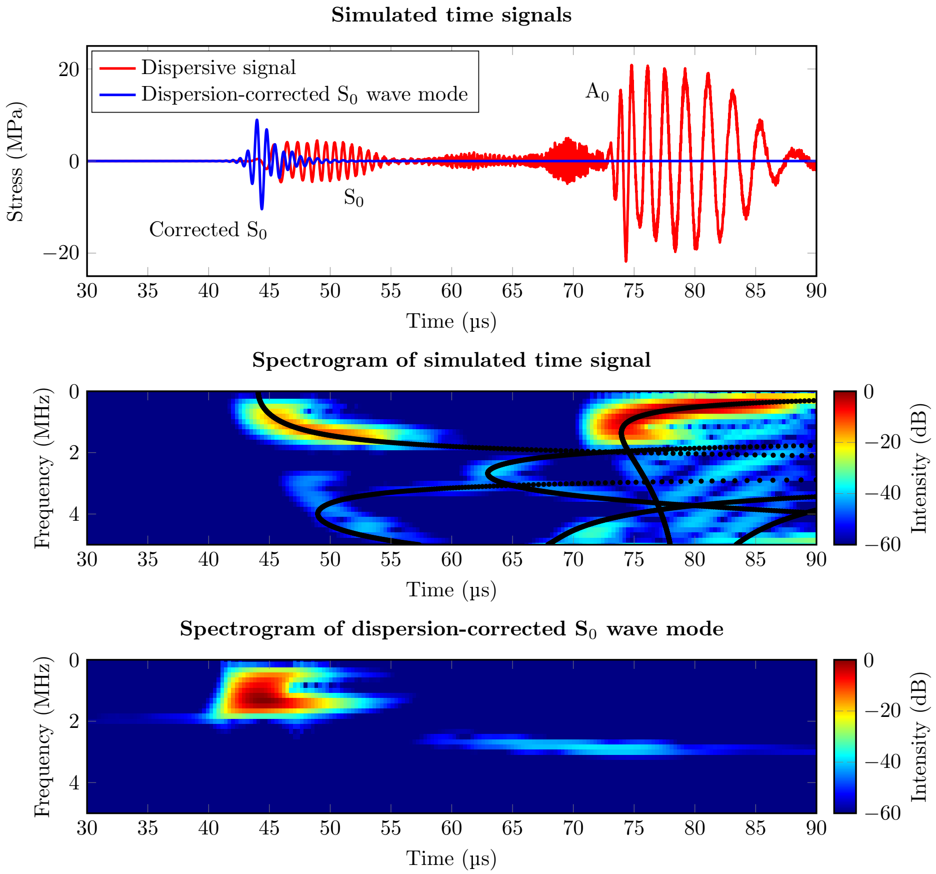

Figure 8.15: Dispersion correction of the S_0 wave mode computed in a Finite Element simulation involving a stainless steel plate with a thickness $h = 1\,\mathrm{mm}$. The black curves in the spectrograms follow from the theoretical group speeds.

To assess the accuracy of the proposed method, a simple flat plate geometry was considered as a valid approximation of a cylindrical pipe wall [25]. Lamb waves were computed 23 cm away from the source. In the process of validating equation (8.10), the S_0 wave mode in Figure 8.14 was considered. After the implementation of the dispersion correction (Figure 8.15), the computed travel path was 22.82 cm, which represents a discrepancy of 0.8 % relative to the true value.

8.4.3. Measurements

The proposed procedure for measurement of the pipe diameter was tested on the aluminium pipe described previously. For this purpose, a single ATL P4-1 phase array probe was placed onto the pipe wall in the circumferential direction (Figure 8.16). Even though most of the piezo-elements were not in mechanical contact with the pipe wall, the one in the middle of the probe was. This element was then excited with a 2-cycle square pulse with a center frequency of 2.25 MHz. The time signal recorded by this element, as well as its spectrogram, are shown in Figure 8.17, in which several round trips of wave modes, such as the L(0, 3), are observed. Based on the pipe parameters measured in the previous section, group speed dispersion curves were computed and theoretical curves for the maxima in the spectrogram were derived and plotted in the spectrogram. These curves show a very good agreement with the locations of the maxima in the measured spectrogram.

Furthermore, the spectrogram of Figure 8.17 shows that the first wave mode to arrive after propagating a full circumference is the L(0, 2). Therefore, this wave mode was windowed-out from the measured time signal and corrected for dispersion. The reference frequency

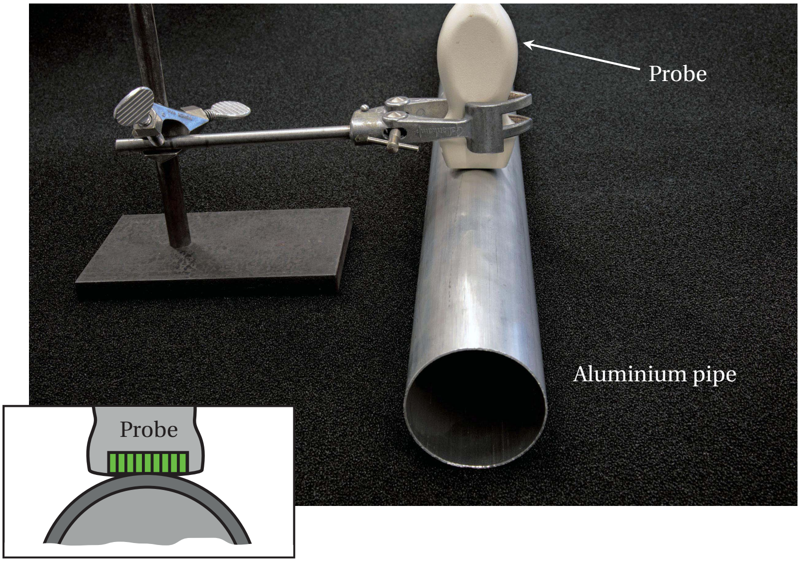

Figure 8.16: Experimental setup to test the proposed procedure for measurement of the pipe diameter, consisting of an aluminium pipe (OD = 60 mm, h = 1 mm), and a P4-1 phased array probe placed on top. The array elements of the probe are oriented perpendicularly to the pipe axis, as indicated by the diagram. A foam layer was placed below the pipe to avoid mechanical coupling and vibrations of the table on which the setup was placed.

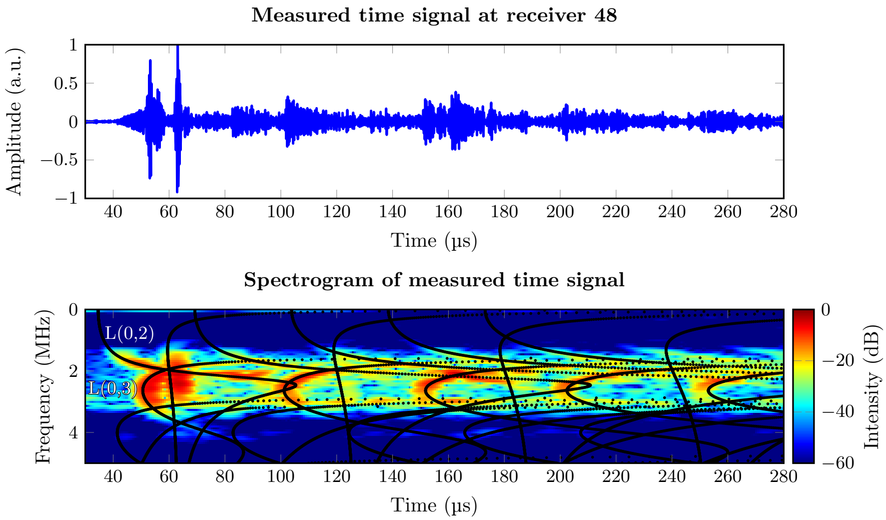

Figure 8.17: Time signal (above) recorded by one piezo-element of the probe in contact with the aluminum pipe, as shown in Figure 8.16, and its spectrogram (below). The black curves in the spectrogram follow from the theoretical group speed computed for the pipe parameters measured in the previous section.

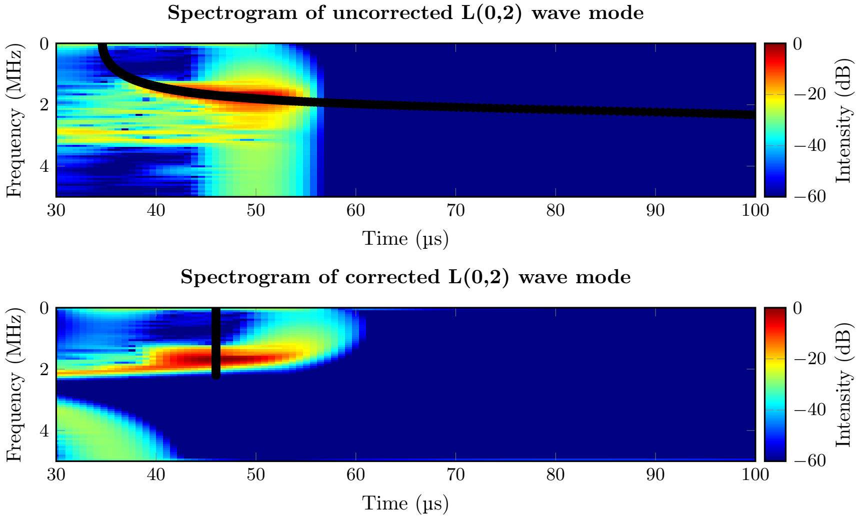

Figure 8.18: Spectrogram, before and after dispersion correction, of a measured L(0, 2) wave mode on the aluminium pipe shown in Figure 8.16. The black curves in the spectrograms follow from the theoretical group speeds.

at which the phase speed dispersion curve of this wave mode was flattened-out was $f_0 = 2\,\text{MHz}$. The proposed dispersion correction algorithm was applied with a sound speed of $c(f_0) = 4294\,\text{m/s}$, and the spectrograms of the measured L(0,2) wave mode before and after dispersion correction are shown in Figure 8.18.

After correction, a transit time of 45.4 µs was obtained. When used in equation (8.5), this gives a pipe outer diameter of OD = 63.05 mm, which implies 5.09 % discrepancy with the real value. Similarly, measurements were performed for a stainless steel pipe (OD = 42 mm, $h = 1\,\text{mm}$), and an outer diameter of OD = 42.83 mm was obtained, which means a discrepancy of 1.98 % with the real value.

Two sources of error were identified. First, it is assumed in equation (8.6) that the piezo-elements are in direct contact with the pipe wall. Since a commercial probe was used to perform the experiments, there is actually a lens between the piezo-elements and the pipe wall, which was not accounted for in equation (8.6). Thus, an effectively longer travel path, and therefore a larger pipe diameter, was obtained. Second, the array probe might have not been placed perfectly perpendicular to the pipe axis. If this was the case, the propagating Lamb wave modes could have traveled around the pipe wall with an angle different from 90° relative to the pipe axis, and the travel path of the wave modes might have been longer than the circumference of the pipe. Both errors can be minimized in the future with custom-made transducer arrays designs, such as the one proposed in [29], in which additional path lengths due to the acoustic stack are known and the Lamb waves may be steered to propagate perfectly perpendicular to the pipe axis.

8.5. Sound Speed of the Liquid

Once the mechanical properties (c_L and c_T) and geometry (h and OD) of the pipe have been characterized, the liquid inside the pipe can also be characterized by measuring its sound speed via pulse-echo measurements. Beam reflections from curved surfaces, such as pipe walls, can modify the waveform and the wave front [8]. To show this effect, a perpendicular cross-section of the measurement setup is considered. Figure 8.19 shows the proposed geometry, where a lead coupling piece is placed in between a 16-element transducer array and a liquid-filled stainless steel pipe.

Excitation of all transducer elements produces an initial plane wave that refracts into the pipe. After reflecting from the pipe bottom, the acoustic beam refocuses during propagation in the liquid, refracts back to the coupling piece, and finally impinges the transducer array as a plane wave.

Certainly, the recorded time signals would show all possible echoes: those from other interfaces, open ends, and also the Lamb waves traveling around the pipe wall. All these echoes impinge on the array at different angles. Nevertheless, due to the geometry, the echo containing information about the liquid would be the only one impinging completely perpendicular on the array surface. Therefore, in the f-k_x domain, it would show-up as an echo with nearly infinite phase speed (i.e. $k_x \cong 0\,\mathrm{rad/m}$), which could be filtered-out to obtain a cleaner and sharper echo, from which a transit time t_a could be finally determined. From this transit time, the sound speed of the liquid c_{liquid} is computed as:

$$c_{\mathrm{liquid}} = \frac{\mathrm{OD} - 2h}{\frac{t_a}{2} - \frac{h}{c_L} - \frac{h_{\mathrm{coup}}}{c_{L,\mathrm{coup}}}} \tag{8.11}$$

where $c_{L,\mathrm{coup}}$ represents the longitudinal bulk wave sound speed of the coupling piece, and h_{coup} its center thickness.

Wave propagation in fluids is assumed to be non-dispersive, therefore, no correction is required on the measured echo from the liquid to estimate the transit time t_a.

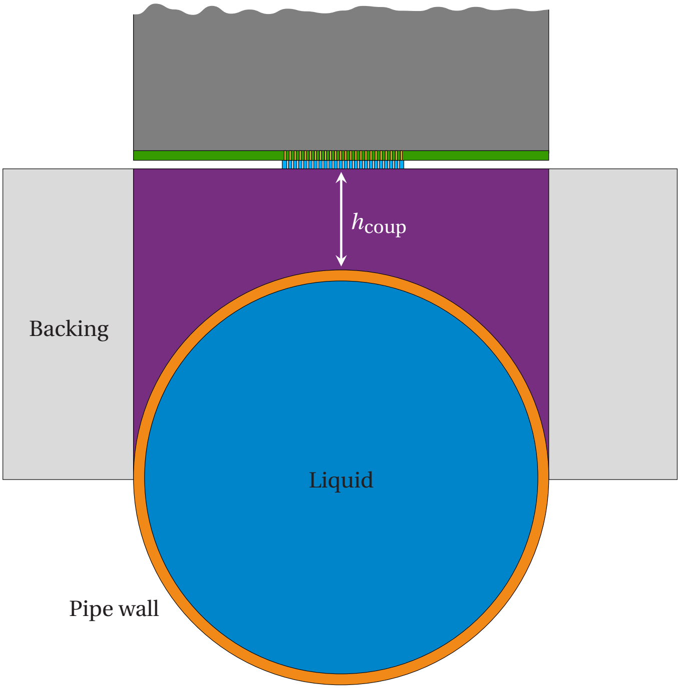

Figure 8.19: Geometry for measurement of the sound speed of the liquid. A 16-element transducer array is placed on top of a lead coupling piece ($c_L = 2200\,\mathrm{m/s}$, $h_{\mathrm{coup}} = 11\,\mathrm{mm}$) on top of a stainless steel pipe (OD = 42 mm, $h = 1\,\mathrm{mm}$). The acoustic stack of the array is based on the design described in [29].

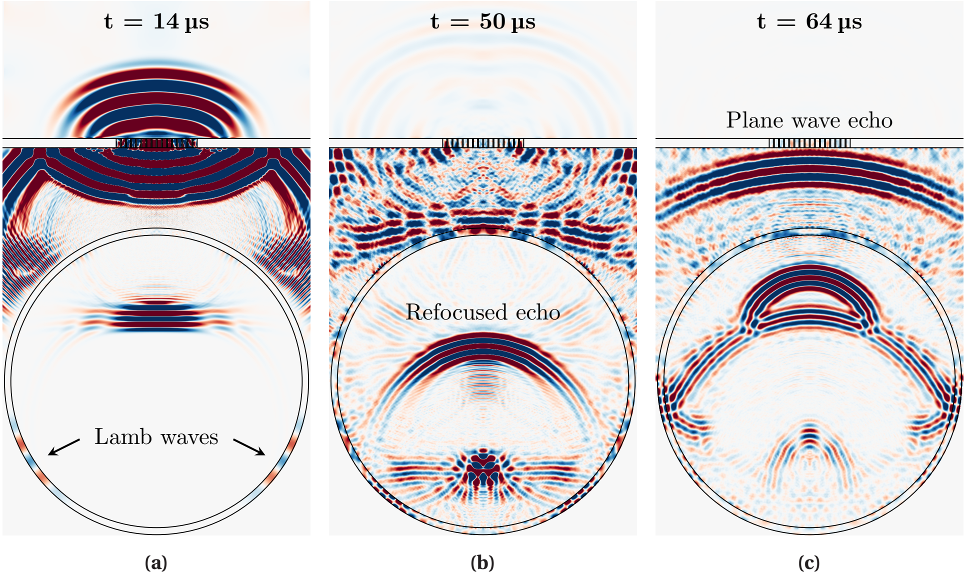

Figure 8.20: Snapshots of a Finite Element simulation of the waves occurring in the measurement of the sound speed of the liquid. The simulated setup contains the array geometry shown in Figure 8.19, including a heavy backing material around the coupling piece (not shown here). The pipe was filled with water. (a) At 14 µs, the acoustic wave is propagating downwards. (b) At 50 µs, the wave refocuses after reflecting from the bottom water-steel interface, and propagates upwards. (c) At 64 µs, the wave is about to arrive within the aperture of the array as a plane wave, as expected.

8.5.1. Simulations

A Finite Element simulation of the waves occurring in the geometry shown in Figure 8.19 was performed using PZFlex. The setup involved a water-filled stainless steel pipe (OD = 42 mm, h = 1 mm) and a lead coupling piece (c_L = 2200 m/s, h_{coup} = 11 mm). The transducer array elements were excited with a 1-cycle sine wave with a center frequency of 1 MHz, and the received voltage of each transducer element was recorded up to 80 µs. To suppress reflections from the open ends of the coupling piece, an attenuating material is placed around it. In simulations, a 20 mm-thick heavy backing (acoustic impedance Z = 20 MRayl and attenuation coefficient α = 20 dB/MHz·cm) was placed around the lead coupling piece. Furthermore, to achieve a real-case scenario, free boundary conditions were implemented at the edges of the simulation geometry. Time snapshots are shown in Figure 8.20, where refraction into the pipe wall, as well as refocusing of the acoustic beam after echoing from the bottom of the pipe wall are observed.

The simulated receive voltages from the transducer elements are shown in Figure 8.21a, from which it is possible to recognize the characteristic plane wave feature of the water

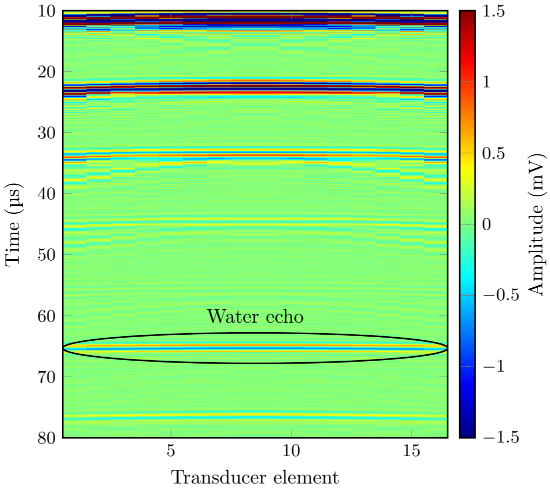

(a)

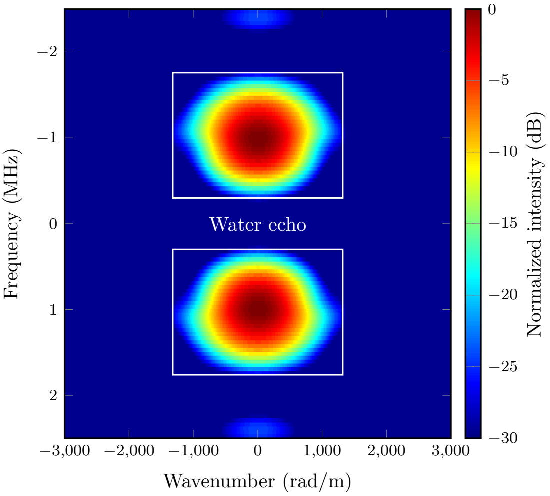

(b)

Figure 8.21: (a) Simulated receive voltages from the 16-element transducer array shown in Figure 8.19. The black ellipse encloses the plane wave water echo. (b) Magnitude of a 2D FFT applied to the tapered data in the time window highlighted in (a). The white rectangles show the band-pass filter applied on the data to dismiss remnant information and achieve a sharper water echo.

echo, arriving at approximately 63 µs. Moreover, it is possible to observe that all the other recorded echoes have a curved shape, which means they arrived at the transducer array under varying angles. The average receive voltage is shown by the orange curve of Figure 8.22, and shows a longer duration than the length of the 1-cycle excitation pulse due to the reverberations of the signal in the pipe wall. This means that a cross-correlation operation between these two signals would not be suitable to estimate the transit time of the water echo, because the peak value of the cross-correlation would be located somewhere along the length of the pulse, and not at its actual start. Therefore, a zero-crossings tracking algorithm would be more suitable to detect the transit time of the echo from the liquid.

However, detecting the first zero-crossing associated to the start of the acoustic signal may be a bit subjective due to the bandwidth-limited nature of the system, as also suggested by the orange curve in Figure 8.22. Moreover, other wave modes may overlap in time with the desired echo from the liquid. Furthermore, equation (8.11) is very sensitive to the transit time being used. Therefore, it would be very useful to apply some filtering to obtain a final signal with a sharper start of the echo and from which to determine the transit time more accurately.

To achieve this, we took the data between 60 µs and 70 µs in Figure 8.21a, tapered this data in both time and space domain using a Hamming window, and applied a 2D FFT. The result is shown in Figure 8.21b, in which the main lobe centered around $k = 0\,\mathrm{rad/m}$ and $f = 1\,\mathrm{MHz}$ corresponds to the plane wave water echo. Within a practical dynamic range of 30 dB, no significant side lobes were present, implying that the implemented tapering is sufficient. By filtering out all the information outside the white rectangles in Figure 8.21b and applying an Inverse Fast Fourier Transform (IFFT), filtered time domain signals were obtained. These were ultimately averaged to achieve an echo with a sharper start (blue curved in Figure 8.22), from which the transit time can be determined more accurately than from the unfiltered version.

An objective method to identify the transit time of the filtered (but still bandwidth-limited) echo may be to scan the time signal from smaller to higher transit times, detect the first amplitude point higher than the noise level, and identify its nearest zero-crossing. The transit time associated to this zero-crossing point may finally be regarded as the transit time of the echo. From the filtered water echo shown in Figure 8.22, a transit time of 63.99 µs was obtained, which according to equation (8.11) resulted in a sound speed of the liquid of $c_{\mathrm{liquid}} = 1491.3\,\mathrm{m/s}$. This value has a discrepancy of 0.31 % with the simulated sound speed value of 1496 m/s for water.

For measurement of the sound speed of the liquid, it is very important to align the transducer array perfectly perpendicular to the pipe axis. Otherwise, the liquid-related echo might also be recorded under an angle relative to the array surface, and it will be more difficult to differentiate it from all the other echoes. At the moment of writing, the transducer array for ultrasonic clamp-on flow metering proposed in [29] is being

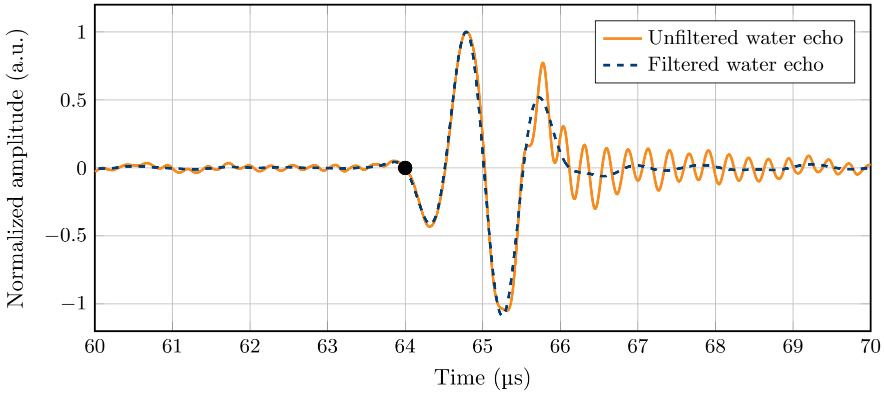

Figure 8.22: Simulated average and normalized water echo voltages, before and after filtering of the echoes impinging under an angle onto the transducer array surface. After filtering, a smoother echo is observed. The black dot located at 63.99 µs represents the zero-crossing point that marks the transit time of the filtered water echo signal.

fabricated. Furthermore, the use of commercial transducer array probes would make the measurement sub-optimal. Due to the same error source described in Section 8.4, the acoustic stack inside commercial probes is unknown, which does not allow to account for possible extra path lengths of the acoustic beam inside the probe before reaching the transducer elements. Therefore, is not yet possible to experimentally implement this measurement procedure.

8.6. Discussion

The results obtained from simulated data show that the proposed fitting approach is capable of retrieving simultaneously the bulk wave sound speeds (c_L, c_T) and thickness (h) of the pipe wall from a single measurement, without the need for initial guess values. The time required to compare the simulated data to a database of $\approx 10^5$ curves was approximately 70 s, showing great promise for in-situ implementation. Furthermore, the accuracy of this method appeared to be determined by the resolution of the database, implying that the computational cost can be tailored to the accuracy requirements of specific applications. Preliminary results on a steel and an aluminium pipe confirmed experimentally the validity of the approach proposed here. By comparing the retrieved material properties with the nominal values of the samples, it was found that the accuracy of the obtained values was lower in experiments than in simulations, especially for the longitudinal bulk wave sound speed. This discrepancy could be imputed, in part, to experimental limitations (e.g. spatial and temporal resolution) that affect measured data. However, as would appear from Figure 8.8, the A_0 and S_0 wave modes are less sensitive to variations of c_L than to variations in c_T and h, potentially impacting the efficacy of the fitting procedure. Moreover, it turned out that the accuracy of the curve-fitting approach increases proportionally to the amount of data points from the wave modes (i.e. f-k_x points) that are available. This means that, to optimize accuracy in practice, it is best to excite the pipe wall with the most broadband signal (i.e. time pulse) possible.

On the other hand, the dispersion effect of Lamb wave modes plays a detrimental role in estimating the outer diameter of the pipe (OD), especially if the wave mode is highly dispersive within the operational frequency range of the transducers, which would complicate its isolation from other potential wave modes by e.g. time-windowing. For this reason, two approaches are recommended to estimate OD: to excite, within the bandwidth of the transducers, a wave mode with a relatively low dispersive behavior or, if this is not possible, to excite the pipe wall with a relatively narrow-band pulse and thereby limit the excitation of many of the highly dispersive frequency components. Another method that might improve the estimation of the pipe diameter would be to cross-correlate consecutive round-trip arrivals of the same wave mode, like those of the L$(0,3)$ wave mode shown in Figure 8.17. Certainly, each arrival of the wave mode needs to be corrected for dispersion before cross-correlating them. As a consequence of exciting just one transducer array element in the experimental setup of Figure 8.16, an acoustic beam with a wide opening angle was generated, which generated all possible Lamb wave modes in the pipe wall and maximized the interference between them, as seen in Figure 8.17. Therefore, the measurement setup of Figure 8.16 may not always guarantee the possibility to isolate a particular wave mode, as needed by our proposed method. However, in a practical flow meter with matrix transducers, a coupling piece will be placed between the transducer array and the pipe wall, such as the one shown in Figure 8.19. In that case, multiple transducer array elements may be used to generate a narrow beam that would impinge the pipe wall under a certain angle, resulting in the generation of only one guided wave mode. Furthermore, with a known dispersion behavior of the guided waves, as determined by the pipe wall thickness and bulk wave sound speeds, wave mode generation could be even more selective by choosing a suitable combination of excitation frequency, pulse length, and beam steering angle.

The matrix arrays can also be used to monitor the quality of their alignment relative to the pipe axis. During sensor alignment, pulse-echo measurements, like those shown in Figure 8.21a, can be performed and monitored in real-time. Misalignment of the matrix array(s) would reflect an asymmetric pattern of the f-k_x plots because the echo from the liquid would impinge on the transducer array under an angle relative to the normal of the aperture.

The implementation of our proposed techniques is performed, by a significant amount, in the Fourier domain. This means that the size of the transducer array aperture (given by the pitch times the amount of elements) influences the accuracy of the results by setting a limit on the resolution of the f-k_x representations and spectrograms, and therefore on the ease with which the different dispersion curves are identified and extracted. Moreover, the pitch of the array should be small enough to spatially sample all expected guided waves. The required pitch depends on the involved wavelengths, which in turn depend on the bulk wave sound speeds of the applied metals and the maximum frequency of the employed signals. The 0.3 mm pitch of the P4-1 probe was enough for proper spatial sampling of the expected wavelengths. Furthermore, the transducer array should remain sufficiently sensitive at lower frequencies , since here the dispersion curves show more sensitivity to the pipe parameters. Based on this point, the 1 MHz lower cutoff frequency of the P4-1 probe may have not been optimal to achieve the most accurate results. However, the goal of this chapter was to prove the feasibility of our proposed techniques. The design of an optimal transducer array for this application is a topic of current research.

8.7. Conclusions

In this chapter, we have presented procedures for the measurement of parameters that will enable auto-calibration of ultrasonic clamp-on flow meters based on a pair of matrix transducer arrays. With such arrays, pipe properties like wall thickness, bulk wave sound speeds, diameter, and the sound speed of the liquid can be extracted from simulated and measured data. In contrast to a manual calibration approach, the procedures proposed here would reduce calibration time and also produce more repeatable results. Furthermore, these procedures may also be implemented regularly, which in combination with beam steering capabilities of transducer arrays, would allow the flow sensor to be properly calibrated at different pressure and temperature conditions throughout its lifetime. In this way, calibration of ultrasonic clamp-on flow meters by manual displacement of the sensors could be rendered unnecessary.

References

[1] J. Massaad, P. L. van Neer, D. M. van Willigen *et al.*, “Measurement of pipe and fluid properties with a matrix array-based ultrasonic clamp-on flow meter,” *IEEE Transactions on Ultrasonics, Ferroelectrics, and Frequency Control*, vol. 69, no. 1, pp. 309–322, 2021.

[2] R. C. Baker, *Flow measurement handbook: industrial designs, operating principles, performance, and applications.* Cambridge University Press, 2005.

[3] D. V. Mahadeva, R. C. Baker, and J. Woodhouse, “Further studies of the accuracy of clamp-on transit-time ultrasonic flowmeters for liquids,” *IEEE Trans. Instrum. Meas.*, vol. 58, no. 5, pp. 1602–1609, 2009.

[4] I. Viktorov, *Rayleigh and Lamb Waves: Physical Theory and Applications.* Plenum, New York, 1967.

[5] G. Farnell, “Properties of elastic surface waves,” *Physical Acoustics*, vol. 6, pp. 109–166, 1970.

[6] P. Chadwick and G. D. Smith, “Foundations of the theory of surface waves in anisotropic elastic materials,” in *Advances in Applied Mechanics.* Elsevier, 1977, vol. 17, pp. 303–376.

[7] H. F. Pollard, *Sound waves in solids.* Pion, 1977.

[8] J. L. Rose, *Ultrasonic guided waves in solid media.* Cambridge University Press, 2014.

[9] H. Überall and H. Huang, “Acoustical response of submerged elastic structures obtained through integral transforms,” in *Physical Acoustics.* Elsevier, 1976, vol. 12, pp. 217–275.

[10] L. Flax, L. Dragonette, and H. Überall, “Theory of elastic resonance excitation by sound scattering,” *The Journal of the Acoustical Society of America*, vol. 63, no. 3, pp. 723–731, 1978.

[11] G. Gaunaurd and A. Akay, “Isolation of the spectrograms and rosettes of insonified sets of submerged, concentric, thin shells,” *J. Vib. Acoust.*, vol. 116, no. 4, pp. 573–577, 1994.

[12] M. Fatemi and J. F. Greenleaf, “Application of radiation force in noncontact measurement of the elastic parameters,” *Ultrasonic Imaging*, vol. 21, no. 2, pp. 147–154, 1999.

[13] F. G. Mitri, P. Trompette, and J.-Y. Chapelon, “Detection of object resonances by vibro-acoustography and numerical vibrational mode identification,” *The Journal of the Acoustical Society of America*, vol. 114, no. 5, pp. 2648–2653, 2003.

[14] K. Heller, L. Jacobs, and J. Qu, “Characterization of adhesive bond properties using Lamb waves,” *NDT &E INT*, vol. 33, no. 8, pp. 555–563, 2000.

[15] K. Lee and S. W. Yoon, “Feasibility of bone assessment with leaky Lamb waves in bone phantoms and a bovine tibia,” *J. Acoust. Soc. Am.*, vol. 115, no. 6, pp. 3210–3217, 2004.

[16] K.-C. T. Nguyen, L. H. Le, T. N. Tran *et al.*, “Excitation of ultrasonic Lamb waves using a phased array system with two array probes: Phantom and in vitro bone studies,” *Ultrasonics*, vol. 54, no. 5, pp. 1178–1185, 2014.

[17] Y.-C. Lee and S.-W. Cheng, “Measuring Lamb wave dispersion curves of a bi-layered plate and its application on material characterization of coating,” *IEEE Trans. Ultrason. Ferroelectr. Freq. Control*, vol. 48, no. 3, pp. 830–837, 2001.

[18] M. Bernal, I. Nenadic, M. W. Urban *et al.*, “Material property estimation for tubes and arteries using ultrasound radiation force and analysis of propagating modes,” *J. Acoust. Soc. Am.*, vol. 129, no. 3, pp. 1344–1354, 2011.

[19] J. Foiret, J.-G. Minonzio, C. Chappard *et al.*, “Combined estimation of thickness and velocities using ultrasound guided waves: A pioneering study on in vitro cortical bone samples,” *IEEE Trans. Ultrason. Ferroelectr. Freq. Control*, vol. 61, no. 9, pp. 1478–1488, 2014.

[20] V. K. Chillara, B. T. Sturtevant, C. Pantea *et al.*, “Ultrasonic sensing for noninvasive characterization of oil-water-gas flow in a pipe,” in *AIP Conference Proceedings*, vol. 1806, no. 1. AIP Publishing LLC, 2017, p. 090014.

[21] V. K. Chillara, B. Sturtevant, C. Pantea *et al.*, “A physics-based signal processing approach for noninvasive ultrasonic characterization of multiphase oil-water-gas flows in a pipe,” *IEEE Transactions on Ultrasonics, Ferroelectrics, and Frequency Control*, 2020.

[22] J. Greenhall, C. Hakoda, E. Davis *et al.*, “Noninvasive acoustic measurements in cylindrical shell containers,” *IEEE Transactions on Ultrasonics, Ferroelectrics, and Frequency Control*, 2021.

[23] D. C. Gazis, “Three-dimensional investigation of the propagation of waves in hollow circular cylinders. I. Analytical foundation,” *J. Acoust. Soc. Am.*, vol. 31, no. 5, pp. 568–573, 1959.

[24] D. C. Gazis, “Three-dimensional investigation of the propagation of waves in hollow circular cylinders. II. Numerical results,” *J. Acoust. Soc. Am.*, vol. 31, no. 5, pp. 573–578, 1959.

[25] A. Velichko and P. D. Wilcox, “Excitation and scattering of guided waves: Relationships between solutions for plates and pipes,” *J. Acoust. Soc. Am.*, vol. 125, no. 6, pp. 3623–3631, 2009.

[26] P. Moore, G. Workman, and D. Kishoni, *Nondestructive Testing Handbook, vol. 7: Ultrasonic Testing*. The American Society of Nondestructive Testing, 1991.

[27] R. Sicard, J. Goyette, and D. Zellouf, “A numerical dispersion compensation technique for time recompression of Lamb wave signals,” *Ultrasonics*, vol. 40, no. 1-8, pp. 727–732, 2002.

[28] P. L. van Neer, B. Quesson, M. van Es *et al.*, “Optimization of acoustic coupling for bottom actuated scattering based subsurface scanning probe microscopy,” *Rev. Sci. Instrum.*, vol. 90, no. 7, p. 073705, 2019.

[29] J. Massaad, D. van Willigen, P. van Neer *et al.*, “Acoustic design of a transducer array for ultrasonic clamp-on flow metering,” in *IEEE International Ultrasonics Symposium (IUS)*. IEEE, 2019, pp. 1133–1136.

9

Measuring Velocity Profiles with Matrix Transducers

Clamp-on flow meters are commonly designed to use a single acoustic path to perform flow measurements. As a result only mean flow can be measured. By using clamp-on matrix transducers, the possibility to steer the beam is created, allowing multiple acoustic paths to be used. This chapter investigates whether the multiple paths from a single pair of transducer arrays can be used to reconstruct a flow velocity profile. This is of interest, because it can increase measurement accuracy and be used to compensate for laminar-to-turbulent flow transitions. Profile measurement with clamp-on flow meters is not trivial, because the transducers are located on the same side of the pipe and have a relatively small aperture. Moreover, only a limited set of acoustic paths can be used, due to the refraction at the steel-water interface.

With a ray-tracing simulation the transit times of the acoustic paths are calculated in order to window the correct peaks in the received signal. Simulations of the transit-time differences based on six acoustic paths were used to fit the power law for laminar and turbulent flow, with an added jitter of 0.1 ns. The simulations indicate that it is possible to estimate the velocity profile based on measurement data. For accurate estimation a significant SNR of the measurement data is quired, with standard deviations below 0.1 ns. Moreover, profile estimation benefits from large steering angles in the circumferential direction, which can be achieved with matrix transducers.

Parts of this chapter are in preparation for submission to the IEEE Transactions on Ultrasonics, Ferroelectrics, and Frequency Control.

9.1. Introduction

Ultrasonic flow meters are attractive for several reasons: they have no moving parts and can be used in a wide range of applications. A special type of flow meter that is gaining popularity is the clamp-on ultrasonic flow meter, because it offers several benefits compared to in-line flow meters. Placement does not require interruption of the flow and no holes are required in the pipe wall, resulting in safer operating conditions. A disadvantage of clamp-on flow meters is that they cannot easily be used to record information about the flow profile. Measuring the velocity profile is valuable because it can be used to determine the true flow rate and to compensate for laminar to turbulent flow transitions, increasing accuracy of the flow measurement.

With in-line transducers, several configurations have been used to measure velocity profiles based on multi-path measurements. Multiple, strategically placed pairs of transducers have been used to reconstruct the velocity profiles based on a limited number of paths [1–4]. A drawback of these methods is that the transducers pierce the pipe wall and the flow meter cannot be installed in operational pipe lines, as is the case with clamp-on flow meters. In an alternative approach, where the pipe wall remains in tact, a tomographic flow meter has been used to measure liquid rheology [5]. This however requires a complex setup that is not easily installed on a pipe in an operational setup.

Array transducers have also been used in flow meters, but in contact with the liquid or gas. In gas flow metering, for example, arrays have been used to compensate for beam sweeping [6]. Mean flow measurements have also successfully been shown with a single clamp-on phased array [7].

In this work we investigate the feasibility of using clamp-on array transducers to perform multi-path measurements. With the extra flow information obtained via additional acoustic paths we aim to estimate the flow velocity profile. With the estimated velocity profile, flow measurements can potentially be corrected for different flow regimes.

This chapter is structured as follows. First we will discuss the method used to calculate the acoustic paths, followed by a discussion of the physical limits that a clamp-on flow meter faces. In Section 9.4 simulations are presented to test the proposed approach. Finally, the practical limitations and alternative methods are then discussed, followed by conclusions.

9.2. Methods

Ultrasonic flow measurement is based on the principle that acoustic waves travel faster with the flow than they travel against the flow. This slight difference in speed results in a transit-time difference between the upstream and downstream signals. The transit-time difference is proportional to the flow velocity (v) of the fluid in the pipe [8]:

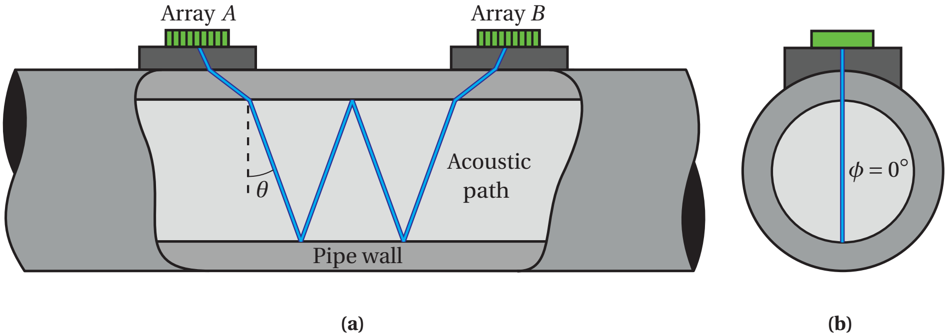

Figure 9.1: Diagram of an array-based clamp-on flow meter and an example of an acoustic path. The side-view (a) and cross-sectional view (b) are shown.

$$\Delta t = \frac{L}{c - v \cdot \sin(\theta)} - \frac{L}{c + v \cdot \sin(\theta)} \approx \frac{2v \cdot L \cdot \sin(\theta)}{c^2}, \tag{9.1}$$

where L is the path length, θ the angle of the acoustic beam in the liquid and c the speed of sound in the liquid. The approximation is valid for low flow speeds ($v \ll c$).

In clamp-on flow meters, the acoustic wave generated by the transducer travels through a coupling piece and the pipe-wall, before refracting into the liquid. Only the part of the path in the liquid contains information about the flow. Figure 9.1 shows a diagram of the clamp-on flow meter used in this work. Two arrays are placed on flat wedges and steer the beam in order to hit the other array with a defined path. An example of an acoustic path with 4 path sections is shown.

In clamp-on flow meters, the acoustic path usually stays within a fixed plane parallel to the pipe axis. Because those paths all intersect the center of the pipe, they will all have the same integral of the velocity profile. To calculate the velocity profile, acoustic paths have to be chosen that take a 3-dimensional path through the fluid. This is the case when the radial angle of the path $\phi \neq 0°$.

9.2.1. Flow Distribution

In circular pipes and far enough from bends or other disturbances, the flow velocity profile can be assumed to be symmetrical around the pipe axis. In such cases, and for Newtonian liquids, the velocity at a radial distance r from the pipe axis can be approximated by the power law [9]:

$$v(r) = v_{\max} \left(\tfrac{r}{R} \left(2 - \tfrac{r}{R}\right)\right)^{1/n} \tag{9.2}$$

where $v_{\max}$ is the peak velocity of the profile, R is the pipe radius, and n is a value ≥ 1 dependent on the flow regime.

9.2.2. Integrating Flow Velocity

In order to calculate the change in transit-time caused by the flow in a cylindrical pipe, the flow velocity has to be integrated across the acoustic path. A line integral can be used to calculate the transit-time difference for each path [4, 10]. Note that the acoustic path can be divided into an integer number of line segments that have, due to the symmetry of the flow profile, identical transit times. The overall transit-time can therefore be calculated from the transit-time associated with one line segment C. A diagram showing such a line segment C in a cross-sectional projection is shown in Figure 9.2.

The line C can be described by in terms of a parameter k:

$$C = \begin{cases} x = x_0 + p \cdot k \\ y = y_0 + q \cdot k \end{cases} \tag{9.3}$$

By taking the center of the pipe as origin and substituting radius R, the line segment becomes:

$$C = \begin{cases} x = 2R\sin(\phi)\cos(\phi) \cdot k \\ y = R - 2R\cos^2(\phi) \cdot k \end{cases} \tag{9.4}$$

within the range $0 \leq k \leq 1$.

The transit time can be found by integrating the flow velocity obtained from the power law (9.2) across this line segment:

$$\int_C v(x,y)\,ds \tag{9.5}$$

Since the transit-time difference is only influenced by the flow, only the vector component of the acoustic path which is in parallel with the flow should be considered. A side-view projection of the pipe is shown in the diagram of figure 9.3, where L_z is the component of the acoustic path which is parallel to the flow. This vector component can be defined by

$$v \cdot L_z = \int_C v(x,y)\,ds \cdot \cos(\phi) \cdot \tan(\theta) \tag{9.6}$$

Substitution of (9.5) and (9.6) in (9.1) leads to an overall transit time of:

$$\Delta t = \int_C v(x,y)\,ds \left(\frac{2b \cdot \cos(\phi) \cdot \tan(\theta)}{c^2} \right), \tag{9.7}$$

where b is the number of path sections inside the pipe.

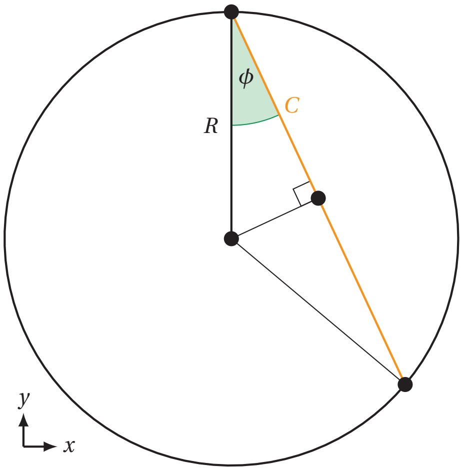

Figure 9.2: Calculation of acoustic path line integral (cross-sectional projection).

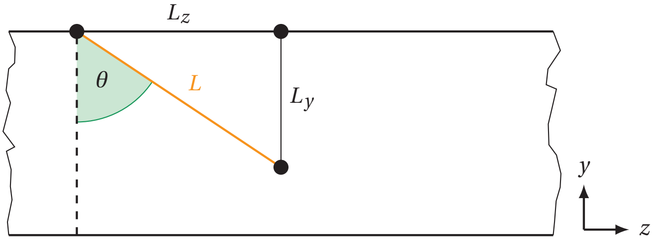

Figure 9.3: Calculation of acoustic path line integral (side projection).

9.2.3. Inversion

A measurement results in a set of transit-time differences corresponding to several acoustic paths. Based on those differences the parameters of a velocity profile (v_{max} and n) have to found. This inversion step is performed using the nonlinear least-squares solver of MATLAB (lsqnonlin). With the solver the parameters are found that minimize the difference between the calculated transit-times and measured transit-times of k acoustic paths:

Table 9.1: A selection of v-shaped acoustic paths ($\phi = 0$).

θ_{tx} (deg.)	Sections	Transit-time (µs)
17.4	8	230
14.5	10	285
12.5	12	340
10.6	14	390
9.4	16	450

$$f(n, v_{\max}) = \begin{cases} f_1(n, v_{\max}) = \Delta t(b_1, \phi_1, \theta_1) - \Delta t_{1,\text{meas}} \\ f_2(n, v_{\max}) = \Delta t(b_2, \phi_2, \theta_2) - \Delta t_{2,\text{meas}} \\ \vdots \\ f_k(n, v_{\max}) = \Delta t(b_k, \phi_k, \theta_k) - \Delta t_{k,\text{meas}} \end{cases}, \tag{9.8}$$

where Δt is calculated with equation (9.7).

9.3. Physical Limits

The possible range of beam steering angles in the fluid is determined by waves that refract into the liquid. For large angles the acoustic beam will completely reflect inside the pipe wall, not producing any signal that refracts into the liquid. This critical angle ϕ_{crit} is defined as:

$$\frac{\sin(\phi_{\text{crit}})}{c_l} = \frac{\sin(90^\circ)}{c_p} \tag{9.9}$$

where c_l is the speed of sound in the liquid and c_p is the shear wave speed of sound in the pipe wall.

The setup used in this work consists of a stainless steel pipe section ($c_p = 3160\,\text{m/s}$) filled with water ($c_l = 1500\,\text{m/s}$), resulting in a critical angle of $\phi = 28.7^\circ$. Acoustic paths only exist when they have a smaller angle in the liquid. Note that this holds for the compound angle of ϕ and θ.

Acoustic paths for which $\phi = 0^\circ$ stay within a fixed plane parallel to the pipe axis. Several of these v-shaped paths can be defined, as listed in Table 9.1. To determine the velocity profile, additional paths are required with different values of ϕ. Acoustic paths with a $\phi \neq 0^\circ$ (star-shaped paths) are shown in Table 9.2.

Figure 9.4 shows one of the star-shaped acoustic paths, consisting of 15 line-sections. In the cross-sectional view (9.4a), the star shape is clearly visible. Note the symmetry of the

Table 9.2: Star-shaped acoustic paths in multi-path measurement.

ϕ_{water} (deg.)	θ_{water} (deg.)	Sections	Transit-time (μs)
6.2	7.4	15	417
7.3	8.4	13	363
8.7	9.9	11	310
10.7	11.9	9	256
13.5	8.1	14	383
14.1	14.9	7	202
15.8	9.4	12	328
18.8	7.8	15	399
19.3	11.2	10	272
20.8	18.4	5	146
21.9	9.0	13	342
23.6	7.5	16	412
24.8	14.1	8	216
26.4	10.8	11	285
27.4	8.7	14	360

acoustic path about the dashed line. When a 1D transducer array is used, two acoustic paths happen simultaneously. One starting towards the right, and one starting towards the left hand side. These waves arrive at the same time, assuming the pipe is perfectly cylindrical. When viewed from the side (9.4b), the 15 equal-length sections of the paths can be distinguished.

Ideally a matrix transducer is used, because it can steer the acoustic beam in both axial (θ) and radial (ϕ) direction. In this work, a 36-element phased array has been used with a relatively large aperture, causing a narrow opening angle of the beam. This limits the amount of star-shaped acoustic paths that arrive at the receiver with sufficient amplitude. The paths in Table 9.2 with a $\phi \geq 14^\circ$ have therefore not been considered. With an optimally sized transducer those paths could be used as well to further increase the accuracy of the estimated velocity profile.

9.4. Simulation Results

Simulations were performed in MATLAB, assuming a point source as transmitter and a 36-element linear array as receiver. A stainless steel pipe with a diameter of 40 mm and thickness of 1 mm was assumed.

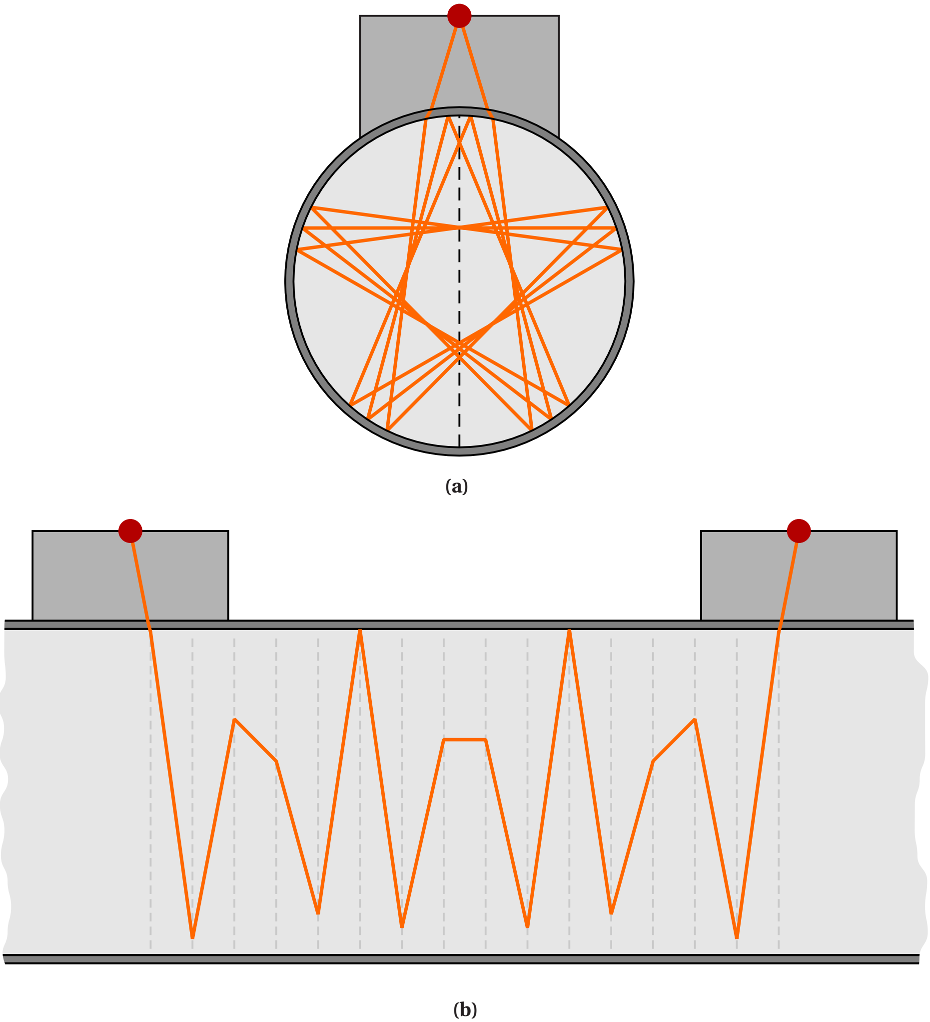

Figure 9.4: Cross-sectional projection (a) and side view projection (b) of a 15-section star-shaped acoustic path, reflecting 14 times inside the pipe.

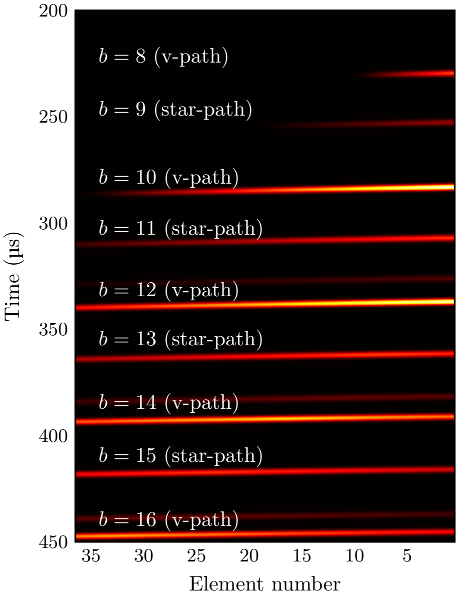

Figure 9.5: Ray tracing simulation of transient waveforms of a 36-element linear array, for a 40 mm diameter pipe. Element 1 is located closest to the transmitter.

9.4.1. Ray Tracing

A ray-tracing simulation was performed to find the acoustic paths that hit the receiver. A simulation with a transmit angle of 12.75° (8.8° in water) is shown in Figure 9.5. Note that the acoustic signal arrives at the receiver via several different acoustic paths. Although the transmit angle is optimal for the 12-section path ($b = 12$), the beam-width and receive aperture are wide enough such that the acoustic beam also reaches the receiver via other paths. The ray tracing simulation can be used to determine which path corresponds to which arriving wavefront, as denoted in Figure 9.5. The amplitudes of the various wavefronts differ because of the finite beam width, as a result of which star-shaped paths have a lower amplitude. Moreover, with some paths the beam only partially reaches the receive array, resulting in a signal only on some of the elements. This is the case for the paths where $b \leq 10$.

9.4.2. Flow Measurement

Flow measurements were simulated, both at laminar ($n = 1$) and at turbulent flow ($n = 7$) with a v_{max} of 0.8 m/s, by using the power law of Equation (9.2). A jitter with a standard deviation of 0.1 ns was added to the calculated transit-time differences. The velocity profile was then estimated based on the simulated transit-time differences of a limited set of acoustic paths. The acoustic paths used for the simulation were based on the assumption that a linear array transducer is used. The relatively narrow opening angle allows paths with a $\phi < 12°$. As a result, a realistic measurement would consist of 4 star-paths and as many v-paths as allowed by the attenuation of the liquid. In this case 2 different v-paths were used. The simulation was repeated 10 times to get an indication of the accuracy of the flow profile estimation. The estimated laminar and turbulent flow profiles are shown in Figures 9.6 and 9.7 respectively.

The laminar profile was estimated with an average v_{max} of 0.80 m/s with a standard deviation of 0.021 m/s. The average n computed with the simulated data was 1.0 with a standard deviation of 0.089.

The estimated profile of the turbulent flow had a significantly larger variation, though each measurement had clearly a distribution expected for turbulent flow with an average v_{max} of 0.80 m/s and std(v_{max}) of 0.03 m/s. The exponent resulted in a mean n of 9.2 (although the profile input was $n = 7.0$) with a standard deviation of 5.5.

9.5. Discussion

The simulations presented in this chapter indicate the possibility to measure velocity profiles with a matrix-based flow meter. An important next step is to validate the simulations with measurements in a flow loop.

The results indicate that a laminar flow profile can be estimated well, but turbulent profiles are significantly harder to fit to the power law. This is due to the turbulent profile being almost flat around the center of the pipe and the relatively small angle of the star-shaped acoustic paths used in the simulations. The simulations were based on the assumption that a linear array transducer is used. When a matrix transducer would be used, star-paths with higher steering angles can be used, significantly improving the profile estimation accuracy of turbulent profiles.

The simulations presented in this Chapter show that, even when steering the acoustic beam in a particular direction, acoustic waves reach the receiver via multiple acoustic paths. This implies that a single element transducer with a wide-enough opening angle could also be used to measure flow via multiple acoustic paths. However, spurious waves in the pipe wall will make it very difficult to distinguish the arrival of the acoustic wavefronts, complicating accurate determination of the transit time. Array transducers enable the possibility to use beamforming techniques on the received signals to reduce the amplitude of spurious waves to a large extent, allowing accurate cross-correlation of the upstream and downstream signal. Moreover, array transducers can also help to reduce the excitation of spurious waves in transmission [12], and a narrower transmit-beam results in better separation between acoustic paths with similar arrival times.

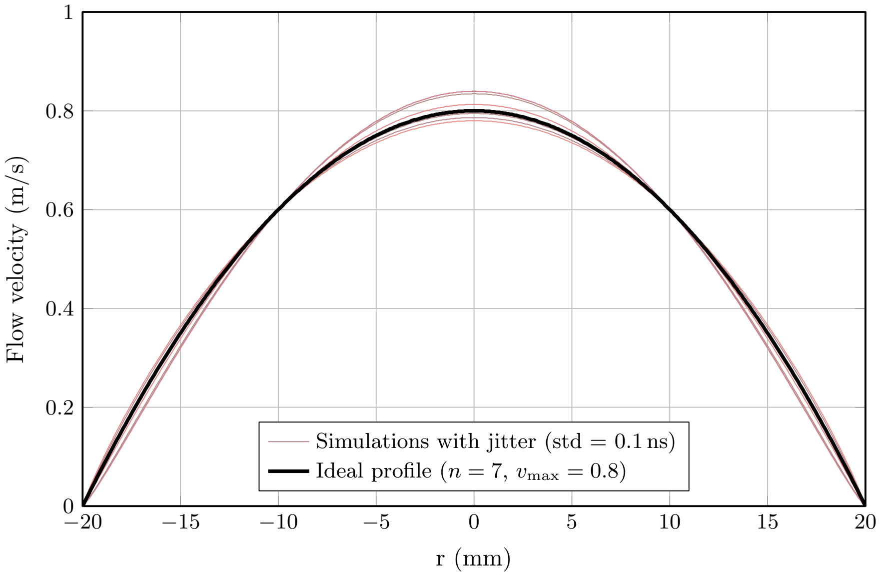

Figure 9.6: Estimation of velocity profiles with simulated data for 10 flow measurements with a jitter of 0.1 ns and laminar flow with $v_{\max} = 0.8\,\mathrm{m/s}$.

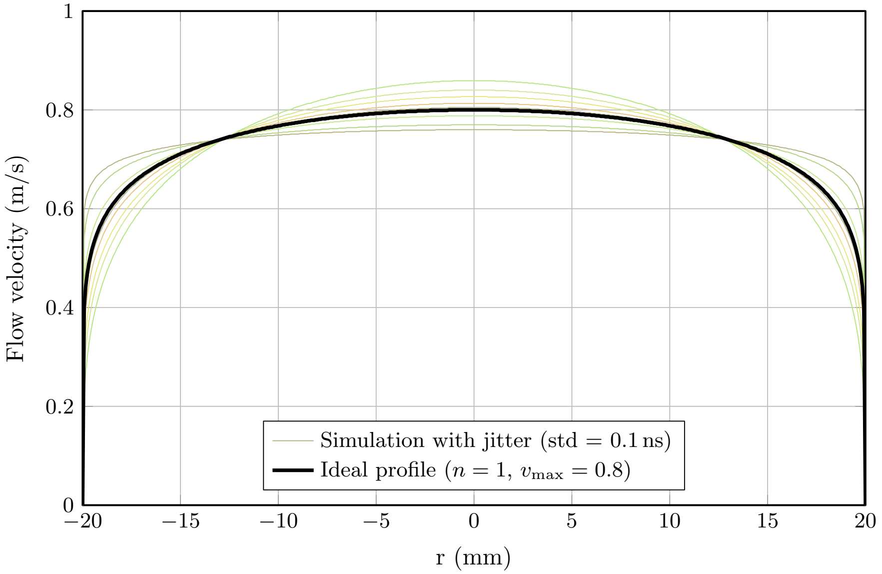

Figure 9.7: Estimation of velocity profiles with simulated data for 10 flow measurements with a jitter of 0.1 ns and turbulent flow with $v_{\max} = 0.8\,\mathrm{m/s}$.

Alternative placement, with the arrays not in an axi-symmetric configuration could be interesting for exploring non-symmetric flow distributions, such as those found behind a bend in a pipe [13].

9.6. Conclusions

Simulation results presented in this chapter indicate that it is feasible to extract information about the velocity profile using clamp-on flow meters based on matrix transducers. The accuracy of the estimated profile depends on the chosen acoustic paths and benefits from the larger steering angles enabled by matrix transducers.

The set of possible acoustic paths can accurately be determined by means of ray tracing. With the simulated transit times of 6 acoustic paths the velocity profiles were estimated. By using more acoustic paths the accuracy of the algorithm can be further improved.

The methods shown in this work open the path towards measuring velocity profiles with clamp-on ultrasonic flow meters.

References

[1] P. I. Moore, G. J. Brown, and B. P. Stimpson, “Ultrasonic transit-time flowmeters modelled with theoretical velocity profiles: methodology,” *Measurement Science and Technology*, vol. 11, no. 12, p. 1802, 2000.

[2] S. Tereshchenko and M. Rychagov, “Acoustical multipath flow measurements based on quadrature integration methods,” *Acoustical Physics*, vol. 50, no. 1, pp. 100–106, 2004.

[3] D. Kurniadi, “Transit time multipath ultrasonic flowmeter: An issue on acoustic path arrangement,” in *Applied Mechanics and Materials*, vol. 771. Trans Tech Publ, 2015, pp. 3–8.

[4] L. Qin, L. Hu, K. Mao *et al.*, “Flowrate determination for arbitrary multipath arrangement based on generalized inverse of matrix,” *IEEE Sensors Journal*, vol. 17, no. 12, pp. 3625–3634, 2017.

[5] P. L. M. J. van Neer, U. Stelwagen, L. F. G. Geers *et al.*, “Development of a non-intrusive in-line tomographic ultrasonic velocity meter to measure liquid rheology,” in *IEEE International Ultrasonics Symposium (IUS)*. IEEE, 2018, pp. 1–4.

[6] C. Haugwitz, C. Hartmann, G. Allevato *et al.*, “Multipath flow metering of high-velocity gas using ultrasonic phased-arrays,” *IEEE Open Journal of Ultrasonics, Ferroelectrics, and Frequency Control*, pp. 1–1, 2022.

[7] T. H. L. Nguyen and S. Park, “Multi-angle liquid flow measurement using ultrasonic linear array transducer,” *Sensors*, vol. 20, no. 2, p. 388, 2020.

[8] G. Rajita and N. Mandal, “Review on transit time ultrasonic flowmeter,” in *2016 2nd International Conference on Control, Instrumentation, Energy & Communication (CIEC)*. IEEE, 2016, pp. 88–92.

[9] L. Salami, “Application of a computer to asymmetric flow measurement in circular pipes,” *Transactions of the Institute of Measurement and Control*, vol. 6, no. 4, pp. 197–206, 1984.

[10] C. Pannell, W. Evans, and D. Jackson, “A new integration technique for flowmeters with chordal paths,” *Flow measurement and Instrumentation*, vol. 1, no. 4, pp. 216–224, 1990.

[11] J. Massaad, D. M. van Willigen, P. L. M. J. van Neer *et al.*, “Acoustic design of a transducer array for ultrasonic clamp-on flow metering,” in *2019 IEEE International Ultrasonics Symposium (IUS)*. IEEE, 2019, pp. 1133–1136.

[12] J. Massaad, P. L. M. J. van Neer, D. M. van Willigen *et al.*, “Suppression of Lamb wave excitation via aperture control of a transducer array for ultrasonic clamp-on

flow metering,” *The Journal of the Acoustical Society of America*, vol. 147, no. 4, pp. 2670–2681, 2020.

[13] P. Synowiec, A. Andruszkiewicz, W. Wędrychowicz *et al.*, “Influence of flow disturbances behind the 90° bend on the indications of the ultrasonic flow meter with clamp-on sensors on pipelines,” *Sensors*, vol. 21, no. 3, p. 868, 2021.

10

Conclusions and Recommendations

This chapter summarizes the main contributions of the work presented in this thesis. The practical aspects and recommendations when implementing this work in an actual flow meter will be discussed as well as ideas to further improve the techniques proposed throughout this thesis.

This thesis has presented techniques and circuits that can be used to improve several aspects of transit-time ultrasonic flow meters. The first chapters introduced methods to reduce the zero-flow error of ultrasonic flow meters. A large part of this thesis revolved around the use of clamp-on array transducers, starting with the design of the acoustic stack itself. With a pair of linear arrays clamped on a stainless steel pipe, flow measurements have been performed successfully. Subsequently an ASIC that drives the array of transducers has been designed and evaluated. In the last chapters, new techniques enabled by the use of array transducers have been studied. Novel methods have been developed to suppress the guided waves in the pipe wall and measure properties of the pipe and the liquid inside it using matrix transducers. Finally, a feasibility study has shown that it is possible to obtain information about the flow velocity profile using multiple acoustic paths with the pair of array transducers clamped at a fixed location on the pipe wall.

10.1. Zero-Flow Error Reduction

In Chapters 2 and 3 the origin of zero-flow errors has been studied and methods have been proposed to reduce the errors by making the right circuit-design choices and by using an additional processing step to calculate the flow velocity with available measurement data.

We have seen that, to minimize the zero-flow error, the circuit has to be made as reciprocal as possible. The best way to make the circuit reciprocal is to ensure an equal circuit impedance in transmission and reception. As it is in practice not always possible to ensure an equal circuit impedance due to the different nature of the transmit circuit and the receive circuit, it is beneficial to design a circuit where those impedances are significantly lower or significantly higher than the impedance of the transducer. For small transducers, such as those in matrix transducers, the optimal choice is a low impedance transmitter (voltage source) and low impedance receiver (current readout), because typically the elements of matrix transducers have an impedance in the order of tens of kilo-Ohms. Based on these findings, the circuit inside the ASIC has been designed.

In Chapter 3 an algorithm has been proposed to further reduce the zero-flow error in common ultrasonic flow meters. With this algorithm flow measurements are performed with a high SNR, by using cross-correlation to calculate the transit-time difference between the upstream and downstream signals. Because cross-correlation inherently has a higher zero-flow error than zero-crossing detection, the latter was used on a long-term average signal to calculate and compensate for the additional offset caused by cross-correlating two signals that are not perfectly reciprocal. The offset caused by cross-correlation was a factor 7 smaller, while the cross-correlation resulted in a 10 times lower random error compared to zero-crossing detection.

We have proven that the zero-flow error can be reduced significantly by applying this algorithm on measurement data. With the algorithm the specifications of current inline flow meters can potentially be improved by an update to the firmware of the flow meter.

10.2. Matrix-Based Flow Meter

Current clamp-on flow meters suffer from several drawbacks. They, for example, require manual alignment and several parameters (e.g. pipe and liquid properties) have to be input manually prior to measurement. To overcome those drawbacks, a clamp-on flow meter based on matrix transducers has been proposed in Chapter 4. The design includes a coupling piece to effectively transmit the acoustic waves generated by piezo transducers into the pipe wall and the liquid inside the pipe.

A matrix transducer has been designed and simulated, and several prototype transducers have been built based on the following specifications:

- Piezo material: HK1HD (early prototypes PZ26)
- Center frequency: 1 MHz
- Element pitch: 0.72 mm
- Number of elements: 37 × 17

The array dimensions were largely based on the required aperture to suppress the Lamb waves in the pipe wall, that would otherwise interfere with the measurement. Suppression of the Lamb waves in the pipe wall has been discussed in detail in Chapter 7. By controlling the amplitude of the individual elements (apodization) an appropriately tapered aperture can be created, which reduces the amplitude of the generated Lamb waves. Most suppression is required in the flow direction, hence the requirement for 37 elements in that direction. For convenience of circuit symmetry and the required configuration data a slight reduction in elements was made, resulting in a final array design of 36 × 16 elements.

Initially several linear arrays were built with 36 rectangular elements. With these transducers the fabrication process was further refined to finally create a set of matrix transducers with 6 × 16 elements. The timeline of the project did not allow for the full 36 × 16 array to be created. However, results obtained with the smaller arrays appear promising and were sufficient to develop prototypes and prove the technical concepts. The transducer arrays performed well with a measured transmit efficiency of 0.82 kPa/V and a -20 dB bandwidth of 130 %.

In Chapter 5 flow measurements have been obtained with a pair of 36-element linear arrays, clamped on a stainless steel pipe filled with water. Two different configurations for the acoustic path were studied. First a path generated by shear waves in the pipe wall was used. Second, a path with compressional waves in the pipe wall was used to measure flow. Both configurations showed good agreement with simulations and resulted in correlation factors between the measured and reference flow speeds above 99 %.

10.3. Transceiver ASIC

Small transducer elements of the array transducers are significantly loaded by the long cables used to connect them to the acquisition system. A compact circuit located close to the transducer would reduce the cable length and therefore significantly reduce the interconnection parasitics, resulting in an improved SNR. An ASIC is a very suitable way of creating a circuit that can be placed close to the array transducers and has the potential to fulfill all the requirements of clamp-on flow measurement. Chapter 6 has described the design of an ASIC that drives and reads out piezoelectric transducer arrays and includes features specifically aimed at clamp-on flow measurement. The ASIC was fabricated in a 0.18 µm BCD technology and covers the following specifications:

- Number of channels: 6×16
- Apodization: On column (5-bit) and row (5-bit) level
- Beam steering: In column (5-bit) and row (4-bit) direction
- Transmit amplitude: ± 4 V
- Receiver: TIA with a programmable gain of 74 dBΩ - 104 dBΩ

Several novel circuit techniques were used to create a compact circuit. Beam steering was implemented with a variable-length shift register, delaying a PWM-waveform with a programmable number of clock cycles. Amplitude apodization has been implemented such that the column and row configurations are multiplied in each channel, requiring a smaller die area and significantly less configuration data ($16+6$ five-bit values) compared to channel level amplitude configuration (16×6 values). The ASIC proved a very compact solution to drive and read-out the many piezoelectric elements of array transducers. The individual functions of the ASIC have been tested and perform well. With a 3-level PWM signal, arbitrary waveforms have been generated and signals could be steered accurately by programming beamforming delays. With a single input the ASIC can be switched between transmit and receive mode, making it very suitable for the alternating operation required in transit-time ultrasonic flow measurement.

In the flow loop, measurements have been performed to align the acoustic beam with the receive array. With the aligned acoustic beam flow measurements have been performed using two linear transducer arrays with 36 elements.

10.4. Calibration Measurements

We have seen that with the ASIC and array-based flow meter, calibration measurements can be performed. First, in chapter 6, it has been shown that beam-steering can be used to align the acoustic beam with the receive array. This step can be automated, making manual alignment of the arrays superfluous.

In Chapter 8 we have also seen that several properties of the pipe wall and liquid can be measured by using the new opportunities enabled by array transducers. The thickness and diameter of the pipe can be determined, as well as the acoustic wave speed in the pipe-wall and the liquid. Automatic measurement of those parameters could improve the accuracy of clamp-on flow meters and reduce installation time by completely taking away the requirement to input these parameters manually.

10.5. Velocity Profile Measurement

In Chapter 9 the feasibility of employing array transducers to measure velocity profiles has been explored. By measuring flow via several different acoustic paths a velocity profile can be reconstructed. Normally, this is done with multiple pairs of single-element transducers. The clamp-on matrix transducer enables measurement via several acoustic paths, while it is fixed onto the pipe in a single location. However, the fixed location also limits the acoustic paths available for measurement. Moreover, the acoustic paths pass relatively close to the center line of the pipe, because larger steering angles result in total internal reflection in the pipe wall. As a result, the transit-time differences of the possible acoustic paths differ only slightly. To determine the velocity profile, a very high SNR on the measurements is therefore required. Simulations have been performed with transit-time differences with a standard deviation around 0.1 ns. Based on 6 acoustic paths, the velocity profile was estimated, by fitting the transit-times to the power law. At low flow velocity, the algorithm estimated a laminar velocity profile while at higher flow velocity a clearly turbulent flow profile was found. The simulations resulted in accurate estimations of the maximum flow velocity with standard deviations below 5 %. The exponent of laminar flow could accurately be estimated within 10 % of the simulation input. Turbulent flows proved harder to estimate due to their relatively flat shape around the center of the pipe, resulting in significant variations of the power law exponent. However, all estimated profiles had a clearly turbulent shape.

These results are promising and with further optimization it seems feasible to estimate the velocity profile with clamped-on array transducers.

10.6. Recommendations

In this thesis only a small selection of techniques enabled by the use of clamp-on array transducers has been studied. Many more techniques can be conceived. This section discusses further ideas and measurement techniques to study with clamp-on array transducers. Also, practical aspects and recommendations when implementing the techniques in industrial applications are discussed.

10.6.1. Measurement Reciprocity

In Chapters 2 and 3 we have seen that the transient waveform, and in particular the zero-crossing time difference contains information about the reciprocity of the measurement setup. By effectively using this information contained in the transient waveforms the state of the flow meter can be monitored. For example, the long term change of reciprocity can be used to monitor the deterioration of transducer elements and warn the user in time when replacement of the transducers might be needed.

We have seen that a system is reciprocal if the impedance of the transmit circuit equals the receive circuit impedance. Ideally, the same circuit is used in transmit and receive. This requires a circuit with a very high dynamic range, but circuit topologies are conceivable that do not require switching between transmit and receive. One such circuit has been presented in [1] where the receive amplifier (a TIA) is also used as the transmitter. An alternative approach could be to create a low-impedance transmitter that is kept at a fixed voltage in receive, while a high-input-impedance amplifier (voltage amplifier) is used to amplify the received acoustic signals. The main difficulty in such a configuration is the amplifier design, because the impedance of the parallel transmit circuit would attenuate the received acoustic signals significantly.

10.6.2. Transducer Arrays

Most of the practical measurements in this thesis have been performed with a linear transducer array rather than a matrix. The design was however based on simulations for a matrix transducer, which enables steering in the circumferential direction of the pipe as well. Unfortunately, the timeline of the project did not allow full testing of the matrix transducer in a flow measurement configuration. It would be very interesting to investigate the possibilities and further improvements that the matrix transducer offers with respect to flow measurement, calibration and the measurement of velocity profiles.

As an initial step, a matrix of 6×16 elements has been fabricated, that can be driven by a single ASIC. A full matrix array of 36×16 elements, as described in Chapter 4, would require a total of 6 ASICs. This creates a significantly more complex flow meter. Looking at the final application in industry, however, applying a full matrix might not be cost-efficient and would likely also generate too much data to process in real-time. A more practical flow meter that includes the same features could contain two linear arrays, of which one is used for flow measurement and the other, mounted orthogonally, would be used for calibration and obtaining the required pipe and liquid parameters. This results in a roughly 10-times reduction in elements, but also compromises on some features. For example, in multi-path measurements the beam can not be steered in the circumferential direction, resulting in measurements with lower SNR.

In a case where the features enabled by a full matrix are desired, data reduction would be an important step towards making a practical flow meter. A way to implement data reduction could be to immediately beamform the received data. As discussed in Appendix C, the flow measurement is only reciprocal if the same beamforming angle is used in transmission and reception, hence the beamforming angle is fixed for a given set of received data. To not completely exclude filtering techniques in the f-k_x domain, beamforming could happen in a single dimension (e.g. tangential direction), leaving a significantly reduced (16 × smaller) set of time-traces.

10.6.3. ASIC Improvements

On many aspects the ASIC achieves good performance for accurate flow measurement. Still, several improvements could be made to make it even more suitable for the flow measurement application. First of all, the transmit voltage is rather limited. The circuit was designed to work with ± 5 V supplies, with intrinsic safety in mind. However, due to the nature of the output amplifier, the output voltage will never swing all the way to the supply lines, because the transistors need headroom to operate. Increasing the supply voltage of the output stage would help to increase the overall SNR of the measurement and thus increase the precision of the flow meter. Although a slight increase in supply voltage would be acceptable, the power dissipation of the class-A output stage would be significant. With a different topology for the output amplifier, the supply voltage can be increased by more than 6 times. The chip-technology would allow voltages up to 65 V.

Another relevant improvement to the ASIC would be the addition of analog-to-digital converters (ADCs). The received signals can then be digitized per channel making the need for an imaging machine superfluous. Also, the output multiplexer could then be omitted, resulting in higher measurement rates. An ADC suitable for this application could have rather straightforward specifications, but would require a significant amount of design work. With those specifications it would be hard to justify the extra work in an academic context. The choice was therefore made to not include it in the design. From an industrial perspective, it would probably be the first thing to include in the design as it currently stands.

10.6.4. Additional Measurement Techniques

As we have seen in this thesis, matrix-based clamp on flow meters enable many new measurement techniques. Only a small part of the possibilities has been explored within the timeline of this project. Here, additional measurement opportunities are discussed.

Practical flow measurement situations often present fluid flows that are much more complex than water flow. The fluid in the pipe can contain particles or bubbles, causing significant issues with transit-time flow measurements, due to attenuation and additional reflections of the acoustic waves. A method that is used in such applications is cross-correlation flow measurement [2, 3], where two transducers measure the acoustic reflections caused by bubbles and/or particles, perpendicular to the pipe-axis. This is a configuration that can be made with the matrix-based flow meter presented in this thesis as well. This can be used as a feature to diagnose the content of the pipe and, if necessary, even to measure the flow speed in an alternative way with the same setup.

The pipe could also be partially filled, which causes the acoustic waves to reflect not onto the pipe wall, but on the liquid-air interface. In situations where the matrix-array would be mounted on the bottom or side of the pipe, the liquid-level could be determined based on inversion of the acoustic paths (length and beam angle).

The feasibility of velocity profile measurement has been studied, based on fitting the data to the power law. A more versatile approach would be to estimate the flow based on cylindrical sections of the pipe. The pipe could be divided in a number concentric sections, for each of which an average flow speed can be determined. This would enable measurement of velocity profiles that do not obey the power law. However, it requires an even higher SNR than the fitting algorithm proposed in Chapter 9.

With the placement of the transducer arrays in a plane parallel to the pipe-axis, only symmetrical flow profiles can be measured. In practice the velocity profile can be asymmetric, especially after a bend in the pipe. Alternative placement of the transducer arrays on the pipe wall might enable measurements of non-symmetric flow profiles. A more extensive study of the possibilities with alternative transducer placement could lead to interesting and very useful measurement opportunities.

References

[1] D. M. van Willigen, E. Kang, J. Janjic *et al.*, “A transceiver asic for a single-cable 64-element intra-vascular ultrasound probe,” *IEEE Journal of Solid-State Circuits*, vol. 56, no. 10, pp. 3157–3166, 2021.

[2] J. Coulthard, “Ultrasonic cross-correlation flowmeters,” *Ultrasonics*, vol. 11, no. 2, pp. 83–88, 1973.

[3] M. Sanderson and H. Yeung, “Guidelines for the use of ultrasonic non-invasive metering techniques,” *Flow measurement and Instrumentation*, vol. 13, no. 4, pp. 125–142, 2002.

A

Matrix Array Fabrication

Throughout this dissertation several transducer arrays have been used in measurement setups. Initially, transducers were fabricated with a 1-dimensional array, or a line of transducer elements. When the fabrication method was developed to a consistent process with a clear production plan, also 2-dimensional matrices were fabricated, creating several new challenges in maintaining reliable transducer fabrication.

This appendix describes the overall process of matrix fabrication as it was implemented for the prototypes presented in this dissertation.

A.1. Fabrication Steps

Transducer array fabrication involves four main steps, depicted in Figure A.1. Each step is discussed briefly below:

1. The design starts with a PCB that has vias at the center of each intended transducer element. At the backside of the PCB the via connects to a connector for actuation and readout of the piezo transducer.

2. A piece of piezo material is glued onto the PCB with a thin layer of conductive glue. Initially 1.67 mm thick PZ26 (Meggit A/S, Kvistgård, DK) piezo material was used. Later 1.24 mm thick HK1HD (TRS Technologies, Inc., State College, PA, USA) was used, because of its superior characteristics.

3. Using a dicing saw small kerfs are cut through the piezo material and into the PCB. These cuts separate the piezo material into individual elements. Dicing is certainly not a trivial step as the diamond saw is very thin and requires very precise positioning. Special attention has to be paid at the glue attaching the piezo material to the PCB, since in some occasions the glue was smeared at the bottom of the kerf, short-circuiting elements. An additional cleanup pass included in the fabrication process solved this issue.

4. Finally, a copper foil is glued on top of the piezo array to create a common ground connection for the transducer. A backing material was cast to improve the acoustic characteristics of the transducer.

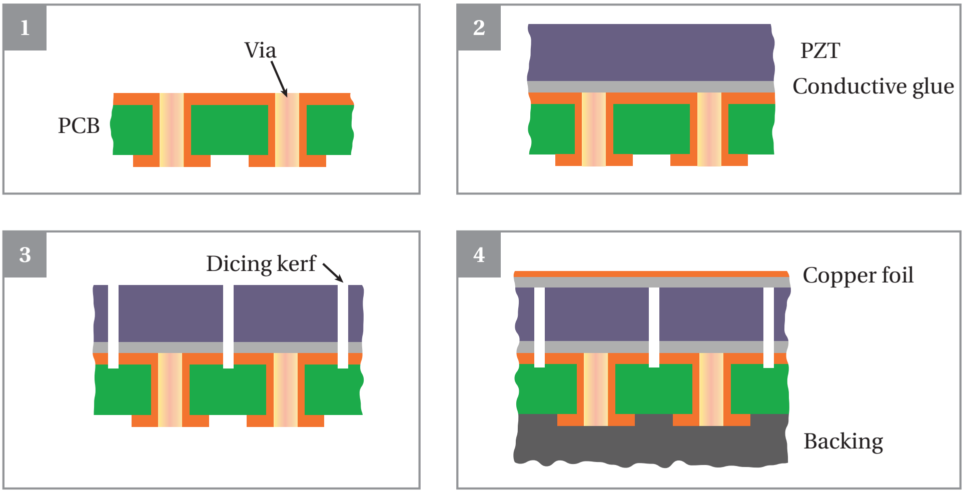

Figure A.1: The four main steps of matrix fabrication.

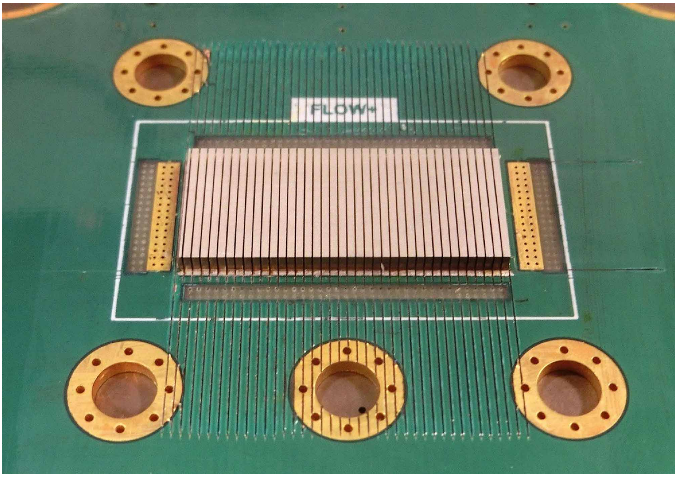

Figure A.2: Linear transducer array with 36 elements, before placing the ground foil.

Figure A.2 shows a linear transducer array before the ground foil was glued on top. The linear transducers have been used to measure flow as well as pipe and liquid properties throughout this thesis. After placing the copper ground foil, protective glue was added around the transducer. The finished linear transducer array is shown in Figure A.3.

A matrix transducer is shown in Figure A.4. The square elements are used for the measurement, while the rectangular elements one the left and right side are dummy elements that are not used in this particular sample. Characterization of the matrix transducers was still in progress at the time of writing, but initial measurements show promising results.

Acknowledgment

Transducer fabrication would not have been possible without all the valuable hard work of our technician Emile Noothout. The author would like to sincerely thank him for his efforts, constructive discussions and countless hours of meticulous work.

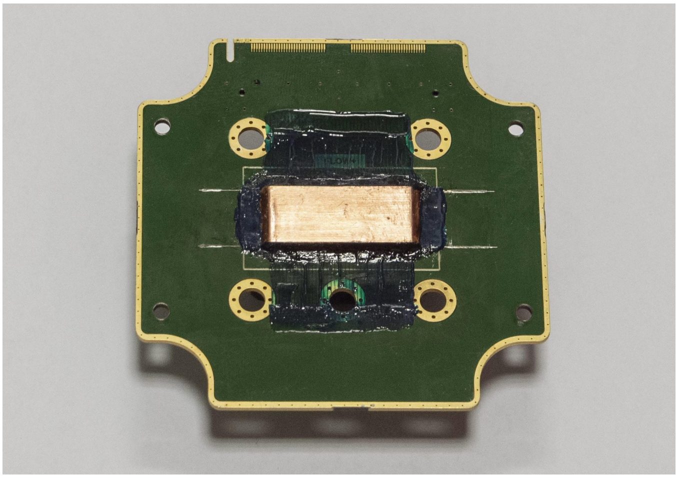

Figure A.3: Finished linear transducer array with 36 elements.

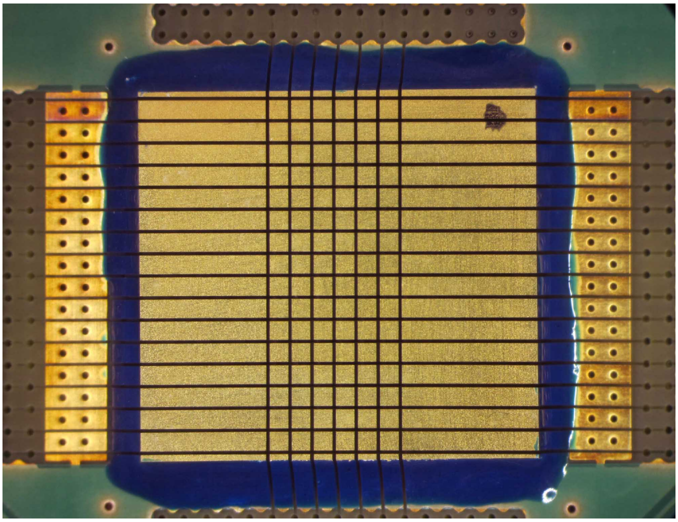

Figure A.4: Matrix transducer with 6 × 16 elements, before placing the ground foil.

B

Improving SNR by Compressing PWM Chirps

A good signal-to-noise ratio is important for accurate flow measurement. In applications where arbitrary waveforms can be used, it is beneficial to use waveforms that have a high time-bandwidth product, i.e. signals with a long duration and a wide bandwidth, because it increases the SNR.

However, long waveforms present the issue that they might overlap with the reverberations or spurious waves in the pipe-wall or even other acoustic paths through the flow. With chirp compression the waveform can be made shorter by correlating it with the transmitted waveform. The resulting compressed waveform can be time-windowed more easily.

This appendix discusses the SNR improvement that can be obtained when generated chirps with commonly-used PWM schemes.

B.1. Types of Pulse-Width Modulation

Pulse-width modulation (PWM) is a way to regulate the power delivered by a supply to a load, by rapidly switching the supply on and off. The switching frequency is higher than that of the desired signal. The longer the supply is switched on, the higher the power delivered to the load. Commonly a PWM signal is low-pass filtered to remove the high-frequency signal components caused by the switching.

A PWM waveform can be derived from a reference signal in many ways [1, 2]. A very simple way is to compare the reference signal with a ramp signal. If the signal level of the source signal is below the ramp signal the PWM output is high, as soon as the signal crosses the ramp amplitude the PWM output turns low. This method is referred to as suboscillation PWM, and is illustrated in Figure B.1.

A limitation of the suboscillation PWM method is that it contains a strong frequency component related to the ramp signal period. An alternative method of generating PWM signals, without this drawback, is hysteresis PWM [2]. The integrated error between the analog signal and PWM signal is calculated, and based on a chosen error-threshold

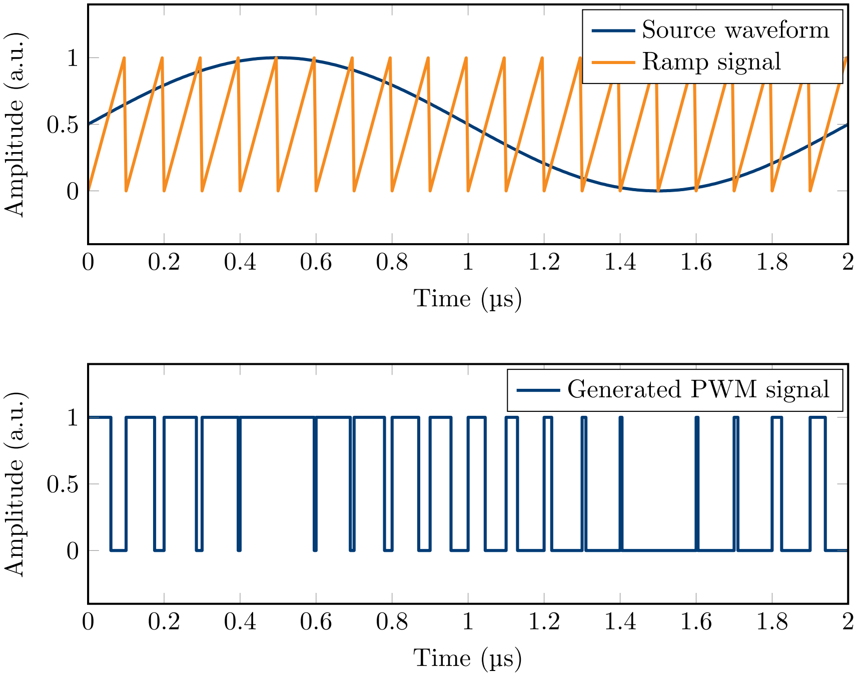

Figure B.1: Suboscillation PWM, based on a ramp signal.

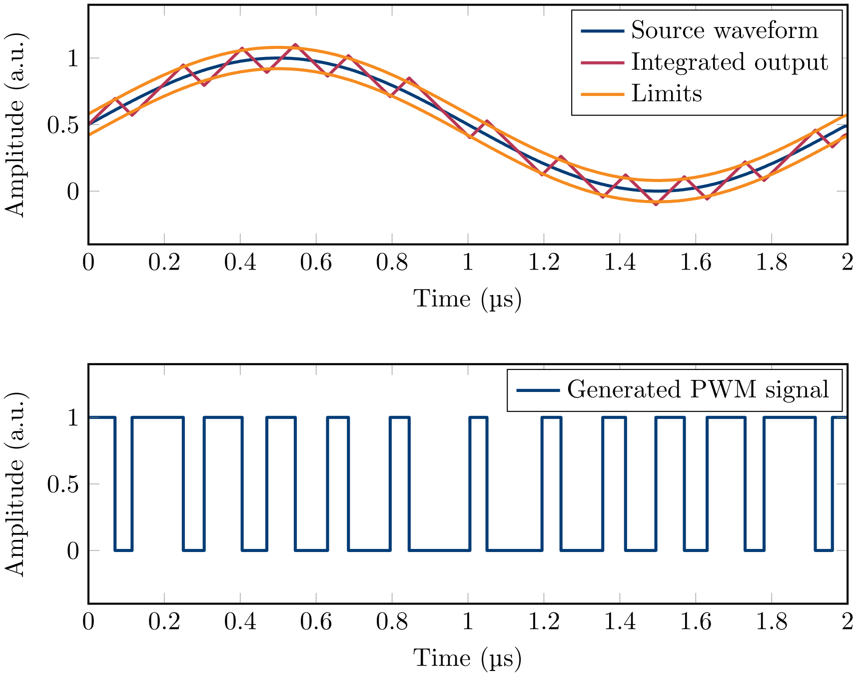

Figure B.2: Hysteresis PWM (sigma-delta PWM) is based on upper and lower error limits.

the PWM output is set high or low. An example of this type of PWM is shown in Figure B.2.

In clock-based systems, such as the ASIC described in this thesis, the accuracy of PWM signals is always limited by the clock frequency of the system. The digital signal can only change state on every clock tick. This causes the signal to sometimes overshoot the reference signal in Figure B.2. Moreover, since the clock frequency is part of every PWM signal, tones will be present at the sampling frequency and its harmonics. Low pass filtering has to be applied, to make sure those harmonics are not seen at the output.

The ASIC uses 3-level PWM signals, implemented by creating a signal for the positive and negative half of the waveform separately.

B.2. Pulse Compression

With the ASIC, signals can be generated for longer durations than a few periods. This enables the use of pulse compression techniques, which are a well known way to increase the SNR of a signal [3]. A commonly used transmit waveform in conjunction with pulse-

(a) Suboscillation PWM **(b)** Suboscillation PWM compr.

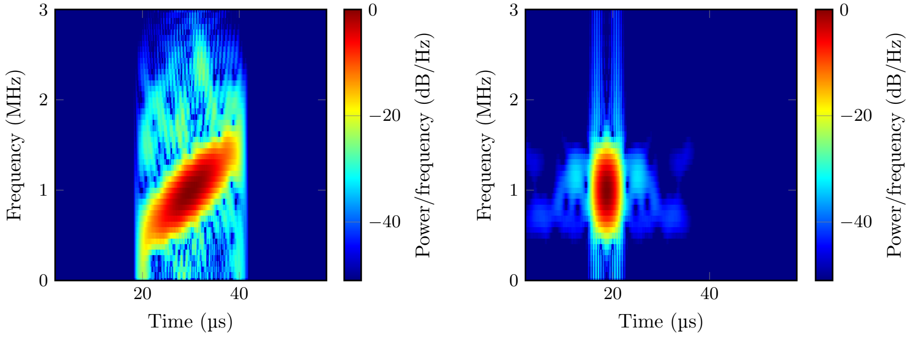

(c) Hysteresis PWM **(d)** Hysteresis PWM compressed

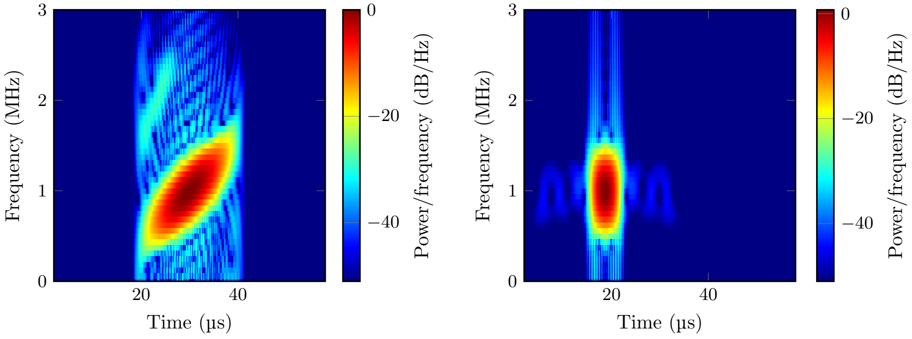

(e) Analog signal **(f)** Analog signal compressed

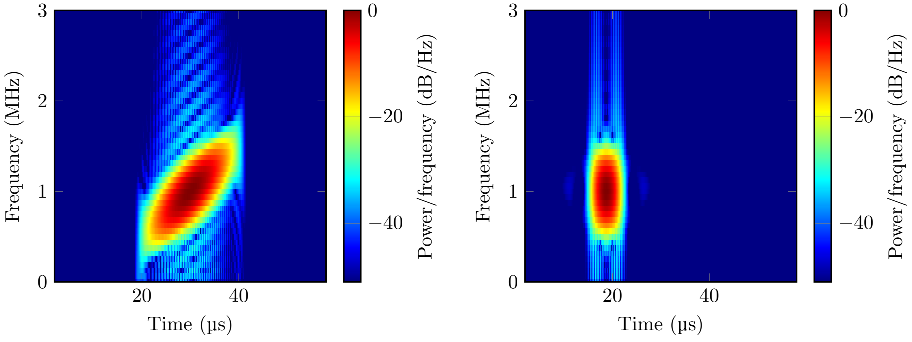

Figure B.3: Spectrograms of linear chirps, generated using suboscillation PWM (a, b), hysteresis PWM (c, d) and analog waveform (e, f) before (left) and after pulse-compression (right).

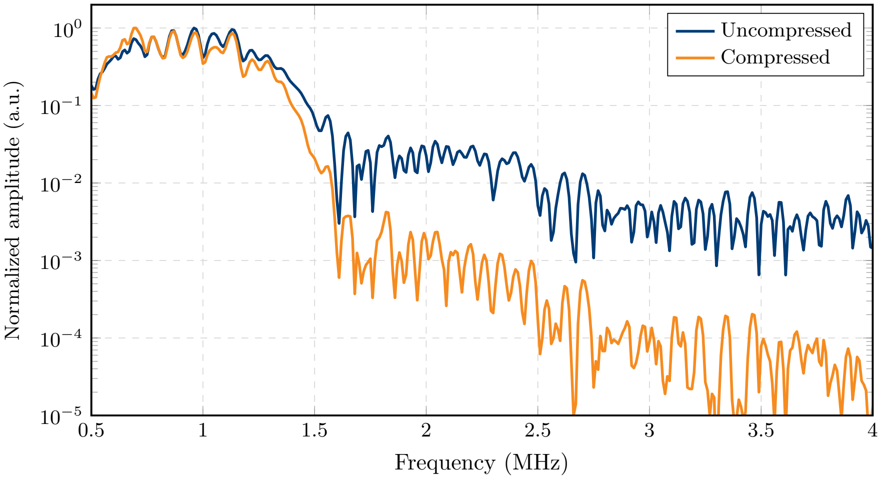

Figure B.4: Normalized power spectrum of acoustic signal recorded from PWM linear chirp before and after signal compression with the TX waveform as template.

compression is the chirp signal, a signal that increases (or decreases) in frequency over time.

When chirp signals are generated with PWM, the artifacts discussed in Section B.1 result in additional clutter after compression, especially around the bandwidth of interest (0.5 - 1.5 MHz). This is clearly visible on spectrograms of the various signals, as shown in Figure B.3. In particular suboscillation PWM results in a lot of clutter (−34 dB) after compression, whereas hysteresis PWM has fewer artifacts, and the main artifact left over is the second-order harmonic. After compression this leads to less clutter (−41 dB). More sophisticated PWM methods exist (e.g. [4]), but are beyond the scope of this appendix.

To get an impression of the effectiveness of applying pulse compression, the acoustic signal of a PWM linear chirp was recorded with a hydrophone in water, at 70 mm from the transducer. The signal was then compressed by cross-correlating it with the electrical signal used in transmission. The chirp signal and hydrophone signal before and after compression are shown in Figure B.5. After compression, the first wavefront (at 45 µs) and reverberation in the coupling piece (at 55 µs) are easily distinguished. The spectrum of the uncompressed signal and the compressed signal are shown in Figure B.4. Clearly, compression increases the SNR.

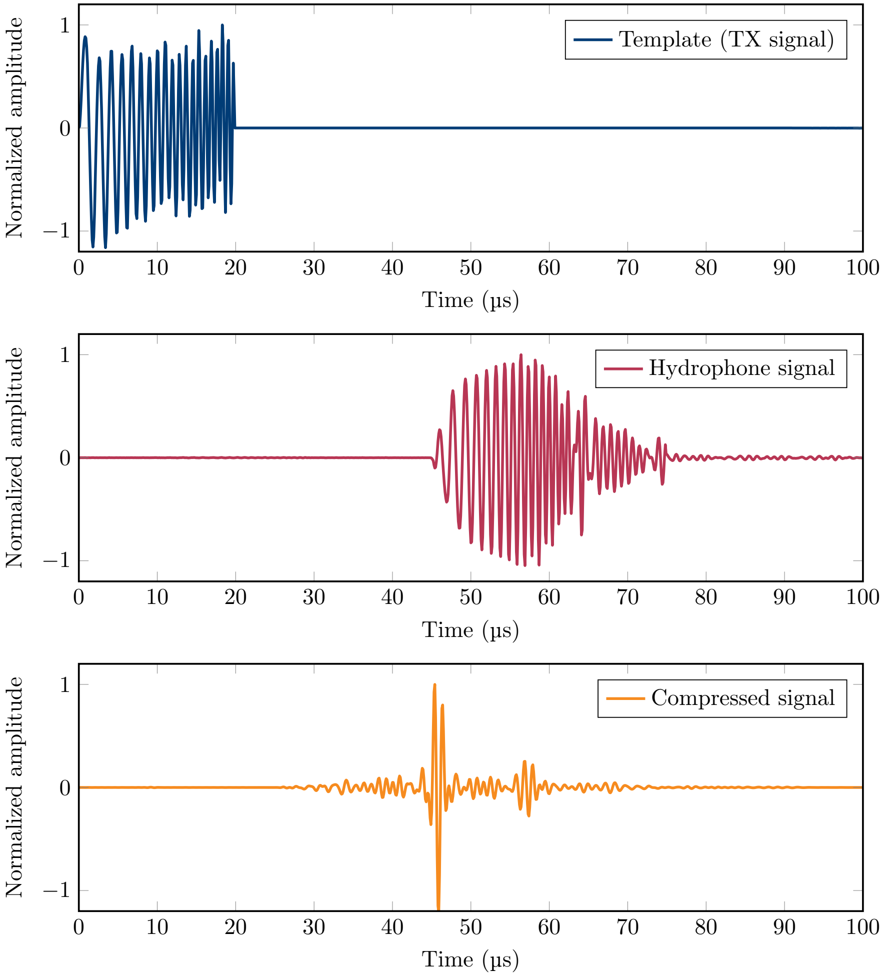

Figure B.5: Signal compression with hydrophone measurement of PWM chirp transmitted with the linear array.

B.3. Conclusion and Discussion

PWM-generation and pulse compression techniques are helpful tools to improve the SNR of flow measurements. Especially where high accuracy is needed, such as when measuring velocity profiles, these techniques prove very valuable.

Comparing the two PWM techniques, it is beneficial to use hysteresis PWM, because it results in less clutter after pulse compression.

References

[1] Z. Yu, A. Mohammed, and I. Panahi, “A review of three pwm techniques,” in *Proceedings of the 1997 American Control Conference*, vol. 1, 1997, pp. 257–261.

[2] K. Nielsen, “A review and comparison of pulse-width modulation (pwm) methods for analog and digital input switching power amplifiers,” in *Audio Engineering Society Convention 102*, 1997.

[3] T. Misaridis and J. A. Jensen, “Use of modulated excitation signals in medical ultrasound. Part I: Basic concepts and expected benefits,” *IEEE Transactions on Ultrasonics, Ferroelectrics, and Frequency Control*, vol. 52, no. 2, pp. 177–191, 2005.

[4] S. Stark, “Direct digital pulse width modulation for class D amplifiers,” 2007.

C

Flow Measurement Errors Introduced by Non-Optimal Beamforming

While performing clamp-on flow measurements with transducer arrays, steering the acoustic beam to precisely hit the receiver array is important. When the steering angle deviates a bit, an error in the flow measurement is introduced.

This appendix discusses the nature of the errors introduced by beamforming of the received signals and investigates how sensitive the flow measurement is to a variation in the beam steering angle.

Understanding this phenomenon is valuable to increase the accuracy of the flow measurements, and might enable compensation of beamforming-related errors when measuring multiple acoustic paths simultaneously.

C.1. Flow Measurement Principle

In array-based clamp-on ultrasonic flow measurement, a pair of transducer arrays is placed with a flat wedge on the pipe wall, as discussed in Chapter 4. The acoustic waves penetrate the pipe wall with an angle determined by the transmit beamforming setting. The angle and center-to-center distance between the transducers determines how many times the acoustic beam reflects inside the pipe, before reaching the other transducer.

When the beamforming angle is set such that the acoustic beam misses the center of the other array, the effective path length of the acoustic beam differs and one has to adjust the flow calculation to this change. If the path-length adjustment is not taken into account, this will result in a gain error in the flow measurement. It can however be a valuable measurement case, because multiple acoustic paths could be measured simultaneously, which can benefit the SNR and accuracy of the flow measurement.

C.2. Electro-Acoustic Reciprocity

For an accurate ultrasonic flow measurement, it is important that the system is kept reciprocal. The system is reciprocal when each transducer is used in the same way in transmit and receive, i.e. the impedance is the same [1, 2]. A system can be used reciprocally with two different transducers, for example a combination of a matrix and a single-element [3], as long as the same transducer is used in TX in the upstream measurement and RX in the downstream measurement and vice versa. When a pair of array transducers is used, the reciprocity criterion only holds when the beamforming angle used in transmit equals the beamforming angle in receive.

C.3. Path Length Approximation

The measured flow is directly related to the acoustic path, it is therefore important to know its exact length. We only need to know the path length parallel to flow, since the flow adds vectorially. In a situation where the beam is properly aligned with the transducers (hitting the center of the other array), the average path length can be calculated based on the beamforming angle (θ), pipe diameter (D) and number of path-sections (b) inside the pipe:

$$x = D \cdot b \cdot \tan(\theta). \tag{C.1}$$

However, as soon as the acoustic beam only partially hits the receive transducer, the average path length has to be adjusted. This is depicted in Figure C.1, where the red part of the beam misses the receiver array.

A more accurate calculation of the path length can be obtained by assuming that the

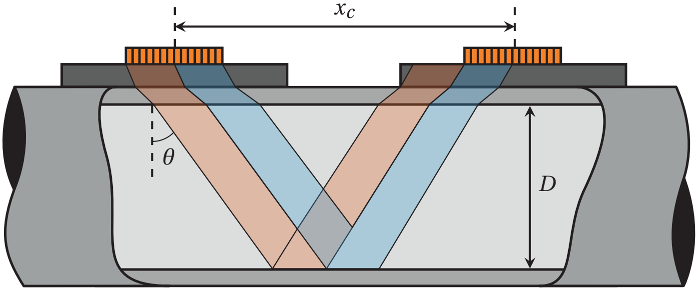

Figure C.1: Diagram of the acoustic beam not hitting the other array in the center. The blue part of the beam hits the receive array, while the red part misses it.

transmitted wave is a plane wave. By calculating the center of the part of the beam that hits the receiver, the acoustic path length parallel to the flow can be calculated:

$$x = \frac{D \cdot b \cdot \tan(\theta) + x_c}{2} \tag{C.2}$$

where x_c is the center-to-center distance of the array.

C.4. Method

A ray tracing simulation is performed to investigate the magnitude of the gain error caused by beamforming with a non-optimal acoustic path. In the simulation, the length of the acoustic path between each of the transmit elements and each of the receive elements is calculated. A Gaussian apodized transmit signal is then used for each of the transmit elements and a signal is constructed for the receiver-elements by summing the time-shifted waveforms of all the transmitters. This process results in 36 transient signals that are subsequently beamformed with the same (but mirrored) delays as the transmitted signals.

C.5. Simulation Results

A simulation of transit-time difference, based on the ray-tracing script is shown in Figure C.2. A flow of 0.5 m/s is simulated for varying beamforming angles. The dashed lines indicate the approximation using equation (C.2). The transit-time difference is measured correctly when the beam hits the receiver in the center (maximum amplitude, highlighted by the black marker), as soon as the beam deviates from the center, an error is introduced.

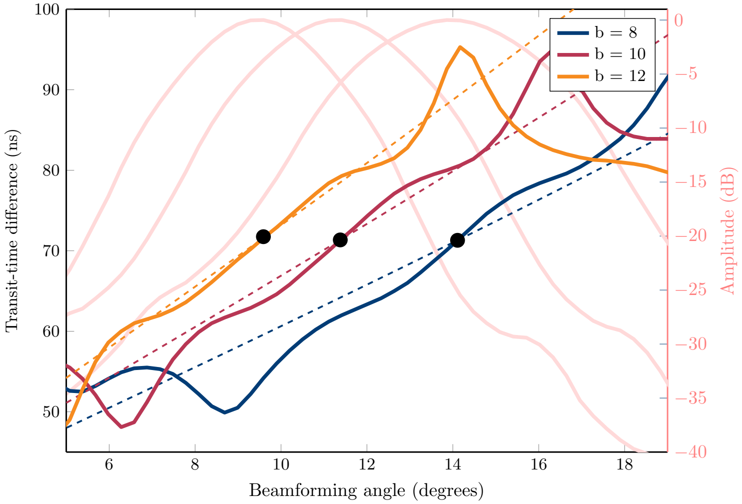

Figure C.2: Influence of the beamforming angle on the transit-time difference for three acoustic paths, simulated using ray-tracing. The dashed lines indicate the transit-time difference calculated using the approximated acoustic path length with equation (C.2). The black markers indicate the optimal steering angle (maximum signal amplitude).

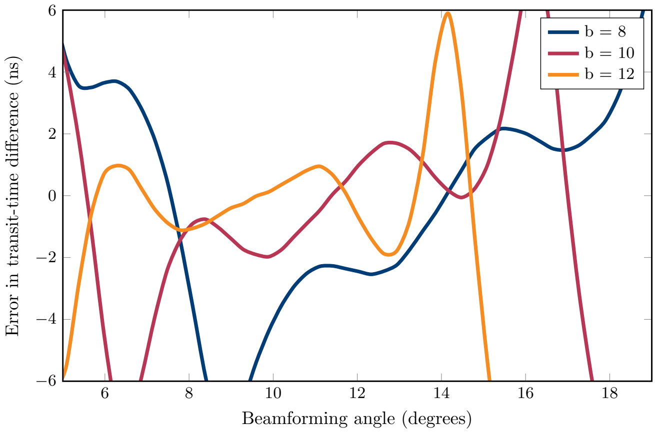

Figure C.3: Error in flow calculation when using the approximated acoustic path length compared to the ray tracing.

For clarity the difference between the equation (C.2) and the ray-tracing simulation is shown in Figure C.3. In the simulation results we also see that the error is more significant for acoustic paths with fewer reflections. This is likely due to the larger steering angle.

C.6. Conclusions and Discussion

It is clear that one can not simply use multiple acoustic paths obtained in a single measurement. The path-difference is significant, causing an error in the calculated flow value. A first order approximation can be made based on the assumption that the transmitter is sending out plane waves, however, in reality this is too simplistic and still a residual error will remain.

Each flow measurement contains the signals of multiple acoustic paths. The use of additional paths could greatly improve the accuracy of the flow measurement. It would therefore be very valuable to further investigate this phenomenon and come up with a technique to compensate for the error discussed in this appendix.

A practical solution for industry could be to create a look-up table with a correction factor for the different beamforming angles. Errors in the path length only result in a gain error in flow measurement, which can easily be corrected by a simple multiplication factor as often already used to compensate for velocity profiles.

References

[1] L. L. Foldy and H. Primakoff, “A general theory of passive linear electroacoustic transducers and the electroacoustic reciprocity theorem. I,” *The journal of the acoustical society of America*, vol. 17, no. 2, pp. 109–120, 1945.

[2] P. Lunde, M. Vestrheim, R. Bo, S. Smorgrav, and A. K. Abrahamsen, “Reciprocal operation of ultrasonic flow meters: Criteria and applications,” in *2007 IEEE International Ultrasonics Symposium (IUS)*. IEEE, 2007, pp. 381–386.

[3] C. Haugwitz, A. Jäger, G. Allevato, J. Hinrichs, A. Unger, S. Saul, J. Brötz, B. Matyschok, P. Pelz, and M. Kupnik, “Flow metering of gases using ultrasonic phased-arrays at high velocities,” in *2019 IEEE International Ultrasonics Symposium (IUS)*. IEEE, 2019, pp. 1129–1132.

Summary

This dissertation describes the design of a clamp-on transit-time ultrasonic flow meter based on transducer arrays. The use of transducer arrays in the context of flow measurement enables several new techniques, which have been studied in this work. With a custom-built prototype consisting of two 36-element linear transducer arrays flow measurements have been performed and new measurements techniques have been explored.

In ultrasonic flow measurements careful design is required to keep a low offset at zero flow. The influence of circuit topologies on the offset (or zero-flow error) has been explored and the choices to reach an optimal design have been discussed in Chapter 2. Based on the findings an algorithm has been presented that reduces the offset in flow measurement but keeps a high precision (Chapter 3).

The first step in creating a clamp-on flow meter with matrix arrays, is the design of the transducer array itself. An acoustic stack has been designed specifically aimed at interfacing with stainless steel pipes, often used in industry. The design has been evaluated in acoustic measurements and a pair of 36-element linear transducers arrays has been used to create a prototype flow meter (Chapter 4).

Flow measurements have been performed in a stainless steel pipe section of a flow loop filled with water. The measurements have been performed with two different types of acoustic paths: a path where shear waves are generated in the pipe wall, that refract under a high angle in the liquid. This paths requires the acoustic beam to cross the liquid only four times. An acoustic path with compressional waves in the pipe wall has also been considered. This requires an acoustic path that crosses the liquid twelve times before reaching the receiver. In water both configurations result in accurate flow measurement with the shorter acoustic path, generated by shear waves in the pipe wall, achieving a better SNR (Chapter 5).

The array transducers have a significant number of elements, requiring a large acquisition system and relatively long cables to connect the array to the system. An ASIC design has been presented and fabricated that can be mounted close to the transducer array, requiring shorter cables and resulting in less attenuation of the acoustic signal by the capacitive load of long cables. Arbitrary waveform generators are integrated with a novel delay circuit to steer the acoustic beam. The circuits have been evaluated electrically and a pair of ASICs has been used to measure flow velocity in a flow loop (Chapter 6).

Transmission of acoustic waves through the pipe wall causes guided waves that travel through the pipe wall to the receiver. These waves can interfere with the measurement and are therefore unwanted. A method has been developed to suppress these guided waves to a level where they do not harm the measurement. Evaluation of this method in an acoustic measurement shows that the guided waves can effectively be suppressed (Chapter 7).

Matrix transducers enable several possibilities to measure the properties of the pipe and the fluid inside. These properties are normally input manually prior to flow measurement. Techniques to determine the thickness and diameter of the pipe, as well as the speed of sound in the pipe and liquid have been proposed. Combining these methods in a calibration phase makes manual calibration redundant (Chapter 8).

The beam steering capability of the transducer arrays allows measurement via several different acoustic paths. By combining acoustic paths of different cross sections through the liquid, information about the velocity profile of the flow can be obtained and when the SNR is high enough flow profiles can even be reconstructed. The feasibility of this method has been studied an evaluated with simulations (Chapter 9).

A concluding chapter discusses the achieved results and possible future improvements. Furthermore, practical aspects of implementing the concepts presented in this dissertation in an industrial setting are discussed.

Samenvatting

Dit proefschrift beschrijft het ontwerp van een opklembare ultrasone stromingsmeter die gebruik maakt van array transducenten. Het gebruik van array transducenten in een ultrasone stromingsmeter maakt verschillende nieuwe technieken mogelijk, die in dit proefschrift bestudeerd worden. Met een op maat gemaakt prototype bestaande uit twee lineaire array transducenten met elk 36 elementen zijn stromingsmetingen gedaan en nieuwe meettechnieken verkend.

Bij ultrasone stromingsmetingen is een zorgvuldig ontwerpproces belangrijk om een lage offset te behouden wanneer er geen stroming is. De invloed van circuittopologieën op de offset is onderzocht in hoofdstuk 2, evenals de keuzes die nodig zijn om een optimaal ontwerp te bereiken. Aan de hand van de bevindingen wordt een algoritme gepresenteerd dat de offset in stromingsmetingen vermindert maar tegelijkertijd een hoge precisie behoudt (hoofdstuk 3).

De eerste stap bij het maken van een opklembare ultrasone stromingsmeter met matrix arrays is het ontwerp van de transducenten zelf. Het akoestisch ontwerp is speciaal gericht op het koppelen van de transducenten met de roestvrijstalen buizen die vaak gebruikt worden in de industrie. Het ontwerp is geëvalueerd met akoestische metingen en met een paar 36-elements array transducenten is een prototype stromingsmeter gemaakt (hoofdstuk 4).

In een roestvrijstalen buis gevuld met water zijn stromingsmetingen gedaan. De metingen zijn uitgevoerd via twee verschillende akoestische paden: een pad waarbij schuifgolven worden opgewekt in de pijpwand, die onder een grote hoek in de vloeistof komen. Via dit pad hoeft de akoestische bundel maar vier keer door de vloeistof te gaan. Een akoestisch pad waarbij compressiegolven worden opgewekt in de pijpwand is ook bekeken. Hiervoor dient het golf de vloeistof twaalf keer te doorsnijden voor hij de ontvanger bereikt. In water resulteren beide configuraties in nauwkeurige stromingsmetingen, waarbij het kortere akoestische pad gegenereerd met schuifgolven een meting met betere SNR behaalt (hoofdstuk 5).

De array transducenten hebben een significant aantal elementen, waardoor een groot acquisitiesysteem met relatief lange kabels nodig is om de array met het acquisitiesysteem te verbinden. Het ontwerp en de fabricage van een ASIC worden gepresenteerd, zodat de elektronica dicht bij de array transducent gemonteerd kan worden. Hierdoor kunnen kortere kabels gebruikt worden wat resulteert in minder verzwakking van het akoestisch signaal. Functiegeneratoren die willekeurige golfvormen kunnen maken zijn geïntegreerd met een nieuw vertragingscircuit om de akoestische bundel te kunnen sturen. De circuits zijn elektrisch geëvalueerd en een paar ASIC's is gebruikt om stromingssnelheid te meten in een stromingslus (hoofdstuk 6).

Het verzenden van akoestische golven door de pijpwand veroorzaakt geleidde golven die zich door de pijpwand voortplanten richting de ontvanger. Deze golven zijn ongewenst omdat ze kunnen interfereren met de metingen. Om deze golven te onderdrukken is een methode ontwikkeld die ervoor zorgt dat ze zwak genoeg zijn om de metingen niet negatief beïnvloed worden. Evaluatie met akoestische metingen laat zijn dat de geleidde golven effectief onderdrukt kunnen worden (hoofdstuk 7).

Matrix transducenten maken het mogelijk om op verschillende manieren de eigenschappen van de pijp en de vloeistof erin te meten. Deze eigenschappen worden normaal handmatig ingegeven voordat metingen gedaan worden. Technieken om automatisch de dikte en diameter van de pijp, evenals de geluidssnelheid in de pijp en vloeistof te bepalen worden gepresenteerd. Door deze methoden te combineren in een kalibratiefase wordt handmatige kalibratie overbodig (hoofdstuk 8).

Doordat array transducenten akoestische bundels in verschillende richtingen kunnen sturen, worden metingen via verschillende akoestische paden mogelijk. Door het combineren van akoestische paden die de vloeistof op verschillende manieren doorkruisen kan informatie over het snelheidsprofiel van de vloeistof achterhaald worden. Wanneer de SNR hoog genoeg is, zouden zelfs stromingsprofielen kunnen worden gereconstrueerd. In een laatste hoofdstuk wordt de haalbaarheid van deze methode onderzocht en geëvalueerd aan de hand van simulaties (hoofdstuk 9).

Een concluderend hoofdstuk bespreekt de behaalde resultaten en mogelijke verbeteringen voor de toekomst. Daarnaast worden de praktische kanten besproken van het implementeren voor industriële toepassingen.

List of Publications

- J. Massaad, P. L. M. J. van Neer, **D. M. van Willigen**, N. de Jong, M. A. P. Pertijs, and M. D. Verweij, “Design and proof-of-concept of a matrix transducer array for clamp-on ultrasonic flow measurements,” *IEEE Transactions on Ultrasonics, Ferroelectrics, and Frequency Control*, 2022
- J. Massaad, P. L. M. J. van Neer, **D. M. van Willigen**, A. Sabbadini, N. de Jong, M. A. P. Pertijs, and M. D. Verweij, “Measurement of pipe and fluid properties with a matrix array-based ultrasonic clamp-on flow meter,” *IEEE Transactions on Ultrasonics, Ferroelectrics, and Frequency Control*, vol. 69, no. 1, pp. 309–322, 2021
- **D. M. van Willigen**, E. Kang, J. Janjic, E. Noothout, Z.-Y. Chang, M. D. Verweij, N. de Jong, and M. A. P. Pertijs, “A transceiver ASIC for a single-cable 64-Element intra-vascular ultrasound probe,” *IEEE Journal of Solid-State Circuits*, vol. 56, no. 10, pp. 3157–3166, 2021
- J. Massaad, P. L. M. J. van Neer, **D. M. van Willigen**, N. de Jong, M. A. Pertijs, and M. D. Verweij, “Exploiting nonlinear wave propagation to improve the precision of ultrasonic flow meters,” *Ultrasonics*, vol. 116, p. 106476, 2021
- **D. M. van Willigen**, P. L. M. J. van Neer, J. Massaad, N. de Jong, M. D. Verweij, and M. A. Pertijs, “An algorithm to minimize the zero-flow error in transit-time ultrasonic flowmeters,” *IEEE Transactions on Instrumentation and Measurement*, vol. 70, pp. 1–9, 2020
- J. Massaad, P. L. M. J. van Neer, **D. M. van Willigen**, M. A. Pertijs, N. de Jong, and M. D. Verweij, “Suppression of lamb wave excitation via aperture control of a transducer array for ultrasonic clamp-on flow metering,” *The Journal of the Acoustical Society of America*, vol. 147, no. 4, pp. 2670–2681, 2020
- J. M. Mouawad, P. L. M. J. van Neer, **D. M. van Willigen**, M. A. P. Pertijs, N. de Jong, and M. d. Verweij, “Towards a calibration-free ultrasonic clamp-on flow meter: Pipe geometry measurements using matrix arrays: Pipe geometry measurements using matrix arrays,” in *Meetings on Acoustics. Proceedings*, vol. 39, no. 1. Acoustical Society of America, 2020, p. 065001
- J. Li, Z. Chen, M. Tan, **D. M. van Willigen**, C. Chen, Z.-y. Chang, E. Noothout, N. de Jong, M. Verweij, and M. Pertijs, “A 1.54 mW/element 150 µm-pitch-matched receiver ASIC with element-level SAR/shared-single-slope hybrid ADCs for miniature 3D ultrasound probes,” in *2019 Symposium on VLSI Circuits*. IEEE, 2019, pp. C220–C221

- **D. M. van Willigen** and M. Pertijs, "Data collection system, in particular suitable for imaging of a distant object," Dutch Patent 2 020 426B1, February 2019
- J. Massaad, **D. M. van Willigen**, P. L. M. J. van Neer, N. de Jong, M. Pertijs, and M. Verweij, "Acoustic design of a transducer array for ultrasonic clamp-on flow metering," in *2019 IEEE International Ultrasonics Symposium (IUS).* IEEE, 2019, pp. 1133–1136
- **D. M. van Willigen**, M. Mozaffarzadeh, E. Noothout, M. Verweij, N. de Jong, M. Pertijs, and V. Daeichin, "Fabrication and characterization of a prototype forward-looking single-cable 64-element intra-vascular ultrasound probe," in *2019 IEEE International Ultrasonics Symposium (IUS).* IEEE, 2019, pp. 978–980
- J. Massaad, P. L. M. J. van Neer, **D. M. van Willigen**, N. de Jong, M. A. P. Pertijs, and M. D. Verweij, "Feasibility of ultrasonic flow measurements via non-linear wave propagation," in *2018 IEEE International Ultrasonics Symposium (IUS).* IEEE, 2018, pp. 1–4
- **D. M. van Willigen**, P. L. M. J. van Neer, J. Massaad, M. D. Verweij, N. de Jong, and M. A. P. Pertijs, "Minimizing the zero-flow error in transit-time ultrasonic flow meters," in *2018 IEEE International Ultrasonics Symposium (IUS).* IEEE, 2018, pp. 1–4
- **D. M. van Willigen**, J. Janjic, E. Kang, E. Noothout, M. D. Verweij, N. de Jong, and M. A. P. Pertijs, "ASIC design for a single-cable 64-element ultrasound probe," in *2018 IEEE International Ultrasonics Symposium (IUS).* IEEE, 2018, pp. 1–4
- **D. M. van Willigen**, E. Mostert, and M. A. Pertijs, "In-air ultrasonic gesture sensing with MEMS microphones," in *SENSORS, 2014 IEEE.* IEEE, 2014, pp. 90–93

About the author

Douwe was born in de Bilt, the Netherlands in June 1991.

He followed primary and secondary education at the Waldorf school in Zeist (Zeister Vrije School and Stichtse Vrije School respectively).

At Delft University of Technology he received the Bachelor of Science in Electrical Engineering, and specialized in microelectronics during his master.

With the Electronic Instrumentation Laboratory he pursued the PhD degree, where he has been working on ultrasonic flow measurement, closely collaborating with the Acoustical Wavefield Imaging group.

In his spare time he enjoys woodworking, photography and rock climbing.

Acknowledgment

In the five years of my PhD journey I've enjoyed working together with many people and meeting with friends, many of whom have helped me throughout this journey. I would like to use this section to thank everyone for their support and fruitful collaborations.

First of all, I would like to thank my supervisor Michiel, for his patience and getting me involved in this project. Although I was fortunate enough to already have been working on projects with you before my PhD, I appreciate you giving me the freedom to decide about starting a PhD, while still giving a slight push in the right direction. I'm very happy to have had such a kind and considerate supervisor! I've appreciated the fact that we could have sparing sessions and meetings where we could be on the same level, never did I have the feeling that I had to justify choices towards you as my boss (other than scientifically). I really appreciate the freedom you gave me to develop myself, find my own weaknesses and strengths, while guiding me to become an independent researcher and person!

This work would not have been possible without the collaboration with my direct colleagues and friends Paul and Jack. Thank you for the nice collaboration, useful conversations, feedback and of course the BBQs!

Within the Electronic Instrumentation Laboratory I was pleased to have colleagues who helped me on several aspects of my PhD. Kofi, thank you for the nice sparing sessions we had, in spite of your busy schedule. Joyce, thank you for all your support in the EI group. Special thanks to our technicians Lukasz, Zu-Yao and Ron, who have helped with the numerous 3D-prints, bonding many ASICs and reviewing PCBs. And Lukasz, I've really appreciated our sparing sessions on mechanical and sometimes unrelated projects!

Also several people in the Acoustical Wavefield Imaging group deserve my gratitude. Nico and Martin, thank you for all the productive feedback during the project. Henri and Emile, thank you for all your technical and practical support. Angela, thanks for being such a positive person always happy to help with planning and solving issues.

A large thanks to my other colleagues and friends at the Electronic Instrumentation Laboratory, and in particular Eunchul, Mingliang, Gerd, Yannick, Arthur, Roger, Yu, Johan, Jan and Thoon. You and the many other people in our group (sorry, I've met too many people in 8 years at EI to name everyone personally) made it such an enjoyable place to work, even in the shadow of MLM tape-outs, getting kicked out of our beloved high-rise building and the covid pandemic.

Just as important as a nice working environment are the caring friends with whom I got to relax and eat home made pizza on many lovely evenings. Dennis, Anne, Roel, Luke, Tim and Annemarijn, thanks a lot for your support and ensuring that I could enjoy my spare time at its best. Dennis in particular, thank you for talking about, and working together on so many (un)finished hobby projects.

Two high school friends have been supporting me for over 15 years, which definitely deserves a special mention. I'm so happy to still get to meet up and enjoy tinkering on nice projects, playing board games and having enjoyable days together. Thank you Laurens and Anouk for your support and being such good friends!

Although I had been climbing for many years already, it was during my PhD that I met a lot of new climbing friends and got to appreciate sporting several times a week. Bryan, Nina, Saskia, Loredana, Kate, Laura, Nathan and Vera, thank you for helping me to clear my mind and recharge in many good climbing sessions! With you guys, I've learned to mentally push my limits and improve several grades! And yes, (sometimes) it works, Lore, to tell me I'm not coming down before I top out the route . . .

I would also like to thank my family: Pien, Edwin, Jelle and Tijmen for their continuous support, not only during my PhD, but well before that time, when I left Zeist to study in Delft.

Possibly the most important person to thank is my loving girlfriend Claudia! Thank you for tolerating all the technical discussions which likely didn't make any sense to you, for cheering me up with board games when there was no progress and for providing your unconditional support.